Selektive Wirt-Gast-Wechselwirkungen in der Metall-organischen Gerüstverbindung MIL-101

Dissertation

zur Erlangung des akademischen Grades eines Doktors der Naturwissenschaften (Dr. rer. nat.) im Fach Chemie an der Fakultät Biologie, Chemie und Geowissenschaften der Universität Bayreuth

vorgelegt von

Thomas Josef Wittmann

geboren in Neustadt a. d. Waldnaab

Bayreuth, 2017

Die vorliegende Arbeit wurde in der Zeit von Januar 2013 bis Oktober 2017 in Bayreuth am Lehrstuhl Anorganische Chemie III unter Betreuung von Herrn Professor Dr. Jürgen Senker angefertigt.

Vollständiger Abdruck der von der Fakultät für Biologie, Chemie und Geowissenschaften den Universität Bayreuth genehmigten Dissertation zur Erlangung des akademischen Grades eines Doktors der Naturwissenschaften (Dr. rer. nat.).

Dissertation eingereicht am: 26.10.2017

Zulassung durch die Promotionskommission: 08.11.2017

Wissenschaftliches Kolloquium: 19.10.2018

Amtierender Dekan: Prof. Dr. Stefan Peiffer

Prüfungsausschuss:

Prof. Dr. Jürgen Senker (Gutachter)

Prof. Dr. Birgit Weber (Gutachterin)

Prof. Dr. Peter Strohriegl (Vorsitz)

Prof. Dr. Markus Retsch

"Roma non fuit una die condita"

Walther von Châtillon (um 1135 - um 1200)

Inhaltsverzeichnis

Abkürzungsverzeichnis

2-AP	2-Aminopyridin
3-AP	3-Aminopyridin
AA	Akzeptor-Akzeptor
AD	Akzeptor-Donor
AO	Atomorbital
CAU	Christian-Albrechts-Universität
CP	Kreuzpolarisation von engl. cross-polarization
CPO	Coordination Polymer of Oslo
CSA	Anisotropie der chemischen Verschiebung von engl. chemical shift anisotropy
CUS	ungesättigte Koordinationsstelle von engl. coordinatively unsaturated site
DD	Donor-Donor
DDA	Donor-Donor-Akzeptor
DEA	Diethylamin
DFT	Dichtefunktionaltheorie
D-HMQC	dipolare Heteronuklear-Multiquantenkohärenz von engl. dipolar multiple-quantum coherence
DMOF	Dabco-MOF
HDvV	Heisenberg-Dirac-van Vleck
HKUST	Hongkong University of Science and Technology
IBU	Anorganische Baueinheit von engl. inorganic building unit
IRMOF	Isoreticular Metal-Organic Framework
LFSE	Ligandenfeldstabilisierungsenergie
MAS	Rotation um den magischen Winkel von engl. magic angle spinning
MIL	Matèriaux de l'Institut Lavoisier
MOF	Metall-organische Gerüstverbindung von engl. metal-organic framework
NMR	magnetische Kernresonanz von engl. nuclear magnetic resonance
ppm	Teile einer Million von engl. parts per million [10^{-6}]
PSM	Postsynthetische Modifizierung

PXRD	Röntgenpulverdiffraktometrie von engl. powder X-ray diffraction
REDOR	NMR Pulssequenz von engl. rotational-echo double-resonance
SBM	Solomon-Bloembergen-Morgan
SCUTC	South China University of Technology
SOMO	Einfach besetztes Molekülorbital von engl. singly occupied molecular orbital
STAM	St. Andrews Metal-Organic Framework
UiO	University of Oslo
UMCM	University of Michigan Crystalline Materials
URPh	Ureaphenyl bzw. Phenylharnstoff
URPy	Ureapyridin bzw. Pyridinharnstoff
UV-VIS	ultraviolett und sichtbar von engl. ultra-violet and visibl

1 Zusammenfassung / Summary

1.1 Zusammenfassung

Die vorliegende Arbeit beschäftigte sich mit der Entwicklung von MIL-101 basierten Metall-organischen Gerüstverbindungen, die selektive Wirt-Gast-Wechselwirkungen nach dem Schlüssel-Schloss-Prinzip in Form von multiplen, korrespondierenden Wasserstoffbrückenbindungen ausbilden.

Durch den postsynthetischen Einbau einer Phenylharnstoffgruppe in Al-MIL-101-NH_2 entstand Al-MIL-101-URPh, das eine zweifache Wasserstoffbrücken-Donor-Donor-Sequenz (DD) aufweist. Quantenchemische Rechnungen bestätigten jedoch, dass die dem Linker benachbarte N-H Einheit der Harnstoffgruppe eine starke Wasserstoffbrückenbindung mit der Carboxylatgruppe des Linkers eingeht. Aus diesem Grund war eine selektive Bindung des Dimethylacetylaceton mit seiner komplementären Akzeptor-Akzeptor-Sequenz (AA) nicht möglich. Stattdessen zeigte Al-MIL-101-URPh im Vergleich zu Al-MIL-101-NH_2 eine deutlich erhöhte Wasserstabilität von einer Woche anstelle von fünf Minuten in flüssigem Wasser und eine Erhöhung um den Faktor zwölf in gesättigter Wasserdampfatmosphäre bei 60 °C. Mit ^{1}H-^{27}Al D-HMQC-Spektroskopie konnte bewiesen werden, dass sich in Al-MIL-101-URPh weniger Wasser in der Nähe der Al^{3+}-Ionen als in Al-MIL-101-NH_2 aufhält, obwohl die Wassersorptionsisothermen eine höhere Wasseraufnahme für Al-MIL-101-URPh zeigten. Folglich ist die Stabilität nicht durch Verdrängung von Wasser aus den Poren von MIL-101 begründet, sondern durch Abschirmung der Al-Terephthalat Bindungen durch die hydrophoben Phenylreste. Demzufolge ist die Wahrscheinlichkeit geringer, dass Wasser gegen die Linker ausgetauscht und somit die Struktur zersetzt wird.

Aufgrund der am Linker gebundenen, geblockten N-H Einheit der Harnstoffgruppe konnte erst mit dem postsynthetischen Einbau einer Pyridinharnstoffgruppe in Al-MIL-101-NH_2 eine effektiv wirkende Wasserstoffbrücken-Donor-Akzeptor-Sequenz (DA) realisiert werden. Die Selektivität von 2-Aminopyridin (2-AP) gegenüber 3-Aminopyridin (3-AP),

die als Modellmoleküle dienten, wurde schließlich in Al-MIL-101-URPy im Vergleich zu Al-MIL-101-NH_2 um den Faktor drei erhöht. Die Begründung lieferten die ^{15}N- Festkörper--NMR-Spektroskopie und quantenchemischen Rechnungen mit der Ausbildung einer zweifachen komplementären Wasserstoffbrücke zu 2-AP (AD-Sequenz). Identisches Adsorptionsverhalten von 2-AP und 3-AP wurde in den entsprechend funktionalisierten, isoretikulären Cr-MIL-101 Verbindungen gefunden. Nach Modifizierung der chemisch stabileren Cr-MIL-101 Derivate mit Diethylamin (DEA) gelang die Steigerung der Selektivität von 2-AP gegenüber 3-AP in Cr-MIL-101-URPy um weitere 50 %, was auf den beobachteten Rückgang der Aufnahme von nur 3-AP zurückgeführt werden konnte.

Die Untersuchung der Ursache für diesen Rückgang der Aufnahme von 3-AP und die Konkurrenzadsorptionen von H_2O, 2-AP, 3-AP und DEA an den für MIL-101 typischen offenen Koordinationsstellen erfolgte mit ^{13}C- und ^{1}H- Festkörper-NMR-Spektroskopie an den paramagnetischen Cr-MIL-101 Derivaten. Durch die hier auftretende Hyperfeinwechselwirkung erfuhren nur diejenigen NMR-Signale der Gastmoleküle einen positiven oder negativen Beitrag zu ihren diamagnetischen chemischen Verschiebungen, die an die Cr^{3+}- Zentren koordiniert sind. Anderweitig physisorbierte Gastmoleküle zeigten hingegen ihre charakteristischen, diamagnetischen chemischen Verschiebungen. Voraussetzung für die Ableitung dieser Adsorptionspräferenzen war eine eindeutige Signalzuordnung. Dies wurde anhand der Kombination von REDOR-Depahsierungswerten und Spin-Gitter-Relaxationszeiten (T_1) mit zusätzlicher Verifizierung der Zuordnungen durch DFT-Rechnungen erreicht. Während die Depahsierungswerte unter Einbeziehung der Dynamik von Linker- und Gastmolekülen sowie der anisotropen ^{1}H-Hyperfeinverschiebungen die Art der chemischen Gruppe festlegten, lieferten die T_1-Daten Abstandsinformationen der Atome zu den paramagnetischen Zentren. Infolgedessen war bei gleichzeitiger Beladung der Gastmoleküle die Beobachtung einer deutlichen Präferenz für 3-AP gegenüber 2-AP bzw. DEA bzgl. der Koordination an die Metallzentren möglich, während für 2-AP eine nur leicht bevorzugte Affinität gegenüber DEA festgestellt werden konnte. Bei gleichzeitiger Beladung von 3-AP und DEA wurden für DEA nur die typischen diamagnetischen Signale beobachtet. Der Rückgang der Aufnahmekapazität von 3-AP in DEA@Cr-MIL-101-URPy ist demnach kein Resultat des koordinierten DEA, sondern einer über starke Wasserstoffbrücken gebundenen DEA-Spezies in der sekundären

Koordinationssphäre, die die offenen Koordinationsstellen effektiv gegen 3-AP blocken kann.

1.2 Summary

The present work was concerned with the development of MIL-101-based metal organic framework compounds, which are designed to form selective host-guest interactions via multiple and corresponding hydrogen bond patterns according to the key-and-lock principle.

The postsynthetic incorporation of a phenylurea group into Al-MIL-101-NH_2 resulted in Al-MIL-101-URPh bearing a double hydrogen donor-donor sequence (DD). However, quantum chemical calculations indicated that the N-H moiety of the urea group adjacent to the linker undergoes strong hydrogen bonds with the carboxylate group of the linker. Thus, the test molecule dimethylacetylacetone with its complementary acceptor-acceptor sequence (AA) could not be selectively bound. Instead, Al-MIL-101-URPh showed a significantly enhanced water stability from five minutes to one week in liquid water and by a factor of twelve in a saturated water vapour atmosphere at 60° C compared to Al-MIL-101-NH_2. It has been demonstrated with solid-state ^{1}H-^{27}Al D-HMQC spectroscopy that Al-MIL-101-URPh contains less water in the vicinity of the Al^{3+}-ions than in Al-MIL-101-NH_2, although the water adsorption isotherms showed a higher water adsorption for Al-MIL-101-URPh. Thus, the stability is not due to displacement of water from the pores of Al-MIL-101, but by shielding the Al-terephthalate bonds by the hydrophobic phenyl residues. This reduces the probability that water will be exchanged against the linkers, which results in the decomposition of the structure.

Due to the blocked N-H unit of the urea group adjacent to the linker, an effective two-fold donor-acceptor (DA) hydrogen bond sequence could only be realized with the postsynthetic incorporation of a pyridine urea group into Al-MIL-101-NH_2. The selectivity of 2-aminopyridine (2-AP) against 3-aminopyridine (3-AP), which served as test molecules, finally increased by a factor of three in Al-MIL-101-URPy compared to Al-MIL-101-NH_2. This was confirmed by solid-state ^{15}N NMR spectroscopy and quantum chemical

calculations with the formation of a twofold complementary hydrogen bond to 2-AP (acceptor-donor sequence). The same adsorption behaviours of 2-AP and 3-AP were found in the correspondingly functionalized isoreticular Cr-MIL-101 compounds. After modification the coordinatively unsaturated sites of the chemically more stable Cr-MIL-101 derivatives with diethylamine (DEA), the selectivity of 2-AP against 3-AP in Cr-MIL-101-URPy was increased by further 50%, which was due to the reduced uptake of only 3-AP.

The reason for the lower uptake of 3-AP as well as the competitive adsorption of H_2O, 2-AP, 3-AP and DEA at the coordinatively unsaturated metal sites, which are typical for MIL-101, were investigated with solid-state ^{13}C and ^{1}H NMR spectroscopy on the paramagnetic Cr-MIL-101 derivatives. As a result of the hyperfine interaction, only those NMR signals of the guests molecules coordinated to the Cr^{3+} centres have a positive or negative contribution to their diamagnetic shifts. The prerequisite for the derivation of the adsorption preferences was an unambiguous signal assignment. This was achieved by combining REDOR dephasing values and spin-lattice relaxation times (T_1) followed by an additional verification of the assignments by DFT calculations of the chemical shifts. While the dephasing values, that take into account the dynamics of linkers and guest molecules as well as the ^{1}H anisotropic hyperfine shifts, determined the nature of the chemical groups, the T_1 data provided distance information of the atoms of the coordinated guest molecules to the paramagnetic centres. Thus, a clear preference for 3-AP versus 2-AP and DEA, respectively, was observed after the concomitant loading of the guest molecules with respect to coordination to the metal centres, whereas a slightly preferred affinity for 2-AP over DEA was evaluated. After the simultaneous loading of 3-AP and DEA, only the diamagnetic signals for DEA were observed. The reduced absorption capacity of 3-AP in DEA@Cr-MIL-101-URPy is, therefore, not due to a coordinated DEA species. Instead, there is a DEA species in the secondary coordination sphere bound by strong hydrogen bonds, which effectively blocks the open coordination sites against 3-AP.

2 Einleitung

2.1 Motivation und Zielsetzung

Die Trennung von Stoffen auf molekularer Ebene, die adsorptive Reinigung von Abwässern und Abgasen, der Einsatz als Katalysator, die Medikamentenverabreichung und Sensorik sind die klassischen Anwendungsgebiete von porösen Materialien.[1–14] Diese Anwendungen basieren in erster Linie auf selektiven Wechselwirkungen zwischen Gastmolekül und Wirtsgitter. Die Selektivitäten werden realisiert, indem die Porengrößen, -formen und -funktionalisierungen den zu trennenden Molekülen angepasst werden.[15–17]

Demnach wird die kinetische Trennung von Molekülen von anorganischen Zeolithen,[18] Aluminophosphaten[18,19] und Aktivkohlen[20] genutzt. Deren Wirkung beruht auf den Molekularsiebeffekt, d. h. die Trennung aufgrund der unterschiedlichen Größe und/oder Form der starren und periodisch angeordneten Porenfenster im Vergleich zur Größe/Form der Gastmoleküle.[21] Thermodynamisch kontrollierte Wechselwirkungen wie die van-der-Waals-Wechselwirkungen, einfache und mehrfache Wasserstoffbrückenbindungen, π-π-Wechselwirkungen und die Bildung von *Lewis*-Säure-Basen Paaren werden durch funktionelle Gruppen realisiert, die in Form und Wechselwirkungsstärke den zu trennenden Molekülen angepasst werden.[8,9,21] Diese Arten der Wechselwirkungen können in erster Linie aufgrund ihres modularen Aufbaus und Hybridcharakters von Metall-organischen Gerüstverbindungen realisiert werden. Insbesondere die organischen Linkermoleküle können verschiedene funktionelle Gruppen (-NH_2, -OH, -COOH) tragen, die postsynthetisch zu größere Funktionalitäten wie Amide, Harnstoffe und Ester umgesetzt werden können.[22–24] Beispielsweise ist für die selektive Adsorption von *ortho*-Xylol gegenüber den *meta* und *para* Analoga in MIL-53 (Al, Fe) sowohl die Form des Gastmoleküls als auch die Geometrie des Gerüstes verantwortlich. Die Orientierung zweier Linker an einem Cluster schließen genau den Winkel ein, so dass nur die zwei Methylgruppen von *ortho*-Xylol gleichzeitig mit je einem Carboxylat-Sauerstoffatom der Terephthalate wechselwirken können.[25,26] Auch ungesättigte Metallzentren in MOFs können stark selektiv wirken. Beispielsweise zeigten MOFs mit harten *Lewis*-sauren Metallen wie Al-, Fe-, Cr- und V-MIL-100[27] sowie Cr-MIL-101[28–30] höhere Selektivitäten für harte *Lewis*-Basen wie N-heterozyklische Aromaten, während MOFs mit weicheren

Lewis-sauren Metallen wie HKUST-1 (Cu)[31] und CPO-27 (Ni, Co)[28,32] weichere *Lewis*-Basen wie schwefelhaltige Heterozyklen bevorzugten.

Jedoch können Wechselwirkungen zu größeren und komplexeren Gastmolekülen mit mehreren funktionellen Gruppen mit dem Molekularsiebeffekt und mit unspezifischen funktionellen Gruppen wie Amino- oder Hydroxylgruppen nicht realisiert werden, sondern benötigen hochspezifische Wechselwirkungen. Diese werden durch supramolekulare Bindungsmotive bereitgestellt, wie sie von Peptiden und DNA-Helices bekannt sind[33,34] und auf multiplen Wasserstoffbrückenbindungen basieren und die geometrische und elektrostatische Komplementarität zwischen Gastmolekül und Wirt deren Assoziation begünstigen.[35,36] Supramolekulare Bindungsmotive sind in Metall-organischen Gerüstverbindungen kaum realisiert worden. Lediglich Yaghi *et al.* bauten Polyethergruppen in MOF-1001 ein, um stereospezifisch Paraquat Dikationen über Ion-Dipol Wechselwirkungen einzulagern.[37] Li *et al.* koordinierten Adenin als Co-Ligand an das Metallzentrum eines Zink-Trimesat-MOFs und beobachteten komplementäre Wasserbrückenbindungen zu Thymin.[38]

Ziel dieser Arbeit war es deshalb, selektive Wirt-Gast-Wechselwirkungen in der Metall-organischen Gerüstverbindung MIL-101 herzustellen und die Wechselwirkungen auf makro- und mikroskopischer Ebene zu analysieren und zu verstehen. Spezieller Fokus sollte dabei auf spezifischen Wechselwirkungen nach dem Konzept der supramolekularen Chemie mit größeren Gastmolekülen gelegt werden. Um diese spezifischen Wechselwirkungen zu erreichen, sollten geeignete Rezeptoren in den Poren des MOFs durch postsynthetische Modifikation eingeführt werden, die mittels multipler komplementärer Wasserstoffbrückenbindungen eine erhöhte Adsorptionsaffinität zu einem gewünschten Gastmolekül aufweisen. Da die selektive Anbindung größerer Moleküle auch größere Rezeptoren voraussetzt, stellte der MOF vom Typ MIL-101 aufgrund seiner mesoporösen Kavitäten und seiner funktionalisierbaren Aminolinker die ideale Plattform dar.[39–41] Davon ausgehend sollen durch postsynthetische Modifizierungen der Aminolinker eine Phenylharnstoffgruppe mit einer Wasserstoffbrücken-Donor-Donor-Sequenz (DD) und eine Pyridinharnstoffgruppe mit einer Wasserstoffbrücken-Donor-Donor-Akzeptor-Sequenz (DDA) bereitgestellt werden. Diese Verbindungen sollen hinsichtlich Struktur, chemischer Zusammensetzung, Porosität und chemischer Eigenschaften im Detail analysiert werden.

Zum Test auf selektive Wechselwirkungen der Phenylharnstoffgruppe soll Dimethylacetylaceton (AA-Sequenz) bzw. der Pyridinharnstoffgruppe sollen 2-Aminopyridin (2-AP, AD-Sequenz) und 3-Aminopyridin (3-AP, D oder A) als Probenmoleküle dienen. Aus deren Adsorptionsverhalten kann das Adsorptionsverhalten von strukturellen ähnlichen, technologisch relevanten Molekülen wie den N-heterozyklischen Aromaten abgeleitet werden. Um die selektive Adsorption der Pyridinharnstoffeinheiten evaluieren zu können, sollten die stark konkurrierenden *Lewis*-sauren Adsorptionsplätze an den Metallionen mit hydrophoben Diethylaminliganden geblockt werden.

Um die Selektivität eines an dem Linker angebrachten Wasserstoffbrückenmusters eindeutig evaluieren zu können, sind Kenntnisse über die Adsorptionsaffinität und Selektivität der anorganischen Baueinheiten, die konkurrierende Adsorptionsplätze darstellen, notwendig. Ein weiteres Ziel dieser Arbeit war es deshalb, spektroskopisch eindeutig nachzuweisen, welche Liganden an die anorganischen Einheiten koordinieren, um die Affinität jener zu strukturell und chemisch ähnlichen Gastmolekülen ableiten zu können. Da dies in mesoporösen MOFs aufgrund der fehlenden Translationssymmetrie und großer Elementarzellen erschwert ist und mit Festkörper-NMR-Spektroskopie an diamagnetischen Verbindungen sowie mit Schwingungs- und UV/VIS-Spektroskopie aufgrund von Signalüberlagerungen erschwert wird, sollten zu diesem Zweck die unterschiedlichen Hyperfeinverschiebungen der Ligandatome in paramagnetischen Cr MIL-101 dienen. Grundvoraussetzung ist eine eindeutige Zuordnung der Signale, das in paramagnetischen Systemen aufgrund der Hyperfeinverschiebung komplizierter ist. Es soll deshalb eine NMR-spektroskopische Methodik entwickelt werden, die anhand der Kenntnis, von welcher chemischen Gruppen das unbekannte Signal erzeugt wird und wie weit die entsprechenden Atomkerne von den paramagnetischen Metallzentren entfernt sind, zur Identifizierung von Signalen führt. Hierfür sollen die N-Heterozyklen 2-Aminopyridin und 3-Aminopyridin sowie das aliphatische Diethylamin als Probenmoleküle untersucht werden. Heterozyklische Aromaten sind wichtige Moleküle in der Umwelt, deren Verständnis seiner Wechselwirkung mit metallischen Koordinationsstellen, sei es beispielsweise für die Adsorption solcher aus Abwässern,[4,7] unabdingbar ist.

2.2 Metall-organische Gerüstverbindungen (MOFs)

Unter Metall-organischen Gerüstverbindungen (*engl.: metal-organic frameworks*) versteht man poröse, anorganisch-organische Hybridmaterialien, die sich aufgrund ihres kristallinen Aufbaus durch eine regelmäßige Anordnung der Poren auszeichnen.[15,16,42–44]

MOFs sind aus zwei zentralen Komponenten aufgebaut: den Konnektoren, die aus Metallkationen oder mehrkernigen Metall-Sauerstoff-Clustern bestehen und als anorganische Baueinheiten (*IBU von engl.: inorganic building units*) bezeichnet werden sowie den organischen Liganden (Linkern), die die anorganischen Baueinheiten über koordinative Bindungen miteinander verknüpfen.[3,15,16,42,43,45] Als Linker werden hauptsächlich chemisch modifizierbare, starre, aromatische und multidentate Carboxylatliganden eingesetzt, so dass außerordentlich stabile Gerüste entstehen.[43] Durch den modularen Aufbau aus Konnektoren und funktionalisierten Linkermolekülen mit unterschiedlicher Anzahl und Anordnungen an Koordinationsstellen resultieren vielfältige Strukturmotive von ein-, zwei- oder dreidimensionalen Netzwerken.[42,43]

Die Porengröße und -geometrie werden dabei maßgeblich von der lokalen Geometrie und Dimensionalität der IBUs und der Länge der organische Linkermoleküle bestimmt.[46,47] Die Geometrie eines Metallclusters bestimmt die räumliche Anordnung der Linker und legt somit die Position des nächsten Metallclusters fest. So realisieren beispielsweise eindimensionale, lineare Ketten aus eckenverknüpften MO_6 Oktaedern ($M = Al^{3+}$, $Cr^{3+,}$ Fe^{3+}), die in MIL-53 mit Terephthalsäure verbunden sind, mikroporöse Kanäle, während jene MO_6 Oktaeder in MIL-101 isolierte trimere μ_3-oxido zentrierte Cluster bilden und mit Terephthalsäure untereinander verknüpft, mesoporöse Kavitäten erzeugen. Ein typisches Beispiel für die Vergrößerung des Porendurchmessers durch längere Linkermoleküle ist die MOF-5 Struktur, in der die ZnO_4 Tetraeder von Terephthalsäure verbrückt werden[48] und man durch deren Ersatz durch Biphenylterephthalsäure und Triphenylterephthalsäure die isoretikulären IRMOF-10 bzw. IRMOF-16 erhält.[49]

Ein Hauptunterschied zu andern porösen Materialien wie den rein anorganischen Zeolithen oder organischen porösen Kohlenstoffen ist die Möglichkeit, die organischen Linkermoleküle gezielt zu funktionalisieren. In einigen Fällen können auch die IBUs funktionalisiert werden, wenn diese offene und zugängliche Koordinationsstellen besitzen.

Die bekanntesten Vertreter hierfür sind HKUST-1(Cu^{2+})[50] und MIL-101(Al^{3+}, Fe^{3+}, Cr^{3+}).[39,51]

Durch die Vielfältigkeit an Porengrößen und -geometrien sowie an Funktionalitäten ergeben sich unterschiedliche und spezielle Anwendungsmöglichkeiten[52] in Speicherung und -trennung[4,7,53] von Stoffen aus der flüssigen und gasförmigen Phase, in heterogener Katalyse, Sensorik[13,14] und Medikamentenverabreichung.[10–12] MOFs können auch als Trägermaterial für katalytisch wirksame Metallkomplexe und Nanopartikel sowie für aktive Spezies dienen, die magnetische und ionenleitfähige Eigenschaften bedingen wie z. B. Spin-Crossover[54] oder Protonenleitfähigkeit.[55,56]

2.2.1 Chemische Funktionalisierungen von MOFs

MOFs können auf verschiedene Arten funktionalisiert werden und somit deren chemischen und physikalischen Eigenschaften wie Polarität oder Säure/Base Charakter den gewünschten Anforderungen angepasst werden.[42] Eine weit verbreite Variante ist der direkte Einsatz von funktionalisierten Linkermolekülen.[49] So konnten beispielsweise auf Terephthalsäure basierende isoretikuläre (d. h. gleichnetzige) Derivate von Cr-MIL-101 mit jeweils nur -NH_2, -NO_2, -Cl, -Br und -SO_3H Gruppen, aber auch jene mit einer Mischung aus solchen Linkern dargestellt werden (*mixed linker MOFs*).[57] Weitere bedeutende Terephthalat-basierte MOFs sind die isoretikulären -NH_2, -NO_2, -Br, -(Br_2), -Cl, -OH, -COOH und -$(COOH)_2$ Derivate von UiO-66,[58,59] in dem die katonischen $Zr_6O_4(OH)_4$ Cluster miteinander verbrückt werden, oder die -Cl, -Br, -CH_3, -NH_2, -NO_2, -$(OH)_2$ und -COOH Derivate von Al-MIL-53.[60–63] Entscheidend für den Erfolg der MOF-Synthese mit Einsatz dieser funktionalisierten Terephthalate ist zum einen die Löslichkeit in dem zur Synthese verwendeten Lösungsmittel und zum anderen die Bedingung, durch die zusätzliche funktionelle Gruppe keine Konkurrenz zu den Carboxylateinheiten bezüglich der Koordination an die Metallionen zu schaffen um so den Aufbau des dreidimensionalen nicht Gerüstes zu verhindern.

Desweiteren können funktionelle, organische Gruppen, die entweder den Aufbau des Gerüstes verhindern oder den drastischen MOF-Synthesebedingungen, insbesondere niedrige pH-Werte und teils solvothermale Bedingungen, nicht standhalten, durch

postsynthetische Modifikation (PSM) eingebaut werden.[23,24,64] Dies bedeutet die nachträgliche Modifizierung der kristallinen, porösen Gerüststruktur nach der eigentlichen Synthese und erfordert die Aktivierung des MOFs, d. h. die Entfernung von synthesebedingt in Porenraum eingelagerten Edukten und Lösungsmittel um den Zugang der PSM-Reaktanden zu den reaktiven funktionellen Gruppen des MOFs zu gewährleisten.
Dabei existiert die Möglichkeit der Koordination von organischen, *Lewis*-basischen Molekülen an die Metallzentren.[24] Voraussetzung hierfür sind MOFs, die zum einen offene, zugängliche Koordinationsstellen aufweisen können (*CUS von engl.: coordinatively unsaturated sites*), z. B. Stellen, an denen nach der Synthese Wassermoleküle terminal koordiniert sind und thermisch entfernt werden können und zum anderen eine stärkere Metall-Ligand Bindung aufweist, als die des Metalls mit dem *Lewis*-basischem PSM Reagens, um die MOF Struktur nicht aufzulösen.[24] So konnten Williams *et al.* nach Entfernung der Wassermoleküle Pyridin an die CUS von HKUST-1 koordinieren, dessen IBUs aus Cu^{2+}-Dimeren bestehen und von Trimesinsäure schaufelradförmig koordiniert werden. Hwang *et al.* konnten die IBUs von Cr-MIL-101 mit verschiedenen Diamin-Liganden und einem Palladium-Amin-Liganden funktionalisieren und so die katalytische Aktivität im Porenraum für die *Knoevenagel*-Kondensation von Benzaldehyd und Ethylcyanoacetat erhöhen.[51] In Cr-MIL-100 konnte die Wasseraufnahmekapazität durch den Einbau von hydrophilen Glykol- und Diamin-Liganden erhöht werden.[65]
Einen weitaus größeren Modifizierungsspielraum hinsichtlich verschiedener und komplexerer Typen an funktionellen Gruppen bietet die kovalente PSM der Linkermoleküle (Abb. 1), da hier funktionelle Gruppen eingebracht werden, indem man auf das breite Spektrum der organischen Chemie zurückgreifen kann.[64] Limitiert ist die kovalente PSM dahingehend, dass die Reaktionen präfunktionalisierte Linker mit einer chemisch reaktiven Gruppe wie $-NH_2$ oder –OH erfordern. Zudem muss die Stabilität des Gerüst gegenüber dem zur PSM verwendeten Lösungsmittel, dem elektrophilen PSM-Reagens, meist ein Derivat eines Anhydrids, Isocyanates oder Säurechlorids, und den Reaktionsbedingungen der PSM gegeben sein. Letztere laufen in der Regel unter milderen Bedingungen (< 100 °C) und unter Verwendung von inerten Lösungsmitteln (Dichlormethan, Chloroform, Toluol) ab. Dabei wurden unter allen präfunktionslierten MOFs die amino-funktionalisierten bevorzugt für PSM-Reaktionen eingesetzt. So konnten beispielsweise die Amino-Gruppen von IRMOF-3,[66,67] dem Amino-Derivat von MOF-5, von UMCM-1-NH_2[68–70] und D-MOF-1-NH_2,[68,71] Al-MIL-53-NH_2,[72,73] UiO-66-NH_2[59,74] und

Cr-MIL-101-NH_2[75,76] mit Carbonsäureanhydriden oder Isocyanaten zu Amid bzw. Harnstoffgruppen umgewandelt werden. Cr-MIL-101-H konnte bisher als einzige Verbindung ausgehend vom Terephthalsäure Linker zum Harnstoffderivat funktionalisiert werden, indem über Nitrierung und anschließende Reduzierung das Nitro- bzw. Amino-Derivat aufgrund ihrer außerordentlichen Stabilität im sauren Medium erhalten werden konnte.[77]

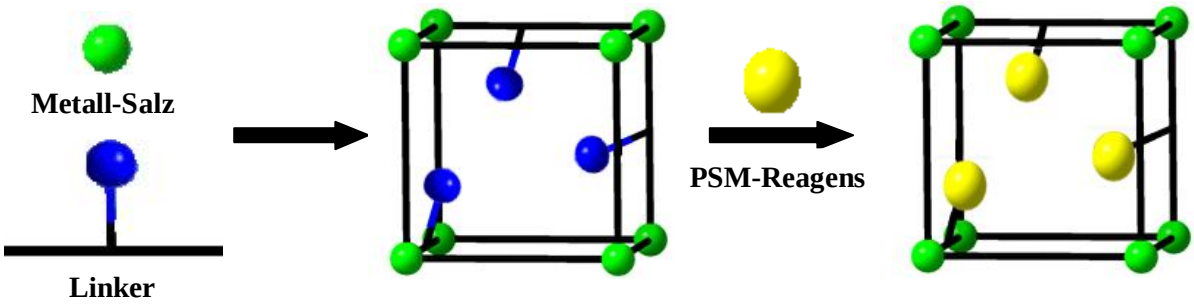

Abb. 1: Schematische Darstellung des modularen Aufbaus von MOFs und deren postsynthetische Modifizierung (PSM).

2.2.2 Stabilität von MOFs

Eine wichtige Voraussetzung für die Funktionalisierung und schließlich Anwendbarkeit von MOFs ist deren chemische und thermische Stabilität. Aufgrund der ständigen Präsenz von Wasser entweder direkt in flüssiger Form oder über die Luftfeuchtigkeit ist die Wasserstabilität für den Einsatz zur Gaspeicherung und -trennung, Adsorption von Stoffen aus der wässrigen Phase in der Katalyse, für pharmazeutische Anwendungen oder als Wärmetauscher von besonderer Bedeutung.[4,7,78,79] Die thermische Stabilität spielt bei der Reinigung von heißen Abgasen eine wichtige Rolle, z. B. zur Abtrennung von CO_2.[9] Während die thermische Stabilität von MOFs aufgrund der Zersetzung des organischen Anteils in der Regel auf 450 °C - 500 °C begrenzt ist,[78,79] wird die chemische Stabilität von der Geschwindigkeit des Linkeraustausches durch Wasser oder anderen koordinationsfähigen Molekülen bestimmt,[80–82] wobei langsamere Austauschraten für Metallionen mit höheren Ladung/Atomradien Verhältnissen beobachtet wurden.[83,84] Weitere einflussreiche Parameter sind die Metall-Ligand-Bindungsstärken, die mit der Oxidationsstufe der Metalle, der *Brönstedt*-Basizität und Zähnigkeit der Linker

korrelieren.[81] Bei Übergangsmetall-basierten MOFs hängt die Stabilität zusätzlich von der Besetzung der d-Orbitale ab, da die daraus resultierende Ligandenfeldstabilisierungsenergie (LFSE) die Austauschrate bestimmt.[85] Bei den Zn^{2+}-basierten MOFs DMOF-1, UMCM-1[83] und MOF-5[86] sind alle d-Orbitale vollständig besetzt (d^{10}), so dass die LFSE keinen Beitrag zur Stabilisierung liefert und demnach jene MOFs hoch feuchtigkeitsempfindlich sind. Für das Cu^{2+}-Trimesat (d^9) HKUST-1 wurde ebenfalls eine geringe Wasserstabilität beobachtet.[87,88] Im Gegensatz dazu weisen die Zr^{4+}-basierten (d^0) UiO-66 Derivate aufgrund der hohen Oxidationsstufe und die Cr^{3+}-Terephthalate (d^3) Cr-MIL-53[84] und Cr-MIL-101[89,90] aufgrund der hohen LFSE eine extrem hohe Wasserstabilität auf. Im Gegensatz zu den Cr-Terephthalaten sind für Al^{3+} und Fe^{3+} nur die MIL-53 Modifikationen in Wasser stabil.[91,92] Der Grund dafür sind die sterisch mehr abgeschirmten eckenverknüpften IBUs in MIL-53, die lineare Ketten ausbilden und einen hohen Verknüpfungsgrad zu benachbarten parallelen Ketten aufweisen. In MIL-101 dagegen liegen isolierte trimere Metallcluster vor, die lediglich zu sechs weiteren Clustern verknüpft sind, so dass die IBUs für Wasser zugänglicher sind und zudem der Austausch eines Linkers gegen Wasser aufgrund des niedrigeren Verknüpfungsgrades schwerer wiegt als bei MIL-53. Ein weiteres Beispiel für eine wasserstabile Al-Terephthalat Modifikation stellt CAU-1 dar, in dem die abwechselnd ecken- und kantenverknüpften IBUs abgeschirmte Acht-Ringe bilden, die wiederum mit zwölf weiteren Acht-Ringen über Terephthalat verknüpft sind.[93]

Jedoch konnte durch Einsatz von alkylierten und fluorierten Linkern wasserstabile MOFs erhalten werden, die isoretikulär zu den wasserempfindlichen Zn^{2+} MOFs MOF-508, SCUTC-18, SCUTC-19,[94] DMOF-1[80,95] und zu HKUST-1[96,97] (Cu^{2+}) sind. Die Stabilitätserhöhungen beruhen dabei auf geringeren Wasseraufnahmekapazitäten aufgrund der hydrophoben Linker.[72,98,99]

2.2.3 Struktur und Eigenschaften von MIL-101

Einer der wichtigsten und meist erforschten MOFs, der auch Gegenstand dieser Arbeit ist, ist MIL-101. Die Struktur von MIL-101 wurde erstmals im Jahr 2005 von der Gruppe um Gerard Ferey am Institut Lavoisier in Versailles postuliert,[39] daher auch der Name MIL (von frz.: Matèriaux de l'Institut Lavoisier). Die Struktur konnte nicht mit Röntgendiffraktionsdaten gelöst werden, sondern durch Abgleich eines experimentellen Pulverdiffraktogramms mit einem simulierten einer der berechneten Strukturen, die durch Kombination von Cr^{3+} Ionen mit Terephthalsäure realisierbar sind. Die anorganischen Einheiten (IBUs) bestehen aus trimeren MO_5X - Oktaedern (M = Al^{3+}, Cr^{3+}, Fe^{3+}, V^{3+}),[39,40,91,100,101] die über ein gemeinsames Sauerstoff-Atom μ_3 eckenverknüpft sind. Die drei Metallatome bilden dabei ein gleichseitiges Dreieck mit dem μ_3- Sauerstoff Atom im Zentrum. Jedes Metallatom wird dabei von zwei Carboxylatgruppen des Linkers mit dem benachbarten Metallatom verbrückt (Abb. 2, links). Vier der sechs Oktaederpositionen pro Metall werden somit von vier Carboxylat-Sauerstoffatomen gestellt. Um die oktaedrische Umgebung zu erfüllen, besitzt jedes M^{3+} Ion einen terminalen Liganden. Zwei der drei M^{3+}-Ionen werden nach der Synthese von Wasserliganden koordiniert, ein M^{3+} ist entweder von einem Chlorid Ion, Fluorid oder Hydroxid Ion besetzt. Für Chloride als Metallquelle ist Chlorid koordiniert wie für Al-MIl-101-NH_2,[41,102] Fe-MIL-101-NH_2,[91] Cr-MIL-101-NH_2 und V-MIL-101.[101] Ist Flusssäure im Reaktionsgemisch vorhanden zur Synthese von Cr-MIL-101 vorhanden, fungiert ein Fluorid Ion als terminaler Ligand.[39,51,77] Hydroxy-Liganden wurden für Cr-MIL-101 mit $Cr(NO_3)_3$ gefunden.

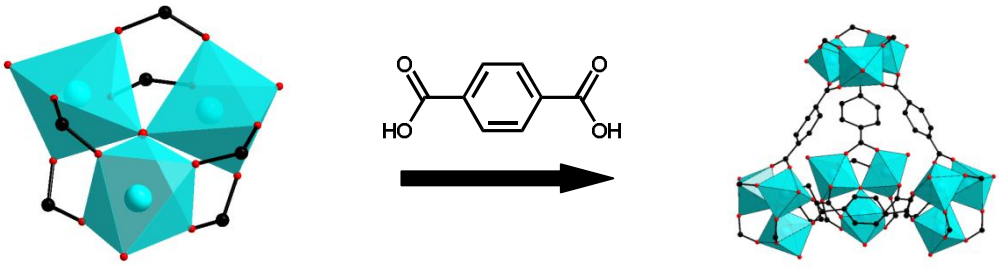

Abb. 2: Trimere μ_3-Sauerstoff verbrückte oktaedrische MO_5X – Cluster (links), die mit Terephthalaten zu Supertetraedern verknüpft werden (rechts).

Die trimeren Cluster werden durch Terephthalat basierte Linker zu sechs weiteren Clustern verbrückt. Somit bilden sich als strukturelle Untereinheit Supertetraeder mit einem Innendurchmesser von 0.8 nm - 0.9 nm aus,[39,41] deren Ecken die IBUs und die Kanten die Linker darstellen (Abb. 2, rechts).

Diese Supertetraeder sind weiterhin so verknüpft, dass sich eine 3D-Netzwerk ausbildet. Daraus entstehen zwei verschieden große mesoporöse Kavitäten mit kristallographischen Durchmessern von 2.9 nm (Abb. 3, oben links) und 3.4 nm (Abb. 3, oben rechts), die im Mengenverhältnis 2:1 vorliegen und über pentagonale bzw. hexagonale Fenster mit Durchmessern 1.2 nm und 1.6 nm (Abb. 3, unten) zugänglich sind.[39,91,101]

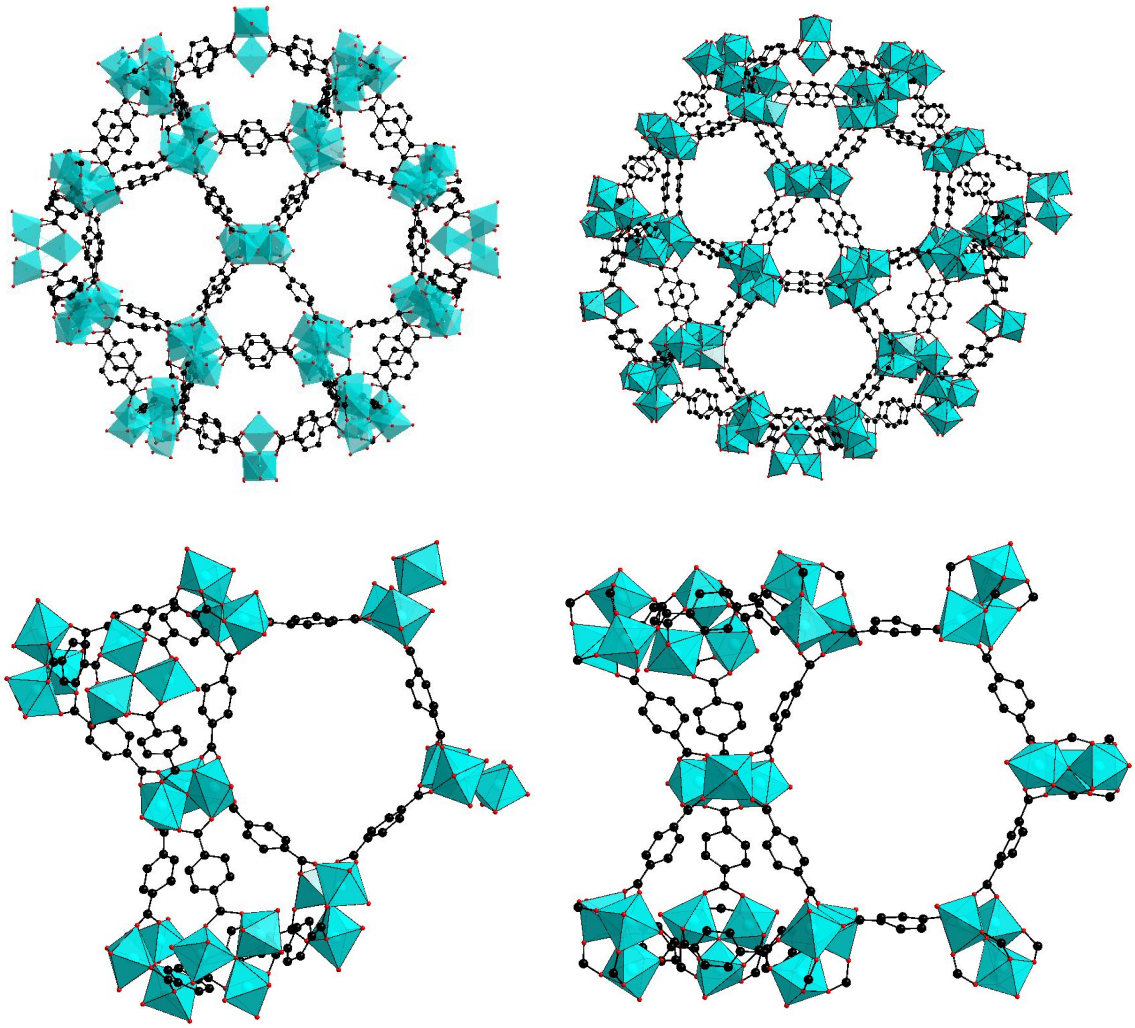

Abb. 3: Schematische Darstellung der mesoporösen Kavitäten (oben) und den pentagonal bzw. Fenstern der Kavitäten (unten).

Die MIL-101 Materialien sind aufgrund ihrer mesoporösen Kavitäten für die Einlagerung und Freisetzung von größeren Molekülen wie das Medikament Indomethacin[103] oder Medikamente gegen Tumore und AIDS,[104–106] zur Entfernung von Medikamenten wie dem Antibiotikum Nitroimidazol oder Naproxen aus dem Wasser[107–109] und von aromatischen N- und S-Heterocyclen wie Indol, Carbazol, Thiophen und Benzothiophen aus fossilen Brennstoffen[28–30,110,111] sowie für katalytische Reaktionen[51,102,112,113] wie beispielsweise von Knoevenagel Kondensation von Benzaldehyd[102] getestet worden.

2.3 Selektive Wirt-Gast-Wechselwirkungen in MOFs

Selektive Wirt-Gast-Wechselwirkungen in porösen Materialien können zum einen kinetisch, zum anderen thermodynamisch kontrolliert sein. Die kinetisch kontrollierten Wechselwirkungen werden maßgeblich durch die Größe und Form der Porenöffnungen geregelt, die den Zugang von größeren Molekülen als den Porendurchmesser bzw. von geometrisch nicht zur Porenöffnung passenden Molekülen verhindert.[21] Thermodynamisch kontrollierte Wechselwirkungen beruhen auf unterschiedlich starken supramolekularen Wechselwirkungen wie Dispersions-, Multipol- und π-π-Wechselwirkungen sowie Wassserstoffbrückenbindungen zwischen dem Wirtsgitter und den Gastmolekülen.[8,9,21] Art und Stärke der Wechselwirkungen, die ein Gastmolekül realisieren kann, hängt im Wesentlichen von der räumlichen Anordnung und Art, d. h. elektronischen Natur seiner funktionellen Gruppen ab. Beispielsweise beruht die Selektivität von Kohlenstoffdioxid gegenüber Stickstoff und Methan in HKUST-1[114,115] und MIL-53(Al, Cr)[116,117] auf der erhöhten Affinität zu polaren Adsorptionsplätzen, das auf dessen höherem Quadrupolmoment basiert.[8] Wack *et al.* konnten durch Einbringen einer Formamidogruppe in Al-MIL-53NH_2 die Selektivität für Aceton gegenüber Wasser und Ethanol aufgrund einer stärkeren Einzelwasserstoffbrückenbindung der Amid N-H Gruppe zum Keto-Sauerstoffatom erhöhen.[118] Für die selektive Adsorption von *ortho*-Xylol gegenüber den *meta* und *para* Analoga in MIL-53 (Al, Fe) ist sowohl die Form des Gastmoleküls als auch die Geometrie des Gerüstes verantwortlich. Die Orientierung zweier Linker an einem Cluster schließen genau den Winkel ein, so dass nur die zwei Methylgruppen von *ortho*-Xylol gleichzeitig mit je einem Carboxylat-Sauerstoffatom der Terephthalate

wechselwirken können.[25,26] Auch ungesättigte Metallzentren in MOFs können stark selektiv wirken. Beispielsweise zeigten MOFs mit harten Lewis sauren Metallen wie Al-, Fe-, Cr- und V-MIL-100[27] sowie Cr-MIL-101[28–30] höhere Selektivitäten für harte *Lewis*-Basen wie N-heterozyklische Aromaten, während MOFs mit weicheren *Lewis*-sauren Metallen wie HKUST-1 (Cu)[31] und CPO-27 (Ni, Co)[28,32] weichere *Lewis*-Basen wie schwefelhaltige Heterozyklen bevorzugten. Spezifische Wechselwirkungen mit Hilfe von supramolekularen Bindungsmustern sind Yaghi *et al.* realisiert worden. Sie bauten Polyethergruppen in MOF-1001 ein, um stereospezifisch Paraquat-Dikationen über Ion-Dipol-Wechselwirkungen einzulagern.[37] Selektive Wechselwirkungen aufgrund von multiplen, komplementären Wassserstoffbrückenbindungen, wie sie von den Peptiden und DNA-Helices bekannt sind,[33,34] sind in MOFs kaum realisiert worden. Lediglich Li *et al.* koordinierten Adenin als Co-Ligand an das Metallzentrum eines Zink-Trimesat-MOFs und beobachteten komplementäre Wasserbrückenbindungen zu Thymin.[38] Der gezielte Einbau solcher supramolekularer Bindungsmuster wie die multiplen Wasserstoffbrückenmotive in MOFs wird deshalb in dieser Arbeit vorangetrieben.

2.3.1 NMR-spektroskopische Untersuchungen von Wechselwirkungen in MOFs

Die Struktur von kristallinen Materialen wird routinemäßig mit Röntgeneinkristall- oder Röntgenpulverdiffraktometrie (XRD von engl.: *X-ray diffraction*) bestimmt. Die Strukturaufklärung von porösen MOFs ist jedoch aufgrund mangelnder Fernordnung durch erhöhte Gitterdynamiken, statistisch verteilte lokale Unordnungen oder statistisch verteilte eingelagerte Gastmoleküle beeinträchtigt. Auch die Tatsache, dass MOFs fast ausschließlich als mikrokristallines Pulver vorliegen und teils riesige Elementarzellen mit mehreren hundert Atomen besitzen, erschwert oder macht die Strukturbestimmung durch breite und sich überlappende Reflexe unmöglich.[118] Die Festkörper-NMR-Spektroskopie dagegen detektiert die lokale Umgebung von Atomen und ist daher die Methode der Wahl sowohl zur Untersuchung der Struktur, als auch von Wechselwirkungen des MOFs mit eingelagerten Gastmolekülen.[103,119] Aus struktureller Sicht können sowohl die organischen Linker, als auch die postsynthetisch eingebrachten organischen Seitengruppen an den

Linkern mit ^{1}H-, ^{13}C-, ^{15}N-, ^{19}F- oder ^{17}O-NMR charakterisiert werden.[41,93,118,120–123] Insbesondere die Seitengruppen verfügen durch den statistischen Einbau oder zu hoher Beweglichkeit keine Fernordnung und sind mittels XRD nicht nachweisbar. Auch die anorganischen Einheiten können mit ^{27}Al-NMR,[41,121,122,124,125] ^{71}Ga-NMR,[126,127] ^{67}Zn-[128,129] oder ^{91}Zr-NMR[128] für die entsprechenden MOFs im Hinblick auf die Koordinationsumgebung oder strukturelle Änderung an dieser untersucht werden. Beispielsweise sind die Linienformen in Al-MOFs, in denen die Al-Atome immer oktaedrisch koordiniert sind, charakteristisch für die Art der Verknüpfung der AlO_6-Oktaeder. So zeigen das ^{27}Al-NMR-Spektrum von Al-MIL-53 eine asymmetrische Linienform aufgrund der *trans*-Eckenverknüpfung der AlO_6-Oktaeder zu unendlich langen anisotropen Ketten,[121] während für die isolierten trimeren AlO_6-Oktaeder in Al-MIL-100[130] und Al-MIL-101-NH_2 mit einer isotropen Umgebung eine isotrope Linienform beobachtet wurde.[40,41]

Aufgrund der Tatsache, dass die chemische Verschiebung von Signalen von der lokalen elektronischen Umgebung der einzelnen Atome des MOFs abhängt, ist die Festkörper-NMR-Spektroskopie die Methode der Wahl um lokale Änderungen durch Wechselwirkung mit eingelagerten Molekülen zu untersuchen. Je nach Größe und Richtung der Änderung der chemischen Verschiebung eines bestimmten Signals kann nachvollzogen werden, mit welchen Positionen des MOFs und mit welcher Stärke das eingelagerte Molekül bevorzugt wechselwirkt. So konnten Wack *et al.* anhand der signifikanten Tieffeldverschiebung des ^{13}C-Carbonylkohlenstoffatoms nur von Aceton nach Einbringen einer Formamido-Gruppe in Al-MIL-53-NH_2 dessen stärkere Wasserstoffbrücken-Wechselwirkung mit dieser und die Selektivität gegenüber Wasser und Ethanol zeigen.[118] ^{1}H-NMR- und ^{15}N-NMR-Studien sind ebenfalls sehr geeignet um Wassserstoffbrückenbindungen zu Gastmolekülen zu analysieren. ^{1}H-NMR-Signale erfahren eine zunehmende Tieffeldverschiebung mit zunehmender Stärke der Wasserstoffbrückenbindung bis zu 10 ppm, wobei der Größe der Verschiebung dirket mit der Länge und der Stärke beispielsweise einer N-H···N-Bindung korreliert werden kann.[131–133] Aufgrund der sehr großen chemischen Verschiebungsdispersion reagieren ^{15}N-NMR-Signale sehr empfindlich auf Wasserstoffbrückenbindungen, dem Grad der Protonierung und auf Säure-Base-Eigenschaften.[134,135] Abhängig von der Art des N-Atoms finden entweder Hoch- oder Tieffeldverschiebungen statt. So erfahren Pyridin-^{15}N-Atome eine Hochfeldverschiebung je nach Stärke bis zu -100 ppm, wohingegen ^{15}N-Amino- und

^{15}N-Harnstoffsignale nur um 5-10 ppm tieffeldverschoben werden.[133,134] Beispielsweise konnten Yaghi *et al.* anhand der Tieffeldverschiebung des ^{15}N-Signals zeigen, dass das ammoniumverwandte Paraquat-Dikation mit der Polyethereinheit von MOF-1001 wechselwirkt.[37] Weiterhin lieferte die Analyse des chemischen Verschiebungstensors (CSA) anhand der Linienform des ^{13}C-Signals von adsorbiertem CO_2 Informationen über die Orientierung und Art der Bewegung innerhalb der Poren von Al-MIL-53[136] und Mg-MOF-74 mit zugänglichen Lewis sauren Metallen.[137]

2.3.2 NMR-Spektroskopie an paramagnetischen MOFs

Da die Festkörper-NMR-Spektroskopie an paramagnetischen Systemen ein wichtiger Bestandteil dieser Arbeit ist, werden hierfür in diesem und nächstem Unterkapitel die theoretischen Grundlagen erläutert.

Untersuchungen zu Struktur als auch zu Wirt-Gast-Wechselwirkungen sind auch an paramagnetischen MOFs möglich, wenn auch deutlich weniger häufig durchgeführt. Dies ist einerseits auf die erschwerte Spektrenaufnahme, als auch auf die erschwerte Spektreninterpretation zurückzuführen.[138–140]

Die magnetischen Momente der ungepaarten Elektronen der Metalle wechselwirken mit magnetischen Momenten der Kerne, was als Hyperfeinwechselwirkung bezeichnet wird.[138–143] Diese zusätzlichen Magnetfelder am Kernort führen einerseits zu Verschiebungen der isotropen, diamagnetischen NMR-Signale, andererseits zu extrem verkürzten Spin-Gitter- und Spin-Spin-Relaxationszeiten.[138–145] Letztere sorgen zusammen mit der Anisotropie der magnetischen Bulk-Suszeptibilität[140,142,146] zu einer Signalverbreiterung, so dass nahe beieinanderliegende Signale überlappen. Jedoch kann der Nachteil sehr breiter Signale durch damit einhergehenden großen positiven oder negativen Hyperfeinverschiebungen von mehreren Hundert ppm kompensiert werden. Die beobachteten Signale im NMR-Spektrum setzten sich somit aus dem diamagnetischen Anteil δ_{dia} und dem Hyperfein-Anteil δ_{hf} zusammen:

$$\delta_{beobachtet} = \delta_{dia} + \delta_{hf} = \delta_{dia} + \delta_{FC} + \delta_{PC} \quad (1)$$

Die Hyperfeinverschiebung eines Signals setzt sich aus den isotropen Teilen des Fermi-Kontakt-Wechselwirkungstensors und des Tensors der dipolaren Elektron-Kern-Kopplung zusammen.[143] Die isotrope Fermi-Kontakt-Verschiebung δ_{FC} entsteht durch das zusätzliche Magnetfeld, das durch das magnetische Moment der ungepaarten Elektronendichte (auch ungepaarte Spindichte genannt) am Kernort entsteht (d. h. in s- oder s-haltigen Hybridorbitalen). Das durchschnittliche magnetische Moment der Elektronen, das die Kerne erfahren, ist proportional zur ungepaarten Spindichte am Kernort, ausgedrückt durch die isotrope Hyperfeinkopplungskonstante A_{iso}, das mit dem zeitlichen gemittelten Boltzmann verteilten Überschuss an Elektronspin $\langle S_z \rangle$ mit paralleler Orientierung zum äußeren Magnetfeld in z-Richtung gewichtet wird. Aufgrund der um mehrere Größenordnungen schnelleren Elektronenspinübergänge als Kernspinübergänge erfahren die Kernspins in ihren M_I Zuständen nicht beide Orientierungen der Elektronenspins M_S = +/- ½, sondern den durch die Elektron-Zeeman Aufspaltung bestimmten Erwartungswert $\langle S_z \rangle$. Die Fermi-Kontakt-Verschiebung für isotrope g-Werte ergibt sich aus dem Quotienten aus Kontakt-Wechselwirkungsenergie und Kern-Zeeman Energie

$$\delta_{FC} = -10^6 \frac{A_{iso}}{\hbar \gamma_I B_0} \langle S_z \rangle = 10^6 \frac{A_{iso}\, g\, \mu_B\, S(S+1)}{3\hbar \gamma_I\, kT} \qquad (2)$$

wobei $\hbar$ das reduzierte Plancksche Wirkungsquantum, γ_I das gyromagnetische Verhältnis des Kerns, B_0 das externe Magnetfeld, g den elektronischen g-Faktor, μ_B das Bohr'sche Magneton, S die Gesamtspinquantenzahl, k die Boltzmann Konstante und T die Temperatur angeben.[138,139,141]

Ungepaarte Spindichte am Kernort kann entweder direkt über chemische Bindungen durch Delokalisation über σ-Bindungen (σ-Delokalisation) oder indirekt durch Spin-Polarisation der Elektronen in den bindenden σ-Orbitalen (1s, 2s, $2sp^2$) durch delokalisierte ungepaarte Spindichte in den π-Orbitalen desselben Atoms (z. B. $2p_z$) erzeugt werden.[138,141,147]

Die Wahrscheinlichkeit, direkt delokalisierte ungepaarte Spindichte (über σ- und π-Bindungen) an einem bestimmten Atom zu finden, hängt vom Ausmaß der Beteiligung seiner Atomorbitale (AOs) zum SOMO (von engl.: *singly occupied molecular orbital*) ab.[147–149] Einen signifikanten Beitrag zum SOMO haben in der Regel die Atomorbitale der

Atome, die bis zu zwei Bindungen vom paramagnetischen Metall entfernt sind. Die Delokalisation signifikanter Mengen an ungepaarter σ- und π-Spindichte erfolgt meist nur bis zu diesen Atomen und hat immer positives Vorzeichen.[147,149] Entsprechend erfahren auch die NMR-Signale dieser Kerne eine positive (Tieffeldverschiebung) Hyperfeinverschiebung. Diese positive ungepaarte Spindichte induziert dann indirekt ungepaarte Spindichte mit alternierendem Vorzeichen in den s-Orbitalen der weiter entfernten Kerne durch Spin-Polarisation.[147–149] Dementsprechend zeigen die nachfolgenden Signale dieser Kerne alternierend negative und positive Hyperfeinverschiebungen.

Über welchen Weg die ungepaarten Elektronen delokalisieren, hängt davon ab, ob sie sich in den σ-symmetrischen d-Orbitalen ($d_{x^2-y^2}$, d_{z^2}) wie z. B. in oktaedrisch koordinierten Ni^{2+}-(d^8) und Cu^{2+}- Verbindungen (d^9) oder in den π-symmetrischen d-Orbitalen (d_{xy}, d_{xz}, d_{yz}) wie z. B. in oktaedrisch koordinierten Cr^{3+}- (d^3) und V^{3+}-Verbindungen (d^2) befinden.[141,150] Es ist auch möglich, dass beide Mechanismen gleichzeitig wirken, wie z. B. in oktaedrisch koordinierten high-spin Fe^{3+}-Verbindungen (d^5).

Da nur die Atome von Molekülen eine Fermi-Kontakt-Verschiebung zeigen, die an die paramagnetischen Metallzentren koordiniert sind, lassen sich mit Festkörper-NMR-Spektroskopie, wie in dieser Arbeit gezeigt, Adsorptionspräferenzen bzgl. der offenen Koordinationstellen in MOFs ableiten.

Einen weiteren Beitrag zur Hyperfeinverschiebung liefert die Pseudo-Kontakt-Verschiebung δ_{PC}, die aus dem Quotienten der dipolaren Elektron-Kern-Wechselwirkungsenergie und der Kern-Zeeman-Energie erhalten wird.[138,139,141,143] Gemäß einer dipolaren Wechselwirkung über den Raum korreliert die Größe der Pseudo-Kontakt-Verschiebung indirekt proportional zur dritten Potenz des Abstandes r von Kern zum ungepaarten Elektron ($\sim 1/r^3$), das vereinfachter Weise als am Metall lokalisierte Punktladung angenommen wird (Metall-zentrierte Punkt-Dipol-Näherung). Weiterhin ist die Pseudo-Kontakt-Verschiebung abhängig von der Orientierung des magnetischen Kernmoments μ_I zur Hauptachse des anisotropen magnetischen Suszeptibilitätstensors χ und wird zu Null für einen Winkel θ von 54.7°, da der orientierungsabhängige Teil dieser dipolaren Wechselwirkung von $(3\cos^2\theta - 1)$ abhängt. Der magnetische Suszeptibilitätstensor ist anisotrop, wenn der g-Tensor anisotrop

ist.[151] Die Differenz der Komponenten eines axialsymmetrischen g-Tensors $g_\perp$ und g_{II} beispielsweise beeinflussen ebenfalls die Größe der Pseudo-Kontakt-Verschiebung, die folglich nur für anisotrope g-Tensoren existieren. Ebenfalls wird die Pseudo-Kontakt-Verschiebung von der Größe der Nullfeldaufspaltung D beeinflusst.[138,139,141,143] Für Cr^{3+}-Verbindungen mit einer Spinquantenzahl von S = 3/2, wie die in dieser Arbeit behandelten Cr-MIL-101-Verbindungen, ist die Pseudo-Kontakt-Verschiebung gegeben durch[139]

$$\delta_{PC} = -\frac{5\mu_B^2 (g_{II}^2 - g_\perp^2)}{12kT} \frac{(3\cos^2\theta - 1)}{r^3} \left[1 - \frac{4\left(g_{II}^2 + \frac{1}{2}g_\perp^2\right)D}{5(g_{II}^2 - g_\perp^2)kT} \right] \quad (3)$$

Da jedoch für die Cr^{3+} Ionen in Cr-MIL-101 nahezu identische Werte für $g_\perp$ und g_{II} (1.985 und 1,980) sowie kleine Werte für D (~ 0.01 cm^{-1}) ermittelt wurden, ist der Beitrag von δ_{PC} für die beobachteten Hyperfeinverschiebung der hier untersuchten Cr-MIL-101-Derivate vernachlässigbar.

Die kurzen Spin-Gitter- (T_1) und Spin-Spin-Relaxationszeiten (T_2) der Kerne in paramagnetischen Verbindungen resultieren aus fluktuierenden Magnetfeldern, die durch die magnetischen Momente der ungepaarten Elektronen verursacht werden. Diese fluktuierenden Magnetfelder sind effiziente Relaxationspfade für Kerne, die mit den ungepaarten Elektronen skalar (über Bindungen) oder dipolar (über den Raum) wechselwirken. Diese schnell fluktuierenden Magnetfelder sind Folge der schnellen elektronischen Relaxationszeiten.[143,144,151] Die schnellen Übergänge der Elektronenspins zwischen den elektronischen Zeeman Niveaus M_s = +/- 1/2 führen zu schnellen Orientierungsänderungen der Elektronenspinvektoren was zu kurzen Elektronenkorrelationszeiten τ_s führt (τ_s ~10^{-10} s - 10^{-11} s für Übergangsmetallionen).[143,144] Die Elektron-Kern-Wechselwirkung wird zusätzlich von der Beweglichkeit von Molekülteilen relativ zum Metallzentrum beeinflusst. Die entsprechende Orientierungsänderung des Kernspinvektors kommt in der Rotationskorrelationszeit τ_r zum Ausdruck.[143,144,151] Elektron- und Rotationskorrelationsraten werden additiv zur Korrelationsrate $1/\tau_c$ zusammengefasst ($1/\tau_c = 1/\tau_s + 1/\tau_r$) und bestimmt die Spektrale

Dichte in der Solomon-Bloembergen-Morgan-Gleichung (SBM), die die Relaxation (T_1 und T_2) der Kerne beschreibt.[142–144,151,152] In die SBM-Gleichung geht zudem die quadratische dipolare Elektron-Kern-Wechselwirkungsenergie ein, so dass die Relaxationszeiten indirekt proportional mit der sechsten Potenz des Kern-Elektron-Abstandes skalieren.[142–144,151] Die Spin-Gitter-Relaxationsrate setzt sich additiv aus der Fermi-Kontakt-, der dipolaren Elektron-Kern- und der Curie-Spin-Relaxationsrate zusammen.[138,143,144,153,154] Bei hohem externen Magnetfeld dominiert in paramagnetischen Festkörpern jedoch nur die dipolare Elektron-Kern-Relaxation, dessen Rate folgendermaßen beschrieben wird:[143,144]

$$\frac{1}{T_1^{para,dipolar}} = \frac{2}{5}\left(\frac{\mu_0}{4\pi}\right)^2 \frac{\mu_B^2\, g_e^2\, \gamma_I^2\, S(S+1)}{r^6}\left[\frac{\tau_C}{1+\omega_I^2\,\tau_C^2}\right] \tag{4}$$

Die Fermi-Kontakt- und Curie-Spin-Beiträge werden ausführlich in Kapitel 6.3.2 behandelt.

τ_C ist in Festkörpern aufgrund geringer Beweglichkeit von τ_S dominiert. Da τ_S wiederum nur vom Übergang der elektronischen Zeeman-Niveaus abhängt und somit für alle Metallionen unabhängig vom koordinierten Liganden identisch ist, ist die beobachtete Relaxationsrate $1/T_{1para}$ gegeben durch:

$$\frac{1}{T_1^{para}} = \sum_{i=1}^{N}\frac{1}{T_1^{Cr^i}} = \sum_{i=1}^{N}\frac{const}{r_{M^i}^6} = const\cdot\sum_{i=1}^{N}\frac{1}{r_{M^i}^6} = const\cdot R \tag{5}$$

wo R die Abstandsumme eines Kernes zu allen paramagnetischen Metallzentren M^i in der Umgebung ist. Folglich ist das Verhältnis der Spin-Gitter-Relaxationsraten zweier Signale *ref* und *x* nur vom Verhältnis der Abstandssummen R der entsprechenden Kerne abhängig:

$$\frac{T_{1,ref}}{T_{1,x}} = \frac{R_x}{R_{ref}} \tag{6}$$

Bei eindeutiger Zuordnung eines Kerns zum Signal *ref* kann durch die Kenntnis von dessen R_{ref} aus einem quantenmechanisch optimierten Strukturmodel und $T_{1,ref}$ sowie durch

Kenntnis von $T_{1,x}$ des unbekannten Signals *x* dessen R_x ermittelt werden. Somit kann das unbekannte Signal *x* eindeutig einem Kern aus dem Strukturmodell zugeordnet werden.
Auch die Breite eines Signals, die u. a. durch die T_2-Relaxationszeit bestimmt wird, kann wichtige Hinweise zur Signalzuordnung liefern, da breitere Signale unter der Voraussetzung, dass die Anisotropie der magnetischen Bulk-Suszeptibilität für alle Atome eines polykristallinen Pulvers im Schnitt konstant ist, kürzere Abstände zum paramagnetischen Metallzentrum implizieren. Die ermittelten Elektron-Kern-Abstände von Gastmolekülen können dazu dienen, diese in den Poren des MOFs zu lokalisieren und somit Aussagen über bevorzugte Adsorptionsplätze zu treffen, die mit XRD-Daten aufgrund der fehlenden Translationssymmetrie nicht möglich sind. Dies macht die Festkörper-NMR-Spektroskopie an paramagnetischen MOFs zu einem wertvollen und sensiblen Werkzeug zur Untersuchung von mikroskopischen Adsorptionsmechanismen.

Von den wenigen NMR-Studien an paramagnetischen MOFs wurden die meisten mit HKUST (Cu^{2+}) durchgeführt. So wurden strukturelle Änderungen sowie die Zersetzung von HKUST durch verschiedene Mengen an adsorbiertem Wasser[88] sowie durch Ammoniak[155] mit ^{1}H- und ^{13}C-NMR verfolgt. Die Untersuchung der Wechselwirkung von HKUST mit CO und CO_2 anhand der isotropen und anisotropen chemischen Verschiebung und des ^{13}C-NMR-Signals[156] sowie die Art der Bewegungsprozesse von ^{13}CO und $^{13}CO_2$ innerhalb der Poren erfolgte anhand der Spin-Gitter-Relaxationszeiten (T_1) bei verschiedenen Temperaturen.[157] Ashbrook *et al.* untersuchten die Struktur von HKUST-1 und STAM-1, ein HKUST-Derivat mit monomethyliertem Linker, sowie deren strukturelle Änderung nach Wasserbeladung.[158] Für die Ibuprofen beladenen Cr-MIL-53 und Fe-MIL-53[159] und die Indomethacin beladenen Cr-MIL-101 und Fe-MIL-101[103] wurden lediglich die ^{1}H- und ^{13}C-NMR Spektren aufgenommen.

2.3.3 NMR-Spektroskopie an austauschgekoppelten Verbindungen

Die Austauschwechselwirkung der ungepaarten Elektronen paramagnetischer Ionen wird durch den Heisenberg-Dirac-van Vleck (HDvV) Hamilton-Operator *H* beschrieben. Im Fall der Cr^{3+} Ionen mit den Spins $S_1 = S_2 = S_3 = 3/2$ in MIL-101 setzt sich *H* aus der Summe der

Skalarprodukte von jeweils zwei Spinvektoren S multipliziert mit den jeweiligen isotropen Kopplungskonstanten J_{12}, J_{13} und J_{23} zusammen:[160,161]

$$H = J_{12} S_1 \cdot S_2 + J_{13} S_1 \cdot S_3 + J_{23} S_2 \cdot S_3 \tag{7}$$

Die Energieeigenwerte des HDvV-Operators stellen die neuen Energieniveaus E_i als Funktion der Gesamtspinzustände S_i dar, die durch Anwendung der Vektoradditionsregel für zwei Spinvektoren erhalten werden. Zunächst werden die Zwischenspinzustände S_{12} durch $|S_1 + S_2|$, $|S_1 + S_2 - 1|$,...,$|S_1 - S_2|$ und schließlich die Gesamtspinzustände S_i durch $|S_{12} + S_3|$, $|S_{12} + S_3 - 1|$,... $|S_{12} - S_3|$ erhalten.[162] Somit ergeben sich für S_{12} die Werte 3, 2, 1, 0 sowie für S_i die Werte 9/2, 7/2 (2), 5/2 (3), 3/2 (4), 1/2 (2). Die Zahlen in den Klammern geben die Häufigkeit der resultierenden Gesamtspinzustände an.

Unter der Annahme, dass die magnetische Anisotropie für das triadische Cr^{3+}-System in MIL-101 bei Raumtemperatur vernachlässigbar ist, sind die drei isotropen Kopplungskonstanten gleich groß, so dass das die Energieeigenwerte E_i durch

$$E_i = -J\left[S_i\left(S_i+1\right) - 3S_{1,2,3}\left(S_{1,2,3}+1\right)\right] \tag{8}$$

gegeben sind.

In die Berechnung der Fermi-Kontakt-Verschiebung fließt neben der Hyperfeinkopplungskonstante A_i für jeden Zustand S_i auch das magnetische Moment jedes S_i Zustandes ein, gewichtet mit der Boltzmann-Besetzung P_i und der jeweiligen Multiplizität $2S_i+1$. Die Gesamt-Fermi-Kontakt-Wechselwirkung für austauschgekoppelte Metallionen ist gegeben durch

$$\delta_{FC} = -\frac{1}{\hbar\gamma_I B_0}\sum_i A_i \langle S_z\rangle_i P_i = \frac{g_e \mu_B}{3\hbar\gamma_I kT}\sum_i A_i S_i\left(S_i+1\right)\frac{\left(2S_i+1\right)\exp\left(-E_i/kT\right)}{\sum_i\left(2S_i+1\right)\exp\left(-E_i/kT\right)} \tag{9}$$

Jeder elektronische Zustand S_i besitzt eine eigene und unbekannte isotrope Hyperfeinkopplungskonstante A_i (i = 1/2, 3/2, 5/2, 7/2, 9/2) zu einem Kern. Um jedoch für jedes an dem magnetischen Austausch beteiligten Metallion j eine Hyperfeinkopplungskonstante A_j angeben zu können, die experimentell oder durch quantenchemische Rechnungen bestimmt werden kann, wird A_j mit dem

Spinprojektionskoeffizienten C_{ij} gewichtet. Dieser gibt den Anteil der einzelnen Metalle A_j zu den jeweiligen A_i der Austausch-gekoppelten Zustände S_i gemäß

$$A_i = A_j\, C_{ij} \tag{10}$$

an.[142,163–165] Die drei Werte für C_j in MIL-101 sind nur von den einzelnen Gesamtspinquantenzahlen S_1, S_2 und S_3 (= 3/2 für Cr^{3+}) und von den Zwischenspinquantenzahlen S_{12} (3, 2, 1, 0 für Cr^{3+}) abhängig und werden folgendermaßen bestimmt:[161,165]

$$C_{1,2} = \frac{(-1)^{2(S_1+S_2+S_3+2S_{12}+S)}\left[S(S+1)+S_{12}(S_{12}+1)-S_3(S_3+1)\right]\left[S_{12}(S_{12}+1)+S_{1,2}(S_{1,2}+1)-S_{2,1}(S_{2,1}+1)\right]}{4\,S_{12}(S_{12}+1)S(S+1)} \tag{11}$$

$$C_3 = \frac{(-1)^{2(S_3+S_{12}+S)}\left[S(S+1)+S_3(S_3+1)-S_{12}(S_{12}+1)\right]}{2\,S(S+1)} \tag{12}$$

Demnach ergibt sich Gleichung (9) zu[163,164,166]

$$\delta_{FC} = -10^6\,\frac{g_e\,\mu_B}{3\hbar\,\gamma_I\,kT}\sum_{j=1}^{3}A_j\sum_i C_{ij}\,S_i(S_i+1)\frac{(2S_i+1)\exp(-E_i/kT)}{\sum_i(2S_i+1)\exp(-E_i/kT)} \tag{13}$$

Zur Berechnung der Energieeigenwerte E_i in Gleichung (8) wird die isotrope Kopplungskonstante J mit Hilfe von Messungen der magnetischen molaren Suszeptibilität χ_M bestimmt und durch Anpassen mit der Bleany-Bowers-Gleichung für ein triadisches System bestimmt. Diese erhält man durch Einsetzen der Energieeigenwerte E_i in die Van-Vleck-Gleichung, so dass für χ_M für MIL-101 unter Vernachlässigung der magnetischen Anisotropie gilt:[160,167–169]

$$\chi_M = \frac{N_A\,g^2\,\mu_B^2}{4kT}\,\frac{2+40\exp\left(3J/kT\right)+105\exp\left(8J/kT\right)+168\exp\left(15J/kT\right)+165\exp\left(24J/kT\right)}{2+8\exp\left(3J/kT\right)+9\exp\left(8J/kT\right)+8\exp\left(15J/kT\right)+5\exp\left(24J/kT\right)} \tag{14}$$

3 Synopsis

Die vorgelegte Dissertation basiert auf drei Publikationen, die von selektiven Wechselwirkungen von mittelgroßen Gastmolekülen mit mehreren funktionellen Gruppen in der Metall-organischen Gerüstverbindung MIL-101 handeln. Diese sollten durch Entwickeln von multiplen Wasserstoffbrückenmustern wie dem zweifachen Wasserstoffbrücken-Donor-Donor-Muster (DD) und dem dreifachen -Donor-Donor-Akzeptor-Muster (DDA) im Porenraum realisiert werden. Eine detaillierte Charakterisierung einer solchen Verbindung mit den Auswirkungen auf die chemischen Eigenschaften wird anhand von Al-MIL-101-URPh, das eine Phenylharnstoffgruppe (DD-Sequenz) aufweist, in Kapitel 3.1 gegeben. Die Erkenntnisse daraus werden genutzt, um selektive Wechselwirkungen der Pyridinharnstoffgruppe (DDA-Sequenz) am Linker in MIL-101-URPy (Al, Cr) mit den Modellmolekülen 2-Aminopyridin (AD-Sequenz) und 3-Aminopyridin (A- oder D-Muster) in Kapitel 3.2 zu erzeugen und zu analysieren. Das Verständnis aller möglichen Wechselwirkungen dieser Moleküle in MIL-101 wird in Kapitel 3.3 vervollständigt. Hier wird gezeigt, dass mit Methoden der Festkörper-NMR-Spektroskopie Wechselwirkungen mit den freien Koordinationsstellen von MIL-101 eindeutig an paramagnetischen Cr-MIL-101 Derivaten evaluiert werden können.

3.1 Wechselwirkung von Al-MIL-101-NH_2 mit Wasser nach Modifizierung der Linker mit hydrophoben Phenylresten

Zur selektiven Adsorption von Gastmolekülen mit einem zweifachen Akzeptor-Akzeptor-Wasserstoffbrückenmuster (AA) wurde Al-MIL-101-URPh synthetisiert. Diese Verbindung besitzt am Linker eine Phenylharnstoff-Ankergruppe (Schema 3.1.1), in der die Harnstoffeinheit als Wasserstoffbrücken-Donor-Donor (DD) fungieren kann.

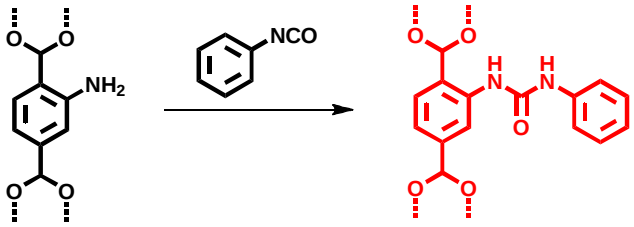

Schema 3.1.1: Postsynthetische Modifikation der Linker von Al-MIL-101-NH_2 (schwarz) zu Al-MIL-101-URPh (rot).

Al-MIL-101-URPh wurde durch Reaktion der Aminogruppe am Linker von Al-MIL-101-NH_2 mit Phenylisocyanat synthetisiert (Schema 3.1.1). Röntgenpulverdiffraktometrie zeigte, dass die Struktur von MIL-101 nach dieser postsynthetischen Modifizierungsreaktion erhalten blieb. Die ^{15}N-NMR-Spektren zeigen die erfolgreiche Umsetzung zur Phenylharnstoffgruppe (Abb. 3.1.2), was nach Auflösen des MOFs mit ^{1}H-NMR-Spektroskopie zu 86 % quantifiziert wurde.

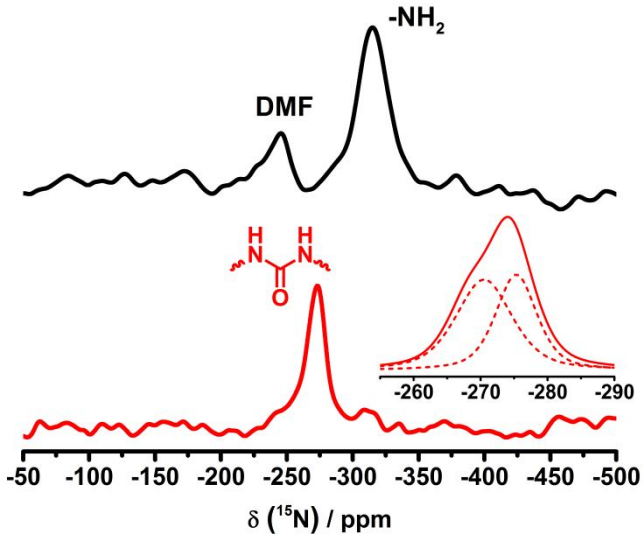

Abb. 3.1.1: ^{15}N-CP-MAS-NMR Spektren von Al-MIL-101-NH_2 (schwarz) und Al-MIL-101-URPh (rot). Die Vergrößerung zeigt die Entfaltung der zwei Harnstoffsignale von Al-MIL-101-URPh mit der Pseudo-Voigt-Funktion bei gleichen Halbwertbreiten FWHM.

Nach Einbau der Phenylharnstoffgruppe reduzierten sich spezifische BET-Oberfläche und totales spezifisches Porenvolumen um einen Faktor zwei, während die Porenradien von 2,5 und 2,9 nm auf 1,9 und 2,2 nm abnahmen. Eine selektive Anbindung von

Dimethylacetylaceton, das eine komplementäre Wasserstoffbrückensequenz (AA) aufweist, an die Harnstoffeinheit von Al-MIL-101-URPh konnte nicht beobachtet werden.

Dass die Phenylharnstoffgruppe nicht als Wasserstoffbrücken-Donor-Donor wirken kann, wurde mit quantenchemische Rechnungen gezeigt. Demnach bildet die N-H Gruppe des Harnstoffs, die sich näher am Linker befindet, starke Wasserstoffbrücken (ca. 76 kJ/mol) mit dem benachbarten Sauerstoffatom der Carboxylatgruppe des Terephthalatlinkers aus (N-H---O Abstand: 1,5 Å, Abb. 3.1.2). Somit kann die DD-Sequenz effektiv nur als einzelne Donor-Brücke wirken. Im nächsten Projekt (Kapitel 3.2) wird deshalb eine DDA-Sequenz eingebaut, die dann effektiv als zweifache DA-Sequenz dienen kann.

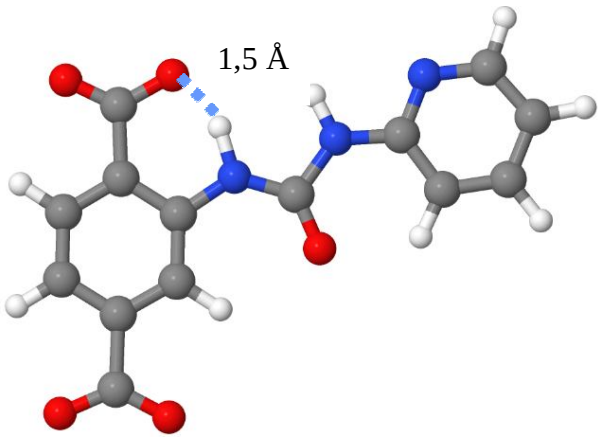

Abb. 3.1.2: Schematische Darstellung der Wechselwirkung der N-H Gruppe der Pyridinharnstoffgruppe mit dem Sauerstoffatom der Carboxylatgruppe.

Stattdessen wies Al-MIL-101-URPh im Gegensatz zu Al-MIL-101-NH_2 eine deutlich erhöhte Wasserstabilität auf. Während Al-MIL-101-NH_2 in flüssigem Wasser bei 25 °C bereits nach fünf Minuten kollabierte, hielt Al-MIL-101-URPh den Bedingungen bis zu einer Woche stand. Außerdem konnte die Zeit bis zur Auflösung des MOFs für Al-MIL-101-URPh bei 100% RH und 60 °C um einen Faktor zwölf bzw. um einen Faktor sechs bei sehr drastischen Bedingungen von 100% RH und 100 °C erhöht werden (Abb. 3.1.3).

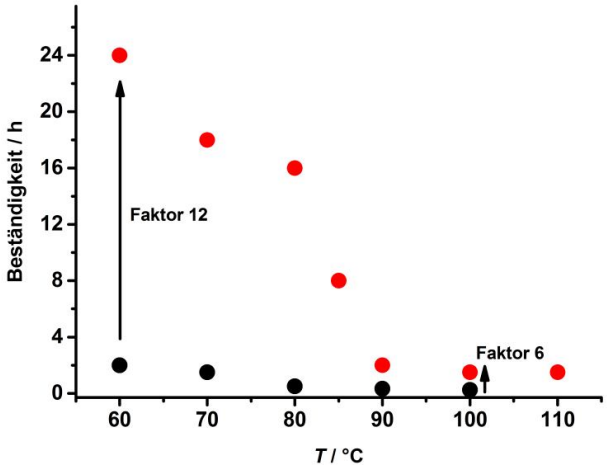

Abb. 3.1.3: Zersetzungszeiten von Al-MIL-101-NH_2 (schwarze Kreise) und Al-MIL-101-URPh (rote Kreise) nach Aufbewahren in wasserdampfgesättigter Atmosphäre (100 % RH) bei verschiedenen Temperaturen.

Da Wasser in flüssiger Form oder als Luftfeuchtigkeit unter realen Bedingungen ständig als Koadsorptiv vorliegt, ist die hinreichende Stabilität eines MOFs gegenüber Wasser eine grundlegende Voraussetzung für dessen Untersuchung von Wechselwirkungen mit Gastmolekülen unter realen Bedingungen wie z. B. der Adsorption schädlicher Umweltgase wie Methan oder CO_2 sowie der Adsorption von Schadstoffen aus feuchten Abgasen. Ein entscheidender Nachteil mancher MOFs gegenüber Zeolithen oder porösen organischen Polymeren ist jedoch deren Empfindlichkeit gegenüber Wasser, das mit dem strukturgebenden Linkern in Konkurrenz zur Koordinationsstelle am Metall tritt. Mit seinen mesoporösen Kavitäten und seiner geringen bis nicht vorhandenen Toxizität ist Al-MIL-101 ein vielversprechender Kandidat, größere, beispielsweise pharmazeutische Moleküle einzulagern, sei es zum Zwecke der Medikamentenfreisetzung oder als Adsorbens zur Extraktion solcher aus Gewässern.

Ziel des Projektes war es deshalb, die Wechselwirkungen von Al-MIL-101-NH_2 und von Al-MIL-101-URPh mit Wasser zu analysieren und die Ursache der erhöhten Stabilität auf mikroskopischer Ebene zu verstehen. Dies soll helfen, das Konzept der Stabilisierung durch postsynthetische Modifizierung gezielt auf andere MOF Systeme übertragen zu können. Um die Ursache dieser Stabilität zu analysieren, wurden die Wasseradsorptionskapazitäten ermittelt. Diese zeigen, dass Al-MIL-101-URPh sogar mehr Wasser aufnehmen kann als Al-MIL-101-NH_2, obwohl die Porenwände durch die Phenylreste in Al-MIL-101-URPh

hydrophober sind als in Al-MIL-101-NH_2 (Abb. 3.1.4a). Eine Stabilisierung aufgrund einer geringeren Wasseraufnahme liegt daher nicht vor.

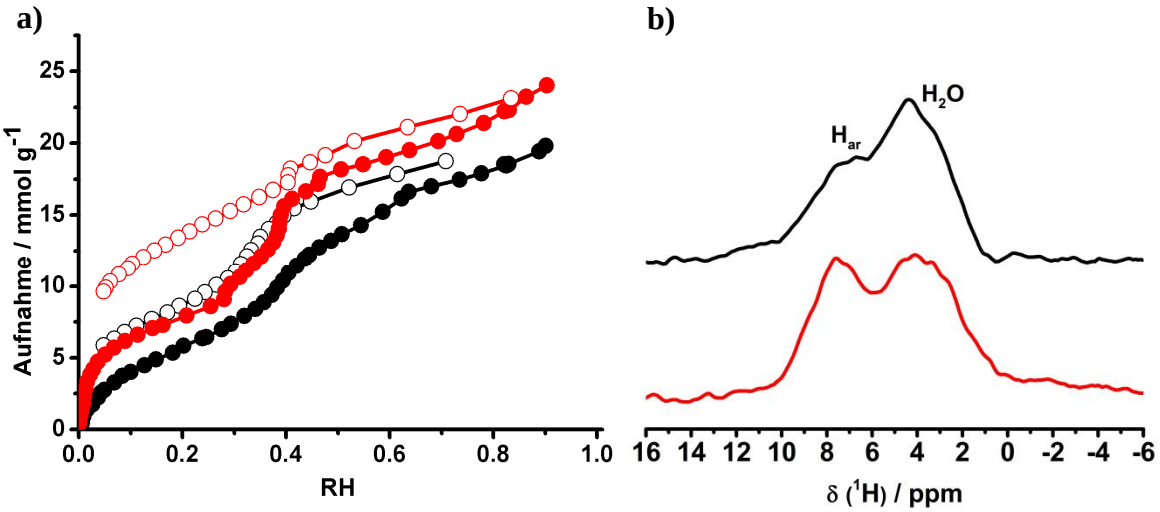

Abb. 3.1.4: a) H_2O-Ad- (volle Kreise) und Desorptionsisothermen (leere Kreise) für Al-MIL-101-NH_2 (schwarz) und Al-MIL-101-URPh (rot); b) 1D-^{1}H-Projektionen der ^{1}H-^{27}Al-D-HMQC-Spektren von Al-MIL-101-NH_2 (schwarz) und Al-MIL-101-URPh (rot).

Die Stabilität von MOFs hängt hauptsächlich von der Stabilität der Metall-Ligand Bindung und von der Geschwindigkeit des Linkeraustausches durch andere koordinationsfähige Moleküle wie Wasser ab. Deshalb wurde mit ^{27}Al-^{1}H D-HMQC-NMR-Spektroskopie untersucht, wie viel Wasser sich in der nächsten Umgebung der Al^{3+} Ionen aufhält. Die 1D-Projektion des ^{27}Al-^{1}H D-HMQC-Spektrums von Al-MIL-101-NH_2 zeigte eine höhere Intensität für die Protonen von Wasser im Vergleich zu den aromatischen Protonen, während Al-MIL-101-URPh gleiche Intensitäten für beide Spezies zeigte (Abb. 3.1.4b). Folglich befindet sich in Al-MIL-101-URPh weniger Wasser in unmittelbarer Nähe der anorganischen Einheiten als in Al-MIL-101-NH_2, obwohl mehr Wasser in Al-MIL-101-URPh enthalten ist. Dies belegt eindeutig einen Abschirmeffekt in Al-MIL-101-URPh gegenüber Wasser.

3.2 Einbringen einer Wasserstoffbrücken-DDA-Sequenz in MIL-101 (Al, Cr) für selektive Wechselwirkungen mit Gastmolekülen

Die Wasserstoffbrücken-Donor-Donor-Akzeptor-Sequenz wurde durch postsynthetische Modifizierung der Aminolinker von MIL-101-NH_2 (Al, Cr) mit Pyridin-2-isocyanat entwickelt. Letzteres konnte jedoch nicht direkt als solches in eine Reaktionsmischung mit dem MOF gegeben werden, da es aufgrund der Dimerisierung nicht als monomeres Molekül vorliegt, was die reaktiven Isocyanatgruppen deaktiviert (Schema 3.2.1).[170] Stattdessen wurde die stabile Vorstufe des Pyridin-2-isocyanates, das Pyridin-2-carbonylazid (**2**), das vorher aus 2-Picolinsäure (**1**) gewonnen wurde, mit den Amino-MOFs suspendiert (Schema 3.2.1). Anschließend wurde durch Temperaturerhöhung in einer *Curtius*-Reaktion die Acyl-Azid Spezies zum entsprechenden Isocyanat umgewandelt (**3**).[170] Dadurch, dass sich Pyridin-2-isocyanat (**3**) nun in Poren von MIL-101 aufhält, erhöhte dies folglich die Wahrscheinlichkeit, bevorzugt mit den Aminogruppen von MIL-101 zum Pyridinharnstoffderivat zu reagieren, als zu dimerisieren (**4**) (Schema 3.2.1). Das Reaktionsprodukt wird mit MIL-101-URPy (Ureapyridin) bezeichnet.

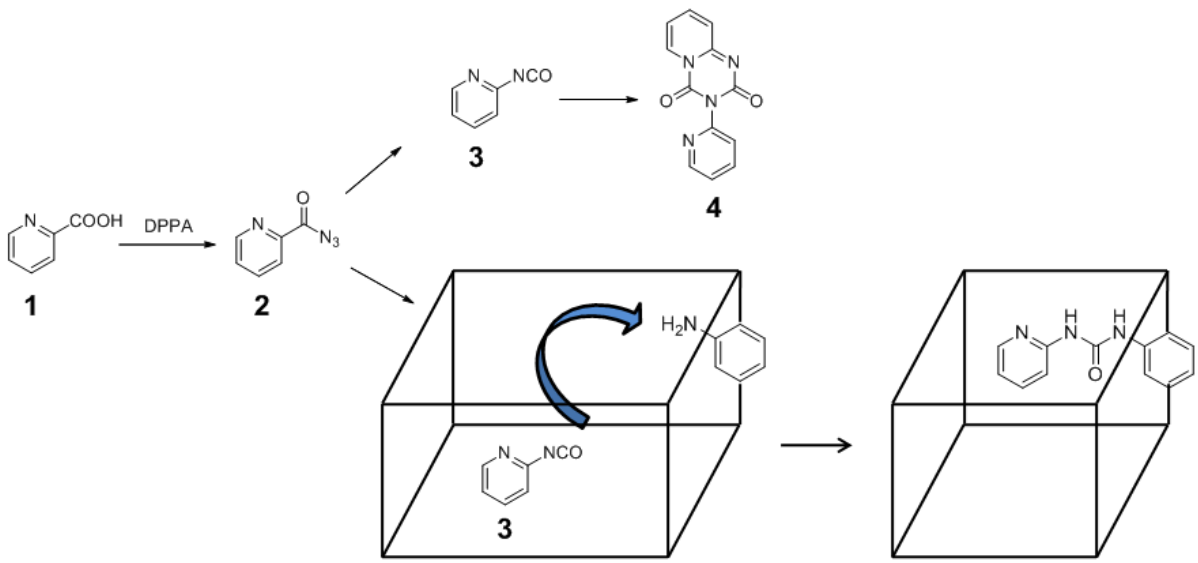

Schema 3.2.1: Schematische Darstellung der postsynthtischen Modifizierung (PSM) von MIL-101-NH_2 (Al, Cr) mit Pyridin-2-isocyanat. Der skizzierten Quader symbolisieren die Käfige von MIL-101.

Mit Röntgenpulverdiffraktometrie und Stickstoffphysisorptionsmessungen wurde gezeigt, dass die Struktur bzw. die Porosität von MIL-101 (Al, Cr) nach der PSM erhalten blieb, wenn auch die Kristallinität bzw. die spezifischen Oberflächen und Porenvolumina aufgrund der erhöhten Unordnung der sperrigen Phenylharnstoffseitengruppen abnahmen. Letztere waren für MIL-101-URPy (Al, Cr) um ca. 50 % reduziert. Die ^{15}N-Festköper-NMR-MAS-Spektren der Al-MOFs zeigten die Umwandlung der Amino- in die Pyridinharnstoffgruppe. (Abb. 3.2.1). Der exakte Umsatz der Al- und Cr- Vertreter von MIL-101-URPy wurde mit ^{1}H-NMR-Spektroskopie in flüssiger Phase zu 90% bestimmt.

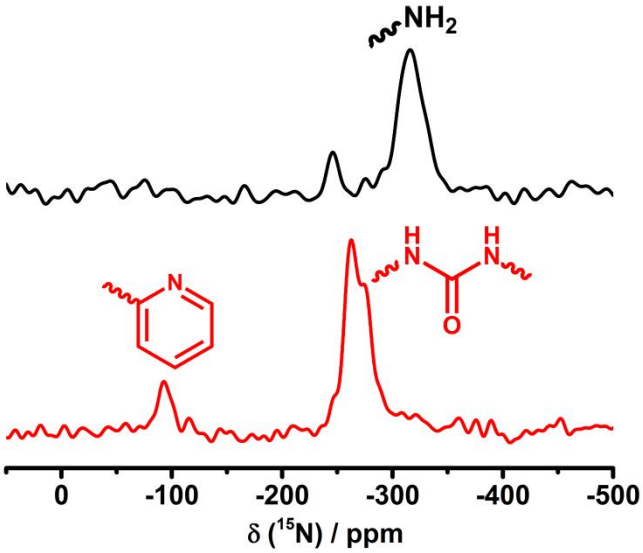

Abb. 3.2.1: ^{15}N-CP-MAS-NMR Spektren von Al-MIL-101-NH$_2$ (schwarz) und Al-MIL-101-URPy (rot).

Da die am Linker gebundene N-H Einheit der Harnstoffgruppe starke Wechselwirkungen mit der Carboxylatgruppe des Linkers eingeht (siehe Kapitel 3.1, Abb. 3.1.2), wurde erwartet, dass die Pyridinharnstoffgruppe in MIL-101-URPy effektiv nur eine DA-Sequenz anbietet. Deshalb wurden die selektiven Adsorptionseigenschaften von MIL-101-URPy (Al, Cr) anhand von 2-Aminopyridin (2-AP) und 3-Aminopyridin (3-AP) getestet. Mit der komplementären AD-Sequenz kann 2-AP gleichzeitig über zweifache Wasserstoffbrücken, 3-AP (A oder D) nur mit einer Wasserstoffbrücke mit der Pyridinharnstoffgruppe wechselwirken.

Da für Al-MIL-101-NH$_2$ und Al-MIL-101-URPy gleiche Selektivitäten wie für Cr-Vertreter bestimmt wurden, werden in Abb. 3.2.2 die Selektivitäten exemplarisch nur der Cr-MIL-101 Verbindungen gezeigt. Die Adsorptionsisothermen der äquimolaren

Lösungen aus 2-AP und 3-AP ergaben eine deutlich erhöhte Selektivität der amino-funktionalisierten MOFs für 3-AP in MIL-101-NH_2 (Abb. 3.2.2, schwarz). Für MIL-101-URPy (Al, Cr) waren die Selektivitäten für 2-AP über 3-AP im Vergleich zu MIL-101-NH_2 (Al, Cr) um den Faktor drei erhöht (Abb. 3.2.2, rot). Trotz der Umwandlung der Amino- zur Pyridinharnstoffgruppe war die Aufnahmekapazität für 3-AP noch unerwartet hoch. Um eine etwaige Konkurrenzadsorption für 3-AP an den offenen Koordinationstellen (CUS) zu untersuchen, wurden diese in Cr-MIL-101-URPy vor dem erneuten Selektivitätsexperiment (2-AP vs. 3-AP) mit Diethylamin (DEA) abgesättigt. Es wurde getestet, ob dessen hydrophobe Ethylgruppen eine abschirmende Wirkung gegenüber 3-AP aufweisen, um so die Wirkung der Pyridinharnstoffgruppe weiter hervorzuheben. In DEA@Cr-MIL-101-URPy konnte schließlich die Selektivität von 2-AP gegenüber 3-AP im Vergleich zu H_2O@Cr-MIL-101-URPy um ca. 50 % erhöht werden (Abb. 3.2.2, blau).

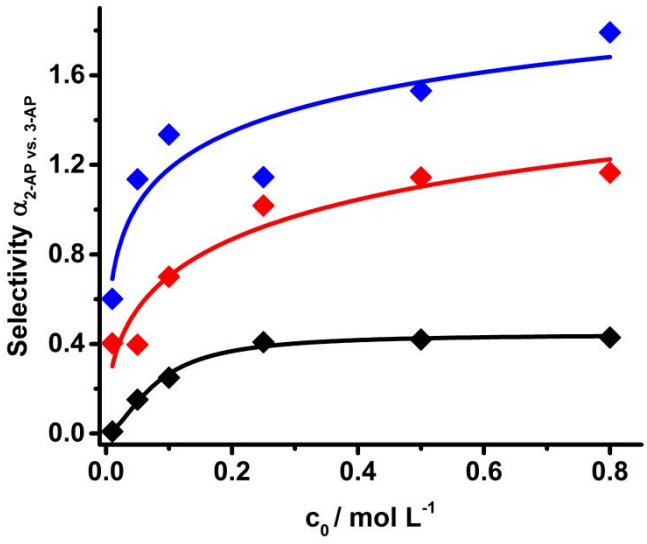

Abb. 3.2.2: Selektivtäten α von H_2O@Cr-MIL-101-NH_2 (schwarz), H_2O@Cr-MIL-101-URPy (rot) und DEA@Cr-MIL-101-URPy (blau).

Die ^{15}N-NMR-Spektren von Al-MIL-101-NH_2 (Abb. 3.2.3a) deuteten aufgrund der größeren Tieffeldverschiebung der Aminogruppe auf stärkere Wechselwirkungen der Aminogruppe mit 3-AP als mit 2-AP hin. In Al-MIL-101-URPy zeigten die ^{15}N-NMR-Spektren jedoch einen größere Tieffeldverschiebung des vom Linker weiter entfernten N-H Signals der Harnstoffgruppe nach Einlagerung von 2-AP (Signal 1, Abb. 3.2.3b), während die N-H Gruppe nahe am Linker erwartungsgemäß (siehe Kapitel 3.1)

keine Verschiebung zeigte. Zusammen mit quantenchemische Rechnungen deutete dies darauf hin, dass die erhöhte Selektivität (Abb. 3.2.2 rot) auf die Ausbildung eines komplementären Wasserstoffbrückenadduktes zwischen der DA-Sequenz der Pyridinharnstoffgruppe und der AD-Sequenz von 2-AP zurückzuführen ist. Somit wechselwirkt 2-AP stärker mit der Pyridinharnstoffgruppe als 3-AP.

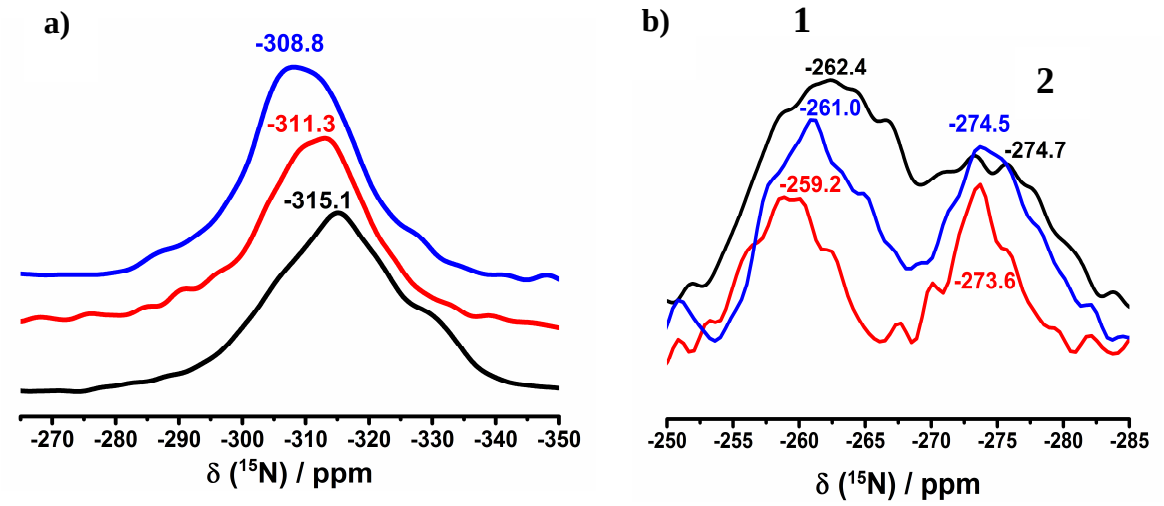

Abb. 3.2.3: ^{15}N-CP-MAS-NMR Spektren von a) Al-MIL-101-NH_2 ohne (schwarz) und nach Einlagerung von 2-AP (rot) und 3-AP (blau) und b) Al-MIL-101-URPy ohne (schwarz) und nach Einlagerung von 2-AP (rot) und 3-AP (blau).

Diese Ergebnisse zeigen, dass die Übertragung eines supramolekularen Bindungsmotivs in Form von multiplen Wasserstoffbrückensequenzen in die Poren von MOFs erfolgreich war. Eine etwaige Konkurrenzadsorption von 3-AP an den offenen Koordinationstellen, die dessen erhöhte Aufnahmekapazitäten trotz der Umwandlung der Amino- in die Pyridinharnstoffgruppe erklären würden, konnte mit ^{15}N-Festkörper-NMR-Spektroskopie an den Al-MOFs jedoch nicht ermittelt werden.

Dies und die Frage, ob ein Blocken der offenen Koordinationsstellen durch die DEA-Spezies die Ursache der erhöhten Selektivität von 2-AP in DEA@Cr-MIL-101-URPy war, wurde detailliert im nachfolgenden Kapitel untersucht. Für ein umfassendes Verständnis der Wirt-Gast-Wechselwirkungen in MIL-101 wurden in Kapitel 3.3 zudem die Adsorptionsaffinitäten von H_2O, 2-AP, 3-AP und DEA bzgl. der offenen Koordinationsstellen von Cr-MIL-101evaluiert.

3.3 Festkörper-NMR-spektroskopische Untersuchung der selektiven Wechselwirkung der anorganischen Baueinheit von paramagnetischen Cr-MIL-101 mit Gastmolekülen

In mesoporösem MIL-101 war die exakte Identifizierung von Wirt-Gast-Wechselwirkungen der gleichzeitig adsorbierten und strukturell ähnlichen Moleküle 2-AP und 3-AP sowie DEA mit den anorganischen Baueinheiten mit Röntgendiffraktion aufgrund dynamischer Fehlordnung und daher geringer Fernordnung erschwert. Multikern-Festkörper-NMR-Spektroskopie an diamagnetischem Al-MIL-101 sowie UV/VIS- und IR-Spektroskopie lieferten aufgrund überlagernder Signale der ähnlichen Moleküle 2-AP und 3-AP nur unzureichende Auskunft über vorliegende Konnektivitäten und letztendlich über selektive Wechselwirkungen.

In diesem Kapitel wurde deshalb die Wechselwirkung von H_2O, 2-AP, 3-AP und DEA mit den offenen Koordinationsstellen mit Festkörper-NMR-Spektroskopie an den paramagnetischen Cr-MIL-101 Verbindungen untersucht. Die auftretenden Hyperfeinverschiebungen (siehe Kapitel 2.3.2) erlaubten hier eine eindeutige Bestimmung der koordinierenden Spezies und daher eine Ableitung einer Adsorptionspräferenz. Im Unterschied zu diamagnetischen Verbindungen war die Aufnahme und Interpretation der NMR-Spektren von paramagnetischen Verbindungen komplizierter. Aufgrund der positiven und negativen Fermi-Kontakt-Verschiebungen um bis zu einige hundert ppm konnten die Signale jedoch trotz ihrer großen Lininenbreiten gut aufgelöst werden.

Zur Signalzuordnung wurde hier auf eine Kombination der Informationen aus einem $^{13}C\{^1H\}$-REDOR ähnlichen Experiment und aus ^{13}C-Spin-Gitter-Relaxationszeiten (T_1) zurückgegriffen. Die Anwendung einer REDOR-Pulssequenz führt zur Modulation der Signalintensitäten der hyperfeinverschobenen ^{13}C-Signale durch Dephasierung. Unter Einbeziehung sowohl der experimentell ermittelten anisotropen ^1H-Hyperfeinverschiebungen, als auch der Bewegungsformen der Terephthalatlinker, von 2-AP und 3-AP in die Simulation der Depahsierungswerte der jeweiligen Kohlenstoffatome, konnten die hyperfeinverschobenen Signale bestimmten chemischen Gruppen (quartäres C, -CH, $-CH_2$, $-CH_3$) zugeordnet werden. Im Falle der Terephthalatlinker (Abb. 3.3.1a), 2-AP (Abb. 3.3.1b) und 3-AP (Abb. 3.3.1c) konnte

eindeutig zwischen C und CH Gruppen und im Fall von DEA (Abb. 3.3.1d) zwischen den CH_2 und CH_3 Gruppen unterschieden werden.

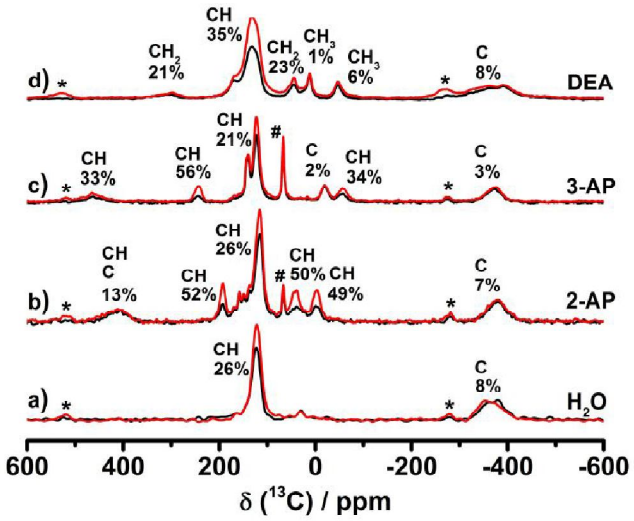

Abb. 3.3.1: ^{13}C-MAS-NMR-Spektren ohne (rot) und mit dipolarer ^{13}C{^{1}H}-Dephasierung (schwarz) von a) H_2O@Cr-MIL-101, b) 2-AP@Cr-MIL-101, c) 3-AP@Cr-MIL-101 und d) DEA@Cr-MIL-101. # kennzeichnet das ^{13}C-Signal des Lösungsmittels 1,4-Dioxan, * die Rotationsseitenbanden.

Um auch zwischen zwei gleichen chemischen Gruppen innerhalb eines koordinierten Gastmoleküls unterscheiden zu können, wurden die jeweiligen Spin-Gitter-Relaxationszeiten (T_1) herangezogen. Nach Gleichung 6 (Kapitel 2.3.2) entspricht das Verhältnis der T_1-Werte zweier Signale genau dem inversen Verhältnis ihrer jeweiligen Abstandssummen R, die anhand von Geometrie-optimierten Strukturfragmenten bestimmt werden (Abb. 3.3.2). Dadurch konnten die hyperfeinverschobenen Signale den entsprechenden Kohlenstoffatomen zugeordnet werden. Die Kombination der Informationen über die Art der chemischen Gruppe und den Abständen zu den Cr_3O-Clustern (Abb. 3.3.2) führte schließlich zu einer eindeutigen Zuordnung aller hyperfeinverschobenen Signale der Linker, 2-AP, 3-AP und DEA (Abb. 3.3.3).

Zur Verifizierung der zugeordneten Signale wurden quantenchemische Rechnungen der chemischen Verschiebungen durchgeführt. Hierfür wurde die Spinfrustration im austauschgekoppelten Cr_3O-Cluster insofern berücksichtigt, dass Daten aus einer magnetischen Suszeptibilitätsmessung einberechnet wurden. Die Vorzeichen der berechneten Hyperfeinverschiebungen für die jeweiligen Kohlenstoffatome stimmten exakt

mit denen überein, die sich aus der experimentellen Zuordnung ergaben. Die Größen der Hyperfeinverschiebungen stimmten mit Abweichungen von ca. 20% mit den experimentell beobachteten überein. Die Abweichungen sind hauptsächlich darauf zurückzuführen, dass die Rechnungen der Verschiebungen an DFT-optimierten Strukturen bei 0 K (Abb. 3.3.2), die experimentellen Messungen jedoch bei 325 K durchgeführt wurden. Kleinste geometrische Änderungen führen zu veränderteren Orbitalüberlappungen und Mengen an delokalisierten Spindichten, die schließlich die Hyperfeinkopplungskonstante bestimmen (siehe Kapitel 2.3.2)

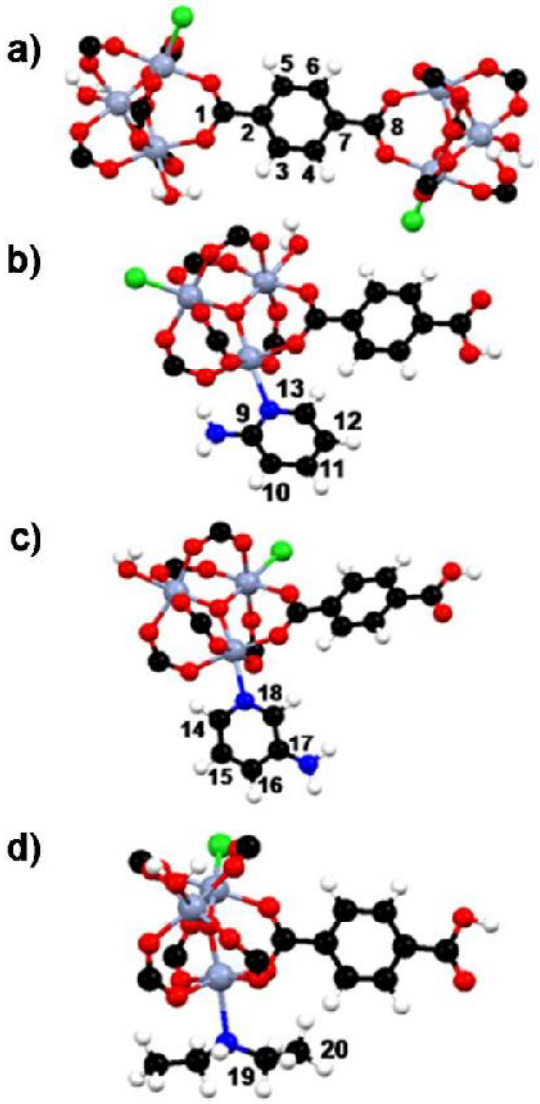

Abb. 3.3.2: Strukturfragmente nach Geometrieoptimierung mittels quantenchemischer Rechnungen auf DFT-Niveau von a) H_2O@Cr-MIL-101, b) 2-AP@Cr-MIL-101, c) 3-AP@Cr-MIL-101 und d) DEA@Cr-MIL-101.

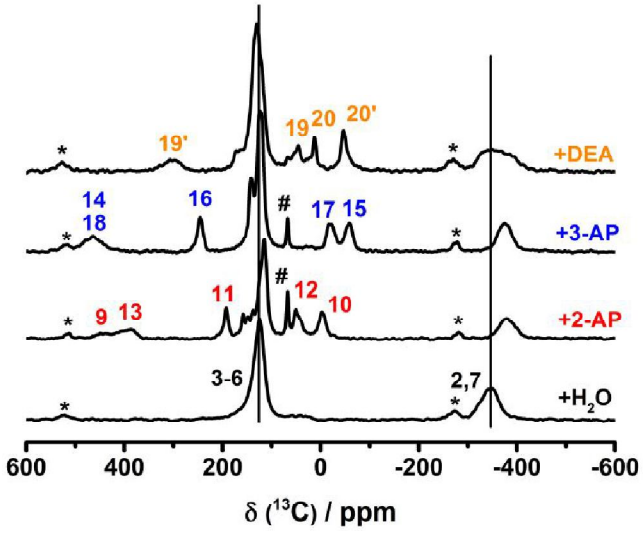

Abb. 3.3.3: ^{13}C-MAS-NMR Spektren von X@Cr-MIL-101 mit X = H_2O (schwarz), 2-AP (rot), 3-AP (blau) und DEA (orange) zusammen mit den Signalzuordnungen. * kennzeichnet die Rotationsseitenbanden und # das ^{13}C-NMR-Signal des Lösungsmittels 1,4-Dioxan.

Basierend auf einer eindeutigen Zuordnung der hyperfeinverschobenen Signale konnten die Adsorptionspräferenzen von H_2O, 2-AP, 3-AP und DEA bzgl. der offenen Koordinationsstellen abgeleitet werden. Während die koordinierenden Moleküle hyperfeinverschobene Signale aufweisen, zeigen nicht-koordinierende bzw. physisorbierte Moleküle ihre typischen diamagnetischen Resonanzen. Die ^{13}C-MAS-NMR Spektren (Abb. 3.3.4) von Cr-MIL-101 zeigten nach Adsorption von Mischungen aus 2-AP und 3-AP bzw. aus 3-AP und DEA nur die hyperfeinverschobenen Signale für 3-AP, während für 2-AP bzw. DEA die diamagnetischen Resonanzen beobachtet wurden. Dies beweist, dass 3-AP gegenüber 2-AP und DEA eine höhere Affinität bzgl. Koordination an die offenen Koordinationstellen von MIL-101 hat. Bei gleichzeitiger Beladung von 2-AP und DEA wurden die charakteristischen hyperfeinverschobenen Signale für beide Spezies beobachtet. Allerdings sind die Signalintensitäten für 2-AP höher als für DEA. Die ^{13}C-Festkörper-NMR-Spektren (Abb. 3.3.4) ermöglichten es schließlich, folgende aufsteigende Bindungsstärke bzgl. der offenen Koordinationsstellen zu bestimmen: H_2O < DEA ≈ 2-AP < 3-AP.

Die erhöhte Affinität von 3-AP bzgl. der offenen Koordinationsstellen (CUS) an den anorganischen Baueinheiten erklärt schließlich auch die relative hohe Aufnahmekapazität

in Cr-MIL-101-URPy (Kapitel 6.2). Nach Adsorption von 3-AP in DEA@Cr-MIL-101 konnte koordiniertes DEA von den Metallzentren entfernt werden, da nur noch dessen diamagentische Resonanzen beobachtet wurden (Signale **19** und **20** in Abb. 3.3.4). Diese DEA-Spezies konnte anhand ihrer Abstandssummen in der sekundären Koordinationssphäre lokalisiert werden, deren hydrophoben Ethylgruppen in den Porenraum zeigen. Den REDOR-Depahsierungswerten zufolge ist diese DEA-Spezies relativ unbeweglich und somit über starke Wasserstoffbrücken gebunden. Demzufolge kann DEA die 3-AP Moleküle nicht daran hindern, an die CUS zu koordinieren, sondern in der sekundären Koordinationssphäre ihre blockende Wirkung gegenüber 3-AP entfalten. 3-AP kann sich folglich dort nicht anlagern, beispielsweise durch Wechselwirkung mit bereits koordinierten 3-AP Molekülen, wie es auch in dessen Kristallstruktur realisiert wird,[171] so dass sich auch dessen Aufnahmekapazität reduziert.

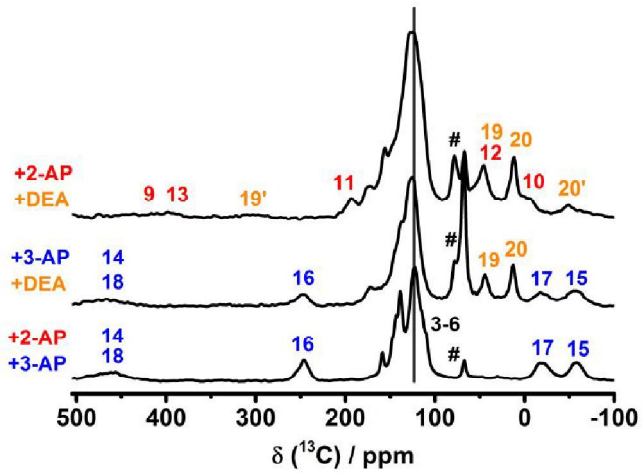

Abb. 3.3.4: Ausschnitte aus den ^{13}C-MAS-NMR Spektren von X@Cr-MIL-101 nach Beladung mit zwei Gastmolekülen mit X = 2-AP + 3-AP, 3-AP + DEA und 2-AP + DEA. # kennzeichnet das ^{13}C-NMR-Signal des Lösungsmittels 1,4-Dioxan.

Dieses Projekt zeigte, dass die Festkörper-NMR-Spektroskopie unter der Voraussetzung, dass alle Signale zugeordnet werden können, die Methode der Wahl ist, um für paramagnetisches Cr-MIL-101 die Art der kordierenden Gäste eindeutig zu bestimmen sowie deren relative Bindungsstärken abzuschätzen. Das hier entwickelte Verfahren kann auch für andere paramagnetische MOFs mit offenen Koordinationsstellen an den anorganischen Baueinheiten wie HKUST-1, CPO-27 und MIL-100 angewendet werden.

Diese MOFs wurden sowohl für Adsorption von CO,[172] CO_2[173] und H_2,[174] als auch für die heterogene Katalyse untersucht. All diese Prozesse hängen stark von der Wechselwirkung mit den offenen Metallzentren abhängen. Unsere Methodik der Signalzuordnung liefert demnach einen wichtigen Beitrag, solche Wechselwirkungen exakt zu verstehen. Das genaue Verständnis von Wirt-Gast-Konnektivitäten ermöglicht es, Struktur-Eigenschaftsbeziehungen abzuleiten und daraus paramagnetische Materialien zielgerichtet für eine bestimmte Anwendung zu designen.

3.4 Schlussfolgerung

In dieser Arbeit wurde gezeigt, dass Bindungsmotive der supramolekularen Chemie wie die multiplen Wasserstoffbrückenbindungen in größere Porenräume von MOFs wie den mesoporösen MIL-101 Verbindungen postsynthetisch eingebaut werden können. Diese nachträglich eingebauten funktionellen Gruppen beeinflussten die chemischen und physikalischen Eigenschaften von MIL-101 wie beispielsweise dessen Wasserstabilität und selektive Wechselwirkungen zu Gastmolekülen mit einer komplementären Wasserstoffbrückensequenz signifikant. So konnte das aus der Natur bekannte Schlüssel-Schloss-Prinzip erfolgreich im Porenraum von MIL-101 realisiert werden. Die Festkörper-NMR-Spektroskopie stellte sich dabei als Methode der Wahl heraus, diese veränderten Eigenschaften auf mikroskopischer Ebene zu analysieren. Mit den hier entwickelten Strategien war es nun möglich, sowohl die Adsorptionen an den anorganischen Baueinheiten, als auch an den organischen Linkern zu erfassen und voneinander zu trennen. Während letztere mit diamagnetischen NMR-Methoden an Al-MIL-101 ausgewertet werden konnten, wurden für erstere eine Methodik zur Signalzuordnung entwickelt, um die Hyperfeinverschiebung von NMR-aktiven Kernen in paramagnetischen Cr-MIL-101-Verbindungen für die Identifikation der koordinierenden Spezies ausnutzen zu können. Aufgrund der Äquivalenz der makroskopischen Adsorptionseigenschaften von 2-AP und 3-AP in Al- und Cr-MIL-101 können nun die analysierten Wechselwirkungen der Linker in Al-MIL-101 auch auf Cr-MIL-101 übertragen werden bzw. die der offenen Koordinationstellen in Cr-MIL-101 auch auf Al-MIL-101.

Erst das ganzheitliche Verständnis der Wechselwirkungen der Linker und der offenen Koordinationsstellen auf mikroskopischer Ebene ermöglicht es, die hier gezeigten chemischen Modifizierungen zukünftig als Konzepte für das anwendungsorientierte Design von anderen MOFs zu nutzen und somit den MOFs als Spezialchemikalien den Weg in den bislang kaum erschlossenen industriellen Markt zu ebnen. So lässt sich beispielsweise über den Anteil an eingebrachten abschirmender, hydrophober Gruppen die Wasserstabilität von wasserempfindlichen MOFs gezielt einstellen. Dies eröffnet neue Anwendungsgebiete wie etwa die Medikamentenverabreichung, wo die MOFs sich nach der dosierten Freisetzung des Wirkstoffes im physiologischen Milieu zersetzen sollen, um so den menschlichen Körper wieder zu verlassen. Vor der Freisetzung der Wirkstoffe können diese über künstlich erzeugte, multiple Wasserstoffbrückenmuster im Porenraum selektiv angebunden werden. Die hier entwickelte Synthesestrategie kann als Rezept dienen, noch ausgedehntere Wasserstoffbrückenmuster für die Anbindung noch komplexerer Moleküle wie beispielsweise den Virustatika und Antibiotika zu entwickeln, die oftmals auf mehrfach funktionalisierte N-Heterozyklen basieren. Derart funktionalisierte MOFs können aber auch für die gezielte Entfernung von Rückständen solcher Stoffe aus Abwässern oder zur Entfernung von N-Heterozyklen aus Kraftstoffen vor deren Verbrennung zu schädlichen NO_x-Radikalen genutzt werden. Durch die geeignete Wahl des Metallions im MOF lassen sich N- und S-Heterozyklen aus Kraftsoffen wie Indol und Thiophen auch durch die Wechselwirkung mit offenen Koordinationsstellen selektiv anbinden.[28–30]

Darüber hinaus kann die hier entwickelte Strategie zur Aufklärung der Wechselwirkungen von Gastmolekülen mit paramagnetischen Metallzentren schließlich auch auf andere poröse Materialklassen mit moderater magnetischer Kopplung übertragen werden. So kann die Wirt-Gast-Chemie von eisen-, kupfer-, mangan- oder nickelhaltigen Zeolithen, Schichtsilikaten und porösen Keramiken sowie Eigenschaften poröser Elektroden von Batteriematerialien untersucht werden. Dies eröffnet ebenso den Weg zur Synthese von Materialien mit innovativen und verbesserten Eigenschaften.

4 Literaturverzeichnis

(1) D'Alessandro, D. M.; Smit, B.; Long, J. R. Carbon Dioxide Capture: Prospects for New Materials. *Angew. Chemie - Int. Ed.* **2010**, *49* (35), 6058–6082.

(2) Liu, J.; Thallapally, P. K.; McGrail, B. P.; Brown, D. R.; Liu, J. Progress in Adsorption-Based CO2 Capture by Metal–organic Frameworks. *Chem. Soc. Rev.* **2012**, *41* (6), 2308.

(3) Janiak, C.; Vieth K. jana. MOFs, MILs and More: Concepts, Properties and Applications for Porous Coordination Networks (PCNs). *New J. Chem.* **2010**, *34* (11), 2366–2388.

(4) Van de Voorde, B.; Bueken, B.; Denayer, J.; De Vos, D. Adsorptive Separation on Metal-Organic Frameworks in the Liquid Phase. *Chem. Soc. Rev.* **2014**, *43* (16), 5766–5788.

(5) Lee, J.; Farha, O. K.; Roberts, J.; Scheidt, K. A.; Nguyen, S. T.; Hupp, J. T. Metal–organic Framework Materials as Catalysts. *Chem. Soc. Rev.* **2009**, *38* (5), 1450–1459.

(6) Mueller, U.; Schubert, M.; Teich, F.; Puetter, H.; Schierle-Arndt, K.; Pastré, J. Metal–organic Frameworks—prospective Industrial Applications. *J. Mater. Chem.* **2006**, *16* (7), 626–636.

(7) Samokhvalov, A. Adsorption on Mesoporous Metal-Organic Frameworks in Solution: Aromatic and Heterocyclic Compounds. *Chem. - A Eur. J.* **2015**, *21* (47), 16726–16742.

(8) Li, J.; Sculley, J.; Zhou, H. Metal–Organic Frameworks for Separations. *Chem. Rev.* **2012**, *112*, 869–932.

(9) Sumida, K.; Rogow, D. L.; Mason, J. A.; Mcdonald, T. M.; Bloch, E. D.; Herm, Z. R.; Bae, T.; Long, R. Carbon Dioxide Capture in Metal-Organic Frameworks. *Chem. Rev.* **2012**, *112*, 724–781.

(10) Horcajada, P.; Gref, R.; Baati, T.; Allan, P. K.; Maurin, G.; Couvreur, P. Metal À Organic Frameworks in Biomedicine. **2012**, 1232–1268.

(11) Horcajada, P.; Chalati, T.; Serre, C.; Gillet, B.; Sebrie, C.; Baati, T.; Eubank, J. F.; Heurtaux, D.; Clayette, P.; Kreuz, C.; Chang, J.-S.; Hwang, Y. K.; Marsaud, V.; Bories, P.-N.; Cynober, L.; Gil, S.; Ferey, G.; Couvreur, P.; Gref, R. Porous Metal-Organic-Framework Nanoscale Carriers as a Potential Platform for Drug Delivery and Imaging. *Nat. Mater.* **2010**, *9* (2), 172–178.

(12) McKinlay, A. C.; Morris, R. E.; Horcajada, P.; Férey, G.; Gref, R.; Couvreur, P.; Serre, C. BioMOFs: Metal-Organic Frameworks for Biological and Medical Applications. *Angew. Chemie - Int. Ed.* **2010**, *49* (36), 6260–6266.

(13) Burrows, A. D. Gas Sensing Using Porous Materials for Automotive Applications.

Chem. Soc. Rev. **2015**, *44* (13), 4290–4321.

(14) Kreno, L. E.; Leong, K.; Farha, O. K.; Allendorf, M.; Duyne, R. P. Van; Hupp, J. T. Metal- Organic Framework Materials as Chemical Sensors. *Chem. Rev.* **2012**, *112*, 1105–1125.

(15) Foo, M. L.; Matsuda, R.; Kitagawa, S. Functional Hybrid Porous Coordination Polymers. *Chem. Mater.* **2014**, *26*, 310–322.

(16) Furukawa, H.; Cordova, K. E.; O'Keeffe, M.; Yaghi, O. M. The Chemistry and Applications of Metal-Organic Frameworks. *Science* **2010**, *9* (6149), 1230444.

(17) Slater, A. G.; Cooper, A. I. Function-Led Design of New Porous Materials. *Science (80-.).* **2015**, *348* (6238), 8075-1–10.

(18) Cheetham, A. K.; Férey, G.; Loiseau, T. Anorganische Materialien Mit Offenen Gerüsten. *Angew. Chemie* **1999**, *111* (22), 3466–3492.

(19) Davis, M. E. Ordered Porous Materials for Emerging Applications. *Nature* **2002**, *417* (June), 813–821.

(20) Marsh, H.; Rodriguez-Reinoso, F. *Activated Carbon*, First Edit.; Elsevier Ltd: London, 2006.

(21) Li, J.-R.; Kuppler, R. J.; Zhou, H.-C. Selective Gas Adsorption and Separation in Metal–organic Frameworks. *Chem. Soc. Rev.* **2009**, *38*, 1477–1504.

(22) Cohen, S. M. Postsynthetic Methods for the Functionalization of Metal Organic Frameworks. *Chem. Rev.* **2012**, *112* (2), 970–1000.

(23) Cohen, S. M. Modifying MOFs: New Chemistry, New Materials. *Chem. Sci.* **2010**, *1* (1), 32.

(24) Wang, Z.; Cohen, S. M. Postsynthetic Modification of Metal–organic Frameworks. *Chem. Soc. Rev.* **2009**, *38* (5), 1315.

(25) Alaerts, L.; Maes, M.; Giebeler, L.; Jacobs, P. A.; Martens, J. A.; Denayer, J. F. M.; Kirschhock, C. E. A.; Vos, D. E. De. Selective Adsorption and Separation of. *Adsorpt. J. Int. Adsorpt. Soc.* **2008**, No. 26, 14170–14178.

(26) Osta, R. El; Carlin-sinclair, A.; Guillou, N.; Walton, R. I.; Vermoortele, F.; Maes, M.; Vos, D. De; Millange, F. Liquid-Phase Adsorption and Separation of Xylene Isomers by the Flexible Porous Metal − Organic Framework MIL-53 (Fe). *Chem. Mater.* **2012**, *24*, 2781–2791.

(27) Dai, J.; Mckee, M. L.; Samokhvalov, A. Adsorption of Naphthalene and Indole on F300 MOF in Liquid Phase by the Complementary Spectroscopic , Kinetic and DFT Studies. *J Porous Mater* **2014**, *21* (5), 709–727.

(28) Maes, M.; Trekels, M.; Boulhout, M.; Schouteden, S.; Vermoortele, F.; Alaerts, L.; Heurtaux, D.; Seo, Y.; Hwang, Y. K.; Chang, J.; Beurroies, I.; Denoyel, R.; Temst, K.; Vantomme, A.; Horcajada, P.; Serre, C.; Vos, D. E. De. Selective Removal of N-Heterocyclic Aromatic Contaminants from Fuels by Lewis Acidic Metal – Organic

Frameworks. *Angew. Chem.* **2011**, *123*, 4296–4300.

(29) Wang, Z.; Sun, Z.; Kong, L.; Li, G. Adsorptive Removal of Nitrogen-Containing Compounds from Fuel by Metal-Organic Frameworks. *J. Energy Chem.* **2013**, *22* (6), 869–875.

(30) Voorde, B. Van De; Boulhout, M.; Vermoortele, F.; Horcajada, P.; Cunha, D.; Lee, J. S.; Chang, J.; Gibson, E.; Daturi, M.; Lavalley, J.; Vimont, A.; Beurroies, I.; Vos, D. E. De. N / S-Heterocyclic Contaminant Removal from Fuels by the Mesoporous Metal − Organic Framework MIL-100 : The Role of the Metal Ion. *J. Am. Chem. Soc.* **2013**, *135* (26), 9849–9856.

(31) Cychosz, K. A.; Wong-foy, A. G.; Matzger, A. J. Liquid Phase Adsorption by Microporous Coordination Polymers : Removal of Organosulfur Compounds. **2008**, 6938–6939.

(32) Achmann, S.; Hagen, G.; Hämmerle, M.; Moos, R. Sulfur Removal from Low-Sulfur Gasoline and Diesel Fuel by Metal-Organic Frameworks. **2010**, No. 2, 275–280.

(33) M. R. Jones, N. C. Seeman, C. A. M. Programmable Materials and the Nature of the DNA Bond. *Science (80-.).* **2015**, *347* (6224).

(34) Sivakova, S.; Rowan, S. J.; Rowan, S. J. Nucleobases as Supramolecular Motifs. *Chem Soc Rev* **2005**, *34*, 9–21.

(35) Wittenberg, J. B.; Isaacs, L. Complementarity and Preorganization. *Supramol. Chem. From Mol. to Nanomater. Online* **2012**, 1–19.

(36) Lehn, J.-M. Perspectives in Supramolecular Chemistry - From Molecular Recognition Towards Molecular Information Processing and Self-Organisation. *Angew. Chem. Int. Ed.* **1990**, *29*, 1304–1319.

(37) Li, Q.; Zhang, W.; Miljanic, O. S.; Sue, C.; Zhao, Y.-L.; Liu, L.; Knobler, C. B.; Stoddart, J. F.; Yaghi, O. M. Docking in Metal-Organic Frameworks. *Science (80-.).* **2009**, *325* (5942), 855–859.

(38) Cai, H.; Li, M.; Lin, X. R.; Chen, W.; Chen, G. H.; Huang, X. C.; Li, D. Spatial, Hysteretic, and Adaptive Host-Guest Chemistry in a Metal-Organic Framework with Open Watson-Crick Sites. *Angew. Chemie - Int. Ed.* **2015**, *54* (36), 10454–10459.

(39) Férey, G.; Mellot-Draznieks, C.; Serre, C.; Millange, F.; Dutour, J.; Surblé, S.; Margiolaki, I. A Chromium Terephthalate – Based Solid with Unusually Large Pore Volumes and Surface Area. *Science (80-.).* **2005**, *309* (September), 2040–2042.

(40) Serra-Crespo, P.; Ramos-Fernandez, E. V; Gascon, J.; Kapteijn, F. Synthesis and Characterization of an Amino Functionalized MIL-101 (Al): Separation and Catalytic Properties. *Chem. Mater.* **2011**, *23* (10), 2565–2572.

(41) Wittmann, T.; Siegel, R.; Reimer, N.; Milius, W.; Stock, N.; Senker, J. Enhancing the Water Stability of Al-MIL-101-NH2 via Postsynthetic Modification. *Chem. - A Eur. J.* **2015**, *21* (1), 314–323.

(42) Férey, G. Hybrid Porous Solids: Past, Present, Future. *Chem. Soc. Rev.* **2008**, *37* (1),

191–214.

(43) Cheetham, A. K.; Rao, C. N. R.; Feller, R. K. Structural Diversity and Chemical Trends in Hybrid Inorganic?organic Framework Materials. *Chem. Commun.* **2006**, No. 46, 4780.

(44) Batten, S. R.; Champness, N. R.; Chen, X.-M.; Garcia-Martinez, J.; Kitagawa, S.; Öhrström, L.; O'Keeffe, M.; Suh, M. P.; Reedijk, J. Terminology of Metal-Organic Frameworks and Coordination Polymers (IUPAC Provisional Recommendation). *Anal. Instrum.* **2008**, 1–12.

(45) Allendorf, M. D.; Stavila, V. Crystal Engineering, Structure–function Relationships, and the Future of Metal–organic Frameworks. *CrystEngComm* **2015**, *17* (2), 229–246.

(46) Shen, K.; Zhang, M.; Zheng, H. Critical Factors Influencing the Structures and Properties of Metal-Organic Frameworks. *CrystEngComm* **2015**, *17*, 981–991.

(47) Rowsell, J. L. C.; Yaghi, O. M. Metal-Organic Frameworks: A New Class of Porous Materials. *Microporous Mesoporous Mater.* **2004**, *73* (1–2), 3–14.

(48) Hailian Li, Mohamed Eddaoudi, M. O'Keeffe, O. M. Y. Design and Synthesis of an Exceptionally Stable and Highly Porous Metal-Organic Framework. *Nature* **1999**, *402* (November), 276–279.

(49) Eddaoudi, M.; Eddaoudi, M.; Kim, J.; Rosi, N.; Yaghi, O. M. Systematic Design of Pore Size and Functionality in Isoreticular MOFs. **2012**, *469* (2002).

(50) Chui, S. S.-Y.; Lo, S. M.-F.; Charmant, J. P. H.; Orpen, A. G.; Williams, I. D. A Chemically Functionalizable Nanoporous Material [Cu3(TMA)2(H2O)3]n. *Science (80-.).* **1999**, *283* (5405), 1148–1150.

(51) Hwang, Y. K.; Hong, D.; Chang, J.; Jhung, S. H.; Seo, Y.; Kim, J.; Vimont, A.; Daturi, M.; Serre, C.; Førey, G. Amine Grafting on Coordinatively Unsaturated Metal Centers of MOFs : Consequences for Catalysis and Metal Encapsulation. *Angew. Chem. Int. Ed.* **2008**, *47*, 4144–4148.

(52) Kuppler, R.; Makal, T. A.; Yuan, D.; Zhou, H. Potential Applications of Metal-Organic Frameworks. **2009**, *253* (October 2016), 3042–3066.

(53) Qiu, S.; Xue, M.; Zhu, G. Metal-Organic Framework Membranes: From Synthesis to Separation Application. *Chem. Soc. Rev.* **2014**, *43*, 6116–6140.

(54) Halder, G. J. Guest-Dependent Spin Crossover in a Nanoporous Molecular Framework Material. *Science (80-.).* **2002**, *298* (5599), 1762–1765.

(55) Xu, H.; Tao, S.; Jiang, D. Proton Conduction in Crystalline and Porous Covalent Organic Frameworks. *Nat. Mater.* **2016**, No. April, 1–6.

(56) Yoon, M.; Suh, K.; Natarajan, S.; Kim, K. Proton Conduction in Metal-Organic Frameworks and Related Modularly Built Porous Solids. *Angew. Chemie - Int. Ed.* **2013**, *52* (10), 2688–2700.

(57) Lammert, M.; Bernt, S.; Vermoortele, F.; Vos, D. E. De; Stock, N.; Kiel, D.-. Single- and Mixed-Linker Cr-MIL-101 Derivatives: A High-Throughput Investigation. **2013**.

(58) Katz, M. J.; Brown, Z. J.; Colón, Y. J.; Siu, P. W.; Scheidt, K. a; Snurr, R. Q.; Hupp, J. T.; Farha, O. K. A Facile Synthesis of UiO-66, UiO-67 and Their Derivatives. *Chem. Commun. (Camb).* **2013**, *49* (82), 9449–9451.

(59) Garibay, S. J.; Cohen, S. M. Isoreticular Synthesis and Modification of Frameworks with the UiO-66 Topology. *Chem. Commun. (Camb).* **2010**, *46* (41), 7700–7702.

(60) Torrisi, A.; Bell, R. G.; Mellot-Draznieks, C. Functionalized MOFs for Enhanced CO2 Capture. *Cryst. Growth Des.* **2010**, *10* (7), 2839–2841.

(61) Torrisi, A.; Bell, R. G.; Mellot-Draznieks, C. Predicting the Impact of Functionalized Ligands on CO2 Adsorption in MOFs: A Combined DFT and Grand Canonical Monte Carlo Study. *Microporous Mesoporous Mater.* **2013**, *168*, 225–238.

(62) Biswas, S.; Ahnfeldt, T.; Stock, N. Solids : Syntheses , Characterization , Sorption , and Breathing Behavior. **2011**, No. 2, 9518–9526.

(63) Munn, A. S.; Pillai, R. S.; Biswas, S.; Stock, N.; Maurin, G.; Walton, R. I. The Flexibility of Modified-Linker MIL-53 Materials. *Dalt. Trans.* **2016**, *45* (10), 4162–4168.

(64) Tanabe, K. K.; Cohen, S. M. Postsynthetic Modification of Metal-Organic Frameworks-a Progress Report. *Chem. Soc. Rev.* **2011**, *40* (2), 498–519.

(65) Jeremias, F.; Khutia, A.; Henninger, S. K.; Janiak, C. MIL-100(Al, Fe) as Water Adsorbents for Heat Transformation Purposes—a Promising Application. *J. Mater. Chem.* **2012**, *22* (20), 10148.

(66) Dugan, E.; Wang, Z.; Okamura, M.; Medina, A.; Cohen, S. M. Covalent Modification of a Metal-Organic Framework with Isocyanates: Probing Substrate Scope and Reactivity. *Chem. Commun. (Camb).* **2008**, *7345* (29), 3366–3368.

(67) Tanabe, K. K.; Wang, Z.; Cohen, S. M. Systematic Functionalization of a Metal-Organic Framework via a Postsynthetic Modification Approach. *J. Am. Chem. Soc.* **2008**, *130* (26), 8508–8517.

(68) Wang, Z.; Tanabe, K. K.; Cohen, S. M. Accessing Postsynthetic Modification in a Series of Metal-Organic Frameworks and the Influence of Framework Topology on Reactivity. *Inorg. Chem.* **2009**, *48* (1), 296–306.

(69) Tanabe, K. K.; Cohen, S. M. Engineering a Metal – Organic Framework Catalyst by Using Postsynthetic Modification. *Angew. Chem. Int. Ed.* **2009**, *48*, 7424–7427.

(70) Kim, M.; Boissonnault, J. a; Allen, C. a; Dau, P. V; Cohen, S. M. Functional Tolerance in an Isoreticular Series of Highly Porous Metal-Organic Frameworks. *Dalton Trans.* **2012**, *41* (20), 6277–6282.

(71) Wang, Z.; Cohen, S. M. Modulating Metal-Organic Frameworks to Breathe: A Postsynthetic Covalent Modification Approach. *J. Am. Chem. Soc.* **2009**, *131* (46),

16675–16677.

(72) Nguyen J.G., C. S. M. Moisture-Resistant and Superhydrophobic Metal-Organic Frameworks Obtained via Postsynthetic Modification. *J. Am. Chem. Soc.* **2010**, *132*, 4560–4561.

(73) Ahnfeldt, T.; Gunzelmann, D.; Loiseau, T.; Hirsemann, D.; Senker, J.; Férey, G.; Stock, N. Synthesis and Modification of a Functionalized 3D Open-Framework Structure with MIL-53 Topology. *Inorg. Chem.* **2009**, *48* (7), 3057–3064.

(74) Kandiah, M.; Usseglio, S.; Svelle, S.; Olsbye, U.; Lillerud, K. P.; Tilset, M. Post-Synthetic Modification of the Metal–organic Framework Compound UiO-66. *J. Mater. Chem.* **2010**, *20* (44), 9848.

(75) Dong, X. W.; Liu, T.; Hu, Y. Z.; Liu, X. Y.; Che, C. M. Urea Postmodified in a Metal-Organic Framework as a Catalytically Active Hydrogen-Bond-Donating Heterogeneous Catalyst. *Chem. Commun.* **2013**, *49* (70), 7681–7683.

(76) Modrow, A.; Zargarani, D.; Herges, R.; Stock, N. Introducing a Photo-Switchable Azo-Functionality inside Cr-MIL-101-NH2 by Covalent Post-Synthetic Modification. *Dalt. Trans.* **2012**, *41* (28), 8690–8696.

(77) Bernt, S.; Guillerm, V.; Serre, C.; Stock, N. Direct Covalent Post-Synthetic Chemical Modification of Cr-MIL-101 Using Nitrating Acidw. *Chem. Commun. Chem. Commun* **2011**, *47* (47), 2838–2840.

(78) Yilmaz, B.; Trukhan, N.; Müller, U. Industrial Outlook on Zeolites and Metal Organic Frameworks. *Chinese J. Catal.* **2012**, *33* (1), 3–10.

(79) Devic, T.; Serre, C. High Valence 3p and Transition Metal Based MOFs. *Chem. Soc. Rev.* **2014**, *43*, 6097–6115.

(80) Jasuja, H.; Burtch, N. C.; Huang, Y. G.; Cai, Y.; Walton, K. S. Kinetic Water Stability of an Isostructural Family of Zinc-Based Pillared Metal-Organic Frameworks. *Langmuir* **2013**, *29* (2), 633–642.

(81) Low, J. J.; Benin, A. I.; Jakubczak, P.; Abrahamian, J. F.; Faheem, S. A.; Willis, R. R. Virtual High Throughput Screening Confirmed Experimentally : Porous Coordination Polymer Hydration. *J. Am. Chem. Soc.* **2009**, *131* (5), 15834–15842.

(82) Burtch, N. C.; Jasuja, H.; Walton, K. S. Water Stability and Adsorption in Metal − Organic Frameworks. *Chem. Rev.* **2014**, *114* (20), 10575–10612.

(83) Schoenecker, P. M.; Carson, C. G.; Jasuja, H.; Flemming, C. J. J.; Walton, K. S. Effect of Water Adsorption on Retention of Structure and Surface Area of Metal – Organic Frameworks E Ff Ect of Water Adsorption on Retention of Structure and Surface Area of Metal − Organic Frameworks. *Ind. Eng. Chem. Res* **2012**, *51*, 6513–6519.

(84) Jhung, S. H.; Khan, N. A.; Hasan, Z. Analogous Porous Metal–organic Frameworks: Synthesis, Stability and Application in Adsorption. *CrystEngComm* **2012**, *14* (21), 7099.

(85) Wiberg, N. *Lehrbuch Der Anorganischen Chemie*, 102nd ed.; deGruyter: Berlin, 2007.

(86) Ming, Y.; Purewal, J.; Yang, J.; Xu, C.; Soltis, R.; Warner, J.; Veenstra, M.; Gaab, M.; Müller, U.; Siegel, D. J. Kinetic Stability of MOF-5 in Humid Environments: Impact of Powder Densification, Humidity Level, and Exposure Time. *Langmuir* **2015**, *31* (17), 4988–4995.

(87) DeCoste, J. B.; Peterson, G. W.; Jasuja, H.; Glover, T. G.; Huang, Y.; Walton, K. S. Stability and Degradation Mechanisms of Metal-Organic Frameworks Containing the Zr6O4(OH)4 Secondary Building Unit. *J. Mater. Chem. A* **2013**, *1* (18), 5642–5650.

(88) Gul-E-Noor, F.; Jee, B.; Pöppl, A.; Hartmann, M.; Himsl, D.; Bertmer, M. Effects of Varying Water Adsorption on a Cu3(BTC)2 Metal–organic Framework (MOF) as Studied by 1H and 13C Solid-State NMR Spectroscopy. *Phys. Chem. Chem. Phys.* **2011**, *13* (17), 7783.

(89) Seo, Y. K.; Yoon, J. W.; Lee, J. S.; Hwang, Y. K.; Jun, C. H.; Chang, J. S.; Wuttke, S.; Bazin, P.; Vimont, A.; Daturi, M.; Bourrelly, S.; Llewellyn, P. L.; Horcajada, P.; Serre, C.; Férey, G. Energy-Efficient Dehumidification over Hierachically Porous Metal-Organic Frameworks as Advanced Water Adsorbents. *Adv. Mater.* **2012**, *24* (6), 806–810.

(90) Ehrenmann, J.; Henninger, S. K.; Janiak, C. Water Adsorption Characteristics of MIL-101 for Heat-Transformation Applications of MOFs. *Eur. J. Inorg. Chem.* **2011**, No. 4, 471–474.

(91) Bauer, S.; Serre, C.; Devic, T.; Horcajada, P.; Stock, N. High-Throughput Assisted Rationalization of the Formation of Metal Organic Frameworks in the Iron (III) Aminoterephthalate Solvothermal System ´ Rard Fe. *Society* **2008**, *47* (17), 7568–7576.

(92) Stavitski, E.; Goesten, M.; Juan-Alcañiz, J.; Martinez-Joaristi, A.; Serra-Crespo, P.; Petukhov, A. V.; Gascon, J.; Kapteijn, F. Kinetic Control of Metal-Organic Framework Crystallization Investigated by Time-Resolved in Situ X-Ray Scattering. *Angew. Chemie - Int. Ed.* **2011**, *50* (41), 9624–9628.

(93) Ahnfeldt, T.; Guillou, N.; Gunzelmann, D.; Margiolaki, I.; Loiseau, T.; Férey, G.; Senker, J.; Stock, N. [Al4(OH)2(OCH3)4(H 2N- Bdc)3]·xH2O: A 12-Connected Porous Metal-Organic Framework with an Unprecedented Aluminum-Containing Brick. *Angew. Chemie - Int. Ed.* **2009**, *48* (28), 5163–5166.

(94) Ma, D.; Li, Y.; Li, Z. Tuning the Moisture Stability of Metal-Organic Frameworks by Incorporating Hydrophobic Functional Groups at Different Positions of Ligands. *Chem. Commun. (Camb).* **2011**, *47* (26), 7377–7379.

(95) Jasuja, H.; Huang, Y. G.; Walton, K. S. Adjusting the Stability of Metal-Organic Frameworks under Humid Conditions by Ligand Functionalization. *Langmuir* **2012**, *28* (49), 16874–16880.

(96) Cai, Y.; Zhang, Y.; Huang, Y.; Marder, S. R.; Walton, K. S. Impact of Alkyl-

Functionalized BTC on Properties of Copper-Based Metal-Organic Frameworks. *Cryst. Growth Des.* **2012**, *12* (7), 3709–3713.

(97) Decoste, J. B.; Peterson, G. W.; Smith, M. W.; Stone, C. a; Willis, C. R. Enhanced Stability of Cu-BTC MOF via Perfluorohexane Plasma Enhanced Chemical Vapor Deposition. *J. Am. Chem. Soc.* **2012**, 2–5.

(98) Chen, T.-H.; Popov, I.; Zenasni, O.; Daugulis, O.; Miljanić, O. Š. Superhydrophobic Perfluorinated Metal-Organic Frameworks. *Chem. Commun.* **2013**, *49* (61), 6846.

(99) Serre, C. Superhydrophobicity in Highly Fluorinated Porous Metal-Organic Frameworks. *Angew. Chemie - Int. Ed.* **2012**, *51* (25), 6048–6050.

(100) Goesten, M. G.; Magusin, P. C. M. M.; Pidko, E. A.; Mezari, B.; Hensen, E. J. M.; Kapteijn, F.; Gascon, J. Molecular Promoting of Aluminum Metal-Organic Framework Topology MIL-101 by N, N-Dimethylformamide. *Inorg. Chem.* **2014**, *53* (2), 882–887.

(101) Biswas, S.; Couck, S.; Grzywa, M.; Denayer, J. F. M.; Volkmer, D.; Van Der Voort, P. Vanadium Analogues of Nonfunctionalized and Amino-Functionalized MOFs with MIL-101 Topology - Synthesis, Characterization, and Gas Sorption Properties. *Eur. J. Inorg. Chem.* **2012**, No. 15, 2481–2486.

(102) Hartmann, M.; Fischer, M. Amino-Functionalized Basic Catalysts with MIL-101 Structure. *Microporous Mesoporous Mater.* **2012**, *164*, 38–43.

(103) Čendak, T.; Žunkovič, E.; Godec, T. U.; Mazaj, M.; Logar, N. Z.; Mali, G. Indomethacin Embedded into MIL-101 Frameworks: A Solid-State NMR Study. *J. Phys. Chem. C* **2014**, *118* (12), 6140–6150.

(104) Horcajada, P.; Chalati, T.; Serre, C.; Gillet, B.; Sebrie, C.; Baati, T.; Eubank, J. F.; Heurtaux, D.; Clayette, P.; Kreuz, C.; Chang, J.-S.; Hwang, Y. K.; Marsaud, V.; Bories, P.-N.; Cynober, L.; Gil, S.; Ferey, G.; Couvreur, P.; Gref, R. Porous Metal-Organic-Framework Nanoscale Carriers as a Potential Platform for Drug Delivery and Imaging. *Nat. Mater.* **2010**, *9* (2), 172–178.

(105) Taylor-Pashow, K. M. L.; Della Rocca, J.; Xie, Z.; Tran, S.; Lin, W. Postsynthetic Modifications of Iron-Carboxylate Nanoscale Metal-Organic Frameworks for Imaging and Drug Delivery. *J. Am. Chem. Soc.* **2009**, *131* (40), 14261–14263.

(106) Huxford, R. C.; Della Rocca, J.; Lin, W. Metal-Organic Frameworks as Potential Drug Carriers. *Curr. Opin. Chem. Biol.* **2010**, *14* (2), 262–268.

(107) Seo, P. W.; Khan, N. A.; Jhung, S. H. Removal of Nitroimidazole Antibiotics from Water by Adsorption over Metal–organic Frameworks Modified with Urea or Melamine. *Chem. Eng. J.* **2017**, *315*, 92–100.

(108) Hasan, Z.; Jeon, J.; Jhung, S. H. Adsorptive Removal of Naproxen and Clofibric Acid from Water Using Metal-Organic Frameworks. *J. Hazard. Mater.* **2012**, *209–210*, 151–157.

(109) Hasan, Z.; Choi, E.-J.; Jhung, S. H. Adsorption of Naproxen and Clofibric Acid over

a Metal–organic Framework MIL-101 Functionalized with Acidic and Basic Groups. *Chem. Eng. J.* **2013**, *219*, 537–544.

(110) Nuzhdin, A. L.; Kovalenko, K. A.; Dybtsev, N.; Bukhtiyarova, G. A. Removal of Nitrogen Compounds from Liquid Hydrocarbon Streams by Selective Sorption on Metal-Organic Framework MIL-101. *Mendeleev Commun.* **2010**, *20*, 57–58.

(111) Ahmed, I.; Khan, N. A.; Hasan, Z.; Jhung, S. H. Adsorptive Denitrogenation of Model Fuels with Porous Metal-Organic Framework (MOF) MIL-101 Impregnated with Phosphotungstic Acid : Effect of Acid Site Inclusion. *J. Hazard. Mater.* **2013**, *250–251*, 37–44.

(112) Bromberg, L.; Su, X.; Hatton, T. A. Aldehyde Self-Condensation Catalysis by Aluminum Aminoterephthalate Metal-Organic Frameworks Modified with Aluminum Isopropoxide. *Chem. Mater.* **2013**, *25* (9), 1636–1642.

(113) Luo, S. Q.; Lu, M.; Hao, C.; Qiu, J.; Li, Y. Organic Electron-Rich N-Heterocyclic Compound as a Chemical Bridge: Building a Brönsted Acidic Ionic Liquid Confined in MIL-101 Nanocages. *J. Mater. Chem.* **2013**, *1*, 6530–6534.

(114) Lau, M. L.; Deng, S.; Wang, Q. M.; Shen, D.; Martin, B.; Fitch, F. R.; Lemcoff, N. O.; Semanscin, J. Metallo-Organic Molecular Sieve for Gas Separation and Purification. **2002**, *55*, 217–230.

(115) Liang, Z.; Marshall, M.; Chaffee, A. L. CO 2 Adsorption-Based Separation by Metal Organic Framework (Cu-BTC) versus Zeolite (13X). **2009**, No. 9, 2785–2789.

(116) Bourrelly, S.; Llewellyn, P. L.; Serre, C.; Millange, F.; Loiseau, T.; Férey, G. Different Adsorption Behaviors of Methane and Carbon Dioxide in the Isotypic Nanoporous Metal Terephthalates MIL-53 and MIL-47. *J. Am. Chem. Soc.* **2005**, *127* (39), 13519–13521.

(117) Llewellyn, P. L.; Bourrelly, S.; Serre, C.; Filinchuk, Y.; Førey, G. How Hydration Drastically Improves Adsorption Selectivity for CO 2 over CH 4 in the Flexible Chromium Terephthalate MIL-53**. **2006**, 7751–7754.

(118) Wack, J.; Ahnfeldt, T.; Stock, N.; Senker, J. Identifying Selective Host − Guest Interactions Based on Hydrogen Bond Donor − Acceptor Pattern in Functionalized Al-MIL-53 Metal − Organic Frameworks. *J. Phys. Chem. C* **2013**, *117*, 11991–20001.

(119) Devautour-vinot, S.; Martineau, C.; Diaby, S.; Ben-yahia, M.; Miller, S.; Serre, C.; Horcajada, P.; Cunha, D.; Taulelle, F.; Maurin, G. Caffeine Confinement into a Series of Functionalized Porous Zirconium MOFs : A Joint Experimental/Modeling Exploration. *J. Phys. Chem.* **2013**, *117*, 11694–11704.

(120) Lincke, J.; Lassig, D.; Stein, K.; Moellmer, J.; Kuttatheyil, A. V; Reichenbach, C.; Moeller, A.; Staudt, R.; Kalies, G.; Bertmer, M.; Krautscheid, H. A Novel Zn4O-Based Triazolyl Benzoate MOF: Synthesis, Crystal Structure, Adsorption Properties and Solid State C-13 NMR Investigations. *Dalt. Trans.* **2012**, *41* (3), 817–824.

(121) Loiseau, T.; Serre, C.; Huguenard, C.; Fink, G.; Taulelle, F.; Henry, M.; Bataille, T.;

Férey, G. A Rationale for the Large Breathing of the Porous Aluminum Terephthalate (MIL-53) upon Hydration. *Chemistry* **2004**, *10* (6), 1373–1382.

(122) Volkringer, C.; Loiseau, T.; Guillou, N.; Férey, G.; Haouas, M.; Taulelle, F.; Elkaim, E.; Stock, N. High-Throughput Aided Synthesis of the Porous Metal-Organic Framework-Type Aluminum Pyromellitate, MIL-121, with Extra Carboxylic Acid Functionalization. *Inorg. Chem.* **2010**, *49* (21), 9852–9862.

(123) Ahnfeldt, T.; Gunzelmann, D.; Wack, J.; Senker, J.; Stock, N. Controlled Modification of the Inorganic and Organic Bricks in an Al-Based MOF by Direct and Post-Synthetic Synthesis Routes. *CrystEngComm* **2012**, *14* (12), 4126.

(124) Reinsch, H.; Marszałek, B.; Wack, J.; Senker, J.; Gil, B.; Stock, N. A New Al-MOF Based on a Unique Column-Shaped Inorganic Building Unit Exhibiting Strongly Hydrophilic Sorption Behaviour. *Chem. Commun.* **2012**, *48*, 9486.

(125) Haouas, M.; Volkringer, C.; Loiseau, T.; Férey, G.; Taulelle, F. Monitoring the Activation Process of the Giant Pore MIL-100(Al) by Solid State NMR. *J. Phys. Chem. C* **2011**, *115* (36), 17934–17944.

(126) Volkringer, C.; Loiseau, T.; Férey, G.; Morais, C. M.; Taulelle, F.; Montouillout, V.; Massiot, D. Synthesis, Crystal Structure and 71Ga Solid State NMR of a MOF-Type Gallium Trimesate (MIL-96) with μ3-Oxo Bridged Trinuclear Units and a Hexagonal 18-Ring Network. *Microporous Mesoporous Mater.* **2007**, *105* (1–2), 111–117.

(127) Hajjar, R.; Volkringer, C.; Loiseau, T.; Guillou, N.; Marrot, J.; Férey, G.; Margiolaki, I.; Fink, G.; Morais, C.; Taulelle, F. 71Ga Slow-CTMAS NMR and Crystal Structures of MOF-Type Gallium Carboxylates with Infinite Edge-Sharing Octahedra Chains (MIL-120 and MIL-124). *Chem. Mater.* **2011**, *23* (1), 39–47.

(128) He, P.; Lucier, B. E. G.; Terskikh, V. V.; Shi, Q.; Dong, J.; Chu, Y.; Zheng, A.; Sutrisno, A.; Huang, Y. Spies within Metal-Organic Frameworks: Investigating Metal Centers Using Solid-State NMR. *J. Phys. Chem. C* **2014**, *118* (41), 23728–23744.

(129) Martineau, C.; Cadiau, A.; Bouchevreau, B.; Senker, J.; Taulelle, F.; Adil, K. SMARTER Crystallography of the Fluorinated Inorganic–organic Compound Zn3Al2F12·[HAmTAZ]6. *Dalt. Trans.* **2012**, *41* (20), 6232.

(130) Volkringer, C.; Popov, D.; Loiseau, T.; Férey, G.; Burghammer, M.; Riekel, C.; Haouas, M.; Taulelle, F. Synthesis, Single-Crystal X-Ray Microdiffraction, and NMR Characterizations of the Giant Pore Metal-Organic Framework Aluminum Trimesate MIL-100. *Chem. Mater.* **2009**, *21* (24), 5695–5697.

(131) Chierotti, M. R.; Gobetto, R. Solid-State NMR Studies of Weak Interactions in Supramolecular Systems. *Chem. Commun.* **2008**, No. 14, 1621–1634.

(132) Gobetto, R.; Nervi, C.; Valfre, E.; Chierotti, M. R.; Braga, D.; Maini, L.; Grepioni, F.; Harris, R. K.; Ghi, P. Y.; Giuria, V. P.; Ciamician, C. G.; Selmi, V. F.; Chimica, D.; Vienna, V. 1 H CPMAS, 15N CPMAS and DFT Investigation of Hydrogen-Bonded Supramolecular Adducts between the Diamine Chain Length MAS , 15 N.

Chem. Mater. **2005**, *17* (6), 1457–1466.

(133) Sharif, S.; Denisov, G. S.; Toney, M. D.; Limbach, H.-H. NMR Studies of Coupled Low-and High-Barrier Hydrogen Bonds in Pyridoxal-5 '-Phosphate-Enzyme Model Systems in Polar Solution Supporting Information. *J. Am. Chem. Soc.* **2007**, *129* (11), 6313–6327.

(134) Levy, G. C.; Lichter, R. L. *Nitrogen-15 Nuclear Magnetic Resonance Spectroscopy*; John Wiley & Sons Inc.,: New York, 1979.

(135) Dos, A.; Schimming, V.; Tosoni, S.; Limbach, H.; Dos, A.; Schimming, V.; Tosoni, S.; Limbach, H. Acid # Base Interactions and Secondary Structures of Poly-L-Lysine Probed by N and C Solid State NMR and Ab Initio Model Calculations 15 N Acid - Base Interactions and Secondary Structures of Poly- L -Lysine Probed by Solid State NMR and Ab Initio Model C. **2008**, 15604–15615.

(136) Baek, S. Bin; Lee, H. C. ^{13} C NMR Study of CO_2 Adsorbed in Highly Flexible Porous Metal-Organic Frameworks. *Bull. Korean Chem. Soc.* **2016**, *37* (4), 588–591.

(137) Kong, X.; Scott, E.; Ding, W.; Mason, J. a; Long, J. R.; Reimer, J. a. CO2 Dynamics in a Metal − Organic Framework with Open Metal Sites. *J. Am. Chem. Soc.* **2012**, *134*, 14341−14344.

(138) Bertini, I.; Luchinat, C.; Parigi, G. Magnetic Susceptibility in Paramagnetic NMR. *Prog. Nucl. Magn. Reson. Spectrosc.* **2002**, *40* (3), 249–273.

(139) Kurland, R. J.; McGarvey, B. R. Isotropic NMR Shifts in Transition Metal Complexes: The Calculation of the Fermi Contact and Pseudocontact Terms. *J. Magn. Reson.* **1970**, *2* (3), 286–301.

(140) Bertmer, M. Paramagnetic Solid-State NMR of Materials. *Solid State Nucl. Magn. Reson.* **2016**, *81* (October 2016), 1–7.

(141) Aime, S., Bertini, I., Luchinat, C. Chapter 2 The Hyperfine Shift. *Coord. Chem. Rev.* **1996**, *150*, 29–75.

(142) Bertini, I.; Turano, P.; Vila, A. J. Nuclear Magnetic Resonance of Paramagnetic Metalloporphyrins. *Chem. Rev.* **1993**, *93*, 2833–2932.

(143) Bertini, Ivano; Luchinat, Claudio; Parigi, Giacomo; Ravera, E. *NMR of Paramagnetic Molecules. Applications to Metalloproteins and Models.*, 2nd ed.; Elsevier: Amsterdam, 2016.

(144) Aime, S., Bertini, I., Luchinat, C. Chapter 3 Relaxation. *Coord. Chem. Rev.* **1996**, *150*, 77–110.

(145) Sharp, R. Paramagnetic NMR Relaxation Enhancement: Recent Advances in Theory. *Prog. Nucl. Magn. Reson. Spectrosc.* **2001**, *38* (2), 115–158.

(146) Nayeem, A.; Yesinowski, J. P. Calculation of Magic-Angle Spinning Nuclear Magnetic Resonance Spectra of Paramagnetic Solids. *J. Chem. Phys.* **1988**, *89* (8), 4600.

(147) Cano, J.; Ruiz, E.; Alvarez, S.; Verdaguer, M. Spin Density Distribution in Transition Metal Complexes: Some Thoughts and Hints. *Comments Inorg. Chem.* **1998**, *20* (1), 27–56.

(148) Adamo, C.; Barone, V.; Subra, R. The Mechanism of Spin Polarization in Aromatic Free Radicals. *Theor. Chem. Acc.* **2000**, *104* (3–4), 207–209.

(149) Ruiz, E.; Cirera, J.; Alvarez, S. Spin Density Distribution in Transition Metal Complexes. *Coord. Chem. Rev.* **2005**, *249* (23), 2649–2660.

(150) Walker, F. A. Pulsed EPR and NMR Spectroscopy of Paramagnetic Iron Porphyrinates and Related Iron Macrocycles: How to Understand Patterns of Spin Delocalization and Recognize Macrocycle Radicals. *Inorg. Chem.* **2003**, *42* (15), 4526–4544.

(151) Clore, G. Marius; Iwahara, J. Theory, Practice and Applications of Paramagnetic Relaxation Enhancement for the Characterization of Transient Low Population States of Biological Macromolecules and Their Complexes. *NIH Public Access* **2008**, *42* (2), 157–162.

(152) Solomon, I. Relaxation Process in a System of Two Spins. *Phys. Rev.* **1955**, *99* (2), 559–565.

(153) Bertini, I.; Galas, O.; Luchinat, C.; Parigi, G.; Spina, G. Nuclear and Electron Relaxation in Magnetic Exchange Coupled Dimers: Implications for NMR Spectroscopy. *J. Magn. Reson.* **1998**, *130* (1), 33–44.

(154) Clementini, V.; Luchinat, C. NMR and Spin Relaxation in Dimers. *Acc. Chem. Res.* **1998**, *31* (6), 351–361.

(155) Peterson, G. W.; Wagner, G. W.; Balboa, A.; Mahle, J.; Sewell, T.; Karwacki, C. J. Ammonia Vapor Removal by Cu(3)(BTC)(2) and Its Characterization by MAS NMR. *J. Phys. Chem. C. Nanomater. Interfaces* **2009**, *113* (31), 13906–13917.

(156) Gul-E-Noor, F.; Mendt, M.; Michel, D.; Pöppl, A.; Krautscheid, H.; Haase, J.; Bertmer, M. Adsorption of Small Molecules on Cu 3(btc)2 and Cu3−xZnx(btc)2 Metal-Organic Frameworks (MOF) As Studied by Solid-State NMR. *J. Phys. Chem. C* **2013**, *117*, 7703–7712.

(157) Gul-E-Noor, F.; Michel, D.; Krautscheid, H.; Haase, J.; Bertmer, M. Investigation of the Spin-Lattice Relaxation of 13CO and 13CO2 Adsorbed in the Metal-Organic Frameworks Cu 3(btc)2 and Cu3-xZnx(btc) 2. *J. Chem. Phys.* **2013**, *139* (3).

(158) Dawson, D. M.; Jamieson, L. E.; Mohideen, M. I. H.; McKinlay, A. C.; Smellie, I. A.; Cadou, R.; Keddie, N. S.; Morris, R. E.; Ashbrook, S. E. High-Resolution Solid-State 13C NMR Spectroscopy of the Paramagnetic Metal–organic Frameworks, STAM-1 and HKUST-1. *Phys. Chem. Chem. Phys.* **2013**, *15* (3), 919–929.

(159) Horcajada, P.; Serre, C.; Maurin, G.; Ramsahye, N. a.; Balas, F.; Sebban, M.; Taulelle, F.; Vallet-Regi, M.; Ferey, G. Flexible Porous Metal-Organic Frameworks for a Controlled Drug Delivery. *J. Am. Chem. Soc.* **2008**, *130* (21), 6774–6780.

(160) Honda, Makoto; Morita, Makoto; Date, M. Electron Spin Resonance in Cr-Trimer Complexes. *J. Phys. Soc. Japan* **1992**, *61* (10), 3773–3785.

(161) Bencini, A.; Gatteschi, D. *EPR of Exchange Coupled Systems*; Springer: Berlin, 1990.

(162) Kambe, K. On the Paramagnetic Susceptibility of Some Polynuclear Complex Salts. *J. Phys. Soc. Japan* **1950**, *5*, 48–51.

(163) Banci, L.; Bertini, I.; Luchinat, C. The 1H NMR Parameters of Magnetically Coupled Dimers - The Fe2S2 Proteins as an Example. In *Bioinorganic Chemistry*; Berlin Heidelberg, 1990; pp 113–136.

(164) Berliner, L. J.; Reuben, J. *NMR of Paramagnetic Molecules*; Springer Science+Business Media: New York, 1993; Vol. 12.

(165) Aime, S., Bertini, I., Luchinat, C. Magnetic Coupled Systems. *Coord. Chem. Rev.* **1996**, *150*, 131–161.

(166) Machonkin, T. E.; York, N.; Westler, W. M.; Markley, J. L. Paramagnetic NMR Spectroscopy and Density Functional Calculations in the Analysis of the Geometric and Electronic Structures of Iron − Sulfur Proteins. **2005**, *44* (4), 779–797.

(167) Graaf, C. De; Broer, R. *Magnetic Interactions in Molecules and Solids*; Springer: Cham/Switzerland, 2016.

(168) Kahn, O. *Molecular Magnetism*; VCH Publishers, Inc. (USA), 1993.

(169) Ferrer, S.; Lloret, F.; Pardo, E.; Clemente-Juan, J. M.; Liu-Gonzalez, M.; Garcia-Granda, S. Antisymmetric Exchange in Triangular Tricopper(II) Complexes: Correlation among Structural, Magnetic, and Electron Paramagnetic Resonance Parameters. *Inorg.Chem.* **2012**, *51*, 985–1001.

(170) Holt, J.; Andreassen, T.; Bakke, J. M.; Fiksdahl, A. Nitropyridyl Isocyanates. *J. Heterocycl. Chem.* **2005**, *42* (2), 259–264.

(171) Chao, B. Y. M., Schempp, E., Rosenstein, R. D. 3-Aminopyridine. *Acta Crystallogr.* **1975**, *B31*, 2924–2926.

(172) Chavan, S.; Vitillo, J. G.; Groppo, E.; Bonino, F.; Lamberti, C.; Dietzel, P. D. C.; Bordiga, S. CO Adsorption on CPO-27-Ni Coordination Polymer : Spectroscopic Features and Interaction Energy. *J. Phys. Chem. C* **2009**, No. 113, 3292–3299.

(173) Dietzel, P. D. C.; Besikiotis, V.; Blom, R. Application of Metal – Organic Frameworks with Coordinatively Unsaturated Metal Sites in Storage and Separation of Methane and Carbon Dioxide. *J. Mater. Chem.* **2009**, *19*, 7362–7370.

(174) Kapelewski, M. T.; Geier, S. J.; Hudson, M. R.; Stück, D.; Mason, J. A.; Nelson, J. N.; Xiao, D. J.; Hulvey, Z.; Gilmour, E.; Fitzgerald, S. A.; Head-Gordon, M.; Brown, C. M.; Long, J. R. M 2 (M - Dobdc) (M = Mg, Mn, Fe, Co, Ni) Metal − Organic Frameworks Exhibiting Increased Charge Density and Enhanced H2 Binding at the Open Metal Sites. *J. Am. Chem. Soc.* **2014**, *2* (136), 12119–12129.

5 Darstellung des Eigenanteils

Die Ergebnisse der vorliegenden Arbeit wurden in Kollaboration mit anderen gewonnen und sind veröffentlicht oder werden wie unten angegeben noch zur Veröffentlichung eingereicht. Im Folgenden wird der Beitrag aller Co-Autoren zu den verschiedenen Publikationen angegeben. Der korrespondierende Autor wurde jeweils mit einem hochgestellten Sternchen gekennzeichnet.

Kapitel 6.1

Enhancing the Water Stability of Al-MIL-101-NH_2 Via Postsynthetic Modification

T. Wittmann, R. Siegel, N. Reimer, W. Milius, N. Stock, J. Senker*, *Chemistry - A European Journal*, **2015**, *21*, 314-323.

Das Konzept der Publikation wurde vollständig von mir und Prof. Dr. Jürgen Senker entwickelt und in einer lehrstuhl- und universitätsübergreifenden Kooperation bearbeitet. Die Synthesen und Beladungen der hier behandelten Verbindungen, die Messung und Interpretation von Röntgenpulverdiffraktogrammen, Flüssig-NMR-, Festkörper-NMR- und IR-Spektren, CHN-Analysen und thermogravimetrischen Analysen wurden von mir durchgeführt. Argon-Isothermen wurden von Dr. Nadine Popp, Wasseradsorptionsisothermen von Dr. Nele Reimer, EDX-Messungen von Beate Bojer, Atomabsorptionsmessungen von Sonja Lutschinger, Hochtemperatur- sowie Feuchtekammer-Röntgenpulverdiffraktogramme von Dr. Wolfgang Milius aufgenommen und jeweils von mir vollständig interpretiert. Dr. Renée Siegel unterstützte mich bei der Aufnahme und Interpretation der ^{1}H-^{27}Al D-HMQC-Spektren.

Die Publikation wurde vollständig von mir verfasst, während sie von Prof. Dr. Norbert Stock und Prof. Dr. Jürgen Senker korrigiert und überarbeitet wurde.

Mein Eigenanteil beläuft sich auf ca. 80 %.

Kapitel 6.2

Introducing Selective Host-Guest Interactions in MIL-101 Frameworks via a Multiple Hydrogen Bond Donor-Acceptor Recognition Site

Thomas Wittmann, Carsten B. L. Tschense, Renée Siegel, Jürgen Senker*, *to be submitted.*

Das Konzept der Publikation wurde vollständig von mir und Prof. Dr. Jürgen Senker entwickelt und in einer lehrstuhlinternen Kooperation bearbeitet. Die Synthesen und postsynthetischen Modifizierungen sowie Charakterisierung der Verbindungen mittels Röntgenpulverdiffraktogrammen, Flüssig-NMR-, Festkörper-NMR- und IR-Spektren, CHN- und AAS-Analysen sowie Gasphysisorptionsisothermen wurden von mir durchgeführt. Die Flüssigphasenadsorptionsisothermen wurden von mir vollständig aufgenommen, ausgewertet und interpretiert. Die 1D-Festkörper-NMR-Spektren der paramagnetischen Verbindungen sowie die ^{15}N-NMR-Spektren mit eingelagerten Gastmolekülen wurden unter Hilfestellung von Dr. Renée Siegel aufgenommen und von mir vollständig interpretiert. Die quantenchemischen DFT-Rechnungen der ^{15}N-chemischen Verschiebungen und Energien der Geometrie-optimierten Anordnungen der Gastmoleküle bezüglich der funktionellen Gruppen in den MOFs wurden von Carsten B. L. Tschense durchgeführt und von mir interpretiert.

Die Publikation wurde vollständig von mir verfasst und von Prof. Dr. Jürgen Senker überarbeitet.

Mein Eigenanteil beläuft sich auf ca. 80 %.

Kapitel 6.3

Probing Interactions of N-Donor Molecules with Open Metal Sites within Paramagnetic Cr-MIL-101: A Solid-State NMR Spectroscopic and Density Functional Theory Study

Thomas Wittmann, Arobendo Mondal, Carsten B. L. Tschense, Johannes J. Wittmann, Ottokar Klimm, Renée Siegel, Bjoern Corzilius, Birgit Weber, Martin Kaupp*, Jürgen Senker*, *J. Am. Chem. Soc.* **2018**, *140*, 6, 2135-2144.

Das Konzept der Publikation wurde vollständig von mir und Prof. Dr. Jürgen Senker entwickelt und in einer lehrstuhl- und universitätsübergreifenden Kooperation bearbeitet. Die Synthesen und Beladungen aller Verbindungen, die Messung und Interpretation von Röntgenpulverdiffraktogrammen, Flüssig-NMR-, Festkörper-NMR- und IR-Spektren, CHN- und AAS-Analysen sowie Gasphysisorptionsisothermen wurden von mir durchgeführt. Die magnetischen Messungen wurden von Ottokar Klimm durchgeführt und zusammen mit mir ausgewertet. Die EPR-Messungen wurden von Dr. Johannes J. Wittmann durchgeführt, ausgewertet und zusammen mit Dr. Björn Corzilius interpretiert. Die REDOR-Simulationen wurden von Carsten B. L. Tschense und Prof. Dr. Jürgen Senker durchgeführt und ausgewertet. Die DFT-Geometrie Optimierungen der Strukturmodelle und die quantenchemischen Rechnungen der Hyperfeinverschiebungen wurden von Arobendo Mondal durchgeführt, ausgewertet und zusammen mit Prof. Dr. Martin Kaupp interpretiert. Dr. Renée Siegel unterstützte mich bei der Aufnahme der 1D-Festkörper-NMR-Spektren, der REDOR-Messungen und der Spin-Gitter-Relaxationszeiten.

Die Publikation wurde hauptsächlich von mir verfasst und von Prof. Dr. Jürgen Senker überarbeitet, wobei der Teil zur Theorie und zur quantenchemischen Berechnung der Hyperfeinverschiebungen von Arobendo Mondal und Prof. Dr. Martin Kaupp geschrieben wurde. Carsten B. L. Tschense, Dr. Renée Siegel, Dr. Johannes J. Wittmann, Dr. Bjoern Corzilius und Prof. Dr. Birgit Weber haben durch wissenschaftliche Diskussionen und Hilfestellungen bei der Entstehung und bei der Überarbeitung der Publikation mitgewirkt.

Diese Publikation ist auch Teil der Doktorarbeit von Arobendo Mondal.

Mein Eigenanteil beläuft sich auf ca. 60 %.

6 Ergebnisse

6.1 Wechselwirkung von Al-MIL-101-NH_2 mit Wasser nach Modifizierung der Linker mit hydrophoben Phenylresten

Enhancing the Water Stability of Al-MIL-101-NH_2 via Postsynthetic Modification

T. Wittmann,[a] R. Siegel,[a] N. Reimer,[b] W. Milius,[c] N. Stock,[b] J. Senker[a]*

Erschienen in:

Chemistry - A European Journal **2015**, *21*, 314-323

[a] Department of Inorganic Chemistry III, University of Bayreuth, Universitätsstraße 30, 95440 Bayreuth (Germany)

[b] Institute of Inorganic Chemistry, Christian-Albrechts-Universität, Max-Eyth-Straße 2, 24118 Kiel (Germany)

[c] Department of Inorganic Chemistry I, University of Bayreuth, Universitätsstraße 30, 95440 Bayreuth (Germany)

* juergen.senker@uni-bayreuth.de

6.1.1 Enhancing the Water Stability of Al-MIL-101-NH_2 via Postsynthetic Modification

ChemPubSoc Europe DOI: 10.1002/chem.201404654 CHEMISTRY A European Journal Full Paper

Metal–Organic Frameworks

Enhancing the Water Stability of Al-MIL-101-NH_2 via Postsynthetic Modification

Thomas Wittmann,[a] Renée Siegel,[a] Nele Reimer,[b] Wolfgang Milius,[c] Norbert Stock,[b] and Jürgen Senker*[a]

Abstract: The resistance of metal–organic frameworks towards water is a very critical issue concerning their practical use. Recently, it was shown for microporous MOFs that the water stability could be increased by introducing hydrophobic pendant groups. Here, we demonstrate a remarkable stabilisation of the mesoporous MOF Al-MIL-101-NH_2 by postsynthetic modification with phenyl isocyanate. In this process 86% of the amino groups were converted into phenylurea units. As a consequence, the long-term stability of Al-MIL-101-URPh in liquid water could be extended beyond a week. In water saturated atmospheres Al-MIL-101-URPh decomposed at least 12-times slower than the unfunctionalised analogue. To study the underlying processes both materials were characterised by Ar, N_2 and H_2O sorption measurements, powder X-ray diffraction, thermogravimetric and chemical analysis as well as solid-state NMR and IR spectroscopy. Postsynthetic modification decreased the BET equivalent surface area from 3363 to 1555 $m^2 g^{-1}$ for Al-MIL-101-URPh and reduced the mean diameters of the mesopores by 0.6 nm without degrading the structure significantly and reducing thermal stability. In spite of similar water uptake capacities, the relative humidity-dependent uptake of Al-MIL-101-URPh is slowed and occurs at higher relative humidity values. In combination with ^1H-^{27}Al D-HMQC NMR spectroscopy experiments this favours a shielding mechanism of the Al clusters by the pendant phenyl groups and rules out pore blocking.

Introduction

Metal–organic frameworks (MOFs) have become increasingly attractive[1–3] for possible applications in separation[4,5] and storage of gases,[5,6] catalysis[5,7,8] and drug delivery.[5,9,10] To qualify MOFs for industrial processes like the purification of flue gases[11] or waste water[12,13] as well as for heat transformation[14] and dehumidification,[15] however, a very critical issue is the stability under humid conditions.[16]

Several recent studies focussed on this aspect and identified the coordinative bonds which connect metal–oxide clusters and organic linkers as the weak points to initiate the hydrolysis by linker exchange with water.[17,18] Low linker exchange rates are generally observed with increasing charge-to-size ratio of metal ions.[19–22] Additional determining factors are the strength of metal–ligand bonds which increase in line with oxidation states of the metals[18] and the Brønstedt-basicity[18,23,24] as well as the denticity of linkers.[18] Regarding transition metals, the electronic configuration of d-orbitals regulates the ligand field stabilization energy (LFSE) which also considerably influences linker exchange rates.[21] However, a relatively low inertness of the metal cations may be compensated by the dimensionality and connectivity of the inorganic building units (IBUs) within the framework.[18]

Consequently, Zn-based/containing (d^{10}) MOFs like DMOF-1, UMCM-1[19] and MOF-5[25] proved to be highly moisture sensitive. They degrade completely after exposure to humidity. In contrast, highly inert terephthalate-based MOFs are for instance represented by Zr^{4+} (d^0)-based UiO-66,[19] the Cr^{3+} (d^3)-containing MIL-53[20] and MIL-101[15,26] as well as the Fe^{3+} (d^5)- and Al^{3+} (d^0)-containing MIL-53.[27,28] However, MIL-101 analogues of Fe^{3+} and Al^{3+} are prone to hydrolysis. While hydrothermal stability for both Cr-MILs[15,18,26] is usually explained by considerably low exchange rates due to the energy gain by LFSE only the sterically more shielded one-dimensional IBUs in MIL-53 compared to the open ones of MIL-101 provide sufficient protection against water attack in the case of Fe^{3+} and Al^{3+}.[27,28] The IBUs of the MIL-53 structure consist of infinite chains of *trans* corner-sharing MO_6-polyhedra (M = Al, Cr, Fe) which are interconnected by terephthalate ions.[18,20,29] Another example for a shielded Al environment is the water-stable Al-MOF CAU-1.[30] Here, the corner- and edge-sharing AlO_6 polyhedra lead to 8-rings linked to twelve other IBUs via aminoterephthalate ions.[30] In contrast, the IBUs of mesoporous MIL-

[a] T. Wittmann, Dr. R. Siegel, Prof. Dr. J. Senker
Department for Inorganic Chemistry III, University of Bayreuth
Universitätsstraße 30, 95440 Bayreuth (Germany)
E-mail: juergen.senker@uni-bayreuth.de
[b] N. Reimer, Prof. Dr. N. Stock
Institute of Inorganic Chemistry, Christian-Albrechts-Universität
Max-Eyth-Straße 2, 24118 Kiel (Germany)
[c] Dr. W. Milius
Department of Inorganic Chemistry I, University of Bayreuth
Universitätsstraße 30, 95440 Bayreuth (Germany)

Supporting information for this article is available on the WWW under http://dx.doi.org/10.1002/chem.201404654.

ChemPubSoc Europe
CHEMISTRY A European Journal Full Paper

101 consist of trimeric μ_3-O-centred clusters which are interconnected by six linker molecules each.[27,31,32]

Up to now various concepts to stabilise microporous MOFs against hydrolysis have been explored. They include introducing hydrophobic linker molecules into the frameworks. Hence, alkylated and fluorinated linkers were applied to obtain water stable MOFs that are isoreticular to the water-sensitive Zn-based compounds MOF-508, SCUTC-18, SCUTC-19,[33] DMOF,[17,34] MOF-5,[35,36] and the Cu-based material HKUST-1.[37,38] Furthermore, the silver azolates FMOF-1 and FMOF-2[39] and the Cu-based compound MOFFs[40] features an extremely high water stability which was attributed to the superhydrophobic properties of the highly fluorinated linkers.[39,40] Cohen et al. were the first to show that modifying amino groups in IRMOF-3 and Al-MIL-53-NH_2 by postsynthetic modification (PSM) with alkyl anhydrides leads to enhanced water stability and hydrophobicity, respectively.[41] In summary, stabilisation of microporous MOFs can be achieved by preventing water from entering pores[37,40–42] or by shielding the inorganic building units.[17,33,34]

To the best of our knowledge, no studies have yet been performed on stabilising mesoporous MOFs. Since pore blocking is very difficult for such systems it is still an open question whether the same stabilisation mechanisms apply to mesoporous MOFs. The most widely used mesoporous MOFs are represented by the MIL-100 and MIL-101 types. The huge variety of possible applications[43] of these MOFs are based upon their mesoporous cavities (Figure 1), large surface areas, the presence of accessible metal sites and their comparatively high thermal and chemical robustness.[31,32,44,45]

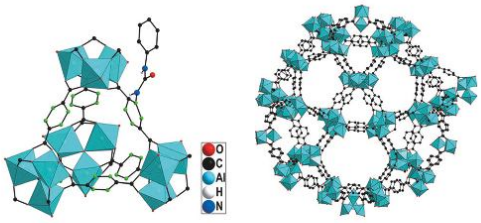

Figure 1. Visualisation of one possible orientation of the introduced phenylurea group relative to the Al clusters by exemplarily placing the latter at one linker of the supertetrahedron. Each linker may bear one functional group at one of the carbon atoms marked in green (left). Linked supertetrahedra generate the mesoporous cavities of the MIL-101 topology with diameters of 2.5 and 2.9 nm (right). Structures were obtained from literature data.[54]

In the present study the water stability of Al-MIL-101-NH_2 (Figure 1) was substantially improved by introducing pendant groups with PSM. Although, PSM on MIL-101-NH_2 materials (Cr, Al, Fe) was carried out before this effect has not been reported so far.[46–48] In Al-MIL-101-NH_2, the μ_3-O-centred trimeric clusters are linked via aminoterephthalate ions forming supertetrahedra which are arranged to generate mesoporous cavities which are accessible by pentagonal and hexagonal microporous windows (Figure 1).[27,31,32] The compound is particularly interesting for industrial purposes due to its inexpensive and abundant metal source as well as its non-hazardous nature and lower density compared to the Cr analogue.[49] Amino-tagged Al-MIL-101 was shown to be promising in the fields of gas separation,[31] heterogeneous catalysis,[31,44,50] and self-detoxification[48] as well as a material for sorption of harmful dyes[52] and sensing of fluoride ions.[53] In the course of our work, we proved that Al-MIL-101-NH_2 is highly sensitive against water which leads to the transformation to thermodynamically more stable Al-MIL-53-NH_2 after dissolution.[28] In addition, we observed a significantly enhanced kinetic resistance towards water resulting from covalent PSM of Al-MIL-101-NH_2 with phenyl isocyanate without reducing the water capacity. Figure 1 includes a sketch of one possible alignment of the pendant phenylurea group with respect to the IBUs.

Results and Discussion

Synthesis and postsynthetic modification of Al-MIL-101-NH_2

Al-MIL-101-NH_2 was prepared and activated by applying a slightly modified synthesis procedure introduced by Hartmann et al.[44] Details are presented in the Experimental Section. The powder X-ray diffraction (PXRD) pattern of the product together with the simulated pattern of Al-MIL-101-NH_2 is shown in Figure 2.[54] The good match of both indicates phase purity and high crystallinity of Al-MIL-101-NH_2; neither residual crystalline inorganic and organic reactants nor side products like MIL-53 were observed under the synthesis conditions (Figure 2).

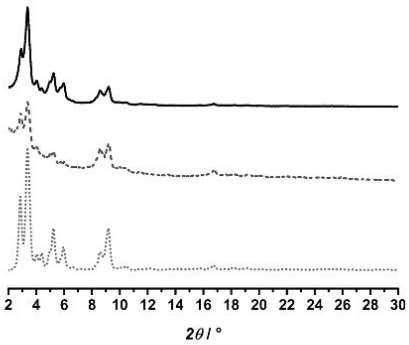

Figure 2. PXRD patterns of Al-MIL-101-NH_2 (black solid line, top) and Al-MIL-101-URPh (grey dashed line, middle). The simulated pattern (light grey dotted line, bottom) was derived as described in the Experimental Section.

PSM to obtain Al-MIL-101-URPh (URPh = phenylurea) was carried out according to a protocol of Cohen et al. (Scheme 1). Adding methanol to the reaction mixture prevents formation of crystalline diphenylurea.[55] The PXRD pattern of Al-MIL-101-URPh shows a higher background and broader reflections indi-

ChemPubSoc Europe
CHEMISTRY A European Journal Full Paper

cating a slightly lower degree of long-range order (Figure 2) which might be induced by a distribution of anchor group orientations with respect to the framework and a slight degradation of the framework, respectively. However, the overall structure is retained.

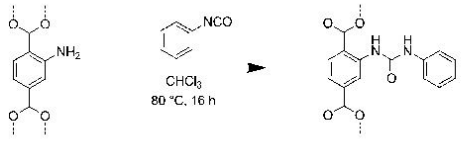

Scheme 1. Postsynthetic modification of Al-MIL-101-NH_2 by treatment with phenylisocyanate.

Integrity of the parent framework before and after PSM is further confirmed by solid-state ^{27}Al and ^{1}H MAS NMR (Figures S1 and S2 in the Supporting Information), ^{13}C and ^{15}N CP MAS NMR (Figure 3 and Figure 4), liquid-state ^{1}H NMR (Figure S4 in the Supporting Information) and IR spectroscopy (Figure 5). The full range ^{13}C CP MAS spectra are provided in Figure S3 in the Supporting Information. In accordance to the literature,[31] the sharp ^{27}Al signal for Al-MIL-101-NH_2 at $\delta(^{27}Al) = 0$ ppm (Figure S1 in the Supporting Information) implies octahedrally coordinated Al sites which are consistent with crystallographic data of the MIL-101 topology. Assignment of ^{1}H, ^{13}C and ^{15}N signals was established by simulating the chemical shifts using the ACD/Labs software package.[56] Proton (Figure S2 in the Supporting Information) and carbon (Figure 3) signals of Al-MIL-101-NH_2 between $\delta(^{1}H) = 8.3$ and 7.0 ppm and between $\delta(^{13}C) = 173$ and 115 ppm, respectively, were unambiguously assigned to the aminoterephthalate linker.

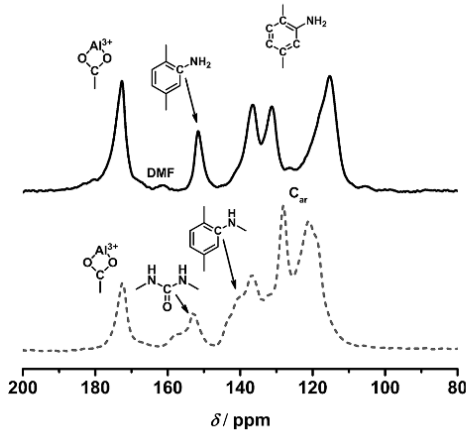

Figure 3. ^{13}C CP MAS NMR spectra of Al-MIL-101-NH_2 (black solid line, top) and Al-MIL-101-URPh (grey dashed line, bottom). The signal at $\delta(^{13}C) = 163$ ppm of Al-MIL-101-NH_2 (top) is caused by residual DMF.

The signal in the ^{1}H MAS spectrum at $\delta(^{1}H) = 5.2$ ppm (Figure S2 in the Supporting Information), the broad signal in the ^{15}N spectrum at $\delta(^{15}N) = -316$ ppm (Figure 4) and the asymmetric and symmetric N–H stretching vibrations at 3488 and 3366 cm^{-1} as well as the primary aromatic C–N stretching vibration at 1262 and 1340 cm^{-1} (Figure 5) verify the presence of amino groups.[57]

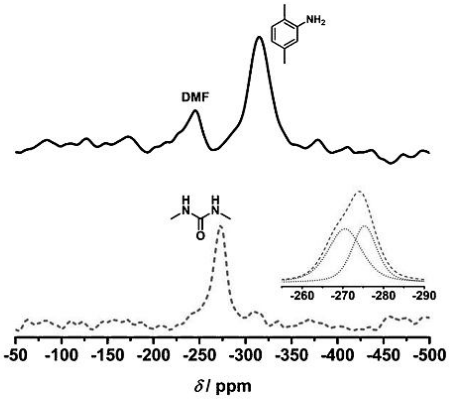

Figure 4. ^{15}N CP MAS NMR spectra of Al-MIL-101-NH_2 (black solid line, top) and Al-MIL-101-URPh (grey dashed line, bottom). The signal at $\delta(^{15}N) = -247$ ppm of Al-MIL-101-NH_2 (top) is due to residual DMF. Deconvolution of the two urea signals (bottom) was performed by applying the pseudo-Voigt profile function with equal FWHMs.

During PSM, the amino groups are converted into urea groups. The sharp signal at $\delta(^{27}Al) = 0$ ppm indicates retention of the octahedral Al environment after PSM. The most characteristic signals to follow the PSM are those of the amino groups (see above) and phenylurea groups. The much lower intensities of the signals of the amino group and the new signals of the phenylurea group suggest a nearly quantitative functionalisation which was determined to 86% by liquid-state ^{1}H NMR spectroscopy (Figure S4 in the Supporting Information and the Experimental Section). Resonances at $\delta(^{1}H) = 9.3$ and 10.9 ppm in the ^{1}H NMR spectrum (Figure S2 in the Supporting Information) as well as at $\delta(^{15}N) = -270$ and -275 ppm in the ^{15}N CP MAS NMR spectrum (Figure 4) of Al-MIL-101-URPh are unequivocally assigned to the urea protons and urea nitrogen atoms, respectively. Furthermore, the N–H vibration at 3302 cm^{-1}, the carbonyl band at 1696 cm^{-1}, the secondary C–N– at 1279 cm^{-1} as well as the asymmetric N–C–N stretching[45] vibration at 1313 cm^{-1} (Figure 5) prove attachment of phenylurea groups. Additionally, the *ipso* carbon signal at $\delta(^{13}C) = 151$ ppm is shifted to $\delta(^{13}C) = 141$ ppm (Figure 3), whereas the signal of the urea carbon atom arises at $\delta(^{13}C) = 154$ ppm. The broad signals between $\delta(^{13}C) = 137$ and 115 ppm are assigned to the residual carbon atoms of linkers and pendant phenyl groups.

Al contents, the Al/Cl ratio as well as C, H and N contents of Al-MIL-101-NH_2 and Al-MIL-101-URPh (86% urea) were deter-

ChemPubSoc Europe
CHEMISTRY A European Journal Full Paper

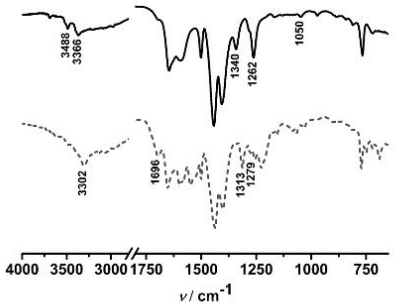

Figure 5. IR spectra of Al-MIL-101-NH_2 (black solid line, top) and Al-MIL-101-URPh (grey dashed line, bottom).

mined using atomic absorption spectroscopy (AAS), energy dispersive X-ray spectroscopy (EDX) and elementary analysis, respectively. The observed Al, Cl, C, H and N contents of 9.96, 4.24, 35.52, 3.80 and 4.98 wt% excellently agree with the theoretical composition of Al-MIL-101-NH_2 (9.94, 4.36, 35.42, 3.84 and 5.16 wt%, respectively) if adding eight water molecules to the formula unit. This results in the following stoichiometry: $[Al_3OCl(H_2O)_2(bdc\text{-}NH_2)_3]\cdot 6H_2O$.[44] Since the framework did not change during PSM (see above), a similar composition was derived for Al-MIL-101-URPh (86% urea). Again, the composition has to be balanced with six water molecules per formula unit to match the experimental (8.24, 3.56, 46.08, 3.63 and 6.74 wt%) and calculated contents (7.82, 3.27, 46.54, 3.71 and 7.20 wt%) resulting in the chemical formula $[Al_3OCl(H_2O)_2(bdc\text{-}URPh)_{2.58}(bdc\text{-}NH_2)_{0.42}]\cdot 4H_2O$. According to the literature,[44] two water molecules per formula unit are coordinated to the IBUs, whereas the residual water is physisorbed. Since the sample preparation was carried out under ambient conditions for these experiments the water is probably adsorbed from air. The existence of one chloride anion as a terminal ligand per formula unit,[44] which was also found in isostructural V-MIL-101[58] and V-MIL-100,[59] concurs with our results. Relative molar masses of the frameworks without coordinated and adsorbed water are calculated as 669.8 and 977.1 g mol^{-1}.

Porosity

To determine the effect of introducing phenylurea groups on the porosity, argon sorption measurements at 87 K were performed for both Al-MIL-101-NH_2 and Al-MIL-101-URPh (Figure 6a). Argon as an adsorptive allows for a more accurate pore size and surface analysis[60,61] compared to the commonly used nitrogen.[31,44,51–53] Surface areas, pore volumes and pore-size distributions (PSD) were derived using the NLDFT method. In order to comply with the cage-like structure of MIL-101 topologies[27,31,32] the argon sphere/cylindrical pore NLDFT kernel at 87 K for the adsorption branch on a silica/zeolite surface was employed. In contrast to the Ar–carbon kernel, this kernel provides pore sizes which match with the crystallographic data.[27,31,32] A comparison between calculated and experimental isotherms is given in Figure S5 in the Supporting Information. Apparent specific surface areas were additionally estimated by applying the BET method. To accommodate for microporous materials[60,61] the relative pressure ranges were limited to $p/p_0 = 0.06$-0.15. Total pore volumes were determined at $p/p_0 = 0.98$ according to the Gurvich rule.[62]

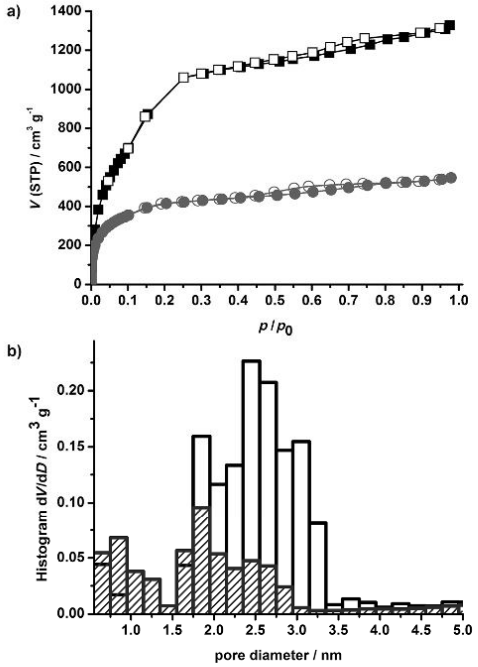

Figure 6. a) Argon adsorption (solid symbols) and desorption (empty symbols) isotherms at 87 K of Al-MIL-101-NH_2 (black squares) and Al-MIL-101-URPh (grey circles). b) Pore-size distribution of Al-MIL-101-NH_2 (black empty columns) and Al-MIL-101-URPh (grey hatched columns).

The argon sorption isotherms of Al-MIL-101-NH_2 and Al-MIL-101-URPh are displayed in Figure 6a. Both materials exhibit a type I isotherm as well as a type H4 hysteresis loop (p/p_0: 0.43–0.80) which is characteristic for materials containing both micro- and mesopores.[61] The sharp rise of the isotherms in the low pressure regime ($p/p_0 < 0.1$) is attributed to filling of the microporous supertetrahedra, whereas the mesoporous cavities are filled in two steps at around $p/p_0 = 0.1$ and $p/p_0 = 0.25$ which is typical for MIL-101 frameworks (Figure 6a).[31,32,44,45,58] These steps are less pronounced in the isotherm of Al-MIL-101-URPh (Figure 6a).

The calculated DFT surface area of 3056 m^2 g^{-1} and DFT pore volume of 1.66 cm^3 g^{-1} for Al-MIL-101-NH_2 agree well with the apparent BET surface area of 3363 m^2 g^{-1} and the calculated total pore volume at $p/p_0 = 0.98$ of 1.67 cm^3 g^{-1} (Table 1). The

ChemPubSoc Europe

CHEMISTRY A European Journal Full Paper

apparent BET surface area of 2880 $m^2 g^{-1}$ derived from a nitrogen sorption isotherm (Figure S6 in the Supporting Information) is lower. Our value is in the same order of magnitude as previously reported ones estimated from nitrogen sorption data which range from 3099,[44] 2600,[51] 2315,[53] 2100[31] to 1980 $m^2 g^{-1}$.[52]

Table 1. Apparent BET and DFT surface areas together with DFT and total pore volumes as well as DFT micropore volumes of Al-MIL-101-NH_2 and Al-MIL-101-URPh.

	Al-MIL-101-NH_2	Al-MIL-101-URPh
S_{BET} [$m^2 g^{-1}$]	3363	1555
S_{DFT}[a] [$m^2 g^{-1}$]	3056	2482
V_{tot}[b] [$cm^3 g^{-1}$]	1.67	0.83
$V_{tot,DFT}$[a] [$cm^3 g^{-1}$]	1.66	0.74
$V_{micro,DFT}$[a,c] [$cm^3 g^{-1}$]	0.32	0.39

[a] DFT surface areas and DFT pore volumes were calculated using the argon spherical/cylindrical pore NLDFT model at 87 K for the adsorption branch on a silica/zeolite surface. [b] Calculated total pore volume at $p/p_0 = 0.98$. [c] Pore volume of pores with diameters smaller than 2 nm.

The PSD of Al-MIL-101-NH_2 and Al-MIL-101-URPh are shown in Figure 6b. As a consequence of the restricted diffusion at low pressures,[63] argon does not access pores smaller than 0.6 nm which poses the lower limit for the experimental PSDs. In analogy to Cr-MIL-101,[32] the observed maxima at 0.7, 1.7, 2.5 and 2.9 nm are attributed to the microporous supertetrahedra, the hexagonal windows of the cages and the two mesoporous cavities, respectively (Figure 6b). Due to an artificial gap in the range from 0.8 to 1.5 nm, the diameter of the pentagonal windows is hidden.[61,63]

While the apparent BET surface area, the total DFT pore volume and the calculated pore volume decreased by a factor of about 2.0 upon introduction of phenylurea groups, the DFT surface area was merely reduced by a factor of 1.3 (Table 1). These observations might be attributed to the reduction of accessible adsorption sites and a slightly decreased crystallinity as observed in the PXRDs (Figure 2). The PSD of Al-MIL-101-URPh reveals a significant shift to smaller values (Figure 6b). The bulky phenylurea groups cause the sizes of the mesoporous cavities to shift to the microporous (1.6–1.9 nm) and smaller mesoporous region (2.2 nm). The dimensions of microporous supertetrahedra (0.7 nm) did not change. Hence, the number ratio of micropores to mesopores increases upon PSM. This observation is also supported by the DFT calculations of the micropore volume ($V_{micro,DFT}$) which increases from 0.32 to 0.39 $cm^3 g^{-1}$ upon PSM (Table 1).

While the DFT pore volume is reasonably consistent with the calculated pore volume of Al-MIL-101-URPh, the large difference between DFT and apparent BET surface areas is worth noting (Table 1). This might be a result of an increased ratio of micropores-to-mesopores (Figure 6b and Table 1) which leads to an even more restricted applicability of the BET method.[61]

Thermal properties

Thermal properties of Al-MIL-101-NH_2 and Al-MIL-101-URPh in air were studied by X-ray thermodiffraction up to 500 °C (Figure 7) and thermogravimetric analysis (TGA) up to 900 °C at 4 K min^{-1} (Figure 8). The corresponding temperature resolved PXRD patterns are shown in Figure 7. Up to 180 °C, the variation of intensities is due to the evaporation of residual solvent and water molecules. Crystallinity of both Al-MIL-101-NH_2 and Al-MIL-101-URPh were sufficiently retained up to 280 °C and full amorphisation is observed above 300 °C (Figure 7). The positions of all Bragg reflections do not shift indicating that the frameworks remain unchanged up to 300 °C.

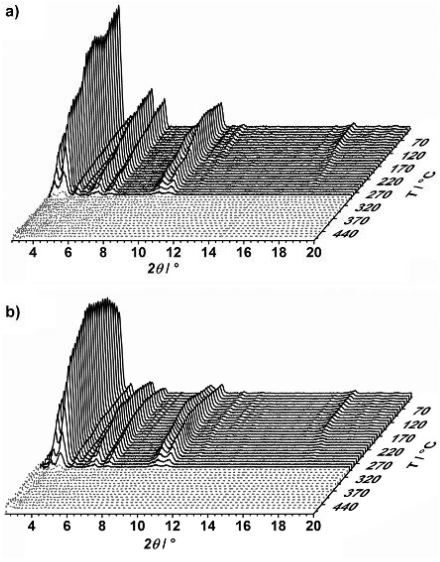

Figure 7. Powder X-ray thermodiffractograms of: a) Al-MIL-101-NH_2, and b) Al-MIL-101-URPh. The black and grey dotted patterns represent crystalline and amorphous regions, respectively.

The thermograms of activated Al-MIL-101-NH_2 and Al-MIL-101-URPh are shown in Figure 8. Prior to TGA, the samples were degassed at 130 °C for 3 h under reduced pressure. The first step up to roughly 120 °C for the amino (black dashed line) and urea MOF (red dashed line) reveal mass losses of 9 wt% (1.2 water molecules per linker, see the Experimental Section) and 2 wt% (0.4 water molecules per linker), respectively, which are mainly attributed to evaporation of physisorbed water molecules. Obviously, water is immediately adsorbed even during a short exposure to air while transferring the samples from the evacuated flasks into the apparatus as rapidly as possible. The 25 wt% of Al-MIL-101-URPh (red dashed line) is lost in the range between 190 and 320 °C which corresponds to a loss of almost all phenylurea groups (calcd:

ChemPubSoc Europe
CHEMISTRY A European Journal Full Paper

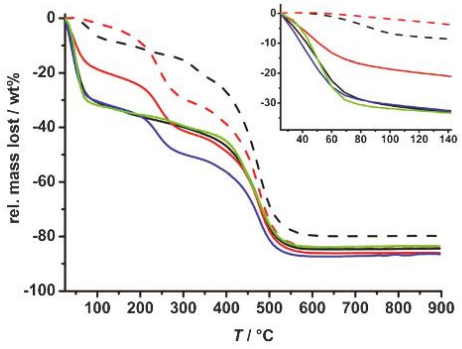

Figure 8. Thermograms of Al-MIL-101-NH_2 (dashed black) and Al-MIL-101-URPh (dashed red) after being degassed and thermograms of the samples exposed to humid air (100% RH) at 25 °C: Al-MIL-101-NH_2 (2 h, black solid), Al-MIL-101-URPh (2 h, red solid), Al-MIL-101-NH_2 (20 h, green solid), Al-MIL-101-URPh (20 h, blue solid).

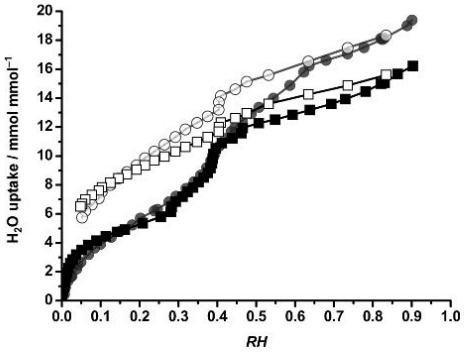

Figure 9. Water adsorption (solid symbols) and desorption isotherms (empty symbols) at 298 K of Al-MIL-101-NH_2 (black squares) and Al-MIL-101-URPh (grey circles). Water-free molar masses are determined as 669.8 and 977.1 g mol^{-1}, respectively.

28 wt%). The weight losses, starting at roughly 380 °C for both materials, mark the degradation of the framework. This degradation temperature in air compares well to the value reported in the literature.[31] TGA and X-ray thermodiffraction reveal no evident decrease of the thermal stability after PSM.

Water sorption behaviour, long-term stability in water and humid atmospheres

The water sorption behaviour of Al-MIL-101-NH_2 and Al-MIL-101-URPh was analysed by means of TGA (Figure 8) and water sorption measurements (Figure 9) at 298 K. Furthermore, in situ PXRD (Figure 10) at various temperatures and relative humidity values was performed to study the stability of both MOFs. In addition both compounds were suspended in liquid water and exposed to water-saturated atmospheres at various temperatures, in order to evaluate the long-term stability.

Figure 8 shows the thermograms of Al-MIL-101-NH_2 and Al-MIL-101-URPh after being exposed to humid atmosphere (100% RH) at 25 °C for 2 h (Figure 8, black and red solid lines) and 20 h (Figure 8, green and blue solid lines), respectively. The water uptakes can be determined from the first plateau at 120 °C and shows a remarkable difference between the two compounds. After 2 h, Al-MIL-101-NH_2 contains six water molecules per linker (black solid line), Al-MIL-101-URPh, however, incorporates 4.2 molecules (red solid line). The water load of the phenylurea MOF after 20 h also corresponds to roughly six water molecules per linker (blue solid line), whereas Al-MIL-101-NH_2 did not adsorb considerably more water indicating its saturation capacity had been reached already after 2 h (green solid line). While both Al-MIL-101-NH_2 and Al-MIL-101-URPh contain roughly six water molecules per linker after 20 h the uptake determined by TGA is much slower for Al-MIL-101-URPh and, therefore, it seems to be kinetically hindered.

The results can be compared with the ones from the water sorption isotherms of Al-MIL-101-NH_2 and Al-MIL-101-URPh at 298 K which are shown in Figure 9. The water uptake is plotted as adsorbed moles of water per mole of water-free MOFs against relative humidity (RH). This graphical representation enables us to easily estimate the water uptake per linker. Water-free molar masses were determined by chemical analysis (see above). The saturation capacities at 90% RH were calculated as 5.5 for Al-MIL-101-NH_2 and 6.5 for Al-MIL-101-URPh (Figure 9) which closely correspond to the adsorbed amounts determined by TGA experiments (Figure 8). The saturation water uptakes of both MOFs are consequently similar even though Al-MIL-101-URPh exhibits only roughly half the pore volume of Al-MIL-101-NH_2 (Table 1). Both MOFs reveal a wide hysteresis (Figure 9) which suggests irreversible water uptake over the whole humidity range as also found for isostructural Cr-MIL-101 analogues.[15,64] Despite a slightly higher water uptake, Al-MIL-101-URPh retains slightly less water (1.9 per linker) at 5% RH compared to Al-MIL-101-NH_2 (2.2 per linker) (Figure 9).

The stepwise water ad- and desorption behaviour of Al-MIL-101-NH_2 and Al-MIL-101-URPh (Figure S7 in the Supporting Information) agrees well with the ones of isostructural MIL-100[14,15] and MIL-101 materials.[15,64,65] Adsorption isotherms of both compounds show rapid water uptakes up to 5% RH due to saturation of open metal sites existing after prior heating. The slope of the isotherm of Al-MIL-101-NH_2 is slightly increased compared to the one of Al-MIL-101-URPh (Figure 9 and Figure S7). The onset of the filling of the microporous supertetrahedra for Al-MIL-101-NH_2 proceeds at a slightly lower RH value (28%) compared to Al-MIL-101-URPh (31%). The small mesoporous cavities of both MOFs start to be filled at 39% RH. The big mesopores of Al-MIL-101-NH_2 already fill at 46% RH, whereas the same process does not start before 62% RH for the phenylurea MOF (Figure S7 in the Supporting Information). The well-resolved adsorption steps are not observed in the water isotherm of Al-MIL-101-URPh which can be explained with the broad distribution of the pore sizes as a conse-

ChemPubSoc Europe
CHEMISTRY A European Journal Full Paper

quence of the incomplete PSM of the cavities (Figure 6b). Both MOFs show marked desorption steps at around 40% RH (Figure 9) being characteristic for emptying the mesoporous cavities.[64] This suggest structural integrity of both MOFs after the water-adsorption process.

The lower uptake up to 5% RH and filling the big mesoporous cavities of Al-MIL-101-URPh at higher RH (Figure 9 and Figure S7 in the Supporting Information) indicate a decreased affinity of water to the hydrophilic adsorption sites of the trimeric IBUs which are oriented towards the mesoporous cages, as discussed above (Figure 6b). This suggests a shielding effect induced by hydrophobic phenylurea groups.

After the water sorption measurements and evacuation at 120 °C the porosity of both compounds was checked by argon sorption measurements (Figure S8 in the Supporting Information). While the apparent BET surface area and total pore volume of Al-MIL-101-URPh were reduced by roughly 17%, no porosity was left in Al-MIL-101-NH_2 (Figure S8). Additionally, an amorphisation of the amino MOF was observed, whereas the structure of the phenylurea MOF was retained as shown in the PXRD patterns recorded after the sorption measurements (Figure S9 in the Supporting Information).

Figure 10 shows the PXRD patterns of Al-MIL-101-NH_2 and Al-MIL-101-URPh collected in situ at different relative humidities and temperatures. This allows us to mimic the conditions of the water sorption measurements (Figure 9) and thus enables us to correlate the effects of the water adsorption on the structures of both compounds. Limited by the device, a maximum RH of 95% could be accomplished up to 40 °C. From 60 °C upward the absolute amount of water was kept constant which leads to a decrease of the RH values. In spite of a considerable decline of crystallinity caused by adsorbed water, Al-MIL-101-NH_2 did not collapse up to 95% RH at 40 °C. However, transformation to the thermodynamically more stable Al-MIL-53-NH_2[28,29] started from 60 °C and 69% RH (Figure 10a, grey dotted patterns). In contrast, Al-MIL-101-URPh shows a significantly higher crystallinity after exposure to humidity indicating a higher stability (Figure 10b). Its structure was completely retained over the whole temperature and humidity range (Figure 10b).

Al-MIL-101-URPh takes up slightly more water than Al-MIL-101-NH_2 (Figure 9) which may indicate that the coverage of the inner surfaces with the hydrophobic pendant groups is too low to significantly affect the total water capacity. Additionally, the structural integrity (Figure S9 in the Supporting Information and Figure 10) and porosity (Figure S8 in the Supporting Information) are retained after water adsorption. These observations imply that the phenylurea groups cause the enhanced water stability. This indicates an improved shielding of the inorganic units from being attacked by water which is, furthermore, supported by collecting ^{1}H-^{27}Al D-HMQC spectra.

These spectra allow us to determine the closest water connectivities around the Al clusters. The 1D ^{1}H MAS and 2D ^{1}H-^{27}Al D-HMQC spectra of water loaded Al-MIL-101-NH_2 and Al-MIL-101-URPh are presented in Figures S10 and S11 in the Supporting Information. The respective 1D ^{1}H projections of the ^{1}H-^{27}Al D-HMQC spectra are displayed in Figure 11. Although

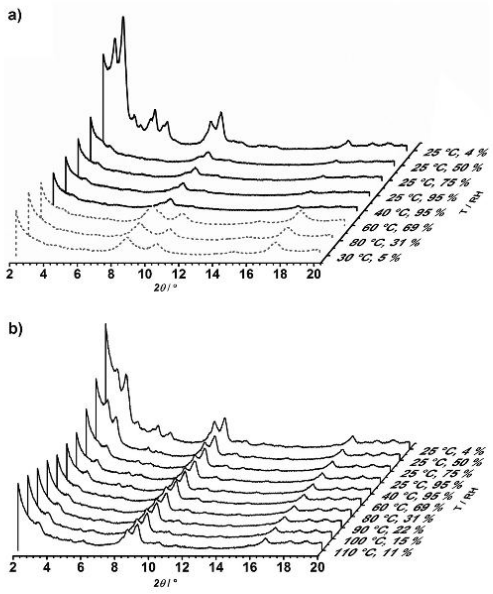

Figure 10. Results of the in situ PXRD measurements of: a) Al-MIL-101-NH_2, and b) Al-MIL-101-URPh exposed to different values of relative humidity and temperature.

the 1D ^{1}H MAS spectra of both MOFs (Figure S10 in the Supporting Information) reveal saturation of the strong adsorption sites around the Al clusters due to the presence of dynamic excess water in the pores, we observe different intensity ratios between adjacent aqueous and aromatic protons in the 1D ^{1}H MAS projections of the ^{1}H-^{27}Al HMQC spectra. Al-MIL-101-NH_2 reveals a higher intensity of H_{H_2O} at $\delta(^1H) = 4.4$ ppm compared to H_{ar} at around $\delta(^1H) = 7$ ppm (Figure 11, top). In contrast, a nearly similar intensity ratio between aromatic and aqueous protons is observed for Al-MIL-101-URPh measured under identical conditions (Figure 11, bottom). This indicates that more water is in a closer proximity to the Al-O clusters in Al-MIL-101-NH_2 than in the phenylurea analogue.

PXRD was used to investigate the effect of shielding on long-term water stability of the Al-MIL-101 framework. The PXRD patterns are shown in Figures S12–S19 in the Supporting Information. Both MOFs were suspended in water at ambient conditions as well as exposed to air with 100% RH, starting from 60 °C. X-ray powder patterns after suspending the MOFs in water and subsequent regeneration at 80 °C showed that the structure of Al-MIL-101-URPh was not affected during seven days (Figure S12). Al-MIL-101-NH_2, however, had already transformed into thermodynamically more stable Al-MIL-53-NH_2 after five minutes (Figure S12).[28,29] Heating during regeneration possibly facilitated the decomposition process.

Figure 12 summarizes the results of Figures S13–S19. The decomposition times of Al-MIL-101-NH_2 and Al-MIL-101-URPh

ChemPubSoc Europe
CHEMISTRY A European Journal Full Paper

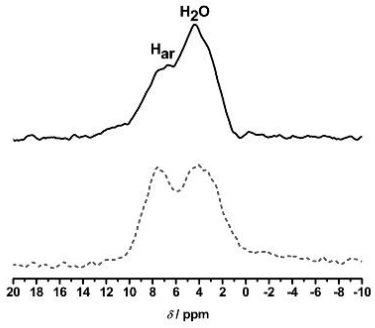

Figure 11. 1D ^{1}H projections of the ^{1}H-^{27}Al D-HMQC NMR spectra of Al-MIL-101-NH_2 (black solid line, top) and Al-MIL-101-URPh (grey dashed line, bottom).

after exposure to 100% RH at different temperatures are shown. In the temperature range from 60 to 110 °C at 100% RH water stability of Al-MIL-101-URPh compared to Al-MIL-101-NH_2 was enhanced by a factor of 12 to 6. Due to the increased framework mobility which leads to a less effective shielding of the IBUs, a decrease in decomposition time from 24 h at 60 °C to 2 h at 90 °C is observed.

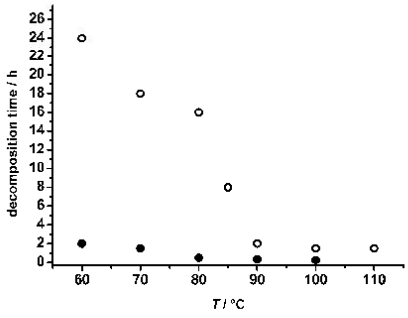

Figure 12. Decomposition times of Al-MIL-101-NH_2 (solid circles) and Al-MIL-101-URPh (empty circles) after exposure to humid air (100% RH) at different temperatures.

Conclusions

Synthesis of Al-MIL-101-NH_2 along with its successful PSM with phenyl isocyanate was unequivocally proven by PXRD, solid-state and liquid-state NMR as well as IR spectroscopy. PSM yielded Al-MIL-101-URPh containing 86% phenylurea groups. Chemical compositions were verified using EDX, AAS and CHN analysis.

Both crystallinity and porosity could be sufficiently retained after PSM. The remarkably high apparent BET surface area of 3363 $m^2 g^{-1}$ (S_{DFT} = 3056 $m^2 g^{-1}$) for Al-MIL-101-NH_2 was reduced to 1555 $m^2 g^{-1}$ (S_{DFT} = 2482 $m^2 g^{-1}$). Analyses with DFT kernels suggested pore diameters of 0.7, 2.5 and 2.9 nm for Al-MIL-101-NH_2, and 0.7, 1.9 and 2.2 nm after introducing phenylurea groups. These can be attributed to the microporous supertetrahedra and the two kinds of mesoporous cavities, respectively. The increase of the ratio of micropores to mesopores (roughly 22%) after PSM indicates that the bulky phenylurea moieties point towards the mesoporous cavities. TGA suggests decomposition of both frameworks at about 380 °C. The loss of the phenylurea groups in Al-MIL-101-URPh starts at roughly 190 °C. X-ray thermodiffraction evidences structural integrity of both Al-MIL-101-NH_2 and Al-MIL-101-URPh being maintained up to 280 °C before amorphisation takes place. Thermal stability is consequently not affected by introducing phenylurea groups.

TGA and water sorption measurements reveal similar water uptakes of roughly six water molecules per linker for both materials despite a lower pore volume of Al-MIL-101-URPh which suggests that the coverage of the inner surfaces with the hydrophobic pendant groups is too low to significantly affect the total water capacity. However, the water uptake of Al-MIL-101-URPh is kinetically hindered compared to Al-MIL-101-NH_2. Filling of the big mesoporous cavities starts at higher relative humidity values which implies the affinity to specific adsorption sites being reduced. In situ PXRD at different combinations of relative humidity and temperature as well as argon sorption isotherms after water sorption measurements demonstrate an enhanced retention of crystallinity and porosity of Al-MIL-101-URPh, respectively. This is due to shielding of the metal–ligand bonds by hydrophobic phenylurea moieties which impede linker–water exchange to occur and the structure to collapse. The shielding effect was additionally probed by solid-state ^{1}H-^{27}Al D-HMQC NMR spectroscopy. The results indicate that more water is in closer proximity to the inorganic units for the amino MOF compared to ones of the phenylurea MOF.

Attaching hydrophobic phenylurea groups results in a considerably enhanced long-term stability in liquid water and humid environments. Stability of the Al-MIL-101 topology could be raised from five minutes to about one week in liquid water and subsequent regeneration at 80 °C. Furthermore, Al-MIL-101-URPh showed a considerably increased resistance to humid air with 100% RH by a factor of about twelve at 60 °C and of about six at 100 °C.

Experimental Section

Synthesis of Al-MIL-101-NH_2

All chemicals were purchased und used without further purification if not explicitly mentioned. Synthesis and activation of Al-MIL-101-NH_2 were carried out applying a modified synthesis procedure established by Hartmann et al.[44] 2-Aminoterephthalic acid (H_2BDC-NH_2; 1.09 g, 6 mmol, ABCR) was dissolved in DMF (80 mL, VWR) at 110 °C. Aluminium chloride hexahydrate ($AlCl_3 \cdot 6H_2O$; 0.97 g, 4 mmol, Sigma Aldrich) was added in seven equal portions (0.139 g, 0.57 mmol) in time steps of 15 min. Having added the last portion, the mixture was stirred at 110 °C for 3 h followed by holding the same temperature for 16 h without stirring. After cooling to room temperature, the yellow solid was filtered, washed with

ChemPubSoc Europe

CHEMISTRY A European Journal Full Paper

DMF (5×15 mL) and ethanol (5×15 mL, VWR) and activated by Soxhlet extraction with ethanol for 24 h. Finally, the solid was dried at 120 °C for 24 h under reduced pressure.

Postsynthetic modification of Al-MIL-101-NH_2

Following the procedure of Dugan et al.[55] Al-MIL-101-NH_2 (180 mg) was suspended in freshly distilled chloroform (8.5 mL, VWR). Subsequently, phenylisocyanate (350 μL, 3.2 mmol, Sigma Aldrich) and methanol (350 μL, 8.6 mmol, VWR) were added. The reaction mixture was stirred at 80 °C for 16 h. The solid was subsequently filtered, washed with chloroform (10×2 mL) and dried at 100 °C for 3 h under reduced pressure.

Long-term stability measurements

Al-MIL-101-NH_2 (15 mg) and Al-MIL-101-URPh (15 mg) were suspended in 1 mL water in a closed glass vessel. Before being analysed with PXRD, the samples were dried at 80 °C for 1 h. Stability experiments in humid air at different temperatures were performed in glass autoclaves which were placed in a preheated convection oven. Al-MIL-101-NH_2 (15 mg) and Al-MIL-101-URPh (15 mg) were loaded in open glass vessels. These were placed inside the glass autoclaves containing water (2 mL).

Characterization methods

All PXRD data were collected in Bragg–Brentano geometry on a Panalytical Xpert Pro diffractometer equipped with a X'Celerator Scientific RTMS detector using Ni filtered $Cu_{K\alpha}$ radiation (λ = 1.54187 Å, 40 kV, 40 mA). Powder patterns at ambient conditions were recorded in the range of 2–30° (2θ) with a step size of 0.017°. Temperature resolved X-ray diffraction studies from 30 to 500 °C in 10 °C intervals were carried out in static air using an Anton Paar XRK 900 device. Between two patterns the samples were heated at a temperature ramp of 10 °C min^{-1} and a dwell time of 15 min. Each pattern was recorded in a 2θ range of 2–25° and step size of 0.017°. Humidity dependent powder X-ray diffraction was performed in an Anton Paar THC humidity chamber in the range 2–20° (2θ) and step size of 0.017° between 25 and 110 °C. Relative humidities (4–95% RH) of the dynamic stream of dry nitrogen (500 mL min^{-1}) were adjusted by a VTI RH-200 relative humidity generator. The theoretical powder pattern was obtained after replacing Cr by Al in a crystallographic information file of Cr-MIL-101.[54] The pattern was simulated using $Cu_{K\alpha}$ radiation in reflection geometry, the Pearson profile function and a germanium monochromator. The half width of the Bragg reflexes was set to 0.25° (2θ). While the space group $Fd\bar{3}m$ (No. 227) of the face centred cubic cell was kept, the cell parameters were refined to 87.7 Å.

Liquid-state ^{1}H NMR spectra were recorded using a Varian INOVA 300 spectrometer operating at a proton frequency of 299.9 MHz. The samples were digested in a 1.25 wt% NaOD/D_2O solution. The yield of PSM was determined by comparing the integrated areas of the aromatic resonances of the modified (δ = 7.70 ppm) and unmodified (δ = 7.54 ppm) linkers in the *meta* position with respect to the amino and urea position, respectively. Chemical shifts are reported in ppm relative to D_2O (δ = 4.67 ppm). The percentage conversions of the amine groups into urea groups were determined by comparing the relative integrated areas of the aromatic resonances of the modified and unmodified linkers.

All MAS NMR measurements were performed under magic-angle spinning using ZrO_2 rotors. Chemical shifts were referenced to TMS for ^{1}H and ^{13}C, nitromethane for ^{15}N and an acidic aqueous solution of $AlCl_3 \cdot 6H_2O$ for ^{27}Al. ^{1}H MAS and ^{27}Al MAS NMR spectra were recorded on a Bruker Avance III HD spectrometer operating at a proton frequency of 600 MHz with a 1.3 mm triple resonance probe at a spinning rate of 62.5 kHz. The 90° pulse excitation times of ^{1}H NMR were set to 1.5 μs. ^{27}Al spectra were recorded using a Hahn-Echo sequence with pulse lengths of 7 and 14 μs for the 90° and 180° pulses and a recycle delay of 1 s. ^{1}H-^{27}Al spectra were obtained using a D-HMQC sequence with a recycle delay of 2 s. ^{13}C CP MAS NMR experiments were performed on a Bruker Avance III HD spectrometer operating at a proton frequency of 400 MHz (100.6 MHz for carbon) using a 4 mm double resonance probe at a spinning rate of 10 kHz. ^{15}N CP MAS NMR measurements were carried out on a Bruker Avance II 300 spectrometer at a rotation frequency of 5 kHz using a 7 mm triple resonance probe operating at a frequency of 30.4 MHz for ^{15}N. ^{13}C and ^{15}N spectra were recorded after 90° pulse excitation of 3.5 μs and applying a ramped CP sequence with contact times of 3 and 5 ms, respectively. The SPINAL64[66] sequence was used for broadband proton decoupling.

Attenuated total reflectance IR spectra were collected between 400 and 4000 cm^{-1} on a Jasco FT/IR-6100 spectrometer equipped with a PIKEGladiATR accessory with a resolution of 4 cm^{-1} at room temperature.

For chemical analysis the samples were handled in air for preparation. Quantitative analysis of aluminium contents by atomic absorption spectroscopy (AAS) were carried out in extinction mode on a Varian AA100 and using a N_2O/acetylene flame. The samples were chemically digested. EDX spectroscopy was performed on a Joel JSM 6400 scanning electron microscope equipped with a Noran energy dispersive X-ray analyser and using a beam voltage of 20 kV. Elementary analysis (CHN) was carried out on a Vario elementar EL III.

Argon sorption isotherms were measured on a Quantachrome Autosorb-1 at 87.5 K. Prior to the measurements, the samples were degassed at 393 K for 14 h under reduced pressure. Apparent specific Brunauer–Emmett–Teller (BET) surface areas were calculated over a relative pressure range between 0.06 and 0.15 to accommodate for microporous materials.[60,61] Specific total pore volumes were estimated at a relative pressure of 0.98. DFT surface areas, DFT pore volumes and pore size distributions were calculated using the argon spherical/cylindrical pore NLDFT model at 87 K for the adsorption branch on a silica/zeolite surface (fitting errors: 0.49% for Al-MIL-101-NH_2 and 0.24% for Al-MIL-101-URPh).

TGA profiles were obtained using a Mettler TGA/SDTA 85 by heating from 25 to 900 °C with a heating rate of 4 K min^{-1} under continuous flow of synthetic air (60 mL min^{-1}). To calculate the water uptake per linker, molar quantities of adsorbed water were referred to molar amount of linkers which are derived from residual mass of Al_2O_3 at 900 °C by assuming that all Al^{3+} originates from the framework and a Al^{3+}/linker ratio of 1:1.

Water vapour sorption isotherms at 298 K were obtained by a volumetric technique using a BELSORP-max apparatus. To avoid water condensation, isotherms were recorded up to 90% RH. The equilibrium time for each single RH value was set to 600 s, which guaranteed pressure fluctuations being not higher than 0.3%. Before starting the measurement, the samples were degassed under reduced pressure for 14 h at 120 °C.

Acknowledgements

The authors acknowledge the Deutsche Forschungsgemeinschaft (SPP1362, SE 1417/3-2, STO 643/5-2 and SFB 840) for

ChemPubSoc Europe

CHEMISTRY A European Journal Full Paper

funding. The authors thank Lena Geiling and Nadine Popp for performing sorption measurements and Beate Bojer for EDX measurements. We gratefully thank Prof. Josef Breu, Prof. Rhett Kempe and Prof. Hans-Werner Schmidt for access to the respective instruments.

Keywords: hybrid materials · metal–organic frameworks · porosity · postsynthetic modification · water stability

[1] H. Furukawa, K. E. Cordova, M. O'Keeffe, O. M. Yaghi, *Science* **2013**, *341*, 1230444.
[2] C. Janiak, J. K. Vieth, *New J. Chem.* **2010**, *34*, 2366 – 2388.
[3] G. Férey, *Chem. Soc. Rev.* **2008**, *37*, 191 – 214.
[4] J.-R. Li, J. Sculley, H.-C. Zhou, *Chem. Rev.* **2012**, *112*, 869 – 932.
[5] R. J. Kuppler, D. J. Timmons, Q.-R. Fang, J.-R. Li, T. A. Makal, M. D. Young, D. Yuan, D. Zhao, W. Zhuang, H.-C. Zhou, *Coord. Chem. Rev.* **2009**, *253*, 3042 – 3066.
[6] S. Ma, H.-C. Zhou, *Chem. Commun.* **2010**, *46*, 44 – 53.
[7] J. Y. Lee, O. K. Farha, J. Roberts, K. A. Scheidt, S. B. T. Nguyen, J. T. Hupp, *Chem. Soc. Rev.* **2009**, *38*, 1450 – 1459.
[8] D. Farrusseng, S. Aguado, C. Pinel, *Angew. Chem.* **2009**, *121*, 7638 – 7649; *Angew. Chem. Int. Ed.* **2009**, *48*, 7502 – 7513.
[9] P. Horcajada, R. Gref, T. Baati, P. K. Allan, G. Maurin, P. Couvreur, G. Férey, R. E. Morris, C. Serre, *Chem. Rev.* **2012**, *112*, 1232 – 1268.
[10] P. Horcajada, C. Serre, M. Vallet-Regi, M. Sebban, F. Taulelle, G. Férey, *Angew. Chem.* **2006**, *118*, 6120 – 6124; *Angew. Chem. Int. Ed.* **2006**, *45*, 5974 – 5978.
[11] A. U. Czaja, N. Trukhan, U. Müller, *Chem. Soc. Rev.* **2009**, *38*, 1284 – 1293.
[12] Z. Hasan, J. Jeon, S. H. Jhung, *J. Hazard. Mater.* **2012**, *209 – 210*, 151 – 157.
[13] N. A. Khan, Z. Hasan, S. H. Jhung, *J. Hazard. Mater.* **2013**, *244 – 245*, 444 – 456.
[14] F. Jeremias, A. Khutia, S. K. Henninger, C. Janiak, *J. Mater. Chem.* **2012**, *22*, 10148 – 10151.
[15] Y.-K. Seo, J. W. Yoon, J. S. Lee, Y. K. Hwang, C.-H. Jun, J.-S. Chang, S. Wuttke, P. Bazin, A. Vimont, M. Daturi, S. Bourrelly, P. L. Llewellyn, P. Horcajada, C. Serre, G. Férey, *Adv. Mater.* **2012**, *24*, 806 – 810.
[16] J. Canivet, A. Fateeva, Y. Guo, B. Coasne, D. Farrusseng, *Chem. Soc. Rev.* **2014**, *43*, 5594 – 5617.
[17] H. Jasuja, N. C. Burtch, Y. Huang, Y. Cai, K. S. Walton, *Langmuir* **2013**, *29*, 633 – 642.
[18] J. J. Low, A. I. Benin, P. Jakubczak, J. F. Abrahamian, S. A. Faheem, R. R. Willis, *J. Am. Chem. Soc.* **2009**, *131*, 15834 – 15842.
[19] P. M. Schoenecker, C. G. Carson, H. Jasuja, C. J. J. Flemming, K. S. Walton, *Ind. Eng. Chem. Res.* **2012**, *51*, 6513 – 6519.
[20] S. H. Jhung, N. A. Khan, Z. Hasan, *CrystEngComm* **2012**, *14*, 7099 – 7109.
[21] N. Wiberg, in *Lehrbuch der Anorganischen Chemie*, 102th ed., De Gruyter, Berlin, **2007**, pp. 1363 – 1368.
[22] F. A. Cotton, G. Wilkinson, in *Advanced Inorganic Chemistry*, 4th ed., Wiley, New York, **1980**, pp. 1185 – 1189.
[23] V. Colombo, S. Galli, H. J. Choi, G. D. Han, A. Maspero, G. Palmisano, N. Masciocchic, J. R. Long, *Chem. Sci.* **2011**, *2*, 1311 – 1319.
[24] H. J. Choi, M. Dinca, A. Dailly, J. R. Long, *Energy Environ. Sci.* **2010**, *3*, 117 – 123.
[25] S. S. Kaye, A. Dailly, O. M. Yaghi, J. R. Long, *J. Am. Chem. Soc.* **2007**, *129*, 14176 – 14177.
[26] J. Ehrenmann, S. K. Henninger, C. Janiak, *Eur. J. Inorg. Chem.* **2011**, 471 – 474.
[27] S. Bauer, C. Serre, T. Devic, P. Horcajada, J. Marrot, G. Férey, N. Stock, *Inorg. Chem.* **2008**, *47*, 7568 – 7576.
[28] E. Stavitski, M. G. Goesten, J. Juan-Alcañiz, A. Martinez-Joaristi, P. Serra-Crespo, A. V. Petukhov, J. Gascon, F. Kapteijn, *Angew. Chem.* **2011**, *123*, 9798 – 9802; *Angew. Chem. Int. Ed.* **2011**, *50*, 9624 – 9628.
[29] T. Loiseau, C. Serre, C. Huguenard, G. Fink, F. Taulelle, M. Henry, T. Bataille, G. Férey, *Chem. Eur. J.* **2004**, *10*, 1373 – 1382.
[30] T. Ahnfeldt, N. Guillou, D. Gunzelmann, I. Margiolaki, T. Loiseau, G. Férey, J. Senker, N. Stock, *Angew. Chem.* **2009**, *121*, 5265 – 5268; *Angew. Chem. Int. Ed.* **2009**, *48*, 5163 – 5166.
[31] P. Serra-Crespo, E. V. Ramos-Fernandez, J. Gascon, F. Kapteijn, *Chem. Mater.* **2011**, *23*, 2565 – 2572.
[32] G. Férey, C. Mellot-Draznieks, C. Serre, F. Millange, J. Dutour, S. Surblé, I. Margiolaki, *Science* **2005**, *309*, 2040 – 2042.
[33] D. Ma, Y. Li, Z. Li, *Chem. Commun.* **2011**, *47*, 7377 – 7379.
[34] H. Jasuja, Y. Huang, K. S. Walton, *Langmuir* **2012**, *28*, 16874 – 16880.
[35] J. Yang, A. Grzech, F. M. Mulder, T. J. Dingemans, *Chem. Commun.* **2011**, *47*, 5244 – 5246.
[36] T. Wu, L. Shen, M. Luebbers, C. Hu, Q. Chen, Z. Ni, R. I. Masel, *Chem. Commun.* **2010**, *46*, 6120 – 6122.
[37] Y. Cai, Y. Zhang, Y. Huang, S. R. Marder, K. S. Walton, *Cryst. Growth Des.* **2012**, *12*, 3709 – 3713.
[38] J. B. Decoste, G. W. Peterson, M. W. Smith, C. A. Stone, C. R. Willis, *J. Am. Chem. Soc.* **2012**, *134*, 1486 – 1489.
[39] C. Yang, U. Kaipa, Q. Z. Mather, X. Wang, V. Nesterov, A. F. Venero, M. A. Omary, *J. Am. Chem. Soc.* **2011**, *133*, 18094 – 18097.
[40] T. H. Chen, I. Popov, O. Zenasni, O. Daugulis, O. Š. Miljanić, *Chem. Commun.* **2013**, *49*, 6846 – 6848.
[41] J. G. Nguyen, S. M. Cohen, *J. Am. Chem. Soc.* **2010**, *132*, 4560 – 4561.
[42] C. Serre, *Angew. Chem.* **2012**, *124*, 6152 – 6154; *Angew. Chem. Int. Ed.* **2012**, *51*, 6048 – 6050.
[43] W. Xuan, C. Zhu, Y. Liu, Y. Cui, *Chem. Soc. Rev.* **2012**, *41*, 1677 – 1695.
[44] M. Hartmann, M. Fischer, *Microporous Mesoporous Mater.* **2012**, *164*, 38 – 43.
[45] S. Bernt, V. Guillerm, C. Serre, N. Stock, *Chem. Commun.* **2011**, *47*, 2838 – 2840.
[46] A. Modrow, D. Zargarani, R. Herges, N. Stock, *Dalton Trans.* **2012**, *41*, 8690 – 8696.
[47] H. Hintz, S. Wuttke, *Chem. Commun.* **2014**, *50*, 11472 – 11475.
[48] K. L. Taylor-Pashow, J. D. Rocca, Z. Zie, S. Tran, W. Lin, *J. Am. Chem. Soc.* **2009**, *131*, 14261 – 14263.
[49] M. Schubert, U. Mueller, C. Kiener (BASF SE), US8313559 B2, **2012**, Ludwigshafen (DE).
[50] L. Bromberg, X. Su, T. A. Hatton, *Chem. Mater.* **2013**, *25*, 1636 – 1642.
[51] L. Bromberg, Y. Klichko, E. P. Chang, S. Speakman, C. M. Straut, E. Wilusz, T. A. Hatton, *ACS Appl. Mater. Interfaces* **2012**, *4*, 4595 – 4602.
[52] E. Haque, V. Lo, A. I. Minett, A. T. Harris, T. L. Church, *J. Mater. Chem. A* **2014**, *2*, 193 – 203.
[53] F. M. Hinterholzinger, B. Rühle, S. Wuttke, K. Karaghiosoff, T. Bein, *Sci. Rep.* **2013**, *3*, 2562.
[54] O. I. Lebedev, F. Millange, C. Serre, G. Van Tendeloo, G. Férey, *Chem. Mater.* **2005**, *17*, 6525 – 6527.
[55] E. Dugan, Z. Wang, M. Okamura, A. Medina, S. M. Cohen, *Chem. Commun.* **2008**, 3366 – 3368.
[56] Predicted NMR data calculated using Advanced Chemistry Development, Inc. (ACD/Labs) Software 1V12.5, **1994 – 2013** ACD/Labs.
[57] T. Ahnfeldt, D. Gunzelmann, T. Loiseau, D. Hirsemann, J. Senker, G. Férey, N. Stock, *Inorg. Chem.* **2009**, *48*, 3057 – 3064.
[58] S. Biswas, S. Couck, M. Grzywa, J. F. M. Denayer, D. Volkmer, P. Van Der Voort, *Eur. J. Inorg. Chem.* **2012**, 2481 – 2486.
[59] A. Lieb, H. Leclerc, T. Devic, C. Serre, I. Margiolaki, F. Mahjoubi, J. S. Lee, A. Vimont, M. Daturi, J.-S. Chang, *Microporous Mesoporous Mater.* **2012**, *157*, 18 – 23.
[60] J. Moellmer, E. B. Celer, R. Luebke, A. J. Cairns, R. Staudt, M. Eddaoudi, M. Thommes, *Microporous Mesoporous Mater.* **2010**, *129*, 345 – 353.
[61] M. Thommes, *Chem. Ing. Tech.* **2010**, *82*, 1059 – 1073.
[62] L. Gurvich, *J. Russ. Phys. Chem. Soc.* **1915**, *47*, 805 – 827.
[63] J. Landers, G. Y. Gor, A. V. Neimark, *Colloids Surf. A* **2013**, *437*, 3 – 32.
[64] J. Canivet, J. Bonnefoy, C. Daniel, A. Legrand, B. Coasne, D. Farrusseng, *New J. Chem.* **2014**, *38*, 3102 – 3111.
[65] G. Akiyama, R. Matsuda, H. Sato, A. Hori, M. Takata, S. Kitagawa, *Microporous Mesoporous Mater.* **2012**, *157*, 89 – 93.
[66] B. M. Fung, A. K. Khitrin, K. Ermolaev, *J. Magn. Reson.* **2000**, *142*, 97 – 100.

Received: July 30, 2014
Published online on October 28, 2014

6.1.2 Supporting Information

CHEMISTRY
A European Journal

Supporting Information

Enhancing the Water Stability of Al-MIL-101-NH_2 via Postsynthetic Modification

Thomas Wittmann,[a] Renée Siegel,[a] Nele Reimer,[b] Wolfgang Milius,[c] Norbert Stock,[b] and Jürgen Senker*[a]

chem_201404654_sm_miscellaneous_information.pdf

Supporting information

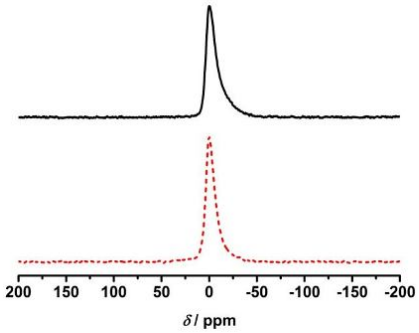

Figure S1. ^{27}Al MAS NMR spectra of Al-MIL-101-NH_2 (black solid line, top) and Al-MIL-101-URPh (red dotted line, bottom). The asymmetric shape for each single resonance at δ (^{27}Al) = 0 ppm on the highfield shoulders indicate a small second order quadrupolar interaction.

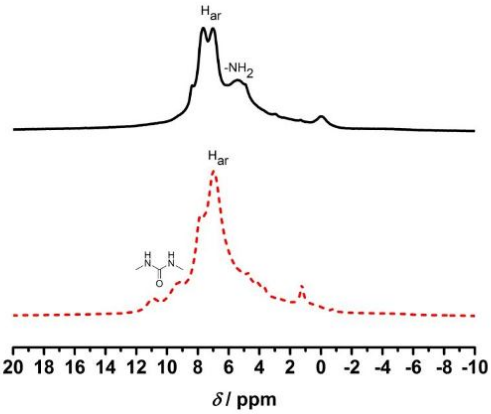

Figure S2. ^{1}H MAS NMR spectra of Al-MIL-101-NH_2 (black solid line, top) and Al-MIL-101-URPh (red dotted line, bottom) after degassing. The signals at around 0 – 1 ppm are attributed to residual ethanol from Soxhlet activation.

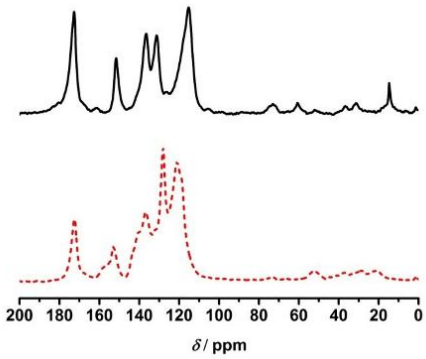

Figure S3. Full range ^{13}C CP MAS NMR spectra of Al-MIL-101-NH_2 (black solid line, top) and Al-MIL-101-URPh (red dotted line, bottom).

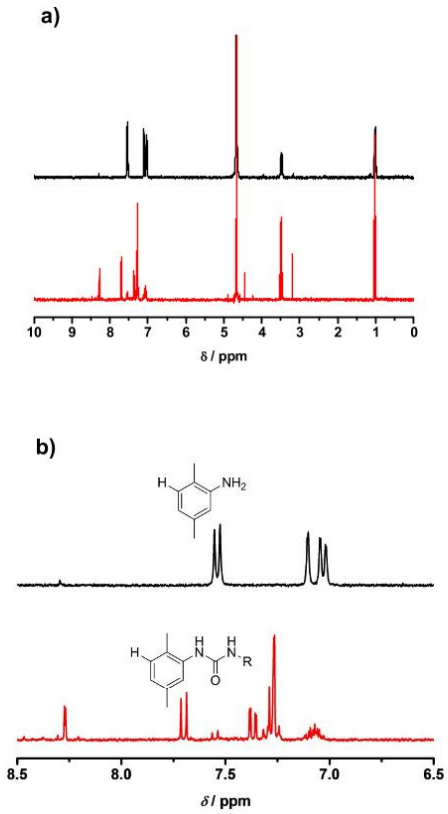

Figure S4: a) Liquid ^{1}H-NMR spectra of Al-MIL-101-NH_2 (top) and Al-MIL-101-URPh (bottom) after digestion in 1.25 wt% NaOD/D_2O. b) Enlarged section of the liquid ^{1}H-NMR spectra of Al-MIL-101-NH_2 (top) and Al-MIL-101-URPh (bottom) from δ = 8.5 ppm to δ = 6.5 ppm.

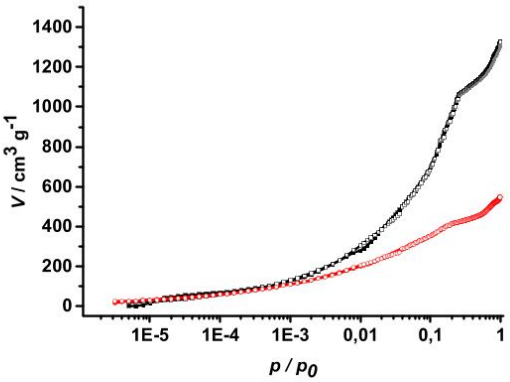

Figure S5. Comparison between measured (filled symbols) and fitted (empty symbols) sorption isotherms of Al-MIL-101-NH_2 (squares) and Al-MIL-101-URPh (circles). Pore volumes were calculated using the argon spherical/cylindrical pore NLDFT model at 87 K for the adsorption branch on a silica/zeolite surface. Fitting errors: 0.49 % for Al-MIL-101-NH_2 and 0.24 % for Al-MIL-101-URPh.

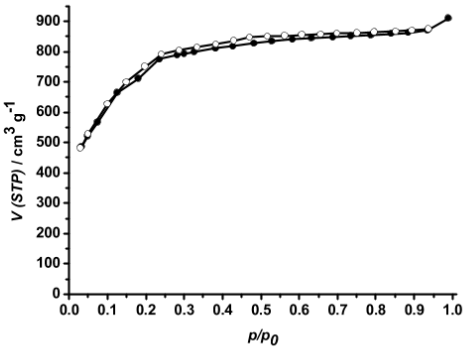

Figure S6. N_2 adsorption (filled circles) and desorption (empty circles) isotherm of Al-MIL-101-NH_2 at 77 K.

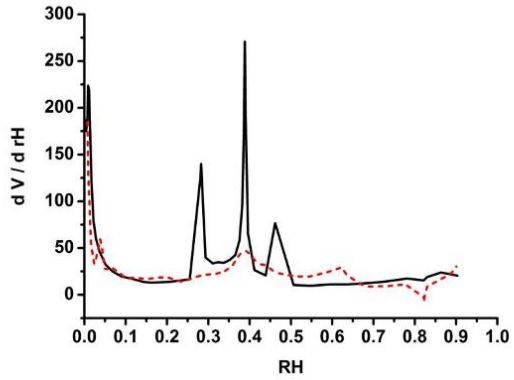

Figure S7. First derivatives of water adsorption isotherms of Al-MIL-101-NH_2 (black solid line) and Al-MIL-101-URPh (red dotted line).

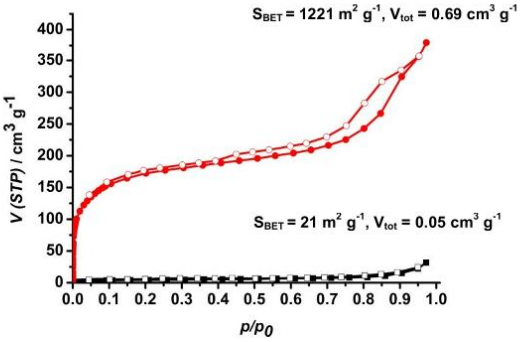

Figure S8. Argon adsorption (filled symbols) and desorption isotherms (empty symbols) at 87 K of Al-MIL-101-NH_2 (squares) and Al-MIL-101-URPh (circles) after water vapour sorption.

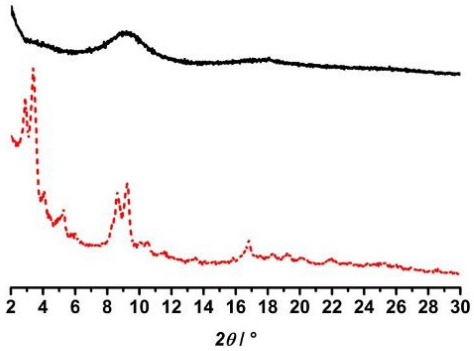

Figure S9. Powder X-ray patterns of Al-MIL-101-NH_2 (black solid line, top) and Al-MIL-101-URPh (red dotted line, bottom) after water sorption measurements.

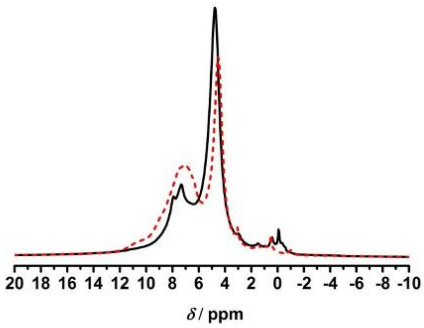

Figure S10. ^{1}H-MAS NMR spectra of Al-MIL-101-NH_2 (black solid line) and Al-MIL-101-URPh (red dotted line) after being degassed and exposure to humid air (100% RH) at 25 °C and equilibration for 30 minutes. Al-MIL-101-NH_2 (black) contains roughly 5 water molecules per linker, Al-MIL-101-URPh (red) roughly 4 water molecules per linker. For the ^{1}H-^{27}Al D-HMQC measurements, therefore, Al-MIL-101-NH_2 exhibits 15 water molecules ($[Al_3(\mu_3\text{-}O)Cl(H_2O)_2(bdc\text{-}NH_2)_3] \cdot 13\ H_2O$), Al-MIL-101-URPh 12 water molecules ($[Al_3(\mu_3\text{-}O)Cl(H_2O)_2(bdc\text{-}NH\text{-}CO\text{-}NH\text{-}Ph)_{2.58}(bdc\text{-}NH_2)_{0.42}] \cdot 10\ H_2O$) per formula unit, respectively. Due to the presence of dynamic excess water in the pores the strong adsorption sites which are determining for the D-HMQC measurements are saturated for both MOFs.

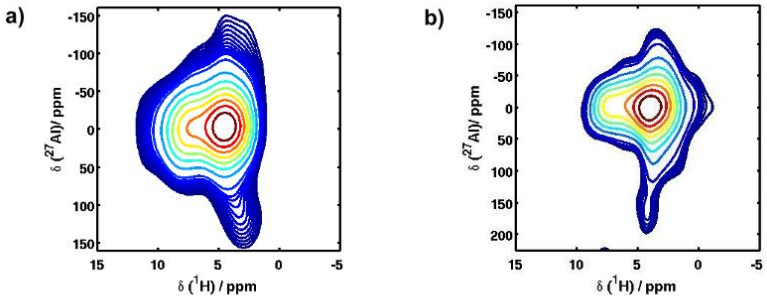

Figure S11. ^{1}H-^{27}Al D-HMQC spectra of a) Al-MIL-101-NH_2 and b) Al-MIL-101-URPh loaded with water.

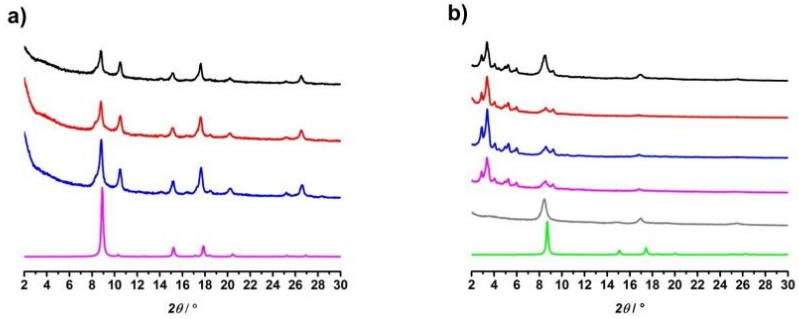

Figure S12. X-ray powder patterns of a) Al-MIL-101-NH_2 after suspension in water (from top to bottom: 5 min, 30 min, 60 min; sim. pattern of Al-MIL-53, as-synthesised form)[29] and of b) Al-MIL-101-URPh after suspension in water (from top to bottom: 24 h, 48 h, 72 h, 7 d, 10 d; sim. pattern of Al-MIL-53, lp form)[29] and subsequent regeneration at 80 °C for 1 h.

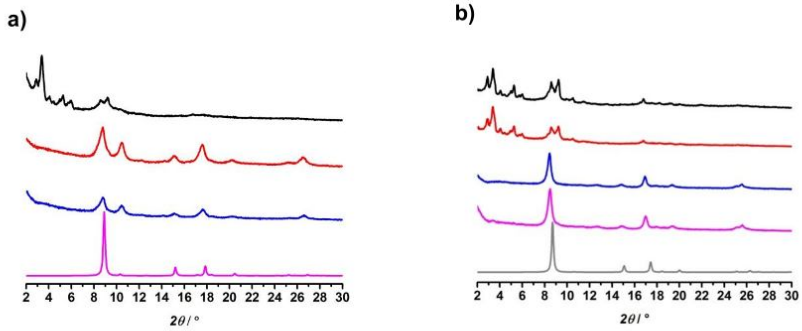

Figure S13. X-ray powder patterns after exposure to 100 % RH at 60 °C of a) Al-MIL-101-NH_2 (from top to bottom: 2 h, 3 h, 4 h, sim. pattern of Al-MIL-53 as)[29] and of b) Al-MIL-101-URPh (from top to bottom: 20 h, 24 h, 30 h, 66 h, sim. pattern of Al-MIL-53 lp).[29]

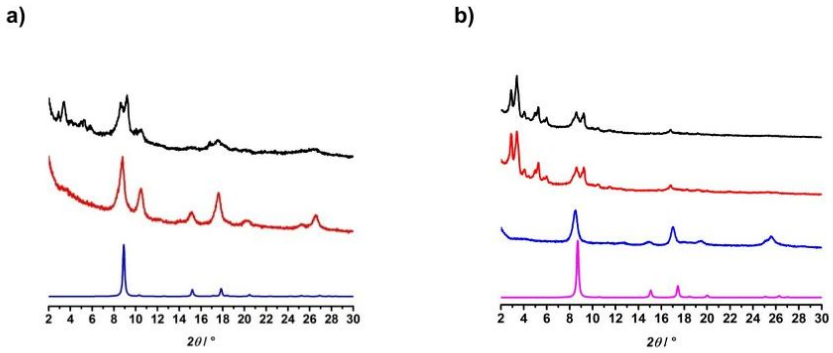

Figure S14. X-ray powder patterns after exposure to 100 % RH at 70 °C of a) Al-MIL-101-NH_2 (from top to bottom: 1.5 h, 2 h, sim. pattern of Al-MIL-53 as)[29] and of b) Al-MIL-101-URPh (from top to bottom: 16 h, 18 h, 20 h, sim. pattern of Al-MIL-53 lp).[29]

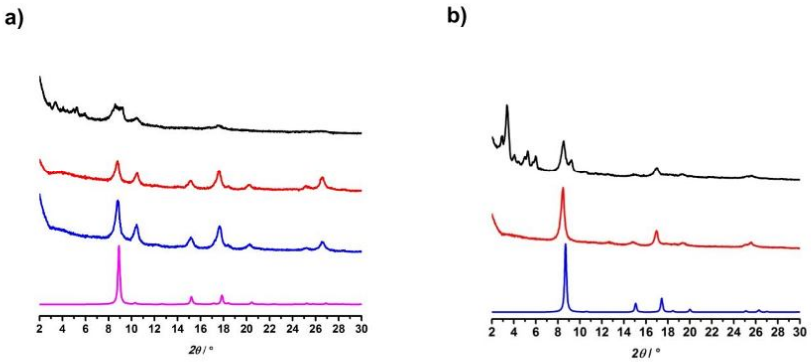

Figure S15. X-ray powder patterns after exposure to 100 % RH at 80 °C of a) Al-MIL-101-NH_2 (from top to bottom: 30 min, 90 min, 180 min, sim. pattern of Al-MIL-53 as)[29] and of b) Al-MIL-101-URPh (from top to bottom: 16 h, 18 h, sim. pattern Al-MIL-53 lp).[29]

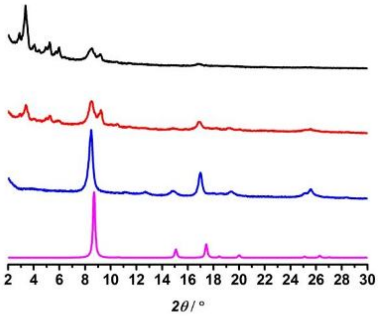

Figure S16. X-ray powder patterns of Al-MIL-101-URPh after exposure to 100 % RH at 85 °C (from top to bottom: 6 h, 8 h, 10 h, sim. pattern of Al-MIL-53 lp).[29]

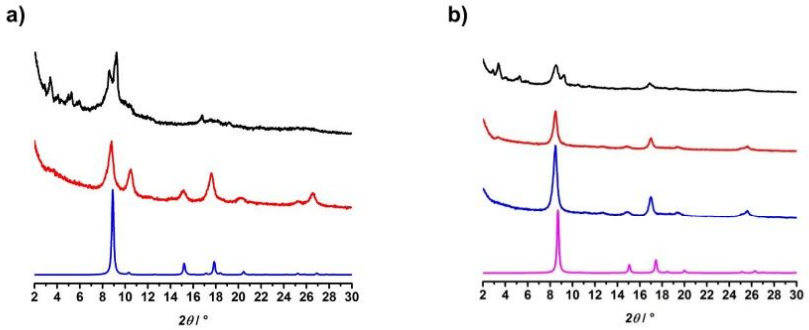

Figure S17. PXRD patterns after exposure to 100 % RH at 90 °C of a) Al-MIL-101-NH_2 (from top to bottom: 25 min, 30 min, sim. pattern of Al-MIL-53 as)[29] and of b) Al-MIL-101-URPh (from top to bottom: 2 h, 4 h, 16 h, sim. pattern of Al-MIL-53 lp).[29]

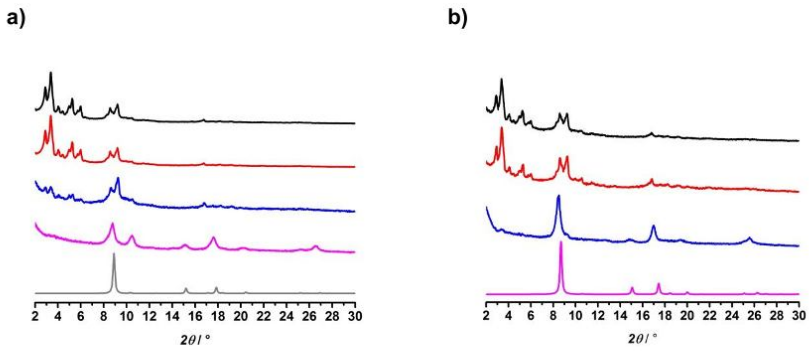

Figure S18. PXRD patterns after exposure to 100 % RH at 100 °C of a) Al-MIL-101-NH_2 (from top to bottom: 10 min, 15 min, 20 min, sim. pattern of Al-MIL-53 as)[29] and of b) Al-MIL-101-URPh (from top to bottom: 1 h, 1.5 h, 2 h, sim. pattern of Al-MIL-53 lp).[29]

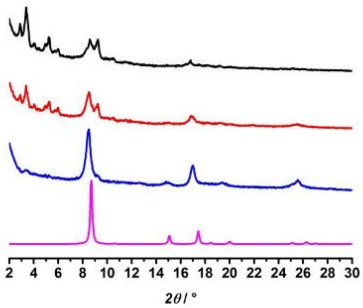

Figure S19. PXRD patterns of Al-MIL-101-URPh after exposure to 100 % RH at 110 °C (from top to bottom: 1 h, 1.5 h, 2 h, sim. pattern of Al-MIL-53 lp).[29]

6.2 Einbringen einer Wasserstoffbrücken-DDA-Sequenz in MIL-101 (Al, Cr) für selektive Wechselwirkungen mit Gastmolekülen

Introducing Selective Host-Guest Interactions in MIL-101 Frameworks via a Multiple Hydrogen Bond Donor-Acceptor Recognition Site

Thomas Wittmann,[†] Carsten B. L. Tschense,[†] Renée Siegel,[†] Jürgen Senker[†,*]

Manuskript vorbereitet zur Einreichung

[†] Department of Inorganic Chemistry III, University of Bayreuth, Universitätsstraße 30, 95440 Bayreuth (Germany)

[*] juergen.senker@uni-bayreuth.de

6.2.1 Introducing Selective Host-Guest Interactions in MIL-101 Frameworks via a Multiple Hydrogen Bond Donor-Acceptor Recognition Site

Introducing selective host-guest interactions in MIL-101 frameworks via a multiple hydrogen bond donor-acceptor recognition site

Thomas Wittmann[†], Carsten Tschense[†], Renée Siegel[†], Jürgen Senker*[†]

[†]University of Bayreuth, Inorganic Chemistry III, Universitätsstraße 30, 95440 Bayreuth, Germany

ABSTRACT: Targeted recognition of medium sized molecules with mixed hydrogen bond units is essential for applications as diverse as molecular separation, sensing and drug delivery. One promising way to achieve selectivity is to make use of the lock-and-key principle known from supramolecular chemistry. In this way, hydrogen bond receptors matching the chemical signature of the target molecules can be provided. Among the class of porous materials metal-organic frameworks are particularly well suited for this purpose, as they allow for functionalizing the inner surfaces with various pending groups. Here we investigated the competitive adsorption behavior of 2-aminopyridine (2-AP) and 3-aminopyridine (3-AP) on mesoporous MIL-101-X (Al, Cr) with X being amino (NH_2) and 2-pyridyl urea (URPy) functionalities to probe the influence of a single D (NH_2) and a triple DDA (URPy) hydrogen bond unit. MIL-101-URPy was synthesized by postsynthetic modification of MIL-101-NH_2 with 2-pyridyl isocyanate and a yield of about 90%. Grafting the coordinatively unsaturated sites (CUS) at the inorganic building units with diethylamine, additionally allowed the adsorption at the CUS to be suppressed and thus to focus on the hydrogen bond receptors. Compared to the single D sites the selectivity of 2-AP over 3-AP is enhanced by a factor of six for the DDA pending groups. Based on ^{15}N NMR spectroscopy and DFT calculations this observation was attributed to the formation of double hydrogen bonds between the pyridyl urea groups and the 2-AP molecules while 3-AP exhibits a single hydrogen bond only. In contrast, at the D site of MIL-101-NH_2 both 2-AP and 3-AP form a single hydrogen bond with a stronger interaction for 3-AP.

Introduction

Porous materials have potential for purification of gasses[1–3] and liquids,[4,5] drug delivery[6–8] and sensing.[9,10] The desired selectivity for host-guest interactions might be achieved by matching size, shape and binding preferences of guest molecules with the framework topology, respectively.[11–13] For example, kinetic separation with respect to size and shape is exploited for molecular sieving with zeolites, which requires rigid and periodic structures with uniform pores and windows.[1] Thermodynamic separation based on preferred binding sites, is achieved by providing chemical functionalities adapted in type and strength to targeted guest molecules. This includes van-der-Waals interactions, single and multiple hydrogen bond pattern, π–π-interactions and reversible bond formation for Lewis acid/base pairs.[1–3] This type of selectivity is widely spread for metal-organic frameworks (MOFs) due to their modular constitution and hybrid character. In particular, the organic linkers can be functionalized in many different ways by direct synthesis and postsynthetic modification (PSM), respectively.[14–18]

For example, subtle differences within the van der Waals interactions by introducing polar framework sites were exploited to increase the affinity for adsorbing carbon dioxide preferentially over nitrogen and methane.[2] Single hydrogen bonds accounted for the enhanced binding strength towards acetone compared to ethanol and water in MIL-53(Al)-X with X being formamido groups.[19] The selectivity for *ortho*-xylene over the *meta* and *para* analogues for MIL-53 (Al, Fe)[20,21] was explained by a simultaneous interaction of the two methyl units with two carboxylate groups of the terephthalate linkers, which is possible only for o-xylene due to the four-sided channel-type pores.[20] In contrast, the pronounced selectivity for p-xylene in MIL-47(V), MIL-125(Ti), MIL-125(Ti)-NH_2 and CAU-1(Al) solely arises from the shape of their cavities promoting a more efficient molecular π-π stacking of the respective isomer.[22,23]

Coordinatively unsaturated metal sites (CUS) lead to even higher sorption affinities and selectivities by adjusting coordination bonds via the Lewis acidity of the metal ions. For instance, CUSs with hard Lewis acidic metals as in MIL-100 (Al, Fe, Cr, V) [24] and MIL-101 (Cr)[20–23] proved to be effective for adsorption of hard Lewis basic N-heterocyclic compounds, whereas CUSs with softer Lewis acidic metals like HKUST (Cu)[29] and CPO-27 (Ni, Co)[25,30] preferred softer Lewis basic sulphur compounds.

However, controlled loading and release of more complex molecules bearing several functional groups like substituted heterocycles cannot be realized by molecular sieving and unspecific functional groups (e.g. -NH_2, -OH); it

requires specific interactions. These might be achieved by supramolecular binding motifs, which are common for the formation of biological and artificial self-assembly systems.[31–34] They strongly rely on non-covalent π-π interactions and multiple hydrogen bond networks[35] where geometric and electrostatic complementarity between host and guest drives their association.[36] This opens up the design of host-guest adducts that respond to certain external physical and chemical stimuli.[32,36,37] The reversibility of such binding patterns mainly depend on the strength of the multiple H-bond pattern and competing solvent-guest interactions. The former can be controlled by size and sequence of donor-acceptor units providing favorable or unfavorable binding sites.[35,38]

Although, the incorporation of supramolecular building blocks into MOFs has been shown in several studies,[39] often crystallinity, permanent porosity and chemical stability suffer.[39] This makes detailed studies of their efficiency with respect to targeted recognition challenging. Yaghi et al. attached macrocyclic polyethers to the linkers of MOF-1001 in order to stereospecifically accommodate paraquat dications via ion-dipole interactions.[40] More recently, Li et al. integrated the nucleobase adenine as a co-ligand into a ZnBTC-MOF and established complementary double hydrogen bonding to thymine.[41]

Here we present the successful incorporation of pyridine substituted urea groups (URPy) pending at the organic linkers of MIL-101 by postsynthetic modification without affecting the long-range order of the framework. The URPy units provide a donor-donor-acceptor sequence (DDA) as recognition pattern, which is also effective in nature[42,43] and obeys the lock-and-key principle.[36,37] We consider MIL-101 (Fig. S1) as an ideal platform due to its high chemical stability, large surface areas and pores in the lower mesoporous regime.[44,45] The pore dimensions meet the requirement for accommodating space demanding anchor groups and guest molecules at the same time.

We studied the sorption properties of the URPy units by using the structural isomers 2-aminopyridine (2-AP) and 3-aminopyridine (3-AP) as probe molecules. Out of these two only 2-AP presents a counterpart to the recognition pattern of the URPy units. To be able to separate the adsorption at the pending groups from the one at the CUS, the latter were also grafted with diethyl amine (DEA).[28,46] All samples were then characterized by combining multinuclear solid-state NMR spectroscopic measurements and DFT chemical shift calculations to derive structural models of preferred host-guest arrangements.

Results and Discussion

Synthesis and characterization

Al- and Cr-MIL-101-NH_2 were prepared as previously reported.[47,48] Al- and Cr-MIL-101-URPy were synthesized after suspending Al- and Cr-MIL-101-NH_2 in a solution of 2-pyridyl acyl azide and subsequent *Curtius* rearrangement to the reactive 2-pyridyl isocyanate (Scheme 1). Attempts to directly use 2-pyridyl isocyanate for the PSM reaction failed because of dimerization of the reactive isocyanates.[49] Therefore, we isolated 2-pyridyl acyl azide after synthesis from 2-picolinic acid (Figure S2-S4, ESI) and homogeneously distributed the azide species over the internal surface of MIL-101-NH_2. Thus, the spatially separated 2-pyridyl isocyanate reacts more likely with the closer amino groups than to undergo a dimerization (Scheme 1). The inorganic building units of Cr-MIL-101-NH_2 and Cr-MIL-101-URPy were grafted with diethylamine (DEA) following the protocol of Hwang et al.[46] For the URPy compound, the activation of the accessible terminal metal sites was carried out at 120 °C to avoid degradation of the URPy pending group at higher temperatures.

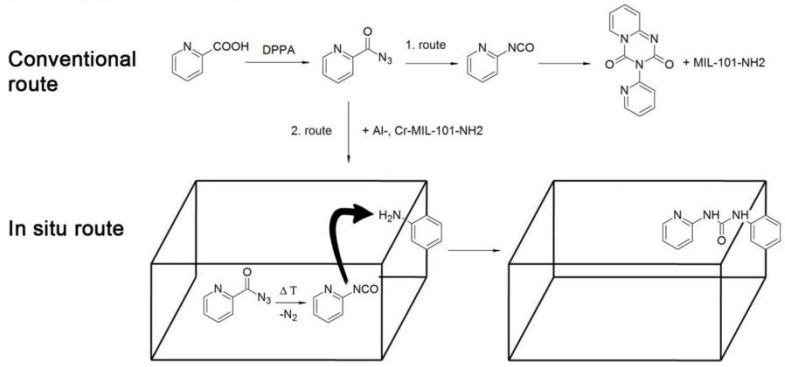

Scheme 1: Synthesis of Al/Cr-MIL-101-URPy in situ (*in situ* route) including the preparation of 2-pyridyl acyl azide, the *Curtius* rearrangement inside the cavities of MIL-101 (represented by the scaffold) to 2-pyridyl isocyanate and the reaction with Al/Cr-MIL-101-NH_2 (represented by the bent blue arrow). Separate synthesis of 2-pryridyl isocyanate (conventional route) proved unsuccessful due to fast dimerization of 2-pyridyl isocyanate.

The PXRD patterns of all products fully coincide with those of the respective parent MOFs and the simulated powder patterns. This confirms successful MOF syntheses and retention of the structure after PSM without formation of crystalline side products (Figure S5, ESI). The slight intensity variations are attributed to disorder of the pending pyridyl urea and diethyl amine groups.

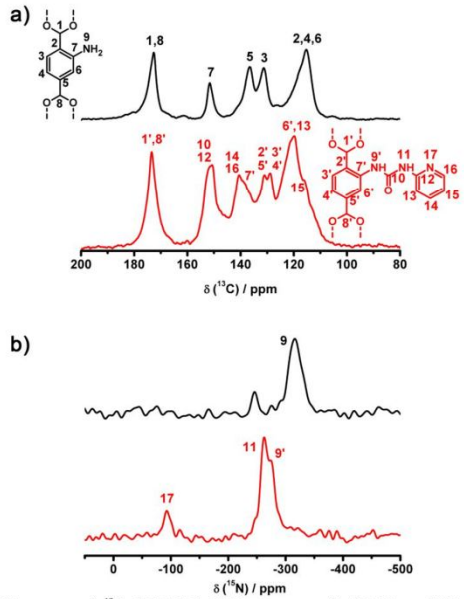

Figure 1: a) ^{13}C CP MAS NMR spectra of Al-MIL-101-NH_2 (black line) and Al-MIL-101-URPy (red line) and b) ^{15}N CP MAS NMR spectra of Al-MIL-101-NH_2 (black line) and Al-MIL-101-URPy (red line). The weak signal at -247 ppm within the ^{15}N MAS spectrum of Al-MIL-101-NH_2 (black line) was attributed to a formamide moiety, which might form by a side reaction of DMF and the amino groups. Its total amount is less than 5%. For more information refer to Figure S6.

The PSM of the organic linkers was monitored by ^{13}C and ^{15}N NMR spectroscopy of the diamagnetic Al-MIL-101 derivatives. The most characteristic changes within the ^{13}C MAS NMR spectra were observed for the signal of the amino bearing carbon at 151.5 ppm (Figure 1a, black line), which shifts to 137.4 ppm upon PSM accompanied by the emergence of a signal for the urea carbon at 152.1 ppm (Figure 1a, red line). The remaining ^{13}C signals are assigned to the amino and pyridyl urea terephthalates (Figure 1a). Upon PSM the ^{15}N NMR amino signal of Al-MIL-101-NH_2 at -316 ppm vanishes (Figure 1b, black line), whereas the ones for the pyridyl urea group appear at -272.7 ppm, -263.7 ppm and -96.5 ppm (Figure 1b, red line). Together with intensity changes for the characteristic vibrational bands of the amino and pyridyl urea groups within the IR spectra (Figure S8), we expect an almost quantitative PSM for the Al- and Cr-MIL-101 derivatives.

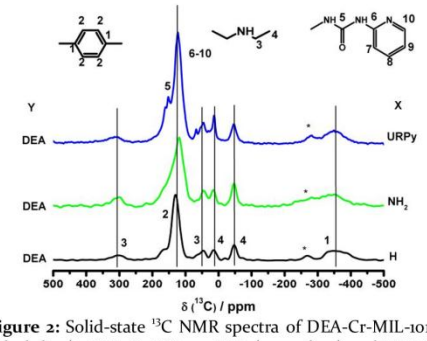

Figure 2: Solid-state ^{13}C NMR spectra of DEA-Cr-MIL-101-H (black line), DEA-Cr-MIL-101-NH_2 (green line) and DEA-Cr-MIL-101-URPy (blue line).

For the DEA grafted Cr-MIL-101 derivatives the ^{13}C pNMR spectra (Figure 2) exhibit both hyperfine shifted and diamagnetic resonances typical for DEA coordinated to the CUS of the IBU and DEA physisorbed in a second coordination sphere.[28] For the DEA@MIL-101-URPy, we observed additional resonances between 140 and 160 ppm, originating from the URPy groups. The incorporation of DEA is also supported by the small blueshifts of 9 cm^{-1} and 7 cm^{-1} for the aliphatic methylene C-H and C-N stretching vibration bands of coordinated DEA and free ligand (Figure S8b). These shifts are in line with the results for other alkyl amines adsorbed at metal centres.[46,50,51]

Tab. 1: Determined formula units for Al-MIL-101-NH_2, Al-MIL-101-URPy, H_2O-Cr-MIL-101-NH_2, DEA-Cr-MIL-101-NH_2, H_2O-Cr-MIL-101-URPy, DEA-Cr-MIL-101-URPy.

	Formula unit
Al-MIL-101-NH_3	$Al_3O(H_2O)_2Cl(bdc)_3$
Al-MIL-101-URPy	$Al_3O(H_2O)_2Cl(bdc\text{-}NH_2)_{0.3}(bdc\text{-}URPy)_{2.7}$
H_2O-Cr-MIL-101-NH_2	$Cr_3O(H_2O)_{2.1}Cl_{0.9}(bdc\text{-}NH_2)_3$
DEA-Cr-MIL-101-NH_2	$Cr_3O(H_2O)_{0.85}(DEA)_{1.5}Cl_{0.95}(bdc\text{-}NH_2)_3$
H_2O-Cr-MIL-101-URPy	$Cr_3O(H_2O)_{2.04}Cl_{0.96}(bdc\text{-}NH_2)_{0.3}(bdc\text{-}URPy)_{2.7}$
DEA-Cr-MIL-101-URPy	$Cr_3O(H_2O)_{1.05}(DEA)_{1.2}Cl_{0.97}(bdc\text{-}NH_2)_{0.3}(bdc\text{-}URPy)_{2.7}$

Based on these result, EDX, AAS, elemental analysis and ^1H solution NMR spectroscopy (after digesting the products in basic solutions) allowed for quantifying the metal, carbon, nitrogen and hydrogen content, the metal to chloride ratio and the yields of the DEA grafting as well as of the PSM (URPy). Details of the corresponding analyses are given in the supporting information (Figures S9 and

S10 and Table S1). The resulting formula units are summarized in Table 1. In total, the PSM of the amino into the pyridine urea pending groups was achieved with a yield of about 90% for both the chromium and aluminum frameworks. For the exchange of water with DEA molecules at the CUS of the Cr-MIL-101-X derivatives a conversion degree larger than 60% was reached.
Nitrogen sorption isotherms reveal lower porosities after PSM for Al-MIL-101-NH_2 and Cr-MIL-101-NH_2 (Figure S11 a,c). The bulkier URPy groups reduced the apparent BET surface areas and total pore volumes by nearly 50 % from 2340 $m^2 g^{-1}$ and 1650 $m^2 g^{-1}$ for Al-MIL-101-NH_2 and Cr-MIL-101-NH_2 to 1325 $m^2 g^{-1}$ and to 779 $m^2 g^{-1}$ for the URPy derivatives (Table S2). The DEA ligands reduced the latter quantities again by about 30 % for Cr-MIL-101-NH_2 and about 20 % for Cr-MIL-101-URPy (Table S2).
This is in line with the pore size distribution analyses. While for the amino derivatives cavity sizes of 2.5 nm and 3.0 nm were obtained, the URPy functionalization reduced the pores to 2.0 nm and 2.7 nm. Grafting the CUS of Cr-MIL-101-X with DEA both pores are reduced in size again by about 0.3 to 0.4 nm (Table S2 and Figure S11 b, d).

Sorption experiments

To characterize the binding preferences and sorption properties of the pending pyridyl urea groups, which could not be incorporated into the pore space of MOFs before, we determined adsorption isotherms for H_2O@Al-MIL-101-X, H_2O@Cr-MIL-101-X and DEA@Cr-MIL-101-X with X equal to amino and pyridyl urea groups. As probe molecules, 2-AP and 3-AP were used in single and competitive experiments. The adsorption isotherms are depicted in Figures 3, S12 and S13 and are expressed as adsorbed molecules per binding formula unit (FU) as function of the equilibrium concentration of the bulk liquid phase. The calculation of the molecular weight per formula unit is based on the chemical compositions of the frameworks (Table 1).
The single adsorption isotherms (Figure S12) show almost identical uptakes for the pair H_2O@Al-MIL-101-NH_2 and H_2O@Cr-MIL-101-NH_2 as well as for the pair H_2O@Al-MIL-101-URPy and H_2O@Cr-MIL-101-URPy. This was observed for 2-AP and 3-AP, respectively. For the Cr-MIL-101 framework it is known, that both probe molecules interact strongly with the CUS at the IBUs.[28] Due to the equivalence of the single adsorption isotherms for the above-mentioned pairs we expect a similar behavior for the Al-MIL-101 derivatives. Indeed, the ^{27}Al MAS NMR spectra of 2-AP@Al-MIL-101-NH_2 and 3-AP@Al-MIL-101-NH_2 show a significantly more asymmetric line shape compared to H_2O@Al-MIL-101-NH_2 (Figure S14). We attribute this to a larger second-order quadrupolar interaction, due to an increasingly asymmetric charge distribution after attaching 2-AP and 3-AP, respectively. By grafting the CUS with DEA prior to the adsorption experiments, we strive to minimize the influence of the CUS on the isotherm to single out the selective adsorption at the pending groups X. Since Al-MIL-101 does not withstand the grafting conditions, these experiments were carried out for the Cr-MIL-101-X derivatives only.
The reduced uptake for both 2-AP and 3-AP for the single isotherms of DEA@Cr-MIL-101-X (Figure S12) shows, that the blocking of the CUS is effective. As such, we take differences in the competitive adsorption isotherms (mixtures of 2-AP and 3-AP) of H_2O@Al-MIL-101-X and DEA@Cr-MIL-101-X and X being amino (Figure 3a) and pyridyl urea (Figure 3b) groups as a measure for the selective adsorption at the pending groups.

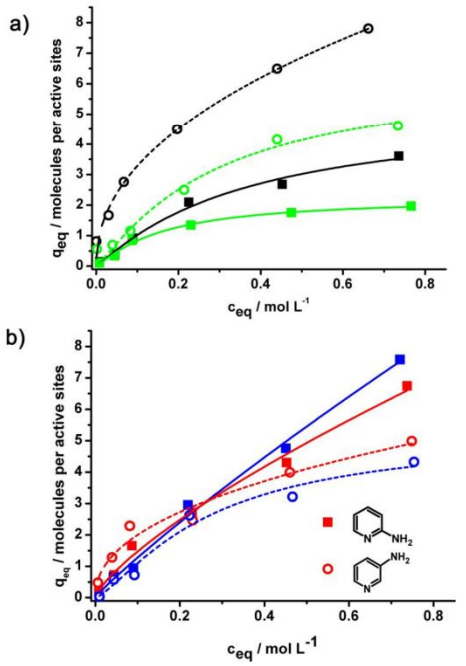

Figure 3: Competitive adsorption isotherms of 2-AP (solid squares) and 3-AP (empty circles) on a) Al-MIL-101-NH_2 (black curves) and DEA-Cr-MIL-101-NH_2 (green curves); b) Al-MIL-101-URPy (red curves) and DEA-Cr-MIL-101-URPy (blue curves).

The competitive adsorption isotherms follow Langmuir type isotherms (Figure 3). The amino bearing derivatives (Figure 3a) take up significantly more 3-AP from the mixture compared to 2-AP. For the highest uptakes this amounts to a factor of two and four for H_2O@Al-MIL-101-NH_2 and DEA@Cr-MIL-101-NH_2, respectively. While the uptake of 2-AP is almost identical for both derivatives, blocking the CUS reduces the uptake of 3-AP by 50%. This follows the binding affinity derived before[28] and

demonstrates that 3-AP is preferentially attached to the CUS, while 2-AP is adsorbed in an unspecific fashion.
For the pyridyl urea derivatives the uptake of 2-AP is strongly enhanced. Compared to the amino MIL-101 this results in a factor of four. Simultaneously, the uptake of 3-AP is slightly reduced compared to the amino derivatives. Grafting the CUS is apparently less effective as the uptake of DEA@Cr-MIL-101-URPy is only slightly lower than the one of H_2O@Al-MIL-101-URPy. This trend is explained by two effects. On the one hand, the grafting reaction is less efficient for the pyridyl urea derivatives leaving roughly 40% of the CUS accessible. On the other hand, the interactions of 3-AP and 2-AP with the pyridyl urea units will be stronger, providing a stronger competition to the CUS. This effect is also observed for the ^{27}Al MAS NMR spectra of 2-AP@Al-MIL-101-URPy and 3-AP@Al-MIL-101-URPy, which are both similar to the one of H_2O@Al-MIL-101-URPy indicating that coordination to the CUS is less relevant. For 2-AP the affinity to the pending groups seems to be significantly more pronounced as shown in the increasing uptake and the expected better match with the DDA recognition pattern.
As a consequence, we observe a clear trend for the selectivity of 2-AP over 3-AP (Figure 4) represented in the selectivity coefficient $\alpha_{2\text{-AP vs. 3-AP}}$ (calculation see experimental section). While amino functionalized derivatives with active CUS exhibit a selectivity of about 0.4 at higher uptakes (Figure 4 black curve), introducing the pyridyl urea groups increases the selectivity by roughly a factor of three. By additionally blocking the CUS, the selectivity raises again by roughly 50 %. In total, the selectivities of the amino and pyridyl urea groups differ by a factor of ≈ 4, demonstrating that the difference for the bonding affinity between a single donor (NH_2) and a donor acceptor pattern (URPy) is large enough to separate 2-AP and 3-AP in solutions.

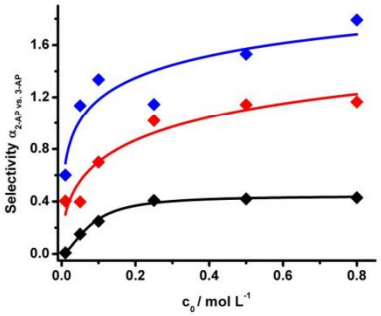

Figure 4: Selectivity values α on Al-MIL-101-NH_2 (black curve), Al-MIL-101-URPy (red curve) and DEA-Cr-MIL-101-URPy (blue curve).

Interactions of guests and pending groups

In order to develop a better understanding for preferred binding sites at the amino and pyridyl urea groups we collected ^{15}N MAS spectra for all Al-MIL-101 derivatives as function of loading with 2-AP/3-AP. These data were compared to results of quantum chemical calculations on DFT level providing energetically favored spatial arrangements for the adducts of guests and pending groups as well as simulated isotropic chemical shifts for the nitrogen sites within these adducts. The corresponding ^{15}N MAS NMR spectra are depicted in Figures 5 – 7 and the simulated δ_{iso} values for the most likely adducts are plotted in colored vertical lines.

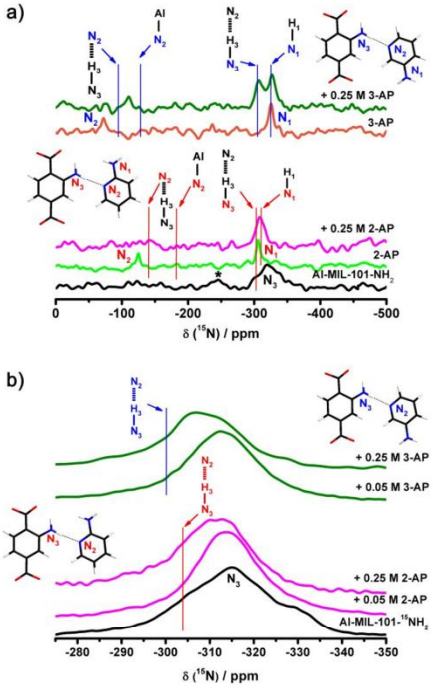

Figure 5: a) ^{15}N NMR CP MAS spectra from top to bottom: 3-AP@Al-MIL-101-NH_2, pure 3-AP, 2-AP@Al-MIL-101-NH_2, pure 2-AP and pure Al-MIL-101-NH_2; **b)** Enlarged section of the ^{15}N NMR (98% ^{15}N labeled) spectra from top to bottom: 0.25 M 3-AP@Al-MIL-101-$^{15}NH_2$, 0.05 M 3-AP@Al-MIL-101-$^{15}NH_2$, 0.25 M 2-AP@Al-MIL-101-$^{15}NH_2$, 0.05 M 2-AP@Al-MIL-101-$^{15}NH_2$ and pure Al-MIL-101-$^{15}NH_2$. The vertical lines in a) and b) represent calculated δ_{iso} values for the model with the best match to the experimental data. The corresponding structure is depicted on the left (3-AP) and the right (2-AP). The asterisk denotes a small impurity of NHCHO units (Figure S6).

The spectrum of 3-AP@Al-MIL-101-NH_2 shows three signals at -109 ppm (N_2), -303 pm (N_3) and -325 ppm (N_1) (Figure 5a, olive line). They match 3-AP@amino adducts best, where the pyridine nitrogen (N_2) of 3-AP is hydrogen bonded to one of the amino protons (N_3-H_3). This causes a downfield shift for N_3 and an upfield shift for N_2 compared to pure 3-AP and H2O@MIL-101-NH_2 (Figure 5a, orange and black lines). The signal for the amino groups of 3-AP (N_1), which do not participate to the adduct formation, is not affected. In spite of the broadening of the resonances within the ^{27}Al MAS spectra of 2-AP/3-AP@MIL-101-NH_2 (Figure S14), which hints towards a competing interaction of the guest molecules with the CUS, no resonances for the corresponding adducts could be singled out within the ^{15}N MAS NMR spectra (Figure 5a). Characteristic resonances for adducts should cause upfield shifts for the pyridine nitrogen (N_2) by approximately 40-50 ppm according to DFT calculations and literature data.[52] We thus conclude that at RT the equilibrium between adsorption at the CUS and the pending groups is dynamic with exchange rates in the fast motion regime. Thus, only one averaged resonance at -109 ppm (N_2, 3-AP) is visible within the ^{15}N MAS NMR spectra.

A similar trend is observed for the ^{15}N MAS NMR spectrum (Figure 5a, magenta line) of 2-AP@Al-MIL-101-NH_2, which exhibits resonances at about -142 ppm (N_2) and -306 ppm (N_3-H_3, N_1). The heavy overlap of the signals for N_3 and N_1, however, does not allow to determine the downfield shift quantitatively and thus prevents to judge the binding preference of 2-AP and 3-AP at the amino function of the framework. The resonance assigned to N_2 matches closely the simulated δ_{iso} for the 2-AP@amino adducts, which hints to a preferential adsorption of 2-AP at the amino function. This in line with the weaker binding strength of 2-AP compared to 3-AP at the CUS.[28]

By labeling Al-MIL-101-NH_2 with ^{15}N at the amino group we could single out the characteristic resonances for the free amino units as well as for the 2-AP/3-AP@amino adducts (Figure 5b). With increasing guest loading the downfield shift rises for both guests reaching 4.4 ppm for 2-AP and 7.5 ppm for 3-AP after equilibrating with solutions of 0.25 M for each guest. This suggests, that 3-AP exhibits a higher binding affinity to the amino function compared to 2-AP, which is in line with an energy lower by 6 kJ/mol for 3-AP as derived from the DFT calculations.

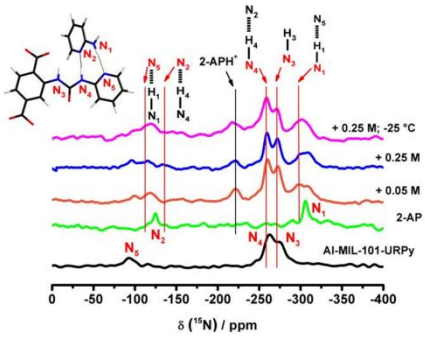

Figure 6: ^{15}N CP MAS NMR spectra of pure Al-MIL-101-URPy (black line), pure 2-AP (green line), 0.05 M 2-AP@Al-MIL-101-URPy (orange line), 0.25 M 2-AP@Al-MIL-101-URPy (blue line) and 0.25 M 2-AP@Al-MIL-101-URPy at -25 °C (magenta line). The red vertical lines indicate the chemical shifts derived from most preferred arrangements of 2-AP within Al-MIL-101-URPy. The black vertical line corresponds to the chemical shift of N_2 for protonated 2-AP (2-APH^+).[53]

In case of Al-MIL-101-URPy the DFT calculations suggest that the urea fragment close to the linker N_3-H_3 forms a strong hydrogen bond with the oxygen atoms of neighboring carboxylate groups of the terephthalates. Therefore, the N_3-H_3 fragment is not available for hydrogen bonding to the guest molecules 2-AP/3-AP and reduces the DDA to a DA pattern. This is experimentally supported as the ^{15}N NMR shift of N_3 at -273.5 ppm is essentially independent of the guest loading (Figure 6 and 7).

The ^{15}N MAS NMR spectra of 2-AP@Al-MIL-101-URPy exhibit resonances typical for the urea pyridyl group and 2-AP molecules (Table S3). With respect to the single component phases 2-AP and Al-MIL-101-URPy the resonances for the amino group N_1, the outer amido fragment N_4 and the pyridyl nitrogen N_2 of 2-AP are downfield-shifted by roughly 9, 3 and 7 ppm. Simultaneously, the pyridyl nitrogen of the URPy unit (N_5) shift upfield by 5 ppm. These trends become more pronounced with higher loading and lower temperatures as the hydrogen bonds between the pending groups and the guests become stronger (Figure 6). These findings are matched best with the prediction of isotropic chemical shifts at the DFT level (vertical lines within Figure 6 and Table S3) for a scenario where 2-AP and the pending URPy groups form the complementary hydrogen bond pattern DA···AD. According to the DFT calculations this scenario it energetically favored by roughly 80 kJ/mol with respect to the single component phases. Additionally, for higher loadings also 2-AP adsorbed in an unspecific fashion was observed as demonstrated by the ^{15}N NMR signal at around -307.0 ppm, which is typical for 2-AP in its crystalline form (Figure 6, green line).

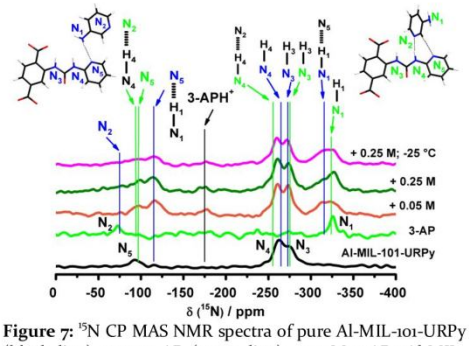

Figure 7: ^{15}N CP MAS NMR spectra of pure Al-MIL-101-URPy (black line), pure 3-AP (green line), 0.05 M 3-AP@Al-MIL-101-URPy (orange line), 0.25 M 3-AP@Al-MIL-101-URPy (olive line) and 0.25 M 3-AP@Al-MIL-101-URPy at -25 °C (magenta line). The red and blue vertical lines indicate the chemical shifts derived from most preferred arrangements shown in Figure 8d and 8e, respectively. The black vertical line corresponds to the chemical shift of N_2 for protonated 3-AP (3-APH$^+$).[53]

In contrast, the DFT calculations suggested at least two possible arrangements for 3-AP within Al-MIL-101-URPy. Both are depicted in Figure 7. For the first one, 3-AP forms weak H bonds between its pyridine nitrogen $\mathbf{N_2}$ and the $\mathbf{N_4}$-$\mathbf{H_4}$ unit of the urea fragment and between the aromatic C-H bond in ortho position to $\mathbf{N_2}$ and the pyridine nitrogen atom $\mathbf{N_5}$ of URPy. This induces significant high- and lowfield shifts for the resonances of $\mathbf{N_2}$ and $\mathbf{N_4}$, while the one for $\mathbf{N_5}$ remains essentially unchanged. The second scenario is stabilized by a single H bond between the amino hydrogen atom $\mathbf{N_1}$-$\mathbf{H_1}$ of 3-AP and the pyridine nitrogen $\mathbf{N_5}$ of the pending urea pyridyl groups. Again, the resonance for the amino function ($\mathbf{N_1}$) is shifted lowfield while the signal for $\mathbf{N_5}$ shifts highfield. While the double H bond scenario is favored by 50 kJ/mol with respect to the single component phases according to the DFT calculations the single H bond scenario is stabilized by roughly 30 kJ/mol. The respective ^{15}N chemical shifts are given in Table S3.

The observed ^{15}N NMR spectra of 3-AP@Al-MIL-101-URPy exhibit resonances typical for of both arrangements (Figure 7 and Table S3) for all loadings and temperatures. In spite of the stronger stabilization for the double H bond scenario no clear trend for the intensities assigned to both scenarios is visible. This indicates that both scenarios exhibit similar interaction strengths experimentally. We attribute this to secondary interactions with further guest and solvent molecules which might lead to additional stabilizing contributions. The latter could not be considered for the DFT calculations.

The previous discussion does not explain the ^{15}N NMR resonances at -220 ppm for 2-AP@Al-MIL-101-URPy (Figure 6) and – 176 ppm for 3-AP@Al-MIL-101-URPy (Figure 7). Both signals are typical however, for guest molecules where the pyridyl nitrogen atoms are protonated.[53] We attribute this to an increased acidity of residual water in the vicinity of the pending URPy groups, which partially protonate the guest molecules.

Conclusion

Here we report on the successful incorporation of a 2-pyridyl urea side group with an apparent DDA hydrogen bond donor acceptor pattern into the mesoporous framework topology MIL-101. For this, the parent material MIL-101-NH_2 was modified postsynthetically by loading it with 2-pyridyl acyl azide solutions. The reactive intermediate 2-pyridyl isocyanate, formed *in situ* in the pore space, then reacts preferentially with the amino functions of the framework to the desired product with a yield of about 90 % instead of undergoing a dimerisation.

The influence of the pending URPy groups on the sorption properties of MIL-101-URPy was studied by using a combination of solution phase sorption experiments, multinuclear MAS NMR spectroscopy and DFT calculations for various model systems. All energetically favored structure models feature a strong intra framework hydrogen bond between the inner urea N-H units and the adjacent carboxylate groups of the terephthalate linkers. We thus expect the pyridyl urea groups to act as a double hydrogen bond donor-acceptor (DA) within the framework instead of the DDA pattern typical for free URPy groups. As probe molecules for the sorption preferences, we thus loaded MIL-101-URPy frameworks with organic solutions of 2-amiopyridine and 3-aminopyridine. While 2-AP matches both function and geometry of the accessible hydrogen bond donor acceptor sequence of the pending URPy groups, 3-AP does not.

By analyzing the response of two pairs of MIL-101 derivatives – Al-MIL-101-NH_2 and Cr-MIL-101-NH_2 as well as Al-MIL-101-URPy and Cr-MIL-101-URPy on single component and competitive adsorption isotherms, we were able to separate the influence of the pending URPy groups from CUSs at the metal centers of the IBUs. While the higher chemical stability of Cr-MIL-101-X enabled us to block the CUS with diethyl amine and thus to reduce their influence on the adsorption isotherms markedly, the diamagnetic Al-MIL-101-X derivatives lead to well resolved ^{15}N MAS NMR spectra. We then compared the observed chemical shifts with the ones calculated for the DFT model systems to probe preferred adsorption sites at the side groups.

Both H_2O@Al-MIL-101-NH_2 and H_2O@Cr-MIL-101-NH_2 showed enhanced uptakes and selectivities for 3-AP. By blocking the CUS with DEA the uptake for both 2-Ap and 3-AP is reduced with a stronger effect for 3-AP. This suggests, that 3-AP exhibits a higher affinity to the CUS compared to 2-AP. At the same time, both guest molecules are attached to the pending amino functions by single hydrogen bonds between the pyridine nitrogen and the NH unit of the amino functions as indicated by the ^{15}N MAS NMR spectra as function of the guest loading.

After introducing the pending URPy groups the selectivity for 2-AP is enhanced by a factor of three and blocking the

CUS for DEA@Cr-MIL-101-URPy increases the selectivity by another 50%. The latter effect is mainly caused by a reduction of the uptake of 3-AP. The ^{15}N MAS NMR spectra collected for 2-AP/3-AP@Al-MIL-101-URPy demonstrated that 2-AP is indeed adsorbed at the pending URPy groups according to the key-and-lock principle via complementary double hydrogen bonds, while for 3-AP two scenarios seem to be equally attractive. Both of these arrangements feature one single hydrogen bond only and are thus less favored by roughly 30 kJ/mol compared to the double hydrogen bond scenario realized with 2-AP.
Our results suggest that introducing selectivity into the sorption processes of MOFs can be established by introducing side groups with multiple hydrogen bonding motifs, which are selected to bind targeted guest molecules via the key-and-lock principle of supramolecular chemistry. The concept is realized straightforwardly and can thus be applied not only to MOFs but to a broad variety of porous materials. This offers potential for targeted recognition of larger and complex molecules, which is necessary for highly specific separation, sensing and delivering applications.

Experimental section

Synthesis of the adsorbents

Al- and Cr-MIL-101-NH_2 were synthesized according to a slightly modified procedure of Hartmann et al.[54] which we previously described in ref. 47 using $AlCl_3 \cdot 6\ H_2O$ and $CrCl_3$ as metal sources.[48]
The synthesis of the ^{15}N enriched amino-terephthalic acid was performed according to the protocol of Morris et al.[55] Diethyl nitro terephthalate was synthesized from reaction of potassium nitrate (^{15}N) with diethyl terephthalate. Afterwards, diethyl amino terephthalate was obtained by treating diethyl nitro terephthalate with hydrogen (5 bar) for 24 h on a Pd/charcoal. Finally, amino terephthalic acid was obtained by reaction of diethyl amino terephthalate (^{15}N) with sodium hydroxide in a methanol/water solution.
Cr- and Al-MIL-101-URPy was obtained as follows. Referring to a synthesis route from Holt *et al.*,[49] triethylamine (1.38 mL, VWR) was added to a solution of 2-picolinic acid (1.23 g, Sigma Aldrich) in dimethylformamide (15 mL, VWR) and stirred for 30 min at RT. Then, a solution of diphenyl phosphoryl azide (2.15 mL, Sigma Aldrich) in dimethylformamide (2.5 mL, VWR) was added within 10 min under stirring. Having stirred for 3 h at RT, we poured the mixture over a water/dichloromethane solution. The organic phase was washed with a saturated solution of sodium hydrogen carbonate (VWR) in water followed by two times washing with water. After removing dichloromethane under reduced pressure, white solid 2-pyridyl acyl azide (1.12 g, 76%) was obtained in high purity as proven by solution ^1H, ^{13}C NMR and ATR-IR spectroscopy (Supporting Information). 2-pyridyl acyl azide was dissolved in dichloromethane (40 mL) and poured over dried Cr- and Al-MIL-101-NH_2 (300 mg). After refluxing for three days, we cooled the suspension to RT, centrifuged and washed two times in fresh dichloromethane. The resulting solid was dried at 100 °C for 2 h.

Liquid-phase adsorptions

Prior to the adsorption experiments, the commercially obtained 2-aminopyridine and 3-aminopyridine (Sigma Aldrich) were purified by sublimation, dried in a desiccator and stored in argon atmosphere. Anhydrous 1,4-dioxane (Sigma Aldrich) was used to prepare the solutions for the adsorption experiments. The adsorbents were dried at 90 °C for 2 h under reduced pressure to remove physisorbed species. The liquid-phase adsorption isotherms were obtained by the batch circulation method using a piston pump (Ismatec® IP 65), where the MOFs were successively equilibrated with the solutions of increasing concentrations. The MIL-101 derivatives (100 mg) were mixed with dried glass beads (250 mg, Ø 30 - 50 µm, Polysciences, Inc.) and packed into a glass pipette under argon atmosphere. This generated a permeable bed which prevented densification of the MIL-101 powder to guarantee a constant flow of the solutions (8 mL) through the MIL-101 derivatives with a rate of 0.5 mL min^{-1} at room temperature. The quasi-equilibrium state was monitored every 60 min and circulation was continued until the quasi-equilibrium state was reached. The uptakes q_{eq} in mol g^{-1} were determined from gas chromatographic data (Agilent 6980N) by using the differences between the initial and quasi-equilibrium concentrations as shown in equation 1

$$q_{eq} = \frac{\left(c_0 - c_{eq}\right) \cdot V}{m} \quad (1)$$

where c_0 is the initial concentration of the guest molecules in the solution, c_{eq} corresponds to the concentration after reaching the quasi-equilibrium state, V is the volume of solution and m is the mass of the adsorbent.
For the GC analyses dodecane was used as the internal standard. The selectivity values α were calculated according to equation 2

$$\alpha = \frac{q_{2-AP}}{q_{3-AP}} \cdot \frac{c_{3-AP}}{c_{2-AP}} \quad (2)$$

where $q_{2\text{-}AP}$ and $q_{3\text{-}AP}$ are the adsorbed amounts (mol g^{-1}) of 2-AP and 3-AP, respectively, per gram of Al/Cr-MIL-101 and $c_{2\text{-}AP}$ and $c_{3\text{-}AP}$ (mol L^{-1}) represent the bulk equilibrium concentrations of the respective target molecules.

Characterization methods

Powder X-ray diffraction (PXRD) experiments were carried out in Bragg-Brentano geometry on a Panalytical X'pert Pro diffractometer equipped with a X'Celerator Scientific RTMS detector using Ni filtered $Cu_{K\alpha}$ radiation (λ = 1.54187 Å, 40 kV, 40 mA). Measurements were performed in the range of 2-30° (2θ) with a step size of 0.017°. The simulated PXRD pattern was obtained by replacing Cr by Al in a published structure model of Cr-MIL-101[56]. The cell parameters of the face centered cubic cell were refined to 87.7 Å while maintaining the space group $Fd\bar{3}m$ (No. 227).
Attenuated total reflectance IR spectra were recorded in the range 400 - 4000 cm^{-1} with a resolution of 4 cm^{-1} on a Jasco FT/IR-6100 spectrometer with a PIKEGladiATR accessory.

The samples for chemical analyses were prepared in a glove box under argon atmosphere after evacuating at 90 °C for 2 h. Carbon, hydrogen and nitrogen contents (wt%) were obtained on a Vario elementar EL III. Aluminum and chromium contents (wt%) were determined by atomic absorption spectroscopy (AAS) in extinction mode on a Varian AA100 using a N_2O/acetylene flame upon chemical digestion in a mixture of hydrochloric acid, nitric acid and sulfuric acid. EDX spectroscopy was carried out on a Joel JSM 6400 scanning electron microscope equipped with a Noran energy dispersive X-ray analyzer and using a beam voltage of 20 kV. Solution ^{1}H and ^{13}C NMR spectra were obtained using a Bruker DRX 500 spectrometer operating at a proton frequency of 500.13 MHz. Chemical shifts are given in parts per million using the DMSO-d6 peak as an internal standard according to literature values (2.54 ppm for ^{1}H and 40.45 ppm for ^{13}C).[57]

All solid-state NMR spectra were acquired under magic-angle spinning using ZrO_2 rotors. The chemical shifts were referenced to TMS for ^{13}C, to nitromethane for ^{15}N and to an aqueous solution of $AlCl_3 \cdot 6\ H_2O$ for ^{27}Al. ^{13}C CP MAS measurements were collected on a Bruker Avance III HD spectrometer at 9.4 T using a 4 mm double resonance probe at a spinning frequency of 10 kHz. ^{15}N CP MAS spectra were recorded on a Bruker Avance II 300 spectrometer at a spinning rate of 5 kHz using a 7 mm triple resonance probe. ^{13}C CP MAS and ^{15}N CP MAS spectra were obtained after 90° pulse excitation of 3.0 µs and 3.5 µs on the ^{1}H channel, respectively, and 6 µs for directly excited ^{15}N. The recycle delays for ^{13}C CP and ^{15}N CP of the frameworks were 2 s, 1800 s for ^{15}N CP of the crystalline guest molecules and 3600 s for the single pulse ^{15}N NMR measurement. The CP mixing times were set to 5 ms for ^{1}H-^{13}C and ^{1}H-^{15}N each. Broadband proton decoupling was achieved by applying the SPINAL64[58] sequence with of nutation frequency of around 80 kHz. The signal assignments of the NMR spectra were based upon simulation of the chemical shifts using the ACD/Labs software package;[59] the IR vibration bands were identified according to literature data.[47,48]

Nitrogen sorption measurements were performed on a Quantachrome NOVA 2000e at 77 K after evacuating the adsorbents at 393 K for 14 h under reduced pressure. Brunauer-Emmet-Teller (BET) equivalent surface areas were determined in the relative pressure range between 0.06 and 0.15 to accommodate for microporous materials.[60] Specific total pore volumes were determined at a relative pressure of 0.98 according to the Gurvich rule.[61] The pore-size distributions were derived using the argon NLDFT model at 77 K for the adsorption branch assuming a silica/zeolite surface and a spherical/cylindrical pore shape which is implemented in the Quantachrome ASiQ v3.0 software package.

Acknowledgement

We gratefully acknowledge financial support by the DFG (SE 1417/7-1 and SE 1417/8-1). We thank Beate Bojer for her steady support with the NMR measurements.

REFERENCES

(1) Li, J.-R.; Kuppler, R. J.; Zhou, H.-C. Selective Gas Adsorption and Separation in Metal–organic Frameworks. *Chem. Soc. Rev.* **2009**, *38*, 1477–1504.

(2) Li, J.; Sculley, J.; Zhou, H. Metal–Organic Frameworks for Separations. *Chem. Rev.* **2012**, *112*, 869–932.

(3) Sumida, K.; Rogow, D. L.; Mason, J. A.; Mcdonald, T. M.; Bloch, E. D.; Herm, Z. R.; Bae, T.; Long, R. Carbon Dioxide Capture in Metal-Organic Frameworks. *Chem. Rev.* **2012**, *112*, 724–781.

(4) Van de Voorde, B.; Bueken, B.; Denayer, J.; De Vos, D. Adsorptive Separation on Metal-Organic Frameworks in the Liquid Phase. *Chem. Soc. Rev.* **2014**, *43*, 5766–5788.

(5) Samokhvalov, A. Adsorption on Mesoporous Metal-Organic Frameworks in Solution: Aromatic and Heterocyclic Compounds. *Chem. - A Eur. J.* **2015**, *21*, 16726–16742.

(6) Horcajada, P.; Gref, R.; Baati, T.; Allan, P. K.; Maurin, G.; Couvreur, P. Metal-Organic Frameworks in Biomedicine. *Chem. Rev.* **2012**, *111*, 1232–1268.

(7) Horcajada, P.; Chalati, T.; Serre, C.; Gillet, B.; Sebrie, C.; Baati, T.; Eubank, J. F.; Heurtaux, D.; Clayette, P.; Kreuz, C.; Chang, J.-S.; Hwang, Y. K.; Marsaud, V.; Bories, P.-N.; Cynober, L.; Gil, S.; Ferey, G.; Couvreur, P.; Gref, R. Porous Metal-Organic-Framework Nanoscale Carriers as a Potential Platform for Drug Delivery and Imaging. *Nat. Mater.* **2010**, *9*, 172–178.

(8) McKinlay, A. C.; Morris, R. E.; Horcajada, P.; Férey, G.; Gref, R.; Couvreur, P.; Serre, C. BioMOFs: Metal-Organic Frameworks for Biological and Medical Applications. *Angew. Chemie - Int. Ed.* **2010**, *49*, 6260–6266.

(9) Burrows, A. D. Gas Sensing Using Porous Materials for Automotive Applications. *Chem. Soc. Rev.* **2015**, *44* (13), 4290–4321.

(10) Kreno, L. E.; Leong, K.; Farha, O. K.; Allendorf, M.; Duyne, R. P. Van; Hupp, J. T. Metal- Organic Framework Materials as Chemical Sensors. *Chem. Rev.* **2012**, *112*, 1105–1125.

(11) Foo, M. L.; Matsuda, R.; Kitagawa, S. Functional Hybrid Porous Coordination Polymers. *Chem. Mater.* **2014**, *26*, 310–322.

(12) Furukawa, H.; Cordova, K. E.; O'Keeffe, M.; Yaghi, O. M. The Chemistry and Applications of Metal-Organic Frameworks. *Science* **2010**, *9* (6149), 1230444.

(13) Slater, A. G.; Cooper, A. I. Function-Led Design of New Porous Materials. *Science (80-.).* **2015**, *348* (6238), 8075-1–10.

(14) Wang, Z.; Cohen, S. M. Postsynthetic Modification of Metal–organic Frameworks. *Chem. Soc. Rev.* **2009**, *38*, 1315.

(15) Ahnfeldt, T.; Gunzelmann, D.; Wack, J.; Senker, J.; Stock, N. Controlled Modification of the Inorganic and Organic Bricks in an Al-Based MOF by Direct and Post-Synthetic Synthesis Routes. *CrystEngComm* **2012**, *14*, 4126.

(16) Lammert, M.; Bernt, S.; Vermoortele, F.; Vos, D. E. De; Stock, N. Single- and Mixed-Linker Cr-MIL-101 Derivatives: A High-Throughput Investigation. *Inorg.Chem.* **2013**, *52*, 8521–8528.

(17) Tanabe, K. K.; Cohen, S. M. Postsynthetic Modification of Metal-Organic Frameworks-a Progress Report. *Chem. Soc. Rev.* **2011**, *40* (2), 498–519.

(18) Tanabe, K. K.; Wang, Z.; Cohen, S. M. Systematic Functionalization of a Metal-Organic Framework via a Postsynthetic Modification Approach. *J. Am. Chem. Soc.* **2008**, *130* (26), 8508–8517.

(19) Wack, J.; Ahnfeldt, T.; Stock, N.; Senker, J. Identifying Selective Host – Guest Interactions Based on Hydrogen Bond Donor – Acceptor Pattern in Functionalized Al-MIL-53 Metal – Organic Frameworks. *J. Phys. Chem. C* **2013**, *117*, 11991–20001.

(20) Alaerts, L.; Maes, M.; Giebeler, L.; Jacobs, P. A.; Martens, J. A.; Denayer, J. F. M.; Kirschhock, C. E. A.; Vos, D. E. De. Selective Adsorption and Separation of. *Adsorpt. J. Int. Adsorpt. Soc.* **2008**, No. 26, 14170–14178.

(21) Osta, R. El; Carlin-sinclair, A.; Guillou, N.; Walton, R. I.; Vermoortele, F.; Maes, M.; Vos, D. De; Millange, F. Liquid-Phase Adsorption and Separation of Xylene Isomers by the Flexible Porous Metal – Organic Framework MIL-53 (Fe). *Chem. Mater.* **2012**, *24*, 2781–2791.

(22) Alaerts, L.; Kirschhock, C. E. A.; Maes, M.; Van Der Veen, M. A.; Finsy, V.; Depla, A.; Martens, J. A.; Baron, G. V.; Jacobs, P. A.; Denayer, J. F. M.; De Vos, D. E. Selective Adsorption and Separation of Xylene Isomers and Ethylbenzene with the Microporous vanadium(IV) Terephthalate MIL-47. *Angew. Chemie - Int. Ed.* **2007**, *46* (23), 4293–4297.

(23) Alaerts, L.; Maes, M.; Jacobs, P. A.; Denayer, F. M.; Vos, D. E. De. Activation of the Metal – Organic Framework MIL-47 for Selective Adsorption of Xylenes and Other Difunctionalized Aromatics W. *Phys. Chem. Chem. Phys.* **2008**, *10*, 2979–2985.

(24) Dai, J.; Mckee, M. L.; Samokhvalov, A. Adsorption of Naphthalene and Indole on F300 MOF in Liquid Phase by the Complementary Spectroscopic , Kinetic and DFT Studies. *J Porous Mater* **2014**, *21*, 709–727.

(25) Maes, M.; Trekels, M.; Boulhout, M.; Schouteden, S.; Vermoortele, F.; Alaerts, L.; Heurtaux, D.; Seo, Y.; Hwang, Y. K.; Chang, J.; Beurroies, I.; Denoyel, R.; Temst, K.; Vantomme, A.; Horcajada, P.; Serre, C.; Vos, D. E. De. Selective Removal of N-Heterocyclic Aromatic Contaminants from Fuels by Lewis Acidic Metal – Organic Frameworks. *Angew. Chemie* **2011**, *123*, 4296–4300.

(26) Wang, Z.; Sun, Z.; Kong, L.; Li, G. Adsorptive Removal of Nitrogen-Containing Compounds from Fuel by Metal-Organic Frameworks. *J. Energy Chem.* **2013**, *22*, 869–875.

(27) Voorde, B. Van De; Boulhout, M.; Vermoortele, F.; Horcajada, P.; Cunha, D.; Lee, J. S.; Chang, J.; Gibson, E.; Daturi, M.; Lavalley, J.; Vimont, A.; Beurroies, I.; Vos, D. E. De. N / S-Heterocyclic Contaminant Removal from Fuels by the Mesoporous Metal – Organic Framework MIL-100□: The Role of the Metal Ion. *J. Am. Chem. Soc.* **2013**, *135*, 9849–9856.

(28) Wittmann, T.; Mondal, A.; Tschense, C. B. L.; Wittmann, J. J.; Klimm, O.; Siegel, R.; Corzilius, B.; Weber, B.; Kaupp, M.; Senker, J. Probing Interactions of N-Donor Molecules with Open Metal Sites within Paramagnetic Cr-MIL-101: A Solid-State NMR Spectroscopic and Density Functional Theory Study. *J. Am. Chem. Soc.* **2018**, *140*, 2135–2144.

(29) Cychosz, K. A.; Wong-foy, A. G.; Matzger, A. J. Liquid Phase Adsorption by Microporous Coordination Polymers□: Removal of Organosulfur Compounds. **2008**, 6938–6939.

(30) Achmann, S.; Hagen, G.; Hämmerle, M.; Malkowsky, I.; Kiener, C.; Moos, R. Sulfur Removal from Low-Sulfur Gasoline and Diesel Fuel by Metal-Organic Frameworks. *Chem. Eng. Technol.* **2010**, *33*, 275–280.

(31) J. S. Lindsey. Self-Assembly in Synthetic Routes to Molecular Devices. Biological Pronciples and Chemical Perspectives. A Review. *New J. Chem.* **1991**, No. 15, 153–180.

(32) Li, M.; Ishihara, S.; Ji, Q.; Akada, M.; Hill, J. P.; Ariga, K. Paradigm Shift from Self-Assembly to Commanded Assembly of Functional Materials: Recent Examples in Porphyrin/fullerene Supramolecular Systems. *Sci. Technol. Adv. Mater.* **2012**, *13*, 53001.

(33) Such, G. K.; Johnston, A. P. R.; Caruso, F. Engineered Hydrogen-Bonded Polymer Multilayers: From Assembly to Biomedical Applications. *Chem. Soc. Rev.* **2011**, *40* (1), 19–29.

(34) Zehe, C. S.; Hill, J. A.; Funnell, N. P.; Kreger, K.; van der Zwan, K. P.; Goodwin, A. L.; Schmidt, H.-W.; Senker, J. Mesoscale Polarization by Geometric Frustration in Columnar Supramolecular Crystals. *Angew. Chemie Int. Ed.* **2017**, *56* (16), 4432–4437.

(35) Wittenberg, J. B.; Isaacs, L. Complementarity and Preorganization. *Supramol. Chem. From Mol. to Nanomater. Online* **2012**, 1–19.

(36) Lehn, J.-M. Perspectives in Supramolecular Chemistry - From Molecular Recognition Towards Molecular Information Processing and Self-Organisation. *Angew. Chem. Int. Ed.* **1990**, *29*, 1304–1319.

(37) Schmuck, C.; Wienand, W. Self-Complementary Quadruple Hydrogen-Bonding Motifs as a Functional Principle: From Dimeric Supramolecules to Supramolecular Polymers. *Angew. Chemie - Int. Ed.* **2001**, *40* (23), 4363–4369.

(38) Jorgensen, W. L.; Pranata, J. Importance of Secondary Interactions in Triply Hydrogen Bonded Complexes: Guanine-Cytosine vs Uracil-2,6-Diaminopyridine. *J. Am. Chem. Soc.* **1990**, *112*, 2008–2010.

(39) Zhang, M.; Gu, Z.; Bosch, M.; Perry, Z.; Zhou, H. Biomimicry in Metal – Organic Materials. *Coord. Chem. Rev.* **2015**, *293–294*, 327–356.

(40) Li, Q.; Zhang, W.; Miljanic, O. S.; Sue, C.; Zhao, Y.-L.; Liu, L.; Knobler, C. B.; Stoddart, J. F.; Yaghi, O. M. Docking in Metal-Organic Frameworks. *Science (80-.).* **2009**, *325*, 855–859.

(41) Cai, H.; Li, M.; Lin, X. R.; Chen, W.; Chen, G. H.; Huang, X. C.; Li, D. Spatial, Hysteretic, and Adaptive Host-Guest Chemistry in a Metal-Organic Framework with Open Watson-Crick Sites. *Angew. Chemie - Int. Ed.* **2015**, *54*, 10454–10459.

(42) M. R. Jones, N. C. Seeman, C. A. M. Programmable

Materials and the Nature of the DNA Bond. *Science (80-.).* **2015**, *347* (6224).
(43) Sivakova, S.; Rowan, S. J.; Rowan, S. J. Nucleobases as Supramolecular Motifs. *Chem Soc Rev* **2005**, *34*, 9–21.
(44) Férey, G.; Mellot-Draznieks, C.; Serre, C.; Millange, F.; Dutour, J.; Surblé, S.; Margiolaki, I. A Chromium Terephthalate – Based Solid with Unusually Large Pore Volumes and Surface Area. *Science (80-.).* **2005**, *309*, 2040–2042.
(45) Serra-Crespo, P.; Ramos-Fernandez, E. V; Gascon, J.; Kapteijn, F. Synthesis and Characterization of an Amino Functionalized MIL-101 (Al): Separation and Catalytic Properties. *Chem. Mater.* **2011**, *23*, 2565–2572.
(46) Hwang, Y. K.; Hong, D.; Chang, J.; Jhung, S. H.; Seo, Y.; Kim, J.; Vimont, A.; Daturi, M.; Serre, C.; Férey, G. Amine Grafting on Coordinatively Unsaturated Metal Centers of MOFs: Consequences for Catalysis and Metal Encapsulation. *Angew. Chem. Int. Ed.* **2008**, *47*, 4144–4148.
(47) Wittmann, T.; Siegel, R.; Reimer, N.; Milius, W.; Stock, N.; Senker, J. Enhancing the Water Stability of Al-MIL-101-NH2 via Postsynthetic Modification. *Chem. - A Eur. J.* **2015**, *21*, 314–323.
(48) Bernt, S.; Guillerm, V.; Serre, C.; Stock, N. Direct Covalent Post-Synthetic Chemical Modification of Cr-MIL-101 Using Nitrating Acidw. *Chem. Commun. Chem. Commun* **2011**, *47*, 2838–2840.
(49) Holt, J.; Andreassen, T.; Bakke, J. M.; Fiksdahl, A. Nitropyridyl Isocyanates. *J. Heterocycl. Chem.* **2005**, *42*, 259–264.
(50) Wickenheisser, M.; Jeremias, F.; Henninger, S. K.; Janiak, C. Grafting of Hydrophilic Ethylene Glycols or Ethylenediamine on Coordinatively Unsaturated Metal Sites in MIL-100 (Cr) for Improved Water Adsorption Characteristics. *Inorganica Chim. Acta* **2013**, *407*, 145–152.
(51) Krishnan, K.; Plane, R. A. Raman and Infrared Spectra of Complexes of Ethylenediamine with Zinc(II), Cadmium(II), and Mercury(II). *Inorg. Chem.* **1966**, 5 (4), 852–857.
(52) Marek, R., Lycka, A. 15N NMR Spectroscopy in Structural Analysis. *Curr. Org. Chem.* **2002**, *6*, 35–66.
(53) Städeli, W.; Philipsborn, W. 15N-NMR. Studies of Aminopyridines, Aminopyrimidines and of Some Diazine N-Oxides. *Helv. Chim. Acta* **1980**, *63*, 504–522.
(54) Hartmann, M.; Fischer, M. Amino-Functionalized Basic Catalysts with MIL-101 Structure. *Microporous Mesoporous Mater.* **2012**, *164*, 38–43.
(55) Morris, W.; Taylor, R. E.; Dybowski, C.; Yaghi, O. M.; Garcia-Garibay, M. A. Framework Mobility in the Metal-Organic Framework Crystal IRMOF-3: Evidence for Aromatic Ring and Amine Rotation. *J. Mol. Struct.* **2011**, *1004* (1–3), 94–101.
(56) Lebedev, O. I.; Millange, F.; Serre, C.; Van Tendeloo, G.; Férey, G. First Direct Imaging of Giant Pores of the Metal-Organic Framework MIL-101. *Chem. Mater.* **2005**, *17*, 6525–6527.
(57) Gottlieb, H. E.; Kotlyar, V.; Nudelman, A. NMR Chemical Shifts of Common Laboratory Solvents as Trace Impurities. **1997**, *3263* (3), 7512–7515.
(58) Fung, B. M.; Khitrin, A. K.; Ermolaev, K. An Improved Broadband Decoupling Sequence for Liquid Crystals and Solids. *J. Magn. Reson.* **2000**, *142* (1), 97–101.
(59) Advanced Chemistry Development, Inc. (ACD/Labs) Software 2013.
(60) Thommes, M. Physical Adsorption Characterization of Nanoporous Materials. *Chemie-Ingenieur-Technik* **2010**, *82*, 1059–1073.
(61) Gurvich, L. N. *J. Russ. Phys. Chem. Soc.* **1915**, *47*, 805–827.

6.2.2 Supporting Information

Supporting Information

for

Introducing Selective Host-Guest Interactions in MIL-101 Frameworks via a Multiple Hydrogen Bond Donor-Acceptor Recognition Site

Thomas Wittmann,[†] Carsten B. L. Tschense,[†] Renee Siegel,[†] Jürgen Senker[†,*]

[†] Department of Inorganic Chemistry III, University of Bayreuth, Universitätsstraße 30, 95440 Bayreuth (Germany)

[*] juergen.senker@uni-bayreuth.de

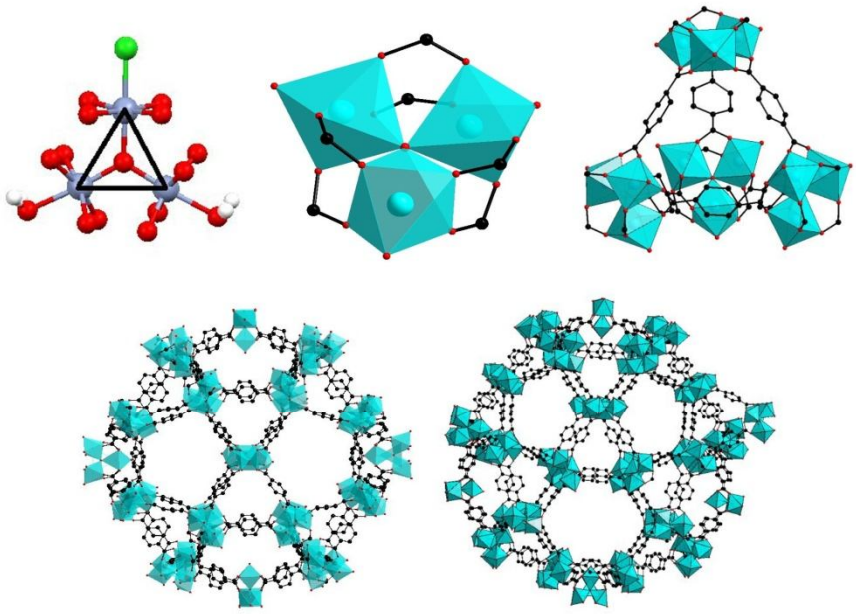

Figure S1: Structure of MIL-101. The metal ions in MIL-101 are arranged to form a equilateral triangle centred with a μ_3-oxygen atom (top left). The metal ions are octahedrally coordinated with four oxygen atoms from the terephthalate linkers, one corner sharing μ_3 oxygen and terminal position. Two of the three terminal positions are occupied by water molecules and one by chloride ions (top middle). The two water ligands can be exchanged by other coordinating species.[1–3] The inorganic building units (IBUs) are connected by terephthalate ligands to form a supertetrahedron with an inner diameter of 0.7 nm (top right). The supertetrahedra are in turn connected to form mesoporous cages with internal diameters of 2.5 nm (bottom left) and 3.0 nm (bottom right), which are accessible and interconnecting through pentagonal and hexagonal windows with diameters of 1.2 nm and 1.6 nm, respectively.

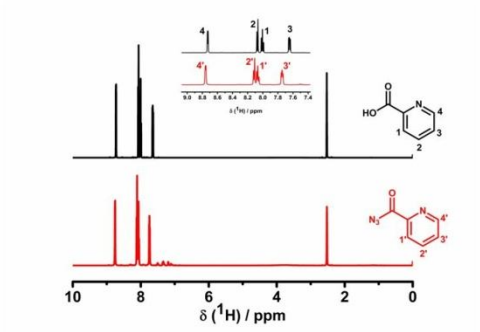

Figure S2: ^{1}H NMR spectra of 2-picolinic acid (top) and 2-pyridyl acyl azide in DMSO-d6 (bottom).

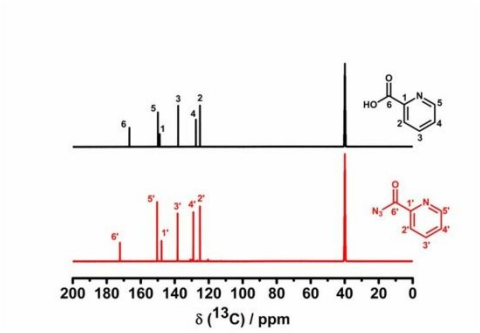

Figure S3: ^{13}C NMR spectra of 2-picolinic acid (top) and 2-pyridyl acyl azide in DMSO-d6 (bottom).

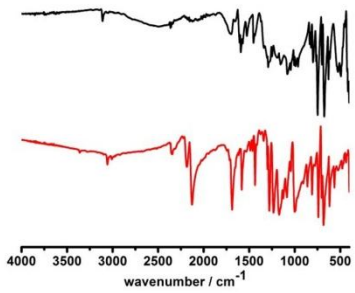

Figure S4: ATR-IR spectra of 2-picolinic acid (top) and 2-pyridyl acyl azide (bottom). The strong band 2130 cm^{-1} is attributed to the asymmetric stretching vibration of the azide group (bottom).

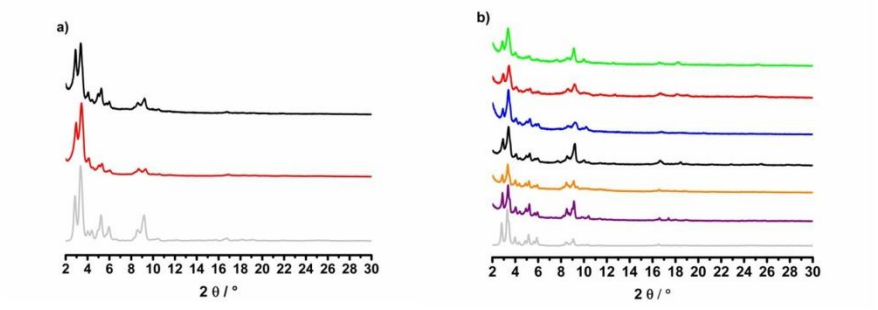

Figure S5: PXRD patterns of a) Al-MIL-101-NH_2 (black), Al-MIL-101-URPy (red) and the simulated pattern of Al-MIL-101 (grey) and of b) DEA-Cr-MIL-101-URPy (green), H_2O-Cr-MIL-101-URPy (red), DEA-Cr-MIL-101-NH_2 (blue), H_2O-Cr-MIL-101-NH_2 (black), DEA-Cr-MIL-101-H (orange), H_2O-Cr-MIL-101-H (violet) and the simulated pattern (grey) obtained from structure data.[4]

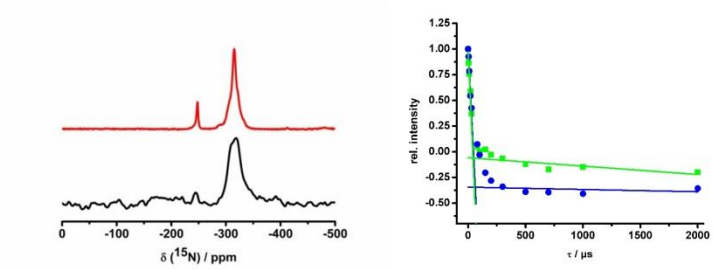

Figure S6: a) ^{15}N CP MAS NMR spectrum of Al-MIL-101-NH_2 (black line) and ^{15}N single pulse (SP) NMR spectrum of Al-MIL-101-NH_2 with 98% abundance of ^{15}N (red line). Both spectra show two signals one at -247 and one at -316 ppm. Based on the SP excitation the intensity ratio was estimated to 5:95.
b) Normalized signal intensities as a function of the inversion time for the signal at -247 ppm (green curve) and for the signal at -316 ppm (blue curve) of the solid-state ^{15}N MAS CPPI spectra of Al-MIL-101-NH_2. The transition points between the fast decaying region (0-200 µs) and the region with the slow decay (300 – 2000 µs) were extrapolated by fitting the trend within both regions with straight lines. The relative intensity at the transition point for a CPPI experiment represents the number of covalently bonded protons attached to one nitrogen atom. The turnover for the signal at -247 ppm occurs at zero while the one for the resonance at -316 ppm takes place at -0.35. The signal at -247 ppm is thus assigned to NH groups, which most probably arise due to a reaction of DMF with the aromatic amino function resulting in NHCHO pending groups. According to the low intensity of the ^{15}N SP NMR spectrum (Figure S6 a) the amount of such units within the final product is below 5%. For the signal at -316 ppm, we observed a turnover typical for NH_2 units and is thus assigned to the aromatic amino function.

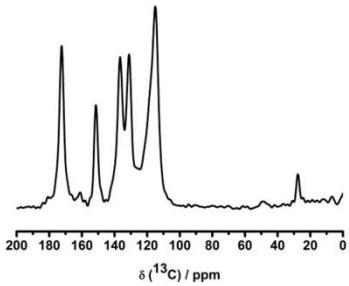

Figure S7: ^{13}C CP MAS spectrum of Al-MIL-101-NH_2 with 98% abundance of ^{15}N.

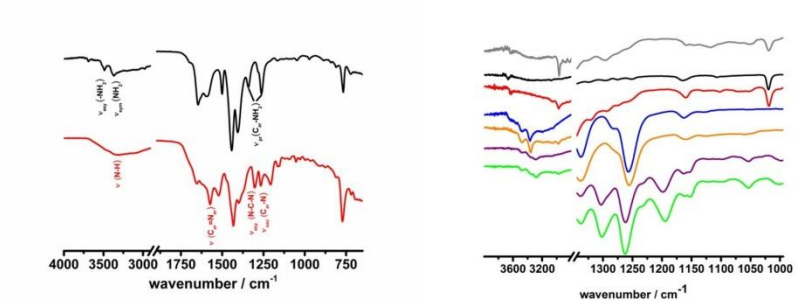

Figure S8: a) ATR-IR spectra of Al-AMIL-101-NH_2 (black line) and Al-MIL-101-URPy (red line); b) ATR-FTIR-spectra from bottom to top: DEA-Cr-MIL-101-URPy (green line), H_2O-Cr-MIL-101-URPy (violet line), DEA-Cr-MIL-101-NH_2 (orange line), H_2O-Cr-MIL-101-NH_2 (blue line), DEA-Cr-MIL-101-H (red line), H_2O-Cr-MIL-101-H (black line) and H_2O-Cr-MIL-101-H (grey line) soaked in diethylamine to evaluate the aliphatic and C-N IR vibrations of non-coordinated diethylamine (grey line). The incorporation of DEA is indicated by the small IR blueshifts of 9 cm^{-1} and 7 cm^{-1} for the aliphatic methylene C-H and C-N stretching vibration bands of coordinated DEA compared to the free ligand (2975 cm^{-1} vs. 2966 cm^{-1} and 1058 cm^{-1} vs. 1051 cm^{-1}, Figure S9b) are in line with the results for other alkyl amines.[2,3,5] In the case of the URPy framework the C-N stretching vibration of DEA is overlaid by the aromatic C-H stretching vibration band at 1053 cm^{-1} of 2-monosubstituted pyridines.[6]

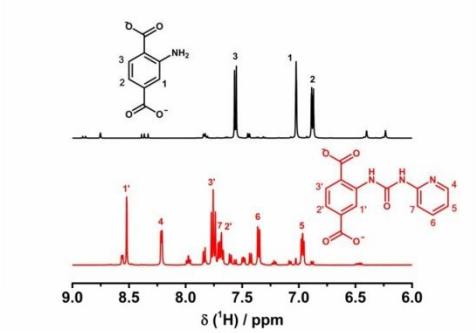

Figure S9: ^{1}H NMR spectra of Al-MIL-101-NH_2 (top) and Al-MIL-101-URPy (bottom) after digestion in 5 wt% of CsF in DMSO-d6/D_2O (5:1) together with the respective signal assignments. The yield of PSM was determined by comparing the integrated areas of the aromatic resonances 1' with 1 of Al-MIL-101-URPy (bottom), representing the ortho-protons of the unmodified and modified linkers relative to the amino and pyridyl urea group, respectively.

Table S1: Al, Cr, C, H, N weight contents and the metal to chloride ratio of Al-MIL-101-NH_2 and Al-MIL-101-URPy, H_2O-Cr-MIL-101-H, DEA-Cr-MIL-101-H, H_2O-Cr-MIL-101-NH_2, DEA-Cr-MIL-101-NH_2, H_2O-Cr-MIL-101-URPy and DEA-Cr-MIL-101-URPy.

	H exp	H theo	C exp	C theo	N exp	N theo	Al/Cr exp	Al/Cr theo	Al/Cr: Cl
Al-MIL-101-NH_2 $Al_3O(H_2O)_2Cl(bdc)_3$	2.79	2.72	42.05	40.88	5.89	5.96	10.87	11.47	3.05:1
Al-MIL-101-URPy (90% URPy) $Al_3O(H_2O)_2Cl(bdc\text{-}NH_2)_{0.3}(bdc\text{-}URPy)_{2.7}$	3.12	2.93	46.63	46.99	10.97	11.51	7.36	7.78	3.05:1
H_2O-Cr-MIL-101-H $Cr_3O(H_2O)_2(OH)_{0.8}(NO_3)_{0.2}(bdc)_3$	2.69	2.34	40.09	39.68	0.38	0.38	22.06	21.47	---
DEA-Cr-MIL-101-H (88% DEA) $Cr_3O(H_2O)_{0.5}(DEA)_{1.76}\text{-}(OH)_{0.8}(NO_3)_{0.2}(bdc)_3$	3.95	4.10	43.85	44.89	3.48	3.22	17.80	18.72	---
H_2O-Cr-MIL-101-NH_2 $Cr_3O(H_2O)_{2.1}Cl_{0.9}(bdc\text{-}NH_2)_3$	2.44	2.49	37.22	37.01	5.32	5.39	18.96	20.02	3.35:1
DEA-Cr-MIL-101-NH_2 (75% DEA) $Cr_3O(H_2O)_{0.85}(DEA)_{1.5}Cl_{0.95}(bdc\text{-}NH_2)_3$	3.73	3.94	41.41	41.56	6.57	6.96	18.71	18.10	3.08:1
H_2O-Cr-MIL-101-URPy (90% URPy) $Cr_3O(H_2O)_{2.04}Cl_{0.96}(bdc\text{-}NH_2)_{0.3}(bdc\text{-}URPy)_{2.7}$	2.81	2.71	43.70	43.42	11.16	10.45	13.65	14.33	3.12:1
DEA-Cr-MIL-101-URPy (90% URPy, 60% DEA) $Cr_3O(H_2O)_{1.05}(DEA)_{1.2}Cl_{0.97}(bdc\text{-}NH_2)_{0.3}(bdc\text{-}URPy)_{2.7}$	3.76	3.63	46.28	45.89	10.97	11.17	13.60	13.49	3.04:1

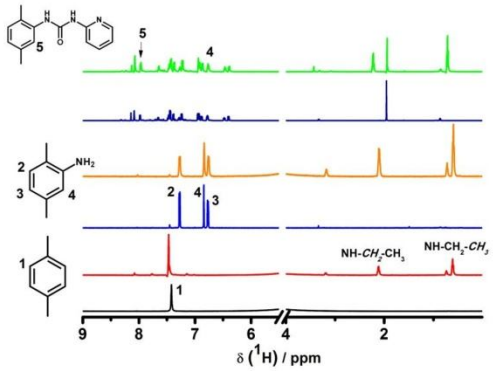

Figure S10: Solution ^{1}H NMR spectra from bottom to top: H_2O-Cr-MIL-101-H (black line), DEA-Cr-MIL-101-H (red line), H_2O-Cr-MIL-101-NH_2 (blue line), DEA-Cr-MIL-101-NH_2 (orange line), H_2O-Cr-MIL-101-URPy (violet line), DEA-Cr-MIL-101-URPy (green line). Due to degradation of the urea pyridine unit in the more basic dissolution medium for the Cr-compounds, the intensities of the 1H NMR spectra for H_2O-Cr-MIL-101-URPy and DEA-Cr-MIL-101-URPy underestimate the degree of the PSM. We thus rely exclusively on the results of the elemental analysis and AAS for quantification for these two cases.

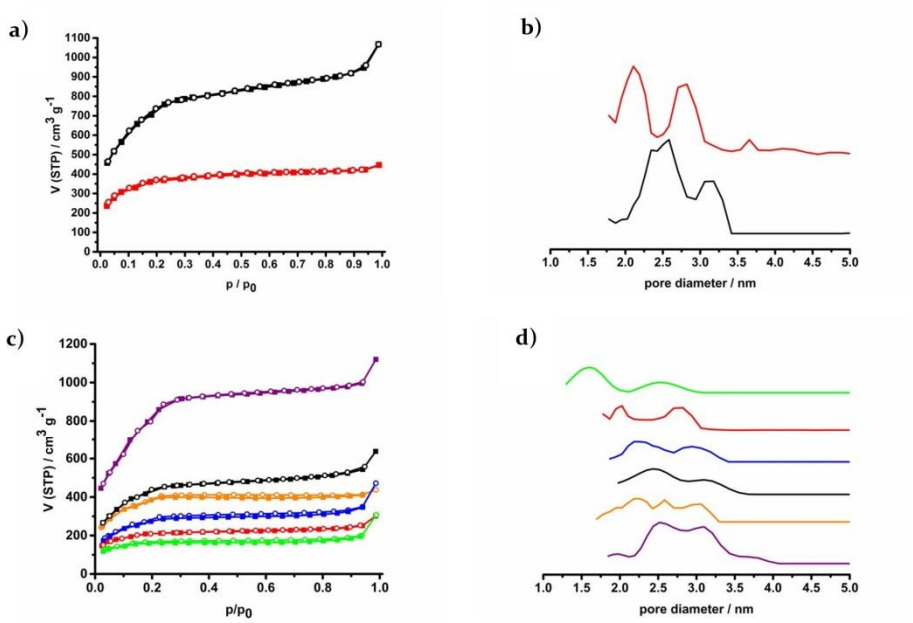

Figure S11: a) N_2 ad- (filled squares) and desorption (empty circles) isotherms at 77 K of Al-MIL-101-NH_2 (black curves) and Al-MIL-101-URPy (red curves); b) NLDFT pore size distribution curves of Al-MIL-101-NH_2 (black curve) and Al-MIL-101-URPy (red curve); c) N_2 ad- (full squares) and desorption isotherms at 77 K (empty circles) of H_2O-Cr-MIL-101-H (violet curves), DEA-Cr-MIL-101-H (orange curves), H_2O-Cr-MIL-101-NH_2 (black curves), DEA-Cr-MIL-101-NH_2 (blue curves), H_2O-Cr-MIL-101-URPy (red curves), DEA-Cr-MIL-101-URPy (green curves); d) NLDFT pore-size distribution curves H_2O-Cr-MIL-101-H (violet curve), DEA-Cr-MIL-101-H (orange curve), H_2O-Cr-MIL-101-NH_2 (black curve), DEA-Cr-MIL-101-NH_2 (blue curve), H_2O-Cr-MIL-101-URPy (red curve), DEA-Cr-MIL-101-URPy (green curve).

Table S2: Apparent BET-surface areas and total pore volumes determined at $p/p_0 = 0.95$ of the Al-MIl-101 Cr-MIL-101 derivatives.

	S_{BET} / $m^2 g^{-1}$	$V_{total\ (p/po\ =\ 0.95)}$ / $cm^3 g^{-1}$
Al-MIL-101-NH_2	2345	1.29
Al-MIL-101-URPy	1325	0.65
H_2O-Cr-MIL-101-H	3011	1.54
DEA-Cr-MIL-101-H	1399	0.64
H_2O-Cr-MIL-101-NH_2	1615	0.84
DEA-Cr-MIL-101-NH_2	1096	0.54
H_2O-Cr-MIL-101-URPy	779	0.39
DEA-Cr-MIL-101-URPy	655	0.31

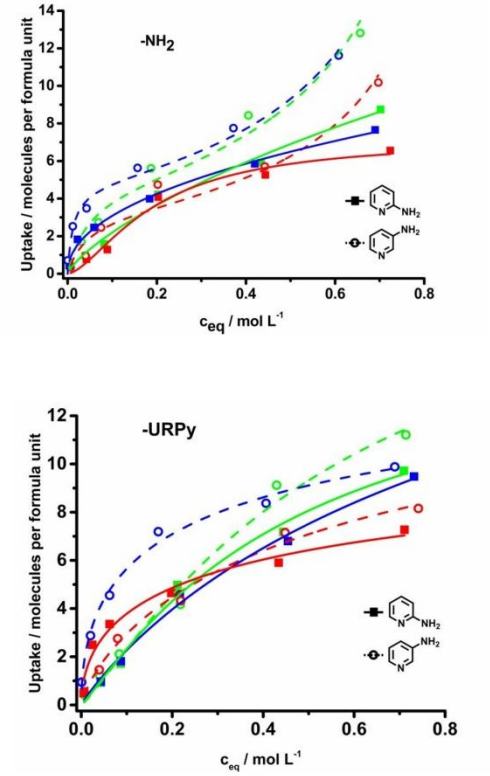

Figure S12: Single adsorption isotherms of 2-AP (solid squares) and 3-AP (empty circles) on a) H_2O-Cr-MIL-101-NH_2 (green curves), DEA-Cr-MIL-101-NH_2 (red curves) and Al-MIL-101-NH_2 (blue curves); b) H_2O-Cr-MIL-101-URPy (green curves), DEA-Cr-MIL-101-URPy (red curves) and Al-MIL-101-URPy (blue curves).

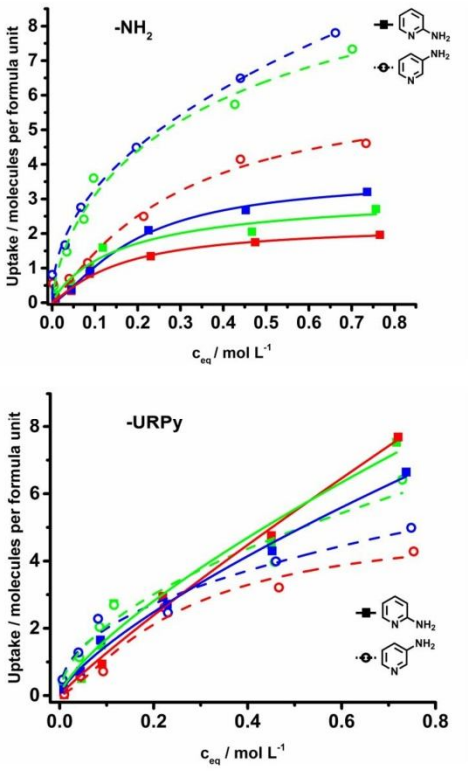

Figure S13: Competitive adsorption isotherms of 2-AP (solid squares) and 3-AP (empty circles) on a) H_2O@Cr-MIL-101-NH_2 (green curves), DEA@Cr-MIL-101-NH_2 (red curves) and Al-MIL-101-NH_2 (blue curves); and b) H_2O@Cr-MIL-101-URPy (green curves), DEA@Cr-MIL-101-URPy (red curves) and Al-MIL-101-URPy (blue curves).

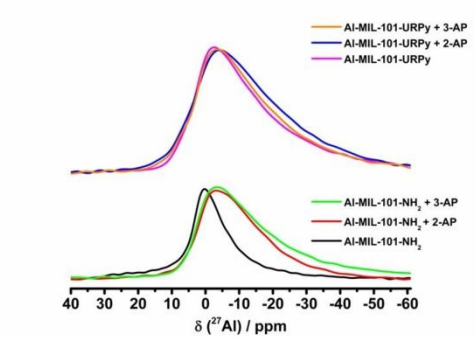

Figure S14: ^{27}Al NMR spectra of Al-MIL-101-NH_2 (black line), 2-AP@Al-MIL-101-NH_2 (red line), 3-AP@Al-MIL-101-NH_2 (green line), Al-MIL-101-URPy (magenta line), 2-AP@Al-MIL-101-URPy (blue line) and 3-AP@Al-MIL-101-URPy (orange line).

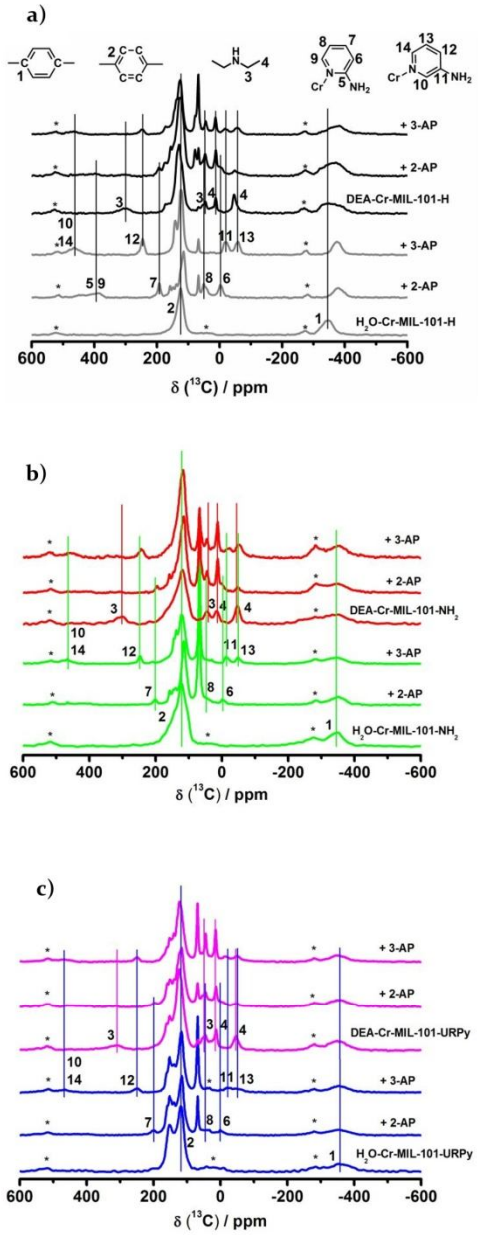

Figure S15: ^{13}C NMR spectra of 2-AP and 3-AP on a) H_2O/DEA-Cr-MIL-101-H, b) H_2O/DEA-Cr-MIL-101-NH_2 and c) H_2O/DEA-Cr-MIL-101-URPy.

Table S3: Comparison of experimental and calculated chemical shifts of Al-MIL-101-URPy, 2-AP@Al-MIL-101-URPy and 3-AP@Al-MIL-101-URPy. All shifts are given in ppm. The calculated shifts are given in color corresponding to the color code used for Figures 5 – 7.

	Assignment	N1	N2	N3	N4	N5
Al-MIL-101-URPy				-273.5	-262.4	-93.1
2-AP		-305.8	-124.2			
3-AP		-326.1	-72.0			
2-AP@Al-MIL-101-URPy	0.05 M	-298.4 / -308.9	-99.4 / -118.6	-272.9	-260.3	-99.4 / -118.6
	0.25 M	-300.2 / -309.5	-115.6 / -134.7	-272.3	-259.5	-115.6 / -134.7
	0.25 M / -25°C	-301.5	-119.9 / -134.7	-271.5	-258.9	-119.9 / -134.7
	DFT calculation	-298.5	-135.6	-272.7	-259.2	-111.8
3-AP@Al-MIL-101-URPy	0.05 M	-314.1 / -322.7	-77.0 / -97.7	-273.4	-261.0	-97.7 / -116.3
	0.25 M	-316.0 / -327.1	-78.3 / -99.0	-273.7	-260.8	-99.0 / -114.2
	0.25 M / -25°C	-315.7 / -323.8	-81.0 to -101.0	-272.3	-260.1	-96.8 / -114.8
	DFT calculation	-315.6	-94.3	-275.3	-254.9	-97.5
	DFT calculation	-324.3	-74.5	-272.8	-264.2	-114.5

References

(1) Wittmann, T.; Mondal, A.; Tschense, C. B. L.; Wittmann, J. J.; Klimm, O.; Siegel, R.; Corzilius, B.; Weber, B.; Kaupp, M.; Senker, J. Probing Interactions of N-Donor Molecules with Open Metal Sites within Paramagnetic Cr-MIL-101: A Solid-State NMR Spectroscopic and Density Functional Theory Study. *J. Am. Chem. Soc.* **2018**, *140*, 2135–2144.

(2) Hwang, Y. K.; Hong, D.; Chang, J.; Jhung, S. H.; Seo, Y.; Kim, J.; Vimont, A.; Daturi, M.; Serre, C.; Férey, G. Amine Grafting on Coordinatively Unsaturated Metal Centers of MOFs: Consequences for Catalysis and Metal Encapsulation. *Angew. Chem. Int. Ed.* **2008**, *47*, 4144–4148.

(3) Wickenheisser, M.; Jeremias, F.; Henninger, S. K.; Janiak, C. Grafting of Hydrophilic Ethylene Glycols or Ethylenediamine on Coordinatively Unsaturated Metal Sites in MIL-100 (Cr) for Improved Water Adsorption Characteristics. *Inorganica Chim. Acta* **2013**, *407*, 145–152.

(4) Lebedev, O. I.; Millange, F.; Serre, C.; Van Tendeloo, G.; Férey, G. First Direct Imaging of Giant Pores of the Metal-Organic Framework MIL-101. *Chem. Mater.* **2005**, *17*, 6525–6527.

(5) Krishnan, K.; Plane, R. A. Raman and Infrared Spectra of Complexes of Ethylenediamine with Zinc(II), Cadmium(II), and Mercury(II). *Inorg. Chem.* **1966**, *5* (4), 852–857.

(6) Socrates, G. *Infrared and Raman Characterisitc Group Frequencies. Tables and Charts*, Third edit.; JOHN WILEY & SONS LTD.: Manchester, 2001.

6.3 Festkörper-NMR-spektroskopische Untersuchung der selektiven Wechselwirkung der anorganischen Baueinheit von paramagnetischen Cr-MIL-101 mit Gastmolekülen

Probing Interactions of N-Donor Molecules with Open Metal Sites within Paramagnetic Cr-MIL-101: A Solid-State NMR Spectroscopic and Density Functional Theory Study

Thomas Wittmann,[a] Arobendo Mondal,[b] Carsten B. L. Tschense,[a] Johannes J. Wittmann,[c] Ottokar Klimm,[d] Renée Siegel,[a] Bjoern Corzilius,[c] Birgit Weber,[d] Martin Kaupp,*,[b] Juergen Senker*,[a]

Erschienen in:

J. Am. Chem. Soc. **2018**, *140*, 6, 2135-2144.

[a] Inorganic Chemistry III, Universitätsstrasse 30, University of Bayreuth, 95447, Bayreuth, Germany

[b] Technical University of Berlin, Institute of Chemistry, Theoretical Chemistry/Quantum Chemistry, Sekr. C7, Straße des17. Juni 135, 10623 Berlin, Germany

[c] Institute of Physical and Theoretical Chemistry and Institute of Biophysical Chemistry, Goethe University Frankfurt, Max-von-Laue-Str. 7-9, 60438 Frankfurt am Main, Germany

[d] Inorganic Chemistry II, Universitätsstrasse 30, University of Bayreuth, 95447, Bayreuth, Germany

* martin.kaupp@tu-berlin, juergen.senker@uni-bayreuth.de

6.3.1 Probing Interactions of N-Donor Molecules with Open Metal Sites within Paramagnetic Cr-MIL-101: A Solid-State NMR Spectroscopic and Density Functional Theory Study

JACS JOURNAL OF THE AMERICAN CHEMICAL SOCIETY
Article
Cite This: J. Am. Chem. Soc. 2018, 140, 2135−2144
pubs.acs.org/JACS

Probing Interactions of N-Donor Molecules with Open Metal Sites within Paramagnetic Cr-MIL-101: A Solid-State NMR Spectroscopic and Density Functional Theory Study

Thomas Wittmann,[†] Arobendo Mondal,[‡] Carsten B. L. Tschense,[†] Johannes J. Wittmann,[§] Ottokar Klimm,[∥] Renée Siegel,[†] Björn Corzilius,[§] Birgit Weber,[∥] Martin Kaupp,*[,‡] and Juergen Senker*[,†]

[†]Inorganic Chemistry III, University of Bayreuth, Universitätsstraße 30, 95447 Bayreuth, Germany
[‡]Institute of Chemistry, Theoretical Chemistry/Quantum Chemistry, Technical University of Berlin, Sekr. C7, Straße des 17. Juni 135, 10623 Berlin, Germany
[§]Institute of Physical and Theoretical Chemistry and Institute of Biophysical Chemistry, Goethe University Frankfurt, Max-von-Laue-Straße 7-9, 60438 Frankfurt am Main, Germany
[∥]Inorganic Chemistry II, University of Bayreuth, Universitätsstraße 30, 95447 Bayreuth, Germany

Supporting Information

ABSTRACT: Understanding host−guest interactions is one of the key requirements for adjusting properties in metal−organic frameworks (MOFs). In particular, systems with coordinatively unsaturated Lewis acidic metal sites feature highly selective adsorption processes. This is attributed to strong interactions with Lewis basic guest molecules. Here we show that a combination of ^{13}C MAS NMR spectroscopy with state-of-the-art density functional theory (DFT) calculations allows one to unravel the interactions of water, 2-aminopyridine, 3-aminopyridine, and diethylamine with the open metal sites in Cr-MIL-101. The ^{13}C MAS NMR spectra, obtained with ultrafast magic-angle spinning, are well resolved, with resonances distributed over 1000 ppm. They present a clear signature for each guest at the open metal sites. Based on competition experiments this leads to the following binding preference: water < diethylamine ≈ 2-aminopyridine < 3-aminopyridine. Assignments were done by exploiting distance sum relations derived from spin−lattice relaxation data and $^{13}C\{^1H\}$ REDOR spectral editing. The experimental data were used to validate NMR shifts computed for the Cr-MIL-101 derivatives, which contain Cr_3O clusters with magnetically coupled metal centers. While both approaches provide an unequivocal assignment and the arrangement of the guests at the open metal sites, the NMR data offer additional information about the guest and framework dynamics. We expect that our strategy has the potential for probing the binding situation of adsorbate mixtures at the open metal sites of MOFs in general and thus accesses the microscopic interaction mechanisms for this important material class, which is essential for deriving structure−property relationships.

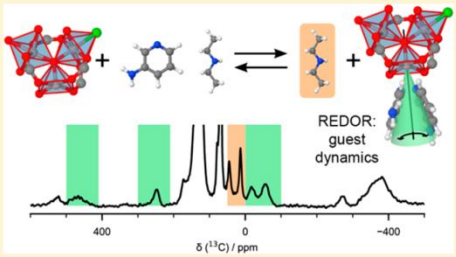

INTRODUCTION

The targeted design of MOFs with chemical functionalities promise advanced applications in the fields of molecular separation[1] and recognition,[2,3] catalysis,[4−6] and drug delivery.[7−9] Such applications crucially rely on selective interactions between the target molecules and the host. Depending on the MOF topology, these interactions are mediated either by the organic linkers[2,10,11] or by strong coordinative interactions between Lewis acidic metal sites and Lewis basic guests.[12−14] Among the latter, aromatic N-heterocyclic compounds like indole,[15−17] carbazole,[15,16] and quinoline[18] derivatives with sizes comparable to the upper limit of micropores (<2 nm) belong to the most environmentally harmful molecules which are, nevertheless, natural components of liquid fuels, petroleum, and refinery streams.[12,13,15,19] Their combustion produces NO_x radicals and contributes to acid rain.[13,19] Considerable effort was made on the removal of such molecules from liquids, in particular with MOFs featuring coordinatively unsaturated metal sites (CUS).[15−20]

Several studies suggest that indeed the formation of coordinative bonds between the CUS and the guest molecules[15,17,18,20] is responsible for the strong adsorption affinities. Adsorption isotherms, calorimetric measurements,

Received: September 22, 2017
Published: January 9, 2018

DOI: 10.1021/jacs.7b10148
J. Am. Chem. Soc. 2018, 140, 2135−2144

and thermogravimetric experiments coupled to an infrared (IR) or a mass spectrometer allow for the determination of adsorption enthalpies and binding preferences.[15,17,19] By combination of microscopic techniques like fluorescence,[21] UV−vis,[22] and Raman/IR[23] spectroscopy as well as solid-state NMR spectroscopy on diamagnetic MOFs,[24,25] considerable progress was made on unraveling active binding sites, and first insights into the microscopic interaction mechanism were provided.

Various MOF types with CUS host paramagnetic transition metal cations like Cu^{2+} in HKUST-1,[26] Ni^{2+} and Co^{2+} in CPO-27,[15,27] and Cr^{3+} and Fe^{3+} in MIL-100[28] and MIL-101.[7,29] Here we show that for adsorption processes involving CUS in such systems, ssNMR studies offer additional insight. While paramagnetic NMR spectroscopic studies on MOFs are still rare, the method is well developed for structure determination of biomolecules in the liquid state.[30−35] Guest molecules coordinated at the CUS will experience large hyperfine shifts leading to differences of several hundreds of ppm compared to non-coordinated and diamagnetic guest molecules.[36] While individual resonances might be severely broadened, large shift dispersions still result in excellent resolution. Even for guest molecules coordinating to the CUS via similar chemical functionalities, we expect pronounced differences, which are only slightly influenced by local static or dynamic disorder. Additionally, it should be possible to distinguish species directly coordinated to the CUS and physisorbed in the periphery of the framework. This helps determining and separating various active binding sites, as well as to derive binding affinities to the CUS, leading to an improved understanding of host−guest interactions, in particular for competitive adsorption processes in the future.

Our analysis benefits from very fast magic angle spinning,[37] which makes proton broadband decoupling unnecessary and enhances the sensitivity due to suppression of spinning sideband intensities. For the assignment of ^{13}C MAS NMR spectra, we present two different but equivalent approaches. The signals might be assigned either experimentally via a combination of spin−lattice relaxation and REDOR (rotational echo double resonance) experiments,[37−39] or by state-of-the-art DFT cluster calculations of the NMR shifts that not only include all contributions to orbital, contact, and pseudo-contact shifts but also account for the magnetic couplings between the paramagnetic metal sites within the Curie−Weiss regime.[40] While the NMR strategy is generally applicable as long as the materials remain paramagnetic, the theory for calculating hyperfine shifts in magnetically frustrated systems is new and still needs to be validated against experimental data. Both strategies avoid isotope labeling,[41] which is usually expensive and not generally possible for all guests. Based on the assignment, the observed intensity modulations by the REDOR sequence provide information about the local reorientational disorder of guest molecules and framework.[42−44]

The expressiveness of this strategy is demonstrated on the model system Cr-MIL-101,[29] which was treated with solutions of diethylamine (DEA), 2-aminopyridine (2-AP), and 3-aminopyridine (3-AP) as well as binary mixtures thereof. The inorganic building unit (IBU) of Cr-MIL-101[29] consists of Cr_3O clusters, where two out of three Cr^{3+} cations exhibit an accessible CUS. The NMR shifts derived from ^{13}C MAS NMR spectra were interpreted in terms of binding sites and adsorption preferences.

THEORETICAL BACKGROUND

The theoretical description of the nuclear shielding tensor is based, with one small modification, on a modern quantum-chemical implementation[45] of Kurland−McGarvey theory,[46] which derives the pNMR shift tensor from EPR spin Hamiltonian parameters (**g**, hyperfine coupling (HFC), and zero-field splitting (ZFS) tensors). The shielding tensor is then given as[45,47−50]

$$\boldsymbol{\sigma}^I = \boldsymbol{\sigma}^I_{\mathrm{orb}} - \frac{\mu_B}{\hbar\gamma_I k}\left\{\frac{1}{T-\Theta}\right\}\mathbf{g}\cdot\langle\mathbf{SS}\rangle\cdot\mathbf{A}^I \tag{1}$$

$$\langle\mathbf{SS}\rangle = \frac{\sum_{nm} Q_{mn}\langle n|\mathbf{S}|m\rangle\langle m|\mathbf{S}|n\rangle}{\sum_n \exp(-E_n/kT)} \tag{2}$$

$$Q_{mn} = \begin{cases} \exp\left(-\dfrac{E_n}{kT}\right), & E_n = E_m \\ -\dfrac{kT}{E_m - E_n}\left[\exp\left(-\dfrac{E_m}{kT}\right) - \exp\left(-\dfrac{E_n}{kT}\right)\right], & E_n \neq E_m \end{cases} \tag{3}$$

where $\boldsymbol{\sigma}_{\mathrm{orb}}$ is the orbital shielding tensor, μ_B the Bohr magneton, k the Boltzmann constant, $\hbar$ the reduced Planck constant, γ_I the nuclear gyromagnetic ratio of nucleus I, T the absolute temperature, Θ the Weiss constant, **g** the electronic g-tensor of the system, and $\mathbf{A}^I$ the HFC tensor of nucleus I. $\langle\mathbf{SS}\rangle$ is a spin dyadic with the components $\langle S_\epsilon S_\tau\rangle$ evaluated in the manifold of eigenstates $|n\rangle$, with the eigenenergies E_n, of the ZFS Hamiltonian.[45,48] Further details for eq 1, including the role of the Weiss constant in the temperature denominator, are given in the Supporting Information. From the shielding tensor, the isotropic shift is derived by eq 4,

$$\delta_{\mathrm{iso}} = \sigma_{\mathrm{ref}} - \frac{1}{3}\mathrm{Tr}[\boldsymbol{\sigma}^I] \tag{4}$$

where σ_{ref} is the isotropic shielding constant of a diamagnetic reference compound and $\mathrm{Tr} = \sigma_{xx} + \sigma_{yy} + \sigma_{zz}$. δ_{iso} includes the Ramsey-type orbital shift (orb), the Fermi-contact (FC), and the pseudo-contact (PC) contributions to the isotropic shift (eq 5):

$$\delta_{\mathrm{iso}} = \delta_{\mathrm{orb}} + \delta_{\mathrm{FC}} + \delta_{\mathrm{PC}} \tag{5}$$

The hyperfine interaction also leads to a shortening of spin−lattice (T_1) and spin−spin (T_2) relaxation times.[31,36,51] The small T_2 and the anisotropic part of the bulk magnetic susceptibility, which is not completely removed by magic-angle spinning, are the main reasons for signal broadening of paramagnetic compounds.[31,52,53] The observed spin−lattice relaxation rates of nuclei in paramagnetic solids probed at high fields are usually dominated by the paramagnetic dipolar relaxation rate, since the Fermi contact contribution becomes negligible due to its dependence of the electronic Larmor frequency (eq S2). $T_1^{\mathrm{para,dipolar}}$ depends on the distance r and on the electron-correlation time τ_s (eqs S3 and S8). Since τ_s only depends on the transition between the electron Zeeman levels, it is considered to be constant for each metal ion independent from the coordinated ligands. The observed relaxation rate $1/T_1^{\mathrm{para}}$ for a specific nucleus is then given by eq 6,

DOI: 10.1021/jacs.7b10148
J. Am. Chem. Soc. 2018, 140, 2135−2144

$$\frac{1}{T_1^{\text{para}}} = \sum_{i=1}^{N} \frac{1}{T_1^{\text{Cr}^i}} = \sum_{i=1}^{N} \frac{\text{const}}{r_{M^i}^6} = \text{const} \cdot \sum_{i=1}^{N} \frac{1}{r_{M^i}^6} = \text{const} \cdot R \tag{6}$$

where R is the distance sum to all paramagnetic centers M^i in its neighborhood. As a consequence, the ratio of the spin−lattice relaxation rates for the two resonances, ref and x, depends only on the ratio of the distance sums R for the corresponding nuclei (eq 7). This will be used as a cost function to rank structure models derived from quantum-chemical calculations (a more detailed discussion is given in the Supporting Information).

$$R_x = \frac{T_1^{\text{ref}}}{T_1^x} R_{\text{ref}} \tag{7}$$

■ RESULTS AND DISCUSSION

Characterization of X@Cr-MIL-101. Synthesis and activation of H_2O@Cr-MIL-101 and DEA@Cr-MIL-101 were performed according to modified literature procedures starting from $Cr(NO_3)_3 \cdot 9H_2O$ and benzene-1,4-dicarboxylic acid (bdc).[54] Subsequently, H_2O@Cr-MIL-101 and DEA@Cr-MIL-101 were grafted with 2-aminopyridine (2-AP) and 3-aminopyridine (3-AP) by equilibrating the activated MOFs with 0.25 M 1,4-dioxane solutions. This concentration guarantees sufficiently high loadings to occupy all favored adsorption sites without completely filling the pores.

All samples have been characterized by powder X-ray diffraction, elemental analysis including atomic absorption spectroscopy, IR spectroscopy, nitrogen physisorption, and solution ^{1}H NMR spectroscopy after digestion of the products. In all cases the integrity of the MIL-101 framework[11,55] remains intact. The incorporation of DEA, 2-AP, and 3-AP is demonstrated by the appearance of their characteristic stretching vibration bands.

The derived stoichiometries (Table 1) prove that water can be replaced by DEA, 2-AP, and 3-AP. However, for DEA@Cr-MIL-101 an equivalent of 0.5 water molecules remain in the formula unit while an equivalent of 1.76 DEA molecules is adsorbed. While activated Cr-MIL-101 takes up 3.5 and 4.5 equiv of 2-AP and 3-AP, respectively, the samples blocked with DEA adsorb significantly less 2-AP (1.8 equiv) and 3-AP (3.4 equiv). The amount of incorporated DEA remains constant even after exchanging with 2-AP and 3-AP. Interestingly, the total amount of adsorbed guest molecules (H_2O, DEA, 2-AP, and 3-AP) exceeds the number of available CUS (two out of three Cr^{3+} cations), indicating that for all samples both coordinated and non-coordinated guests are present. The reduction of the apparent BET surface areas, which is roughly halved from H_2O@Cr-MIL-101 (~3000 $m^2\ g^{-1}$) to 3-AP+DEA@Cr-MIL-101 (~1687 $m^2\ g^{-1}$), and the decrease of the pore sizes by ca. 0.5 nm seem to correlate with the amount of adsorbed guest molecules, which increases from DEA over 2-AP, 3-AP, and DEA + 2-AP to DEA + 3-AP (Table 1). Further details of the basic characterization are given in the Supporting Information.

Table 1. Determined Formula Units of the Compounds X@Cr-MIL-101, with X = H_2O, 2-AP, 3-AP, DEA, 2-AP + DEA, and 3-AP + DEA

X	formula unit
H_2O	$Cr_3O(H_2O)_2(OH)_{0.8}(NO_3)_{0.2}(bdc)_3$
DEA	$Cr_3O(H_2O)_{0.5}(DEA)_{1.76}(OH)_{0.8}(NO_3)_{0.2}(bdc)_3$
2-AP	$Cr_3O(2\text{-AP})_{3.5}(OH)_{0.8}(NO_3)_{0.2}(bdc)_3$
3-AP	$Cr_3O(3\text{-AP})_{4.5}(OH)_{0.8}(NO_3)_{0.2}(bdc)_3$
2-AP + DEA	$Cr_3O(2\text{-AP})_{1.8}(DEA)_{1.75}(OH)_{0.8}(NO_3)_{0.2}(bdc)_3$
3-AP + DEA	$Cr_3O(3\text{-AP})_{3.4}(DEA)_{1.75}(OH)_{0.8}(NO_3)_{0.2}(bdc)_3$

The magnetic susceptibility χ was measured exemplarily for H_2O@Cr-MIL-101 (Figure S7) as a function of temperature and modeled with a Bleany−Bowers equation consisting of only one coupling constant $J = -13\ cm^{-1}$ (eq S7). The excellent match indicates that the three Cr^{3+} ions form an equilateral triangle ($J = J_{12} = J_{23} = J_{13}$). The g-value of 1.985 matches the one derived from EPR data and DFT calculations (Figure S6, Tables S3 and S4), and the fraction α of isolated Cr^{3+} ions is below 5%. $\chi^{-1}(T)$ above 50 K (Figure S7) obeys the Curie−Weiss law with an effective magnetic moment μ_{eff} of 3.566 μ_B per Cr^{3+} and a Weiss temperature θ of −102 K. μ_{eff} is lowered compared to the "spin-only" value for Cr^{3+} ($\mu_{\text{eff}} = 3.87\ \mu_B$), which agrees well with values observed for isolated Cr_3O clusters.[56] These results hint to an antiferromagnetic interaction between the three Cr^{3+} ions at low temperatures, mediated via a superexchange through the μ_3-oxygen atom and to a lower extent by the carboxylate groups, which each bridge two Cr^{3+} ions.[57,58]

^{13}C MAS NMR Spectroscopy of X@Cr-MIL-101. *Single Adsorption of N-Donor Compounds.* The ^{13}C NMR spectra of H_2O@Cr-MIL-101, 2-AP@Cr-MIL-101, 3-AP@Cr-MIL-101, and DEA@Cr-MIL-101 (Figure 1, right column) exhibit resonances in the typical diamagnetic shift region (0−180 ppm). In addition, hyperfine shifts are observed with positive (180−500 ppm) and negative (−380−0 ppm) signs. For each isotropic resonance, a maximum of two weak spinning sidebands is observed at a spinning speed of 40 kHz, indicating that the magnitude of the anisotropy of the hyperfine shift is below 250 ppm for all observed resonances. Similarly, the ^{1}H anisotropic hyperfine shifts were estimated to 200−240 ppm (Table S6). Such moderate anisotropies suggest a significant flexibility of the bdc units and the adsorbed guest molecules, also explaining the quite narrow signals. Combined with the short spin−lattice times, which allow for very fast sampling, and ultrafast magic angle spinning, spectra with an excellent resolution could be obtained in a reasonable period of time.

Nevertheless, since the classic correlations between shift and chemical fragment are established for diamagnetic compounds only, additional information is needed to assign the ^{13}C MAS spectra. Here we present a strategy based on the combined use of distance relations derived from spin−lattice relaxation experiments[38] and spectral editing relying on a heteronuclear ^{13}C−^{1}H dipolar dephasing induced with a REDOR experiment.[37,39] While most of the resonances can already be assigned by matching experimental distance sums R_x derived from the T_1 ratios (eq 7) to the ones (R_{DFT}) calculated for characteristic structural fragments, the ^{13}C{^{1}H} REDOR data provide complementary information by discriminating between resonances according to the numbers of protons attached to the carbon atoms responsible for the targeted signal.

Even more importantly, deviations between the experimentally observed and expected dephasing values for rigid C, CH, CH_2, and CH_3 units are unequivocally caused by dynamic reorientational processes since the strength of the dipolar coupling between a carbon atom and its covalently bonded protons is well-known and relatively independent of the local structural properties. Reductions of the expected CH and CH_2

DOI: 10.1021/jacs.7b10148
J. Am. Chem. Soc. 2018, 140, 2135−2144

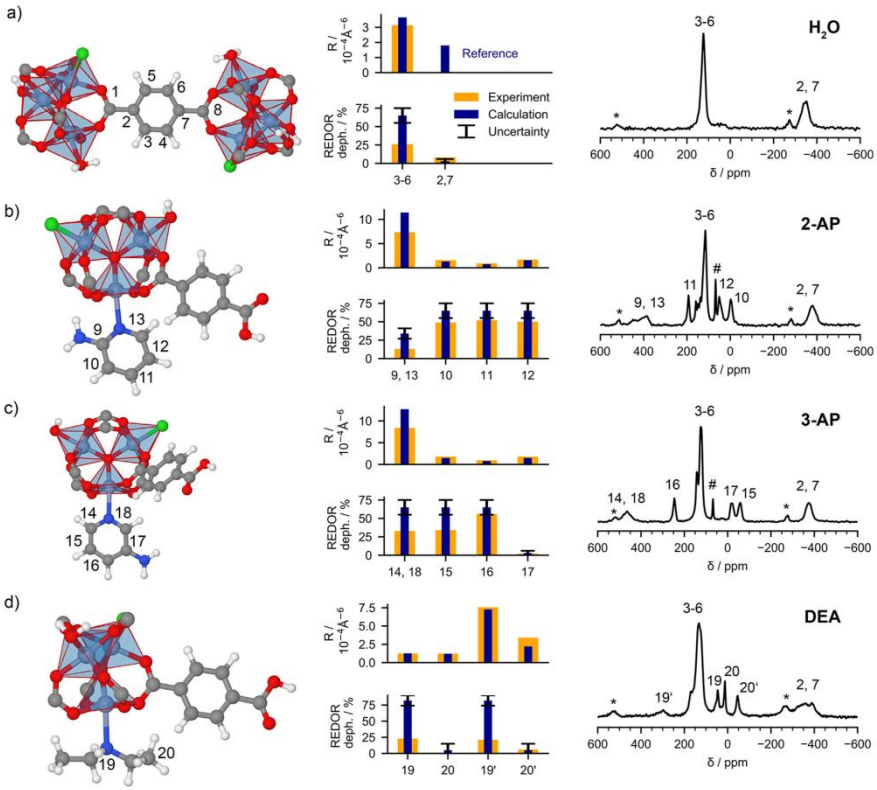

Figure 1. DFT-optimized structural fragments (left column). Comparison between experimental and calculated distance sums and $^{13}C\{^1H\}$ REDOR dephasing values (middle column) and ^{13}C MAS NMR spectra (right column) of (a) H_2O@Cr-MIL-101, (b) 2-AP@Cr-MIL-101, (c) 3-AP@Cr-MIL-101, and (d) DEA@Cr-MIL-101 including assignment. 1,4-Dioxane could be easily removed by evaporation in vacuum, and only traces remain. Key: #, ^{13}C signal of the solvent 1,4-dioxane; *, spinning side bands.

coupling constants have been frequently used to identify motional processes in the past.[42−44] Such analyses provide similar results compared to ^2H NMR studies in the fast motion limit and avoid chemical labeling. We make use of this within our strategy not only to get insight into the preferred adsorption sites and their structural build-up but also to derive a reasonable picture of the local dynamics at the adsorption sites.

For H_2O@Cr-MIL-101, 2-AP@Cr-MIL-101, 3-AP@Cr-MIL-101, and DEA@Cr-MIL-101, we extracted structural fragments (Figures 1 and S8) from the framework, large enough to allow for the calculation of the distance sums R_{DFT} (eq 6) between the Cr^{3+} cations of the IBU and the carbon atoms of both the bdc linkers and the adsorbed molecules, but still small enough to allow for fast structure optimizations at DFT level. The adsorbate molecules were placed at the CUS of the IBU with their Lewis basic centers bonded to the Lewis acidic Cr^{3+} ions and relaxed freely. The calculated distance sum R_{DFT} of one carbon atom was chosen as reference R^{ref}_{DFT}. All the other R_{DFT} values for the other carbon atoms were then compared to the experimental ones (R_x) derived from the ratio of the spin−lattice relaxation times for the reference signal T_1^{ref} and the targeted resonance T_1^x as given in eq 7.

For the reference, we chose the signal at −350 ppm, since it is well separated from any other observed resonance and is present in all four compounds. It exhibits a very small intensity reduction in the $^{13}C\{^1H\}$ REDOR spectra well below 10% (Figures 1 middle column and S9) and thus originates from the quaternary carbon atoms **1,8** or **2,7** of the bdc linkers. When assigning the atoms **1,8** to the reference signal at −350 ppm, R^{ref}_{DFT} calculates to 30.3×10^{-4} Å^{-6} for H_2O@Cr-MIL-101. Using eq 7, R_x for the second observed signal at 130 ppm is calculated based on T_1 (Table S5) to 17.4×10^{-4} Å^{-6}, which is 1 order of magnitude larger compared to the R_{DFT} values for carbon atoms **3−6** and **2,7** (Figure 1 middle column). In contrast, when assigning carbon atoms **2,7** to the reference signal ($R^{ref}_{DFT} = 3.66 \times 10^{-4}$ Å^{-6}), R_x(130 ppm) is 2.10×10^{-4} Å^{-6}, which matches the expectation of $R_{DFT} = 1.80 \times 10^{-4}$ Å^{-6} for the aromatic CH units of the bdc linkers. This assignment is furthermore, supported by the stronger intensity reduction

DOI: 10.1021/jacs.7b10148
J. Am. Chem. Soc. 2018, 140, 2135−2144

within the $^{13}C\{^1H\}$ REDOR spectra, suggesting proton bearing carbon atoms.

The assignment for 2-AP@Cr-MIL-101, 3-AP@Cr-MIL-101, and DEA@Cr-MIL-101 was done in a similar way, and the result is summarized in Figure 1. Additionally, a full list of spin−lattice relaxation times and experimental distance sums is given in Table S5 together with the calculated R_{DFT} values obtained from the model fragments. The general agreement between R_{exp} and R_{DFT} is very good with the exception of the carbon atoms closest to the paramagnetic centers. Examples are the ortho carbon atoms **9**,**13** of 2-AP as well as **14**,**18** of 3-AP. With the exception of meta carbon atoms **15**,**17** for 3-AP@Cr-MIL-101, the T_1 data are decisive enough to assign all resonances. However, for the latter case the intensity modulation of the $^{13}C\{^1H\}$ REDOR spectra allowed to distinguish between the C−NH_2 and C−H units unambiguously.

For DEA two different adsorbate species could be distinguished. While the distance sums for the resonances at 300 and −46 ppm hint to DEA molecules (**19**′, **20**′) coordinated to the CUS, the significantly smaller R values for the signals **19** and **20** at the typical diamagnetic shifts of DEA indicate additional physisorbed DEA species in a second coordination sphere. Taking into account the results of the chemical analysis (Table 1), the CUS are probably occupied by the remaining 0.5 water molecules, and only 1.5 equiv are saturated with DEA molecules. This leaves an equivalent of residual 0.26 DEA molecules uncoordinated but still close to the IBU.

In particular, for 3-AP, DEA, and the bdc linkers, the intensity reduction of the signals for the CH and CH_2 units within the $^{13}C\{^1H\}$ REDOR spectra is considerably less pronounced as expected for rigid CH_x fragments (Figure 1, middle column). The predicted dephasing values were derived using a diamagnetic model system by simulating the intensity reductions for a dephasing time τ_{deph} as short as one rotor period based on the spin-density matrix[59] approach. The effect of the hyperfine interaction during τ_{deph} and the hard 180° pulses on the carbon-13 and proton channels were modeled by treating the anisotropic part of the hyperfine interaction as chemical shift anisotropy. The corresponding coupling constants δ_{hyper} for ^{13}C (Figure 1 right column) and ^1H (Figure S10) were estimated based on spinning sideband intensities of the MAS spectra (a more detailed description is given in the Supporting Information).

For the presented analysis, we used a REDOR sequence with conventional 180° pulses, instead of more advanced recoupling and polarization transfer schemes[60−62] relying on adiabatic pulses. On the one hand, due to the inherent flexibility of the X@Cr-MIL-101 compounds the observed δ_{hyper} are relatively small, allowing for a sufficiently homogeneous excitation with short and hard 180° pulses. On the other hand, adiabatic 180° pulses are inevitably on the same order as τ_{deph} when using ultrafast MAS to match the adiabaticity condition, which makes simulations more demanding and might complicate the extraction of dynamical information from the observed intensity reductions. A detailed description of the model system and the simulations is given in the Supporting Information. Summarizing, without dynamic disorder, we expect intensity reductions of well below 10% for C and CH_3 units and around 65% as well as 80% for CH and CH_2 units, respectively, for the experimentally used conditions of the $^{13}C\{^1H\}$ REDOR experiments (Table S7). Please note that we allow for a variation of roughly 10% for the expected intensity reductions to account for structural changes for the targeted materials and finite size effects within the simulations.

Large deviations between the observed and simulated intensity reductions must be caused by fast large-angle reorientations of guest molecules and bdc linkers, since they are the only motional processes, which influence the dephasing enough on the order of a few tens of μs. To keep the models as simple as possible, we used simple reorientational jump models adapted to the local environment and symmetry to calculate the reduced dipolar coupling constants for the C−H bonds of CH and CH_2 units, following strategies given in refs 37 and 39. The coupling constants were then fed back into the REDOR simulations to derive the dephasing under the influence of motion. We observed that only specific jump models match the observed and calculated dephasing values (Figure 2).

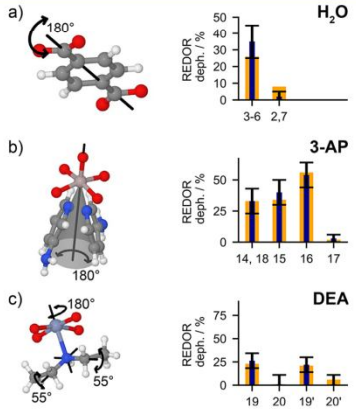

Figure 2. Sketch of the large-angle reorientational jump models (left) used to match the intensity reductions of the $^{13}C\{^1H\}$ REDOR spectra for (a) H_2O@Cr-MIL-101, (b) 3-AP@Cr-MIL-101, and (c) DEA@Cr-MIL-101.

For H_2O@Cr-MIL-101, a fast 180° reorientational jump of the bdc linkers around their C_2 axis reduces the REDOR dephasing of 65% for rigid CH units of the benzene ring to 35% (Figures S16 and S17). We take into account that this process will be accompanied by an additional librational motion reducing the dephasing even further. The match with the experimentally observed dephasing of 26% (Figure 2a) is sound and thus strong evidence that this process is activated and fast at room temperature. Indeed, 180° jumps of the bdc linkers have been observed for various MOFs,[63,64] but were not reported for H_2O@Cr-MIL-101 up to now. For 3-AP only a uniaxial 180° jump of the pyridine ring about the N−Cr bond axis overlaid with a small librational toggling motion on a cone with a half opening angle of 20° (Figure 2b) accounts for the different effect on the CH units in ortho/meta positions (**14**, **15**, **18**) with respect to the one in para position (**16**). In contrast, the steric demand of the ortho amino group in the case of 2-AP hinders both 90° and 180° jumps around the N−Cr axis. Deviations between simulated and observed REDOR dephasings are much less pronounced (Figure 1b middle column) compared to the other guest molecules and are well

DOI: 10.1021/jacs.7b10148
J. Am. Chem. Soc. 2018, 140, 2135−2144

accounted for by small-angle librations. For DEA two large-angle reorientations are necessary to match the simulated and observed intensity reductions within the $^{13}C\{^1H\}$ REDOR spectra. The first is a 180° jump around the N−Cr axis combined with a reorientation of the CH_2 units around the C−N bond with an amplitude of about 55° (Figure 2c), reflecting the high flexibility of the aliphatic amine compared to the aromatic counterparts 2-AP and 3-AP.

For systems with isolated paramagnetic centers, quantum-chemical shift calculations provide an alternative route to a spectral assignment, and they provide further microscopic insight.[65−69] The applicability of eq 1, that includes the Weiss constant to account for residual magnetic couplings in the Curie−Weiss temperature regime for spin-coupled clusters (see refs 40 and 72 for related applications to solid-state calculations), still needs careful validation, which is possible with due to the available experimental NMR data. We thus applied the full formalism of eq 1 at DFT level (cf. Experimental Section and Supporting Information) to the structural fragments displayed in Figure 1 and compared the results with the experimental assignment. While we have computed all terms in eq 1, in the following the main discussion will focus only on the FC contributions. The reason is that our computations confirm the expectation of small g- and ZFS-anisotropies (see g-tensor and ZFS data in Tables S3 and S4, which are in perfect agreement with the measured EPR spectrum, Figure S6). As a consequence, the PC contributions to the isotropic ^{13}C shifts (Table 2 and S8) are small. The observed and calculated ^1H shifts are shown in Figure S18 and Table S9. The orbital shifts reflect the chemical environment of the nucleus in question in a similar way as for diamagnetic analogues (Tables S8 and S9) and will also not be discussed in detail.

The total computed ^{13}C shifts given in Table 2 and S8 do thus reflect particularly the FC contribution and therefore the delocalization of spin density over the ligand framework, as well as to some extent spin polarization effects. The sign and magnitude of the computed ^{13}C (Table 2 and S8) and ^1H (Table S9) hyperfine shifts agree well with experimental data, and the computed data have been helpful in the signal assignment. Notably, the reduction of hyperfine shifts due to the Curie−Weiss regime by a factor $T/(T-\Theta) = 0.761$ for H_2O@Cr-MIL-101 brings computed and experimental shifts into significantly better agreement. We used the experimentally determined reduction factor for all X@Cr-MIL-101 derivatives, since we do not expect large differences for their magnetic susceptibilities compared to the one of H_2O@Cr-MIL-101. This assumption is based on the magnetic properties for molecular compounds with isolated Cr_3O clusters with H_2O and pyridine-based ligands.[57,58,71] The corresponding exchange constants are similar to the one observed for H_2O@Cr-MIL-101 and vary only between 10 and 13 cm^{-1}. Additionally, for a simulation temperature of 325 K, a change of Θ by 20 K only affects the hyperfine shifts by less than 5%. We note that the negative deviations of the g-tensor from the free-electron value only reduce the computed shifts additionally by about 1%.

The shifts may be rationalized to a great extent by the spin-density plots for the cluster models (Figure 3). For H_2O@Cr-MIL-101, ^{13}C nuclei **1**−**8** split into two sets: carbons **2** and **7** have negative spin densities, while the others exhibit positive spin densities. 2-AP@Cr-MIL-101 and 3-AP@Cr-MIL-101 exhibit additionally alternating positive and negative spin densities within the aminopyridine ring. For carbon atoms **9**−**18** we may distinguish negative spin densities for atoms **10**,

Table 2. Comparison of Observed and Calculated Isotropic and Hyperfine ^{13}C Shifts, δ_{iso} (δ_{FC}), for X@Cr-MIL-101[a]

	^{13}C δ_{iso} (δ_{FC})/ppm	
signal	obsd	calcd
	X = H_2O	
1,8	–	1683 (+1503)
2,7	−350 (−523)	−411 (−552)
3,4,5,6	130 (−5)	129 (−6)
	X = 2-AP	
9	415 (+251)	396 (+231)
10	−4 (−116)	−34 (−145)
11	192 (+46)	235 (+89)
12	49 (−65)	−12 (−126)
13	415 (+251)	444 (+288)
	X = 3-AP	
14	468 (+324)	457 (+314)
15	−59 (−187)	−127 (−255)
16	246 (+121)	290 (+165)
17	−20 (−167)	−80 (−227)
18	468 (+324)	459 (+317)
	X = DEA	
19	47	52
20	13	18
19′	300 (+248)	246 (+194)
20′	−46 (−59)	0 (−18)

[a]Detailed analyses in terms of δ_{orb}, δ_{FC}, and δ_{PC} are given in Table S8.

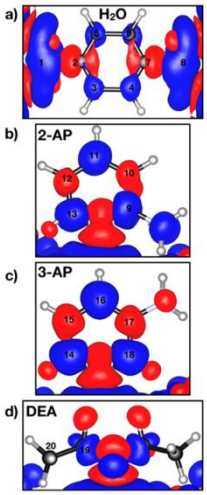

Figure 3. Spin-density plots of (a) H_2O@Cr-MIL-101, (b) 2-AP@Cr-MIL-101, (c) 3-AP@Cr-MIL-101, and (d) DEA@Cr-MIL-101. The blue and red colors represent positive and negative spin-density isosurfaces (±0.0001 au), respectively.

DOI: 10.1021/jacs.7b10148
J. Am. Chem. Soc. 2018, 140, 2135−2144

12, **15**, and **17**, and positive spin densities for the remaining atoms. For DEA@Cr-MIL-101, carbons **19′** and **20′** for the DEA molecules attached to the CUS have positive and negative spin densities, respectively, while the non-coordinated ones (carbons **19** and **20**) exhibit the diamagnetic shifts only.

In all cases, the sign of the assigned hyperfine shifts (see Table 2) agrees perfectly with these spin-density analyses. We note that the extremely large positive spin densities at the carboxyl carbon atoms **1** and **8** in H_2O@Cr-MIL-101 (Figure 3a) give rise to very large positive computed shifts at around +1683 ppm. However, the large positive π-spin density also causes very short transverse (T_2) relaxation times that result in severe signal broadening. As a consequence, the signal disappears in the noise level. In all cases, negative spin densities, and thus negative hyperfine shifts, are due to π–σ-spin polarization mechanisms. Positive spin-delocalization and negative spin-polarization contributions may also partly compensate. Carbon atoms of the linkers **3**–**6** in H_2O@Cr-MIL-101 are examples of such a cancellation (Figure 3a), giving rise to signals near the positions expected for such nuclei in diamagnetic samples (Table 2).[10]

Competitive Adsorption of N-Donor compounds. Based on the results obtained for X@Cr-MIL-101 with X being either H_2O, 2-AP, 3-AP, or DEA, it is now possible to analyze competition experiments with two components. If 3-AP is coadsorbed with 2-AP and DEA, respectively, only the characteristic hyperfine-shifted ^{13}C NMR signals (Figure 4)

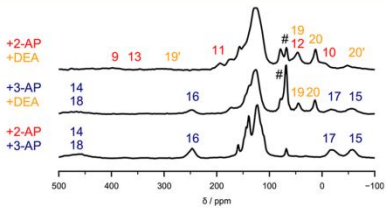

Figure 4. Cutout of the ^{13}C MAS NMR spectra of X@Cr-MIL-101 loaded with two components X = 2-AP + 3-AP (red and blue), 2-AP + DEA (red and orange), and 3-AP + DEA (blue and orange), together with the signal assignment. Key: # ^{13}C signal of the solvent.

for 3-AP are observed (**14**–**18**) while for the other components only the typical diamagnetic shifts were found. In contrast, for adsorbate mixtures of 2-AP and DEA both guest molecules show hyperfine-shifted and diamagnetic signals. The most pronounced hyperfine-shifted ones are **11** and **10** of 2-AP and **19′** as well as **20′** of DEA, representative for ligands coordinated to the CUS. Notably, the peaks for coordinated 2-AP are more intense compared to bonded DEA. Consequently, we conclude that the binding strength at the CUS increases in the order H_2O < DEA ≈ 2-AP < 3-AP. This is somewhat surprising as it opposes the chemical intuition that the strongest base 2-AP should exhibit the highest binding affinity. Since the computed binding energies of 142.6 kJ/mol (2-AP) and 143.4 kJ/mol (3-AP) are very similar, we attribute this to the steric hindrance of the amino group in ortho position. The markedly higher mobility of 3-AP (Figure 2) leads to higher entropic contributions to the equilibrium and thus to a stronger binding affinity.

Nevertheless, a similar trend was observed for the larger adsorption band for the d-d transitions of Cr^{3+} around 600 nm in the UV–vis spectra of the X@Cr-MIL-101 derivatives (Figure S19). DEA, 2-AP, and 3-AP give rise to increasing blue-shifts with respect to H_2O@Cr-MIL-101, indicating the strongest interaction between Cr^{3+} and 3-AP, while DEA and 2-AP exhibit similar and smaller shifts, respectively. In contrast to the NMR data, which allowed us to distinguish between guest molecules coordinated at the CUS and those physisorbed in a second coordination sphere, the UV–vis spectra are not sufficiently discriminating to answer this question (Figure S19).

The trend of the binding strength seems to be reflected in the magnitude of the hyperfine shifts, if atoms with the same number of bonds away from the paramagnetic center are compared. For example, the hyperfine shifts (δ_{FC}) of the signals for **19′** (DEA), **9**, and **13** (2-AP) as well as for **14** and **18** (3-AP) increase from 248 to 324 ppm (Table 2). However, the same values scatter markedly within the quantum-chemical calculations (Table 2), which indicates that the hyperfine interaction depends not only on the binding strength but also on the structure and the dynamics of the complex and thus on computational aspects such as model construction and method used for structure optimization.

■ CONCLUSION

H_2O@Cr-MIL-101 was successfully synthesized and loaded with 2-AP, 3-AP, and DEA as well as binary mixtures of these ligands. The well-resolved ^{13}C MAS NMR spectra of the individual Cr-MIL-101 derivatives feature both hyperfine-shifted signals and resonances within the typical shift region of the diamagnetic guest molecules. By combining distance relations derived from spin–lattice relaxation data and structural fragments with REDOR recoupling experiments to group the carbon atoms into C or CH_3 and CH or CH_2 moieties, we were able to unambiguously assign all these resonances. While the hyperfine shifted signals are characteristic for guest molecules coordinated to the CUS, the other resonances represent unspecifically physisorbed guests in a second coordination sphere. In particular, the hyperfine shifted signals present a clear signature for each guest, and thus allow us to decide which of the guest molecules is coordinated to the CUS even for competition experiments using binary mixtures. The derived binding preference depicts the following order: H_2O < DEA ≈ 2-AP < 3-AP.

The experimental assignment has been used to evaluate a computational approach, which amends a modern implementation of the Kurland–McGarvey theory for chemical shifts of systems with arbitrary spin multiplicity by a scaling to the Curie–Weiss regime of magnetically coupled metal centers above the transition temperature. The computed hyperfine shifts are dominated by the Fermi-contact term, which in turn accurately reflects the computed spin-density distributions within the clusters. The Curie–Weiss scaling brings the computed shifts to within about ±20% of the experimental values, also allowing shifts to be predicted in cases where paramagnetic line broadening did not allow detection. This demonstrates the potential of the modified cluster approach to obtain accurate chemical shifts also for exchange-coupled systems like the present MOFs.

Our results show that both the experimental and computational approaches present equivalent assignment strategies and might be used independently in the future. Nevertheless, the NMR experiments offer additional information about the dynamical disorder of the guest molecules and the framework, as the intensity modulations for the $^{13}C\{^1H\}$ REDOR spectra

DOI: 10.1021/jacs.7b10148
J. Am. Chem. Soc. 2018, 140, 2135–2144

of proton-bearing carbon atoms are sensitive to reorientations of the CH bonds. While the bdc linkers as well as the 3-AP and DEA molecules perform fast thermally activated large angle jumps combined with toggling motions, 2-AP molecules coordinated to the CUS are largely immobile. We attribute this to the considerable steric hindrance of the amino function in ortho-position with the IBU.

Our study shows that for the Cr-MIL-101 derivatives, solid-state ^{13}C NMR spectroscopy is well suited to identify the coordinating species as well as to determine their relative interaction strengths, as long as an unambiguous assignment can be achieved. Cr-MIL-101 is, however, only one example among the prominent class of MOFs featuring coordinatively unsaturated sites with paramagnetic metal ions including HKUST, CPO-27, and MIL-100, which were discussed for probing or recovering small gas molecules like CO,[72] CO_2,[73] and H_2[74] as well as for catalysis. All these applications crucially rely on the interaction between the gas molecules and the preferred adsorption sites. The presented strategy has the potential to provide a better understanding for the nature of such host–guest interactions, since it allows one to unveil guest-specific coordination at the CUS, separate them from physisorbed guests, and provide a microscopic picture of the adsorption mechanisms.

■ EXPERIMENTAL SECTION

Powder X-ray diffraction (PXRD) experiments were carried out in Bragg–Brentano geometry on a Panalytical X'pert Pro diffractometer equipped with a X'Celerator Scientific RTMS detector using Ni filtered Cu Kα radiation (λ = 1.54187 Å, 40 kV, 40 mA). Measurements were made in the range of 2°–30° (2θ) with a step size of 0.017°. The theoretical PXRD pattern was simulated from an optimized structure (using the Universal force field of the Forcite tool implemented in Materials Studio 5.0) obtained from a crystallographic information file.[75] The pattern was simulated with Cu Kα radiation, reflection geometry, and the Pearson profile functions. The half-width of the Bragg reflections was set to 0.15°. The parameters of the cubic cell of the space group $Fd\bar{3}m$ (No. 227) were set to 87.5 nm.

Attenuated total reflectance (ATR) IR spectra were recorded in the range 400–4000 cm^{-1} with a resolution of 4 cm^{-1} on a Jasco FT/IR-6100 spectrometer with a PIKEGladi ATR accessory.

The samples for chemical analyses were prepared in a glovebox under argon atmosphere after evacuating at 90 °C for 2 h. Carbon, hydrogen, and nitrogen contents (wt%) were obtained on a Vario elementar EL III. Chromium contents (wt%) were determined by atomic absorption spectroscopy in extinction mode on a Varian AA100 using a N_2O/acetylene flame upon chemical digestion. EDX spectroscopy was carried out on a Jeol JSM 6400 scanning electron microscope equipped with a Noran energy-dispersive X-ray analyzer and using a beam voltage of 20 kV.

Nitrogen sorption measurements were performed on a Quantachrome Nova 2000e at 77 K after evacuating the adsorbents at 363 K for 2 h under reduced pressure. Brunauer–Emmet–Teller (BET) equivalent surface areas were determined in the relative pressure range between 0.06 and 0.15 to accommodate for microporous materials.[76] Specific total pore volumes were determined at a relative pressure of 0.98 according to the Gurvich rule.[77] The pore-size distributions were derived using the nitrogen NLDFT model at 77 K for the adsorption branch assuming a silica/zeolite surface and a spherical/cylindrical pore shape which is implemented in the Quantachrome ASiQ v3.0 software package.

Dissolving the frameworks in a NaOD/D_2O solution of pH = 8.5 and precipitating the paramagnetic $Cr(OD)_3$ allowed us to record well-resolved solution ^1H NMR spectra and to quantify the modification degrees of both the linkers and IBUs by comparing the signal areas of products with that of the educts.

Diffuse reflectance UV/vis absorption spectra were recorded on an Agilent Cary 300 Scan spectrometer in the range from 190 to 800 nm with scan speeds of 0.5 nm/s.

The magnetic susceptibility data of H_2O@Cr-MIL-101 were collected using a MPMSXL-5 SQUID magnetometer under an applied field of 1591540 A/m over the temperature range 50–400 K. The solid sample was prepared in a gelatin capsule. The agreement factor R between the experimental and simulated data was calculated as $R = \sum_i(\chi_M^{exp} - \chi_M^{simp})^2/\sum_i(\chi_M^{simp})^2$.

The EPR spectrum was recorded at X-band frequencies (9.4 GHz) by sweeping the external magnetic field from 0.1 to 0.6 T. A modulation frequency 100 kHz and an amplitude of 0.2 mT were used. The conversion time was set to 40.96 ms.

^{13}C MAS spectra were acquired using a 1.9 mm triple resonance probe (Bruker) and a spinning speed of 40 kHz. A Hahn-echo pulse sequence with an interpulse distance of 25 μs (one rotor period) was applied for background suppression. Due to fast spinning heteronuclear proton broadband decoupling did not have an influence on the spectral resolution and was thus omitted. The 90° pulse length and recycle delay were set to 2.0 μs and 50ms, respectively. The averaged temperature in the rotor at ν_{rot} = 40 kHz was determined to 325 K by referencing with $Pb(NO_3)_2$.[78] The spin–lattice relaxation times T_1 were obtained with the inversion recovery method with a recycle delay of 0.3 s and time increments ranging from 0.5 to 256 ms. The $^{13}C-^1H$ REDOR-type recoupling experiments were performed with two 180° pulses on the ^1H channel at the center of each of the two rotation periods (τ_{deph} = 50 μs) while a 180° pulse was applied on the ^{13}C at the center of the two rotation periods. ^1H and ^{13}C 180° pulse lengths are 2.8 and 4 μs, respectively.

DFT computations of the ^{13}C and ^1H shifts were done at structures of the four model clusters optimized at PBE0-D3/def2-TZVP level,[79−83] using the Turbomole program.[84] Subsequently, the magnetic-resonance parameters have been computed using appropriate 9s7p4d metal[85] and IGLO-II main-group element[86] basis sets. In these calculations, a ferromagnetically coupled spin arrangement within the cluster has been chosen. The HFC and g-tensor calculations with the ORCA code[87] used a modified PBE40 hybrid functional (PBE0 with increased 40% exact-exchange admixture) that we recently found to perform well for solid-state pNMR shift calculations,[70] and which is also known to give excellent HFCs and g-tensors in relativistic computations for molecules.[88] The computed HFCs have been normalized to the number of spin centers present.[89] ZFS tensors were computed using the PBE exchange-correlation functional[90] and the Pederson–Khanna second-order perturbation approach[91] with van Wüllen's prefactors.[92] For both g-tensors and ZFS, the necessary spin–orbit matrix elements were computed within the spin–orbit mean-field approximation[93] implemented in ORCA. Orbital shieldings were obtained with the PBE40 functional using Gaussian09 (for both open- and closed-shell cases).[94] All pNMR computations have been performed for T = 325 K. The value of the Weiss constant (Θ = −102 K) has been taken from experiment (Figure S7). Both ^1H and ^{13}C shifts were referenced to tetramethylsilane (TMS) at the same level (using a PBE/def2-TZVP structure for TMS; the values are σ_{ref}^C = 189.23 ppm and σ_{ref}^H = 31.68 ppm).

■ ASSOCIATED CONTENT

Supporting Information

The Supporting Information is available free of charge on the ACS Publications website at DOI: 10.1021/jacs.7b10148.

Detailed description of the theory used for the chemical shift calculations and the spin–lattice relaxation analysis; PXRD pattern, IR spectra, chemical compositions, ^1H liquid NMR spectra, nitrogen sorption isotherms, and pore size distributions of X@Cr-MIL-101 with X = H_2O, DEA, 2-AP, and 3-AP; EPR spectrum and analysis of H_2O@Cr-MIL-101; calculated g- and ZFS-tensors of X@Cr-MIL-101; fit of the magnetic susceptibility χ and χ^{-1} of H_2O@Cr-MIL-101; full DFT-optimized fragment

DOI: 10.1021/jacs.7b10148
J. Am. Chem. Soc. 2018, 140, 2135–2144

clusters of X@Cr-MIL-101; ^{13}C spin−lattice relaxation data and distance sums; $^{13}C\{^1H\}$ REDOR spectra of X@Cr-MIL-101; ^1H MAS NMR spectra of X@Cr-MIL-101; dephasing values of L-histidine·HCl·H_2O with and without the influence of the hyperfine interaction; influence of large angle jumps on the $^{13}C\{^1H\}$ dephasing values of MIL-101; detailed comparison between calculated and observed ^{13}C and ^1H chemical shifts of X@Cr-MIL-101; and UV−vis spectra of X@Cr-MIL-101 (PDF)

SIMPSON inputs for the simulations of the $^{13}C\{^1H\}$ REDOR dephasing for carbons C1 to C6 of histidine as well as for all carbon atoms within 3-aminopryridine and diethylamine adsorbed to the CUS (ZIP)

AUTHOR INFORMATION

Corresponding Authors

*martin.kaupp@tu-berlin.de

*juergen.senker@uni-bayreuth.de

ORCID

Björn Corzilius: 0000-0003-3937-9137

Birgit Weber: 0000-0002-9861-9447

Martin Kaupp: 0000-0003-1582-2819

Notes

The authors declare no competing financial interest.

ACKNOWLEDGMENTS

We gratefully acknowledge financial support by the DFG (SE 1417/7-1 and SFB 840). Work in Berlin has been funded by the EU 7th Framework Programme within the Marie Curie Actions Initial Training Network scheme, under grant agreement no. 317127, the "pNMR project". B.C. has received funding from the Deutsche Forschungsgemeinschaft (DFG) through Emmy Noether grant CO802/2-1; further support from the BMRZ is acknowledged. We thank Beate Bojer for her steady support with the NMR measurements.

REFERENCES

(1) Qiu, S.; Xue, M.; Zhu, G. *Chem. Soc. Rev.* **2014**, *43*, 6116.

(2) Li, Q.; Zhang, W.; Miljanic, O. S.; Sue, C.; Zhao, Y.-L.; Liu, L.; Knobler, C. B.; Stoddart, J. F.; Yaghi, O. M. *Science* **2009**, *325*, 855.

(3) Cai, H.; Li, M.; Lin, X. R.; Chen, W.; Chen, G. H.; Huang, X. C.; Li, D. *Angew. Chem., Int. Ed.* **2015**, *54*, 10454.

(4) Lee, J.; Farha, O. K.; Roberts, J.; Scheidt, K. A.; Nguyen, S. T.; Hupp, J. T. *Chem. Soc. Rev.* **2009**, *38*, 1450.

(5) Czaja, A. U.; Trukhan, N.; Müller, U. *Chem. Soc. Rev.* **2009**, *38*, 1284.

(6) Ma, L.; Abney, C.; Lin, W. *Chem. Soc. Rev.* **2009**, *38*, 1248.

(7) Horcajada, P.; Chalati, T.; Serre, C.; Gillet, B.; Sebrie, C.; Baati, T.; Eubank, J. F.; Heurtaux, D.; Clayette, P.; Kreuz, C.; Chang, J.-S.; Hwang, Y. K.; Marsaud, V.; Bories, P.-N.; Cynober, L.; Gil, S.; Ferey, G.; Couvreur, P.; Gref, R. *Nat. Mater.* **2010**, *9*, 172.

(8) Horcajada, P.; Gref, R.; Baati, T.; Allan, P. K.; Maurin, G.; Couvreur, P.; et al. *Chem. Rev.* **2012**, *112*, 1232.

(9) McKinlay, A. C.; Morris, R. E.; Horcajada, P.; Férey, G.; Gref, R.; Couvreur, P.; Serre, C. *Angew. Chem., Int. Ed.* **2010**, *49*, 6260.

(10) Wack, J.; Ahnfeldt, T.; Stock, N.; Senker, J.; et al. *J. Phys. Chem. C* **2013**, *117*, 19991.

(11) Wittmann, T.; Siegel, R.; Reimer, N.; Milius, W.; Stock, N.; Senker, J. *Chem. - Eur. J.* **2015**, *21*, 314.

(12) Van de Voorde, B.; Bueken, B.; Denayer, J.; De Vos, D. *Chem. Soc. Rev.* **2014**, *43*, 5766.

(13) Samokhvalov, A. *Chem. - Eur. J.* **2015**, *21*, 16726.

(14) Li, J.-R.; Kuppler, R. J.; Zhou, H.-C. *Chem. Soc. Rev.* **2009**, *38*, 1477.

(15) Maes, M.; Trekels, M.; Boulhout, M.; Schouteden, S.; Vermoortele, F.; Alaerts, L.; Heurtaux, D.; Seo, Y.; Hwang, Y. K.; Chang, J.; Beurroies, I.; Denoyel, R.; Temst, K.; Vantomme, A.; Horcajada, P.; Serre, C.; De Vos, D. E. *Angew. Chem.* **2011**, *123*, 4296.

(16) Van de Voorde, B.; Boulhout, M.; Vermoortele, F.; Horcajada, P.; Cunha, D.; Lee, J. S.; Chang, J.; Gibson, E.; Daturi, M.; Lavalley, J.; Vimont, A.; Beurroies, I.; De Vos, D. E. *J. Am. Chem. Soc.* **2013**, *135*, 9849.

(17) Nuzhdin, A. L.; Kovalenko, K. A.; Dybtsev, N.; Bukhtiyarova, G. A. *Mendeleev Commun.* **2010**, *20*, 57.

(18) Ahmed, I.; Khan, N. A.; Hasan, Z.; Jhung, S. H. *J. Hazard. Mater.* **2013**, *250−251*, 37.

(19) Seo, P. W.; Ahmed, I.; Jhung, S. H. *Phys. Chem. Chem. Phys.* **2016**, *18*, 14787.

(20) Ahmed, I.; Jhung, S. H. *Chem. Eng. J.* **2014**, *251*, 35.

(21) Dai, J.; Mckee, M. L.; Samokhvalov, A. *J. Porous Mater.* **2014**, *21*, 709.

(22) Alaerts, L.; Maes, M.; Van Der Veen, M. A.; Jacobs, P. A.; De Vos, D. E. *Phys. Chem. Chem. Phys.* **2009**, *11*, 2903.

(23) Van de Voorde, B.; Boulhout, M.; Vermoortele, F.; Horcajada, P.; Cunha, D.; Lee, J. S.; Chang, J.; Gibson, E.; Daturi, M.; Lavalley, J.; Vimont, A.; Beurroies, I.; De Vos, D. E. *J. Am. Chem. Soc.* **2013**, *135*, 9849.

(24) Devautour-vinot, S.; Martineau, C.; Diaby, S.; Ben-Yahia, M.; Miller, S.; Serre, C.; Horcajada, P.; Cunha, D.; Taulelle, F.; Maurin, G. *J. Phys. Chem. C* **2013**, *117*, 11694.

(25) Čendak, T.; Žunkovič, E.; Godec, T. U.; Mazaj, M.; Logar, N. Z.; Mali, G. *J. Phys. Chem. C* **2014**, *118*, 6140.

(26) Chui, S. S.-Y.; Lo, S. M.-F.; Charmant, J. P. H.; Orpen, A. G.; Williams, I. D. *Science* **1999**, *283*, 1148.

(27) Achmann, S.; Hagen, G.; Hämmerle, M.; Malkowsky, I.; Kiener, C.; Moos, R. *Chem. Eng. Technol.* **2010**, *33*, 275.

(28) Jeremias, F.; Khutia, A.; Henninger, S. K.; Janiak, C. *J. Mater. Chem.* **2012**, *22*, 10148.

(29) Férey, G.; Mellot-Draznieks, C.; Serre, C.; Millange, F.; Dutour, J.; Surblé, S.; Margiolaki, I. *Science* **2005**, *309*, 2040.

(30) Bertini, I.; Luchinat, C.; Parigi, G. *Eur. J. Inorg. Chem.* **2000**, *2000*, 2473.

(31) Bertini, I.; Turano, P.; Vila, A. J. *Chem. Rev.* **1993**, *93*, 2833.

(32) Wicholas, M.; Mustacich, R.; Jayne, D. *J. Am. Chem. Soc.* **1972**, *94*, 4518.

(33) Wilkens, S. J.; Xia, B.; Volkman, B. F.; Weinhold, F.; Markley, J. L.; Westler, W. M. *J. Phys. Chem. B* **1998**, *102*, 8300.

(34) Walker, F. A. *Inorg. Chem.* **2003**, *42*, 4526.

(35) Banci, L.; Bertini, I.; Luchinat, C.; Pierattelli, R.; Shokhirev, N. V.; Walker, F. A. *J. Am. Chem. Soc.* **1998**, *120*, 8472.

(36) Bertini, I.; Luchinat, C.; Parigi, G. *Prog. Nucl. Magn. Reson. Spectrosc.* **2002**, *40*, 249.

(37) Ishii, Y.; Wickramasinghe, N. P.; Chimon, S. *J. Am. Chem. Soc.* **2003**, *125*, 3438.

(38) Wickramasinghe, N. P.; Shaibat, M. A.; Ishii, Y. *J. Phys. Chem. B* **2007**, *111*, 9693.

(39) Wickramasinghe, N. P.; Shaibat, M. A.; Jones, C. R.; Casabianca, L. B.; De Dios, A. C.; Harwood, J. S.; Ishii, Y. *J. Chem. Phys.* **2008**, *128*, 052210.

(40) Kim, J.; Middlemiss, D. S.; Chernova, N. A.; Zhu, B. Y. X.; Masquelier, C.; Grey, C. P. *J. Am. Chem. Soc.* **2010**, *132*, 16825.

(41) Dawson, D. M.; Jamieson, L. E.; Mohideen, M. I. H.; McKinlay, A. C.; Smellie, I. A.; Cadou, R.; Keddie, N. S.; Morris, R. E.; Ashbrook, S. E. *Phys. Chem. Chem. Phys.* **2013**, *15*, 919.

(42) Saalwächter, K. *Prog. Nucl. Magn. Reson. Spectrosc.* **2007**, *51*, 1.

(43) Bärwinkel, K.; Herling, M. M.; Rieß, M.; Sato, H.; Li, L.; Avadhut, Y. S.; Kemnitzer, T. W.; Kalo, H.; Senker, J.; Matsuda, R.; Kitagawa, S.; Breu, J. *J. Am. Chem. Soc.* **2017**, *139*, 904.

(44) Schanda, P.; Meier, B. H.; Ernst, M. *J. Am. Chem. Soc.* **2010**, *132*, 15957.

DOI: 10.1021/jacs.7b10148
J. Am. Chem. Soc. 2018, 140, 2135−2144

(45) Vaara, J.; Rouf, S. A.; Mares, J. *J. Chem. Theory Comput.* **2015**, *11*, 4840.
(46) Kurland, R. J.; McGarvey, B. R. *J. Magn. Reson.* **1970**, *2*, 286.
(47) Pennanen, T. O.; Vaara, J. *Phys. Rev. Lett.* **2008**, *100*, 133002.
(48) Rouf, S. A.; Mares, J.; Vaara, J. *J. Chem. Theory Comput.* **2015**, *11*, 1683.
(49) Cahill, L. S.; Chapman, R. P.; Kirby, C. W.; Goward, G. R. *Appl. Magn. Reson.* **2007**, *32*, 565.
(50) Soncini, A.; Van Den Heuvel, W. *J. Chem. Phys.* **2013**, *138*, 021103.
(51) Bertini, I.; Luchinat, C.; Parigi, G.; Ravera, E. *NMR of Paramagnetic Molecules. Applications to Metalloproteins and Models*, 2nd ed.; Elsevier: Amsterdam, 2016.
(52) Nayeem, A.; Yesinowski, J. P. *J. Chem. Phys.* **1988**, *89*, 4600.
(53) Bertmer, M. *Solid State Nucl. Magn. Reson.* **2017**, *81*, 1.
(54) Hwang, Y. K.; Hong, D.; Chang, J.; Jhung, S. H.; Seo, Y.; Kim, J.; Vimont, A.; Daturi, M.; Serre, C.; Férey, G. *Angew. Chem., Int. Ed.* **2008**, *47*, 4144.
(55) Livage, C.; Guillou, N.; Chaigneau, J.; Rabu, P.; Drillon, M.; Férey, G. *Angew. Chem., Int. Ed.* **2005**, *44*, 6488.
(56) Welo, L. A. *Philos. Mag.* **1928**, *6*, 481.
(57) Honda, M.; Morita, M.; Date, M. *J. Phys. Soc. Jpn.* **1992**, *61*, 3773.
(58) Tadros, A. M.; Royko, M. M.; Kelley, S. P.; Belmore, K.; Rogers, R. D.; Vincent, J. B. *Polyhedron* **2015**, *100*, 17.
(59) Bak, M.; Rasmussen, J. T.; Nielsen, N. C. *J. Magn. Reson.* **2000**, *147*, 296.
(60) Kervern, G.; Pintacuda, G.; Emsley, L. *Chem. Phys. Lett.* **2007**, *435*, 157.
(61) Pell, A. J.; Sanders, K. J.; Wegner, S.; Pintacuda, G.; Grey, C. P. *J. Chem. Phys.* **2017**, *146*, 194202.
(62) Pell, A. J.; Pintacuda, G. *Prog. Nucl. Magn. Reson. Spectrosc.* **2015**, *84*−*85*, 33.
(63) Kolokolov, D. I.; Stepanov, A. G.; Jobic, H. *J. Phys. Chem. C* **2014**, *118*, 15978.
(64) Kolokolov, D. I.; Stepanov, A. G.; Guillerm, V.; Serre, C.; Frick, B.; Jobic, H. *J. Phys. Chem. C* **2012**, *116*, 12131.
(65) Dawson, D. M.; Ke, Z.; Mack, F. M.; Doyle, R. A.; Bignami, G. P. M.; Smellie, I. A.; Buhl, M.; Ashbrook, S. E. *Chem. Commun.* **2017**, *53*, 10512.
(66) Bühl, M.; Ashbrook, S. E.; Dawson, D. M.; Doyle, R. A.; Hrobárik, P.; Kaupp, M.; Smellie, I. A. *Chem. - Eur. J.* **2016**, *22*, 15328.
(67) Benda, L.; Mareš, J.; Ravera, E.; Parigi, G.; Luchinat, C.; Kaupp, M.; Vaara, J. *Angew. Chem., Int. Ed.* **2016**, *55*, 14713.
(68) Novotný, J.; Sojka, M.; Komorovsky, S.; Nečas, M.; Marek, R. *J. Am. Chem. Soc.* **2016**, *138*, 8432.
(69) Rouf, S. A.; Jakobsen, V. B.; Mareš, J.; Jensen, N. D.; Mckenzie, C. J.; Vaara, J.; Nielsen, U. G. *Solid State Nucl. Magn. Reson.* **2017**, *87*, 29.
(70) Mondal, A.; Gaultois, M. W.; Pell, A. J.; Iannuzzi, M.; Grey, C. P.; Hutter, J.; Kaupp, M. *J. Chem. Theory Comput.* **2018**, *14*, 377−394.
(71) Gavrilenko, K. S.; Addison, A.; Thompson, L.; Pavlishchuk, V. V. *Theor. Exp. Chem.* **2004**, *40*, 214.
(72) Chavan, S.; Vitillo, J. G.; Groppo, E.; Bonino, F.; Lamberti, C.; Dietzel, P. D. C.; Bordiga, S. *J. Phys. Chem. C* **2009**, *113*, 3292.
(73) Dietzel, P. D. C.; Besikiotis, V.; Blom, R. *J. Mater. Chem.* **2009**, *19*, 7362.
(74) Kapelewski, M. T.; Geier, S. J.; Hudson, M. R.; Stück, D.; Mason, J. A.; Nelson, J. N.; Xiao, D. J.; Hulvey, Z.; Gilmour, E.; Fitzgerald, S. A.; Head-Gordon, M.; Brown, C. M.; Long, J. R. *J. Am. Chem. Soc.* **2014**, *136*, 12119.
(75) Lebedev, O. I.; Millange, F.; Serre, C.; Van Tendeloo, G.; Férey, G. *Chem. Mater.* **2005**, *17*, 6525.
(76) Thommes, M. *Chem. Ing. Tech.* **2010**, *82*, 1059.
(77) Gurvich, L. *J. Russ. Phys. Chem. Soc.* **1915**, *47*, 805.
(78) Guan, X.; Stark, R. E. *Solid State Nucl. Magn. Reson.* **2010**, *38*, 74.
(79) Weigend, F.; Ahlrichs, R. *Phys. Chem. Chem. Phys.* **2005**, *7*, 3297.
(80) Weigend, F. *Phys. Chem. Chem. Phys.* **2006**, *8*, 1057.
(81) Adamo, C.; Barone, V. *J. Chem. Phys.* **1999**, *110*, 6158.
(82) Grimme, S.; Antony, J.; Ehrlich, S.; Krieg, H. *J. Chem. Phys.* **2010**, *132*, 154104.
(83) Perdew, J. P.; Burke, K.; Ernzerhof, M. *Phys. Rev. Lett.* **1996**, *77*, 3865.
(84) *TURBOMOLE*, V7.0, a development of University of Karlsruhe and Forschungszentrum Karlsruhe; TURBOMOLE GmbH, 2015.
(85) Munzarová, M.; Kaupp, M. *J. Phys. Chem. A* **1999**, *103*, 9966.
(86) Kutzelnigg, W.; Fleischer, U.; Schindler, M. In *NMR Basic Principles and Progress*; Diehl, E., Fluck, E., Günther, H., Kosfeld, R., Seelig, J., Eds.; Springer: Berlin, 1991.
(87) Neese, F. *ORCA*, An Ab Initio, Density Functional and Semiempirical Program Package, V.3, 2012.
(88) Gohr, S.; Hrobárik, P.; Repiský, M.; Komorovsky, S.; Ruud, K.; Kaupp, M. *J. Phys. Chem. A* **2015**, *119*, 12892.
(89) Sinnecker, S.; Neese, F.; Noodleman, L.; Lubitz, W. *J. Am. Chem. Soc.* **2004**, *126*, 2613.
(90) Perdew, J. P.; Burke, K.; Ernzerhof, M. *Phys. Rev. Lett.* **1996**, *77*, 3865.
(91) Pederson, M. R.; Khanna, S. N. *Phys. Rev. B: Condens. Matter Mater. Phys.* **1999**, *60*, 9566.
(92) Schmitt, S.; Jost, P.; Van Wüllen, C. *J. Chem. Phys.* **2011**, *134*, 194113.
(93) Neese, F. *J. Chem. Phys.* **2005**, *122*, 034107.
(94) Frisch, M. J.; Trucks, G. W.; Schlegel, H. B.; Scuseria, G. E.; Robb, M. A.; Cheeseman, J. R.; Scalmani, G.; Barone, V.; Mennucci, B.; Petersson, G. A.; Nakatsuji, H.; Caricato, M.; Li, X.; Hratchian, H. P.; Izmaylov, A. F.; Bloino, J.; Zheng, G.; Sonnenberg, J. L.; Hada, M.; Ehara, M.; Toyota, K.; Fukuda, R.; Hasegawa, J.; Ishida, M.; Nakajima, T.; Honda, Y.; Kitao, O.; Nakai, H.; Vreven, T.; Montgomery, J. A., Jr.; Peralta, J. E.; Ogliaro, F.; Bearpark, M. J.; Heyd, J.; Brothers, E. N.; Kudin, K. N.; Staroverov, V. N.; Kobayashi, R.; Normand, J.; Raghavachari, K.; Rendell, A. P.; Burant, J. C.; Iyengar, S. S.; Tomasi, J.; Cossi, M.; Rega, N.; Millam, N. J.; Klene, M.; Knox, J. E.; Cross, J. B.; Bakken, V.; Adamo, C.; Jaramillo, J.; Gomperts, R.; Stratmann, R. E.; Yazyev, O.; Austin, A. J.; Cammi, R.; Pomelli, C.; Ochterski, J. W.; Martin, R. L.; Morokuma, K.; Zakrzewski, V. G.; Voth, G. A.; Salvador, P.; Dannenberg, J. J.; Dapprich, S.; Daniels, A. D.; Farkas, Ö.; Foresman, J. B.; Ortiz, J. V.; Cioslowski, J.; Fox, D. J. *Gaussian 09*; Gaussian, Inc.: Wallingford, CT, 2009.

DOI: 10.1021/jacs.7b10148
J. Am. Chem. Soc. 2018, 140, 2135−2144

6.3.2 Supporting Information

Supporting Information

for

Probing Interactions of N-Donor Molecules with Open Metal Sites within Paramagnetic Cr-MIL-101: A Solid-State NMR Spectroscopic and Density Functional Theory Study

Thomas Wittmann,[a] Arobendo Mondal,[b] Carsten B. L. Tschense,[a] Johannes J. Wittmann,[c] Ottokar Klimm,[d] Renée Siegel,[a] Björn Corzilius,[c] Birgit Weber,[d] Martin Kaupp,* [b] Juergen Senker* [a]

[a] Inorganic Chemistry III, University of Bayreuth, Universitätsstrasse 30, 95447, Bayreuth, Germany,

[b] Institute of Theoretical Chemistry/Quantum Chemistry, Technical University of Berlin, Sekr. C7, Straße des 17. Juni 135, 10623 Berlin, Germany,

[c] Institute of Physical and Theoretical Chemistry and Institute of Biophysical Chemistry, Goethe University Frankfurt, Max-von-Laue-Str. 7-9, 60438 Frankfurt am Main, Germany,

[d] Inorganic Chemistry II, University of Bayreuth, Universitätsstrasse 30, 95447, Bayreuth, Germany

Further theoretical background

Quantum-chemical calculations

In contrast to the treatment of isolated paramagnetic systems in refs.1,2, Eq. 1 in the main text replaces T by T–Θ in the prefactor to the hyperfine shifts to account for the residual exchange couplings of the extended solid-state system in question, assuming Curie-Weiss behavior at the temperatures probed experimentally. Introduction of the Weiss constant Θ accounts for the contributions of ferromagnetic or antiferromagnetic couplings to the magnetic behavior of such materials when present in the high-temperature paramagnetic regime (where the exchange interactions can be treated within a mean-field approach).[3,4] Such a temperature dependence is also observed for the paramagnetic shifts in exchange-coupled systems and thus introduced into Eq. 1.[5–8] The Weiss constant obtained by extrapolation of the high-temperature part of the magnetic susceptibility for H_2O@Cr-MIL-101 is used (see experimental part in main text). We note that a change of 20 K in Θ affects the computed hyperfine shifts at most by 5%, which renders our use of the same Weiss constant for the other derivatives a reasonable approximation.

We may decompose the A- and g-matrices of Eq. 1 (main text) into their individual contributions: $\mathbf{A} = A_{FC}\mathbf{1} + \mathbf{A}_{dip} + A_{pc}\mathbf{1} + \mathbf{A}_{dip,2} + \mathbf{A}_{as}$, where $\mathbf{1}$ is a 3 × 3 unit matrix, and A_{FC} as well as A_{dip} are the nonrelativistic isotropic contact coupling and anisotropic dipolar coupling tensors, respectively. A_{pc} is the isotropic pseudocontact coupling, $A_{dip,2}$ is the corresponding anisotropic and symmetric "second-order dipolar term", and A_{as} is the antisymmetric term. These three contributions are due to the perturbational relativistic spin-orbit (SO) corrections to the HFC,[9] the use of which is justified for the light ligand nuclei in 3d complexes. The g-tensor may be written as $\mathbf{g} = (g_e + \Delta g_{iso})\mathbf{1} + \Delta\tilde{\mathbf{g}}$, where g_e is the isotropic free-electron g-value, Δg_{iso} the isotropic deviation, and $\Delta\tilde{\mathbf{g}}$ the traceless anisotropic part. Since $\mathbf{A}_{dip}$, $\mathbf{A}_{dip,2}$ and $\Delta\tilde{\mathbf{g}}$ are traceless, the contributions to the isotropic chemical shift up to the order of α^4 in the fine structure constant α are given as[1,10]

$$\sigma_{iso}^{I} = \sigma_{orb,iso}^{I} - \frac{\mu_B}{\hbar\gamma_I k}\left\{\frac{1}{T-\Theta}\right\}\left(\begin{array}{c} g_e\mathbf{1}\cdot\langle\boldsymbol{SS}\rangle\cdot A_{FC}^{I}\mathbf{1} + \Delta g_{iso}\mathbf{1}\cdot\langle\boldsymbol{SS}\rangle\cdot A_{FC}^{I}\mathbf{1} + g_e\mathbf{1}\cdot\langle\boldsymbol{SS}\rangle\cdot A_{PC}^{I}\mathbf{1} + \\ g_e\mathbf{1}\cdot\langle\boldsymbol{SS}\rangle\cdot\mathbf{A}_{dip}^{I} + g_e\mathbf{1}\cdot\langle\boldsymbol{SS}\rangle\cdot\mathbf{A}_{dip,2}^{I} + \Delta g_{iso}\mathbf{1}\cdot\langle\boldsymbol{SS}\rangle\cdot\mathbf{A}_{dip}^{I} \\ + \Delta\tilde{\mathbf{g}}\cdot\langle\boldsymbol{SS}\rangle\cdot A_{FC}^{I}\mathbf{1} + \Delta\tilde{\mathbf{g}}\cdot\langle\boldsymbol{SS}\rangle\cdot\mathbf{A}_{dip}^{I} \end{array}\right)_{iso} \quad \text{(S1)}$$

Comparing thus Eq. S1 to Eq. 5 in the main text, obviously $\sigma_{orb,iso}$ corresponds to δ_{orb}^{exp}. The sum of the three terms depending on $g_e\mathbf{1}\cdot\langle\boldsymbol{SS}\rangle\cdot A_{FC}^{I}\mathbf{1} + \Delta g_{iso}\mathbf{1}\cdot\langle\boldsymbol{SS}\rangle\cdot A_{FC}^{I}\mathbf{1} + g_e\mathbf{1}\cdot\langle\boldsymbol{SS}\rangle\cdot A_{PC}^{I}\mathbf{1}$ corresponds to δ_{FC}, and the remaining five terms together correspond to δ_{PC}. From Eq. S1 it is clear that for the systems having small anisotropy in the g-tensor and negligible ZFS, the PC shifts will be very small, and the contact term will be decisive.

Relaxation

The hyperfine interaction also leads to a shortening of spin-lattice (T_1) and spin-spin (T_2) relaxation times.[11–13] The small T_2 and the anisotropic part of the bulk magnetic susceptibility, which is not completely removed by magic-angle spinning are the main reasons for signal

broadening for paramagnetic compounds.[11,14,15] The observed spin-lattice relaxation rates of nuclei in paramagnetic compounds are the sum of the diamagnetic and the paramagnetic contributions ($1/T_1^{exp} = 1/T_1^{dia} + 1/T_1^{para}$).[11,16,17] Due to the usually larger T_1^{dia} values, T_1^{exp} is dominated by T_1^{para}. T_1^{para} is composed of the Fermi-contact, the electron-nuclear dipolar and the Curie-spin relaxation rates $\left(\frac{1}{T_1^{para}} = \frac{1}{T_1^{para,contact}} + \frac{1}{T_1^{para,dipolar}} + \frac{1}{T_1^{para,Curie}}\right)$, which are given by

$$\frac{1}{T_1^{para,contact}} = \frac{2}{3}\left(\frac{A^{iso}}{\hbar}\right)^2 S(S+1)\left[\frac{\tau_S}{1+(\omega_I-\omega_S)^2\tau_S^2}\right] \quad \text{(S2)}$$

$$\frac{1}{T_1^{para,dipolar}} = \frac{2}{5}\left(\frac{\mu_0}{4\pi}\right)^2 \frac{\mu_B^2 g_e^2 \gamma_I^2 S(S+1)}{r^6}\left[\frac{\tau_C}{1+\omega_I^2\tau_C^2}\right] \quad \text{(S3)}$$

$$\frac{1}{T_1^{para,Curie}} = \frac{6}{5}\left(\frac{\mu_0}{4\pi}\right)^2 \frac{\omega_I^2 g_e^4 \mu_B^4 S^2(S+1)^2}{(3kT)^2 r^6}\left[\frac{\tau_r}{1+\omega_I^2\tau_r^2}\right] \quad \text{(S4)}$$

where τ_s is the electron-correlation time and ω_I the nuclear Larmor frequency.

The Fermi-contact contribution (Eq. S2) to T_1 becomes negligible due to the several orders of magnitude higher ω_S compared to the nuclear ω_I ($\omega_S \approx 16300\ \omega_I$ for ^{13}C at $B_0 = 9.4$ T).

$T_1^{para,dipolar}$ (Eq. S3) is described by the Solomon-Bloembergen-Morgan (SBM) equation which assumes a metal centered point-dipole approximation, isotropic g-values and a negligible zero-field-splitting.[13,18,19] It is determined by the squared dipolar coupling constant and the spectral density (last term in brackets in Eq. S3). The former is modulated by the metal-nucleus distance ($T_1 \sim r^6$) and the latter by τ_c which is composed of τ_s and τ_r ($1/\tau_c = 1/\tau_s + 1/\tau_r$).[11,16]

In the solid state, motions are generally slowed which results in several orders of magnitude longer τ_r than τ_s so that τ_c is dominated by τ_s.[16,20] The Curie-spin contribution (Eq. S4) arises from the dipolar interaction between the nuclear magnetic moment and the induced net electron magnetic moment caused by the Boltzmann populated electron Zeeman levels. As $T_1^{para,Curie}$ solely depends on τ_r[11,13,16] it has only a minor influence on T_1^{para}. Thus, T_1^{para} is to the biggest part determined by $T_1^{para,\ dipolar}$ (Eq. S3).

For exchange-coupled systems T_1 is influenced by the magnetic coupling. It relies on the new energy states resulting from exchange coupling between the metal ions, which is described by the Heisenberg-Dirac-vanVleck (HDvV) Hamiltonian. The HDvV Hamiltonian for an equilateral triangle of Cr^{3+} in the Cr_3O plane of Cr-MIL-101 (Eq. S5) is given by the sum of the scalar products of each pair of the three spin operators S_1, S_2, S_3. Each pair is multiplied with the respective exchange coupling constants J_{12}, J_{13} and J_{23}[21,22] so that

$$H = J_{12}\,\mathbf{S_1}\cdot\mathbf{S_2} + J_{13}\,\mathbf{S_1}\cdot\mathbf{S_3} + J_{23}\,\mathbf{S_2}\cdot\mathbf{S_3} \quad \text{(S5)}$$

If J_{12}, J_{13} and J_{23} are equal the energy eigenvalues E_i of the new total electron spin levels S_i result in:[21,22]

$$E_i = -J\left[S_i(S_i+1) - 3\,S_1(S_1+1)\right] \quad \text{(S6)}$$

For calculating E_i in Eq. S6 the isotropic J values are derived by fitting the magnetic susceptibility χ with the Bleany-Bowers equation, which results from inserting the energy eigenvalues E_i into the Van-Vleck formula.[23,24] The molar magnetic susceptibility χ_M for the

trimeric coupled Cr-MIL-101 results in[21,25]

$$\chi_M = \frac{N_A g^2 \mu_B^2}{4kT} \frac{2 + 40\exp\left(3J/kT\right) + 105\exp\left(8J/kT\right) + 168\exp\left(15J/kT\right) + 165\exp\left(24J/kT\right)}{2 + 8\exp\left(3J/kT\right) + 9\exp\left(8J/kT\right) + 8\exp\left(15J/kT\right) + 5\exp\left(24J/kT\right)} \quad \text{(S7)}$$

For exchange-coupled systems the dipolar contribution $T_1^{\text{para, dipolar}}$ is given by[26,27]

$$\frac{1}{T_1^{para,dipolar}} = \frac{2}{5}\left(\frac{\mu_0}{4\pi}\right)^2 \gamma_I^2 g_e^2 \mu_B^2 \sum_{j=1}^{3} \frac{\sum_i C_{ji}^2 S_i \left(S_i + 1\right)\left(2S_i + 1\right)\exp\left(-E_i/kT\right)}{r_{Cr_j-C}^6 \sum_i \left(2S_i + 1\right)\exp\left(-E_i/kT\right)} \left(\frac{\tau_s}{1+\omega_I^2\tau_s^2}\right) \quad \text{(S8)}$$

Basic characterization of the Cr-MIL-101 derivatives

The positions of the Bragg reflections in the powder X-ray diffraction (PXRD) patterns of all Cr-MIL-101 derivatives (Figure S1) coincide well with the simulated ones for H_2O@Cr-MIL-101 obtained from a DFT-optimized structure[28] showing the integrity of the framework for all samples (Figure S1). We attribute the slight variation of the Bragg intensities for the individual materials to variations of electron density within the pores due to adsorption of DEA, 2-AP and 3-AP and excess solvent.

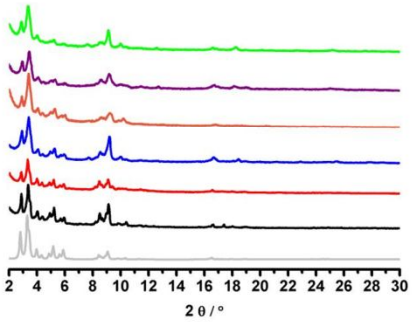

Figure S1: PXRD patterns from bottom to top: Simulation for H_2O@Cr-MIL-101 (grey line) according to ref.[28], H_2O@Cr-MIL-101 (black line), 2-AP@Cr-MIL-101 (red line), 3-AP@Cr-MIL-101 (blue line), DEA@Cr-MIL-101 (orange line), 2-AP+DEA@Cr-MIL-101 (violet line) and 3-AP+DEA@Cr-MIL-101 (green line).

The incorporation of the guest species is also demonstrated by the characteristic IR stretching vibration bands for the aliphatic methylene and methyl groups as well as the aromatic C-H units of 2-AP and 3-AP, which all appear in the region between 3000 cm^{-1} and 2900 cm^{-1} (Figure S2).

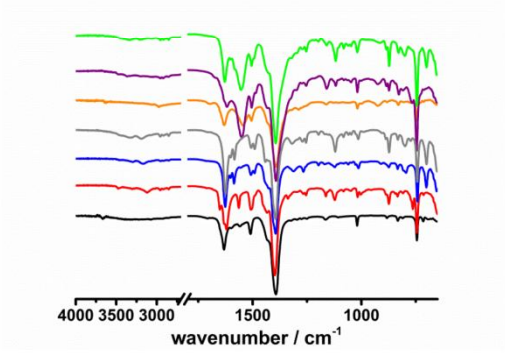

Figure S2: ATR-FTIR-spectra from bottom to top: H_2O@Cr-MIL-101 (black), 2-AP@Cr-MIL-101 (red), 3-AP@Cr-MIL-101 (blue), DEA@Cr-MIL-101 (orange), 2-AP+DEA@Cr-MIL-101 (violet), 3-

AP+DEA@Cr-MIL-101 (green) and H_2O@Cr-MIL-101 soaked in diethylamine to evaluate the aliphatic and C-N IR vibrations of non-coordinated diethylamine (grey line).

The sample compositions were determined using AAS and elementary analysis for the atom contents of Cr, C, H and N (Table S1). The amount of included DEA, 2-AP and 3-AP were taken from ^{1}H solution NMR spectra (Figure S3). The formula units of the materials are summarized in Table 1.

Table S1: Experimental and theoretical H, C, N and Cr weight contents of the X@Cr-MIL-101 derivatives.

Compound	H exp	H theo	C exp	C theo	N exp	N theo	Cr exp	Cr theo
H_2O@Cr-MIL-101 $Cr_3O(H_2O)_2(OH)_{0.8}(NO_3)_{0.2}(bdc)_3$	2.69	2.34	40.09	39.68	0.38	0.38	22.06	21.47
DEA@Cr-MIL-101 (88% DEA) $Cr_3O(H_2O)_{0.24}(DEA)_{1.76}$-$(OH)_{0.8}(NO_3)_{0.2}(bdc)_3$	3.95	4.00	43.85	45.19	3.59	3.32	17.80	18.92
2-AP@Cr-MIL-101 $Cr_3O(2\text{-}AP)_{3.5}(OH)_{0.8}(NO_3)_{0.2}(bdc)_3$	4.10	3.58	47.73	47.99	10.59	9.98	15.36	14.97
3-AP@Cr-MIL-101 $Cr_3O(3\text{-}AP)_{4.5}(OH)_{0.8}(NO_3)_{0.2}(bdc)_3$	4.00	3.82	49.88	49.31	12.31	11.63	14.12	13.73
2-AP+DEA@Cr-MIL-101 $Cr_3O(2\text{-}AP)_{1.8}$ $(DEA)_{1.75}(OH)_{0.8}(NO_3)_{0.2}(bdc)_3$	3.94	4.43	46.96	47.82	9.48	8.02	15.62	15.47
3-AP+DEA@Cr-MIL-101 $Cr_3O(3\text{-}AP)_{3.4}(DEA)_{1.75}$ $(OH)_{0.8}(NO_3)_{0.2}(bdc)_3$	5.06	4.69	49.37	49.90	10.49	10.85	13.80	13.46

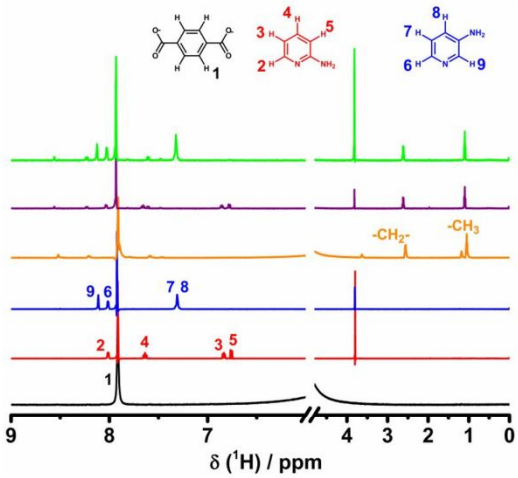

Figure S3: Solution ^{1}H NMR spectra from bottom to top: H_2O@Cr-MIL-101 (black line), 2-AP@Cr-MIL-101 (red line, ratio of signal 2 : signal 1 amounts to 0.29:1 leading to 3.5 2-AP per FU), 3-AP@Cr-MIL-101 (blue line, ratio of signal 9 : signal 1 amounts to 0.375:1 leading to 4.5 3-AP per FU), DEA@Cr-MIL-101 (orange line, ratio of CH_2 signal : signal 1 amounts to 0.58:1 leading to 1.75 DEA per FU), 2-AP+DEA@Cr-MIL-101 (violet line, ratio of signal 2 : signal 1 amounts to 0.15:1 leading to 1.8 2-AP per FU and ratio of the CH_2 signal : signal 1 amounts to 0.59:1 leading to 1.75 DEA per FU), 3-AP+DEA@Cr-MIL-101 (green line, ratio of signal 9 : signal 1 amounts to 0.283:1 leading to 3.4 3-AP per FU and ratio of the CH_2 signal : signal 1 amounts to 0.59:1 leading to 1.75 DEA per FU).

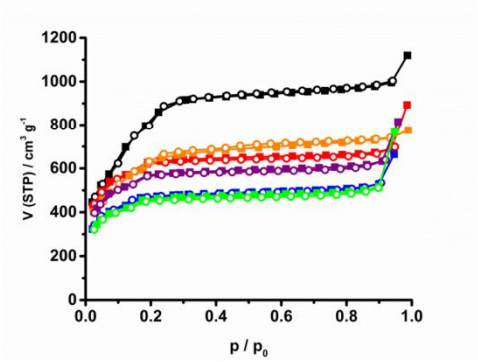

Figure S4: Nitrogen ad- (full squares) and desorption (empty circles) isotherms at 77 K of H_2O@Cr-MIL-101 (black curves), 2-AP@Cr-MIL-101 (red curves), 3-AP@Cr-MIL-101 (blue curves), DEA@Cr-MIL-101 (orange curves), 2-AP+DEA@Cr-MIL-101 (violet curves), 3-AP+DEA@Cr-MIL-101 (green curves).

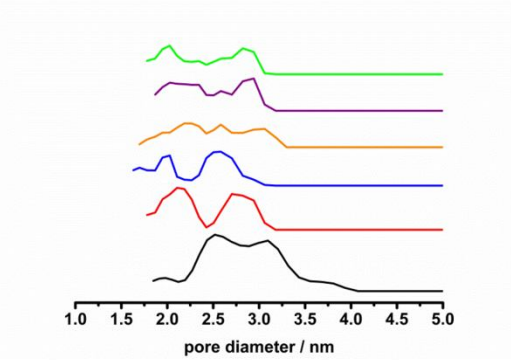

Figure S5: NLDFT pore-size distribution curves H_2O@Cr-MIL-101 (black), 2-AP@Cr-MIL-101 (red), 3-AP@Cr-MIL-101 (blue), DEA@Cr-MIL-101 (orange), 2-AP+DEA@Cr-MIL-101 (violet), 3-AP+DEA@Cr-MIL-101 (green).

Table S2: Apparent BET-surface areas and total pore volumes determined at $p/p_o = 0.95$ of the Cr-MIL-101 derivatives.

Compound	S_{BET} / $m^2\ g^{-1}$	$V_{total\ (p/po\ =\ 0.95)}$ / $cm^3\ g^{-1}$
H_2O@Cr-MIL-101	3011	1.54
DEA@Cr-MIL-101	2200	1.14
2-AP@Cr-MIL-101	2047	1.07
3-AP@Cr-MIL-101	1687	0.82
2-AP+DEA@Cr-MIL-101	1947	0.97
3-AP+DEA@Cr-MIL-101	1650	0.80

Magnetic susceptibility and EPR analysis

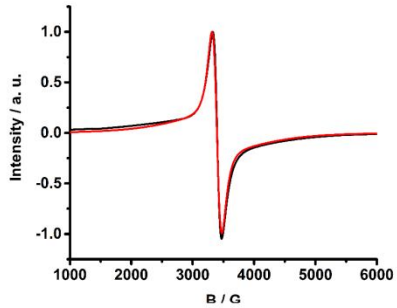

Figure S6: Experimental (black line) and simulated CW-EPR spectrum (red line) of H_2O@Cr-MIL-101.

The EPR signal of H_2O@Cr-MIL-101 at 298 K (Figure S6) is dominated by anisotropic line broadening due to unresolved hyperfine couplings and distributions (strain) of the zero-field interaction parameters. This indicates small structural variations from one paramagnetic center to the next. The EPR signal crosses the zero line at B_0 = 3398 G, which corresponds to a g-value of 1.985 (Figure S6). The small deviation of the g-value from the free-electron value (~2.0023) originates from a not completely quenched spin-orbit coupling of the electrons in Cr^{3+}. Fitting the system with three coupled Cr^{3+} (S = 3/2) ions using the EasySpin software package[29] resulted in a slightly anisotropic, axial g-tensor with $g_{\parallel}$ = 1.988 and $g_{\perp}$ = 1.980 which is in line with the quantum-chemical calculations (Table S3). The fit gave a zero-field splitting (ZFS) parameter D of 100 MHz (~ 0.01 cm^{-1}) which also agrees with the computed values (Table S4). The Gaussian distributions of the axial and rhombic ZFS parameters D and E are characterized by FWHMs of 3000 +/- 2000 MHz (~ 0.1 cm^{-1}) indicating a rhombic zero-field splitting tensor.

Table S3: Comparison of computed[a] g-tensors of the Cr-MIL-101 compounds.

Compound	g_{11}	g_{22}	g_{33}	g_{iso}
H_2O@Cr-MIL-101	1.98155	1.98318	1.98443	1.98306
2-AP@Cr-MIL-101	1.98134	1.98269	1.98408	1.98270
3-AP@Cr-MIL-101	1.98134	1.98258	1.98412	1.98268
DEA@Cr-MIL-101	1.98141	1.98277	1.98409	1.98276

[a]The cluster-model computations were done at PBE40/IGLO-II/9s7p4d level (see Computational Details in the main text). The experimental g-tensor for H_2O@Cr-MIL-101 (axial fit) is $g_{\parallel}$ = 1.988, $g_{\perp}$ = 1.980, g_{iso}= 1.985 (see main text).

Table S4: Comparison of computed[a] D-tensor components of the Cr-MIL-101 compounds.

Compound	$D_{11}(cm^{-1})$	$D_{22}(cm^{-1})$	$D_{33}(cm^{-1})$	$D(cm^{-1})$	E/D
H_2O@Cr-MIL-101	-0.0018	-0.0045	0.006266	0.0094	0.1443
2-AP@Cr-MIL-101	-0.0045	-0.0076	0.012064	0.0181	0.0856
3-AP@Cr-MIL-101	-0.0058	-0.0065	0.012320	0.0185	0.0198
DEA@Cr-MIL-101	-0.0016	-0.0101	0.011731	0.0176	0.2423

[a]The cluster-model computations were done at PBE40/IGLO-II/9s7p4d level (see Computational Details in main text). The experimental value for H_2O@Cr-MIL-101 is D = 0.01 cm^{-1}.

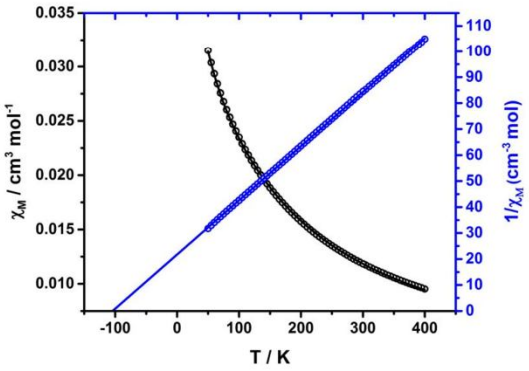

Figure S7: Thermal variation of χ_M vs. temperature (black circles) and of χ_M^{-1} vs. temperature (blue circles) of H_2O@Cr-MIL-101. The black and blue lines represent fits of χ_M vs. T and χ_M^{-1} vs. T (rms = $5.8 \cdot 10^{-5}$), respectively, with the Bleany-Bowers equation (Eq. S7). The fit of χ_M^{-1} vs. T (blue line) yielded a Curie constant C of 4.795 $cm^3\ mol^{-1}$ K and a Weiss temperature of -102 K. C corresponds to μ_{eff} = 3.566 per Cr^{3+} ion.

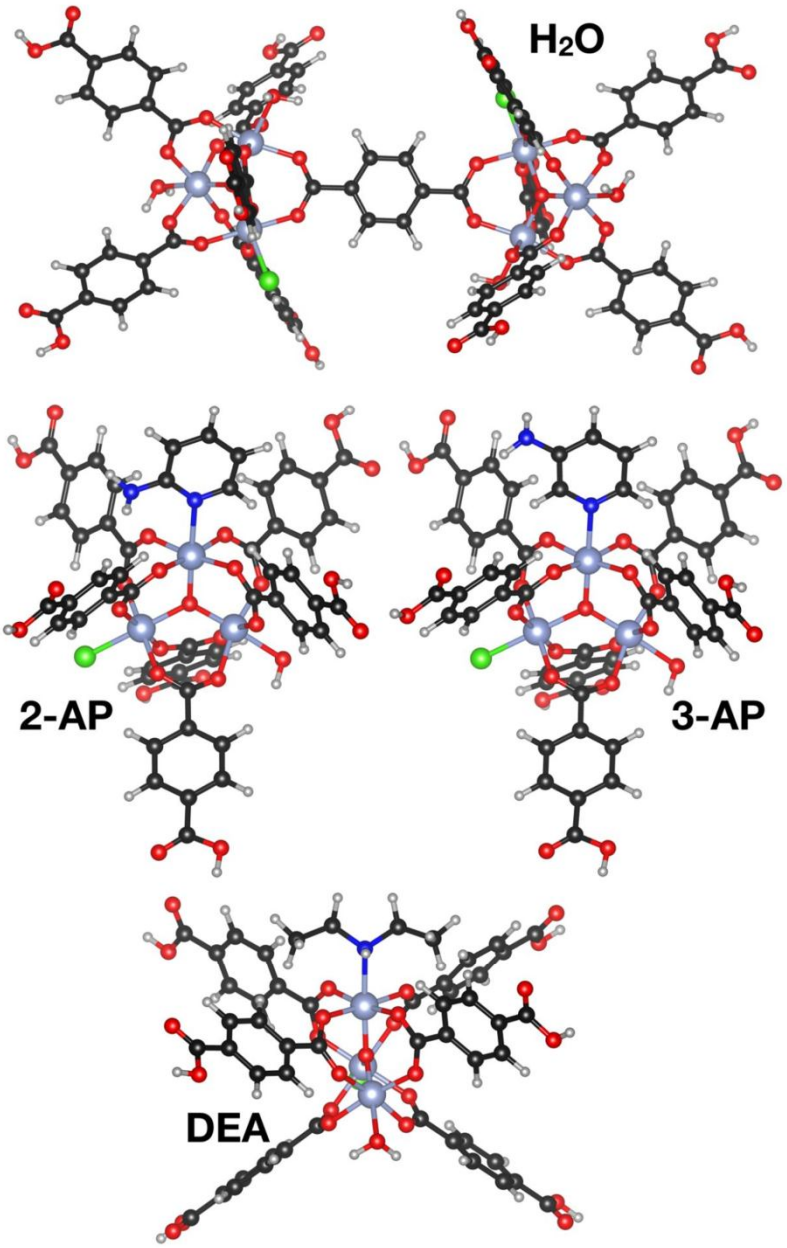

Figure S8: DFT-optimized fragment clusters used for the computational work: a) H_2O@Cr-MIL-101, b) 2-AP@Cr-MIL-101, c) 3-AP@Cr-MIL-101, and d) DEA@Cr-MIL-101.

^{13}C spin-lattice relaxation for X@Cr-MIL-101

Table S5: Observed ^{13}C spin-lattice relaxation times T_1 for X@Cr-MIL-101 and derived distance sums R_{exp} together with the assignment and the corresponding R_{DFT} values. For all compounds the resonance at -350 ppm which is assigned to the carbon atoms **2**, **7** of the bdc linkers was used as reference.

X	Assignment	δ (^{13}C) / ppm	^{13}C T_1 / ms	R_{exp}/ 10^{-4}Å^{-6}	R_{DFT} / 10^{-4}Å^{-6}
H_2O	**3, 4, 5, 6**	130	9.55	2.10	1.80
	2, 7	-350	5.48	ref.	3.66
	1, 8	---	---	---	30.3
2-AP	**3, 4, 5, 6**	130	9.515	2.09	1.49
	2, 7	-350	5.74	ref.	3.48
	9	415	2.71	7.36	9.53
	13	415	2.71	7.36	13.3
	12	49	11.79	1.69	1.57
	10	-4	12.77	1.56	1.29
	11	192	22.17	0.90	0.74
3-AP	**3, 4, 5, 6**	130	10.74	1.74	1.41
	2,7	-350	5.55	ref.	3.37
	14, 18	468	2.72	8.40	12.7
	17	-20	10.56	1.80	1.50
	15	-59	10.74	1.79	1.49
	16	246	20.50	0.96	0.77
DEA	**3, 4, 5, 6**	130	11.75	1.55	1.44
	2,7	-350	5.38	ref.	3.39
	19	47	14.19	1.24	1.27
	20	13	15.08	1.22	1.21
	19'	300	2.71	7.56	7.27
	20'	-46	8.28	3.40	2.22

The broad signal around 415 ppm is assigned to the *ortho* carbon atoms **9** and **13** of 2-AP, which could not be resolved experimentally. As mentioned in the manuscript the closeness to the paramagnetic centres accounts for the deviation of the calculated and observed distance sums. Nevertheless, the intensity reduction of the ^{13}C{^{1}H} REDOR spectra (Figure S9 and Table S7), which is too small for a CH unit suggests that the signals of a quaternary carbon atom and a CH units are superimposed.

$^{13}C\{^{1}H\}$ REDOR dephasing of for X@Cr-MIL-101

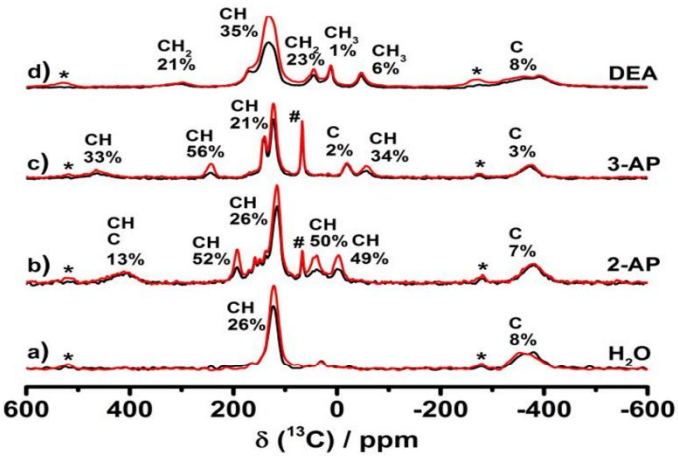

Figure S9: ^{13}C MAS NMR spectra without (red lines) and with ^{13}C-^{1}H dipolar dephasing (black lines) of a) H_2O@Cr-MIL-101, b) 2-AP@Cr-MIL-101, c) 3-AP@Cr-MIL-101, d) DEA@Cr-MIL-101. Key: # ^{13}C signal of the solvent 1,4-dioxane; * spinning side bands.

Since maximal only one spinning side band was observed for all ^{13}C NMR resonances, the anisotropic part of the hyperfine interaction is below 250 ppm for all carbon atoms. The corresponding values for the ^{1}H MAS NMR spectra (Figure S10) are given in Table S6.

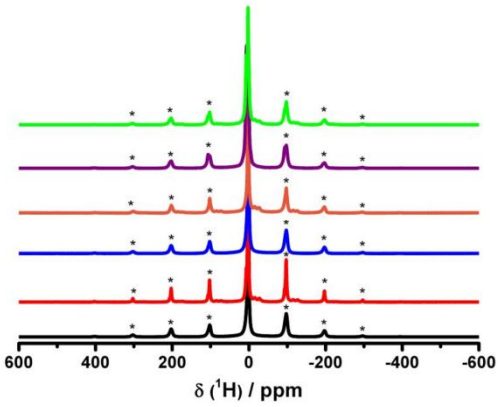

Figure S10: ^{1}H MAS NMR spectra of H_2O@Cr-MIL-101 (black), 2-AP@Cr-MIL-101 (red), 3-AP@Cr-MIL-101 (blue), DEA@Cr-MIL-101 (orange), 2-AP+DEA@Cr-MIL-101 (violet) and 3-AP+DEA@Cr-MIL-10 (green). Key: * spinning sidebands.

Table S6: ^{1}H offset and δ_{hyper} values for the calculation of the dephasing value for L-histidine.

Chemical group	δ_{iso} ^{1}H / ppm	δ_{aniso} (^{1}H) / ppm
CH_{bdc}	200	200
$CH_{3\text{-}AP}$	200	200
CH_2	200	235

$^{13}C\{^1H\}$ REDOR dephasing with L-histidine·HCl·H_2O as model compound

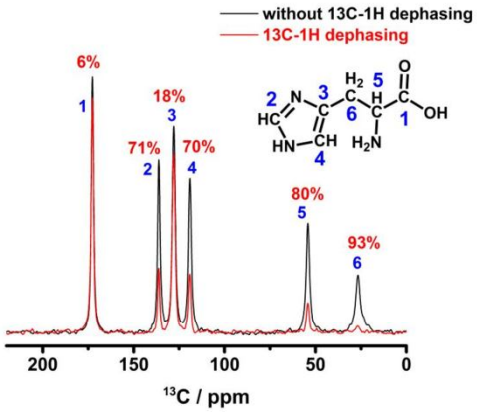

Figure S11: ^{13}C CP MAS NMR spectra of L-histidine hydrochloride with ^{13}C-^1H dephasing (red curve) and without ^{13}C-^1H dephasing (black curve) ($\tau_{deph} = 2 \cdot \tau_{rot} = 50$ µs). The values given in red represent the intensity reduction of the $^{13}C\{^1H\}$ REDOR spectrum.

We estimated the dephasing efficiency of the ^{13}C NMR resonances of C, CH, CH_2 and CH_3 units by simulations for diamagnetic molecular solids without pronounced dynamical disorder based on spin systems derived from L-histidine hydrochloride monohydrate (Figure S11). To simulate the influence of molecular motion and a potential hyperfine interaction on the REDOR dephasing we set up several SIMPSON[30] NMR calculations using our in-house modelling software. For L-histidine · H2O · HCl the crystal structure from the literature[31] was optimized using CASTEP 17.2[32] with the PBE[33] functional and the semi-empirical dispersion correction scheme by Tkatchenko and Scheffler.[34] No symmetry was imposed on the structures and calculations were performed with fixed cell constants. A basis set energy of 900 eV and 4 Monkhorst-Pack grid k-points were used. Then, chemical shifts were calculated[35] and included in the creation of the SIMPSON spin system input data. With our software, we set up several of these calculations with one central carbon atom and a varying number of surrounding ^1H atoms.
All SIMPSON simulations were carried out using the "direct computation mode" where the time evolution of the density matrix is evaluated in a point to point fashion starting with single quantum coherence on the carbon channel ($\hat{I}_x$ start operator). The time steps for which the interaction Hamiltonian is considered to be time independent was set to 1 µs and the REPULSION scheme[36] was used to model random crystallite orientations typical for a powder. For all spins included, the CSA and dipolar interaction tensors were incorporated using coupling constants δ and asymmetry parameters η for the anisotropy as well as Euler angle sets (α, β, γ) for their orientation as extracted from the quantum mechanical calculations. To determine a reasonable but sufficiently large number of crystallite orientations and gamma angles for the simulations, we tested their convergence exemplarily for carbon atom C2 (CH unit). The spin system was set up with a central ^{13}C carbon nucleus and all protons within a sphere of 3 Å around the ^{13}C spin, which includes the covalently bonded proton and two additional ones (see Listing 1 for the SIMPSON input file). The results depicted in Figure S12 show that beyond 144 powder and 4 gamma angles only small changes for the dephasing ΔS occur. All simulations were carried out with 320 crystallite orientations and 18 [illegible] angles.

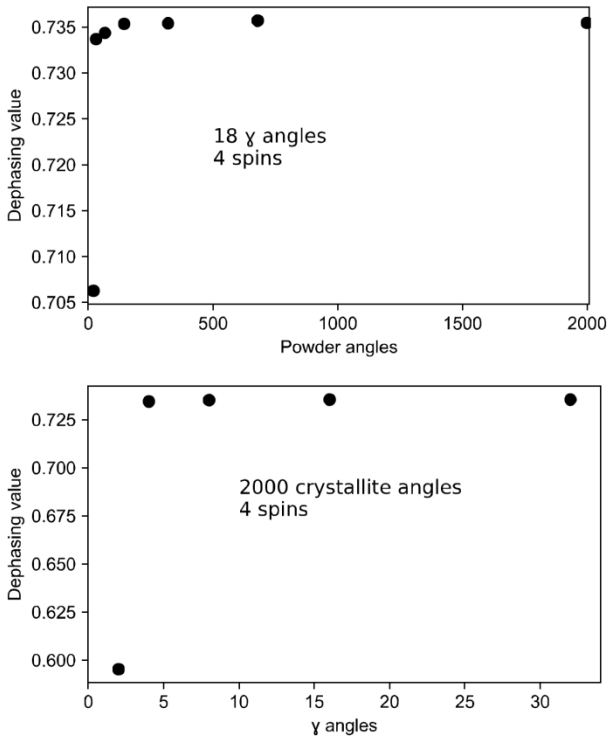

Figure S12: ^{13}C-^{1}H dephasing values of the histidine C2 atom, using varying number of crystallite orientations. Top: Number of crystallite orientations following the REPULSION scheme, while using 18 γ angles. Bottom: Number of γ angles, while using 2000 REPULSION angles.

To test whether the number of proton spins within the limit of 3 Å chosen for the simulations is sufficient to extract meaningful ΔS values, additionally, the effect of the spin system size was evaluated exemplarily for one C (C1), CH (C2) and CH2 (C6) unit, respectively. Their convergence is given in Figure S13 and demonstrates that spin system sizes between 4 spins for C2 and 9 spins for C1 are sufficient to reach an accuracy of about 3 %. Due to dipolar truncation, for CH and CH_2 units significantly smaller spins system sizes are sufficient compared to quaternary ^{13}C nuclei. Since we expect larger variations on the order of 10 % when changing from one material to another due to changes of the dipolar coupling constants a radius of 3 Å turned out to be sufficient for the simulations.

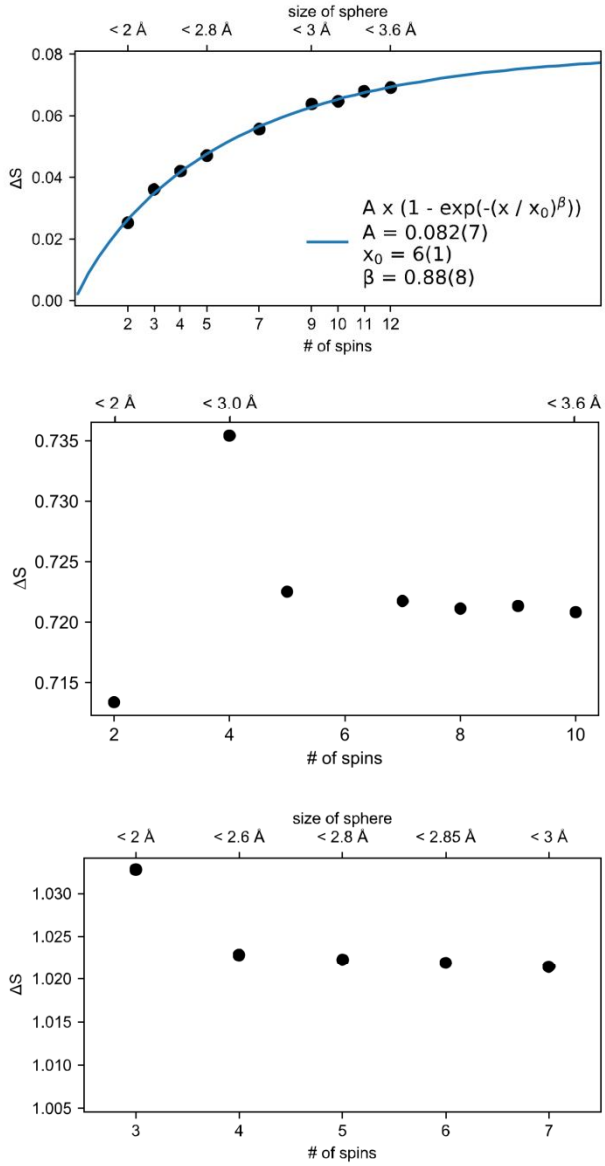

Figure S13: ^{13}C-^{1}H dephasing values ΔS for top) C (C1), middle) CH (C2) and bottom) CH_2 (C6) units of histidine, taking into account a varying number of surrounding ^{1}H atoms.

To additionally probe the influence of the small angle motion the dipolar coupling constants were reduced by 10 and 15%, respectively (Figure S14). Additionally, the influence of the hyperfine interaction on the dephasing efficiency was simulated by altering the spin systems in their isotropic and anisotropic chemical shift parameters for both ^{13}C and ^{1}H (Figure S15). The corresponding values δ_{iso} and δ_{aniso} were estimated from the experimental ^{13}C and ^{1}H spectra (Figures S9 and S10) and the thus determined parameters are listed in Table S6.
For dephasing times τ_{deph}, as short as one rotor period the following regions for the intensity reduction were identified and listed in Table S7. They agree well to the experimental findings (Figure S11). The dephasing efficiency for the methyl groups is weak due to the fast methyl rotation, which reduces the dipole couplings by a factor of three.[37,38] These results are in line with findings of Ishii et al.[39,40] For the X@Cr-MIL-101, on average the dephasing becomes less effective by roughly 15 % for CH and CH_2 and by about 5 % for C and CH_3 (Table S7 and Figure S14). This reduction is mainly caused by the hyperfine shifts of the protons, while the hyperfine interaction for the carbon atoms has little effect (Figure S15).

Table S7: Expected intensity reduction ΔS in percent within a $^{13}C\{^{1}H\}$ REDOR experiment for $\tau_{deph} = 2 \cdot \tau_{rot}$ for diamagnetic and X@Cr-MOL-101 without dynamic disorder. For details of the simulation refer to Figures S14 and S15.

ΔS / %	**C**	**CH**	**CH_2**	**CH_3**
Diamagnetic	8 ± 3	80 ± 10	97 ± 8	10 ± 10
Paramagnetic	3 ± 3	65 ± 10	82 ± 8	5 ± 10

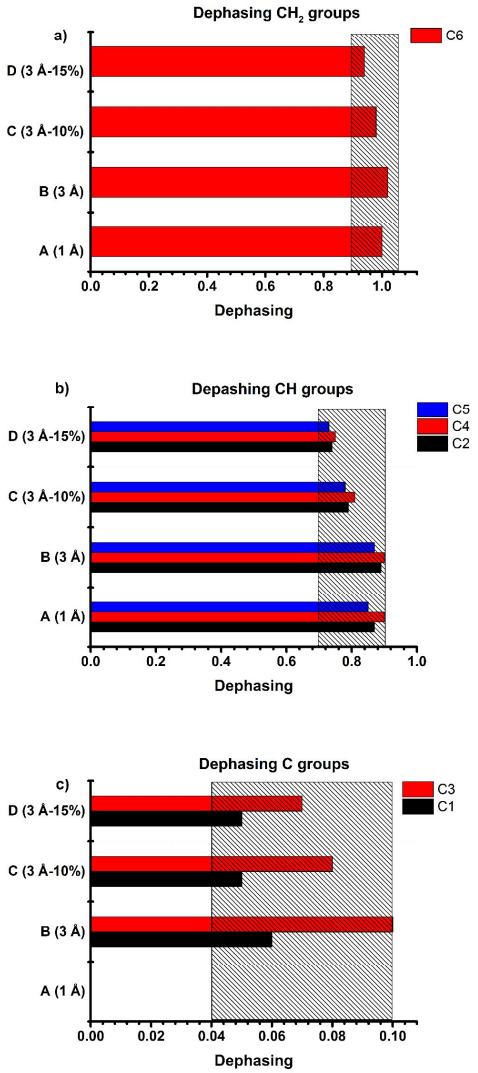

Figure S14: ^{13}C-^{1}H dephasing values of the a) CH_2, b) CH and c) C units after taking into account all protons in the neighbourhood of 1 Å (spin system A) and 3 Å (spin system B). Additionally, the influence of the small angle motion was simulated by reducing the dipolar coupling constant of spin system B by 10% and by 15%, resulting in spin system C and D, respectively. The grey boxes represent the acceptable dephasing regions for the respective chemical groups.

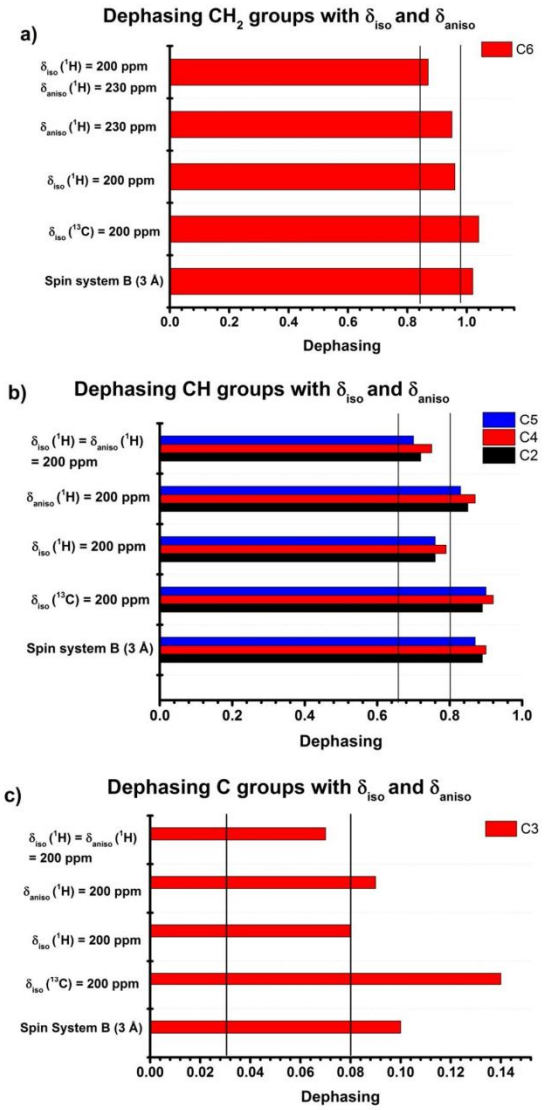

Figure S15: ^{13}C-^{1}H dephasing values of the a) CH_2, b) CH and c) C units for spin system B under the influence of chemical shift type hyperfine interaction for the proton and the carbon nuclei. The values for the isotropic offset (δ_{iso}) and the anisotropic coupling constant (δ_{aniso}) were estimated from the experimentally determined parameters (Table S6). The dephasing values under the influence of the hyperfine interaction are marked with the left black vertical line. The right black lines mark the values without the hyperfine interaction.

Influence of large-angle jumps on the $^{13}C\{^1H\}$ REDOR dephasing

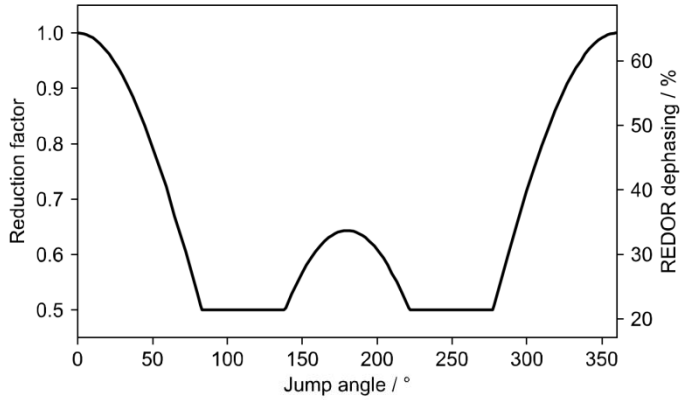

Figure S16: Reduction factor of the $^{13}C\{^1H\}$ dipolar coupling constant (left y axis) and the corresponding REDOR dephasing value (right y axis) for the C–H carbon atom of the bdc unit for a two site reorientational jump. The flip angle is the opening angle between the two sites. Reduced coupling constants were calculated by averaging the dipolar tensors with both sites. The REDOR dephasing values were calculated with an additional 15% reduction of the coupling constant to take librational motions into account. Only directly bonded protons were included in the SIMPSON simulations. The value of the static C–H coupling was -23.5 kHz and the ^1H CSA anisotropy was set to -200 ppm.

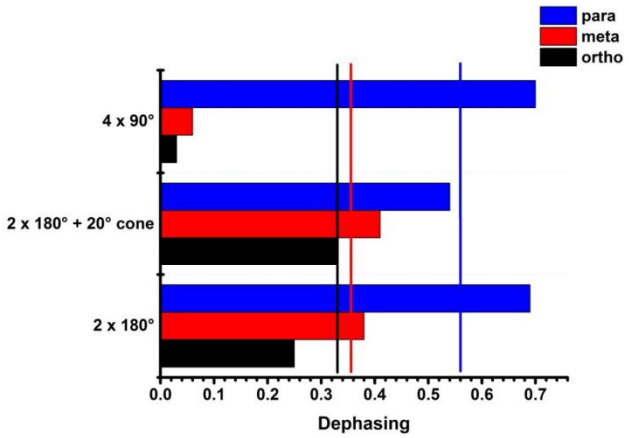

Figure S17: $^{13}C\{^1H\}$ REDOR dephasing values of the ortho, meta and para C-H units of 3-AP grafted to the CUS of Cr-MIL-101 for reorientational 90° jumps and 180° jumps of the 3-AP molecules around the Cr-N axis. Additionally, a jump model is considered where the 180° reorientation is overlaid with toggling motion around a half cone angle of 20°. The vertical lines represent the corresponding experimental dephasing values. Calculations were performed as described in Figure S16.

```
spinsys {
  channels 13C 1H
  nuclei 13C 1H 1H 1H
  shift 1 62.7p -89.92650131449896p 0.2034120030365161 27.000404335
86.6229431501 -30.4955059426
  shift 2 205.94p -207.220167606933217p 0.23469181159900376 0 0 0
  shift 3 214.8p -217.89932248611956p 0.2851857008429031 0 0 0
  shift 4 209.92p -209.916655312794873p 0.5678786206888683 0 0 0
  dipole 1 2 -23450.3574988 0.0 146.795199876 59.4695735096
  dipole 1 3 -3212.24998106 -0.0 112.119681686 -118.080023987
  dipole 1 4 -3356.78425517 0.0 46.7381910769 59.7548613545
  dipole 2 3 -7214.17889566 -0.0 87.4047555941 -118.652259927
  dipole 2 4 -7594.20185998 0.0 21.4731456273 59.9398618345
  dipole 3 4 -1718.54157564 0.0 57.3831188035 60.9749091645
}

par {
  proton_frequency 400e6
  spin_rate        40000.
  sw               spin_rate*2.0
  np               2
  crystal_file     rep320
  gamma_angles     18
  start_operator   I1x
  detect_operator  I1p
  verbose          1
  variable rf1H      180000.
  variable rf13C     125000.
}

proc pulseq {} {
  global par

  maxdt 1.0

  set t180H [expr 0.5e6/$par(rf1H)]
  set t180C [expr 0.5e6/$par(rf13C)]
  set tr2 [expr 0.5e6/$par(spin_rate)-$t180H*0.5]
  set tr3 [expr $tr2-$t180C*0.5]

  reset
  acq
  delay $tr2
  pulse $t180H 0 x $par(rf1H) x
  delay $tr3
  pulse $t180C $par(rf13C) x 0 x
  delay $tr3
  pulse $t180H 0 x $par(rf1H) x
  delay $tr2
  acq

}

proc main {} {
  global par

  set    f [fsimpson]
  fsave $f $par(name).fid
}
```

Listing 1: Exemplary input file for the SIMPSON simulation of the histidine C2 CH group, including a correction for the hyperfine interaction by the inclusion of an additional CSA anisotropy of 200 ppm.

Comparison between calculated and experimental ^{13}C and ^{1}H hyperfine shifts

Table S8: Comparison of calculated[a] and observed isotropic ^{13}C chemical shifts.

	^{13}C calculated (ppm)				^{13}C observed (ppm)	
Signal	δ_{orb}	δ_{FC}	δ_{PC}	δ_{total}	δ_{FC}	δ_{total}
X = H_2O						
1, 8	180.62	1502.72	0.04	1683.38	---	---
2, 7	140.41	-552.08	0.03	-411.65	-523	-350
3, 4, 5, 6	134.92	-6.44	0.03	128.51	0	130
X = 2-AP						
9	164.08	231.37	0.05	395.50	251	415
10	111.85	-145.45	0.00	-33.60	-116	-4
11	145.62	89.72	0.01	235.35	46	192
12	113.56	-125.81	-0.03	-12.28	-65	49
13	156.47	288.08	-0.07	444.48	251	415
X = 3-AP						
14	143.92	313.56	-0.03	457.45	324	468
15	127.98	-254.68	-0.03	-126.92	-187	-59
16	125.38	164.77	0.02	290.17	121	246
17	146.84	-226.92	0.00	-80.09	-167	-20
18	141.84	316.82	0.06	458.71	324	468
X = DEA						
19'	51.77	193.81	-0.01	245.57	248	300
20'	18.00	-18.48	-0.01	0.49	-59	-46

[a]All cluster-model computations were done using IGLO-II/9s7p4d basis sets. Orbital shielding, HFC and g-tensor were computed with the PBE40 hybrid functional, ZFS contributions with the PBE functional (see Computational Details in main text). Eq. 1 (main text) with a temperature of 325 K and a Weiss constant Θ = -102 K taken from experiment (Figure S7) were used. ^{13}C shifts were referenced to tetramethylsilane (TMS) at the same level ($\sigma_{ref}^{C} = 189.23$ ppm).

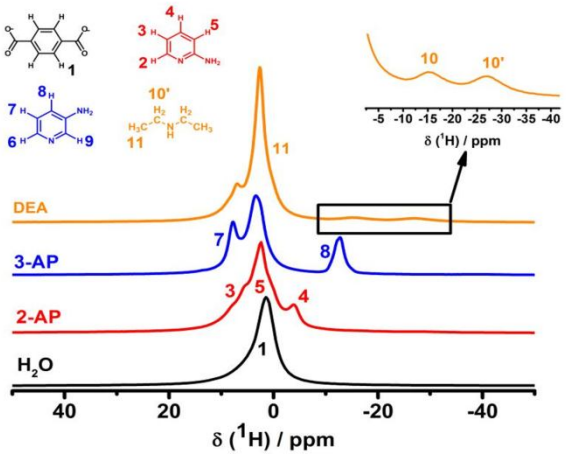

Figure S18: ^{1}H NMR MAS spectra of H_2O@Cr-MIL-101 (black), 2-AP@Cr-MIL-101 (red), 3-AP@Cr-MIL-101 (blue) and DEA@Cr-MIL-101 (orange).

Table S9: Comparison of calculated[a] and observed isotropic ^{1}H chemical shifts.

	^{1}H calculated (ppm)				^{1}H observed (ppm)	
Signal	δ_{orb}	δ_{FC}	δ_{PC}	δ_{total}	δ_{FC}	δ_{total}
X = H_2O						
1	8.22	-4.56	0.03	3.69	-5.22	3.00
X = 2-AP						
2	8.41	-41.91	0.00	-33.50	---	---
3	6.49	3.42	0.00	9.91	4.01	10.50
4	7.64	-14.37	0.00	-6.73	-11.64	-4.00
5	6.43	-5.29	0.00	1.14	-4.38	2.05
X = 3-AP						
6	8.35	-62.12	0.04	-53.73	-49.35	-41.00
7	7.21	7.24	-0.01	14.43	6.03	13.24
8	7.18	-24.86	0.00	-17.68	-19.83	-12.65
9	8.25	-61.43	-0.10	-53.28	-49.25	-41.00
X = DEA						
10	3.00	-19.21	0.00	-16.22	-18.50	-15.50
10'	2.45	-26.87	-0.01	-24.27	-29.45	-27.00
10"	3.54	-11.56	0.00	-8.01	---	---
11	1.54	0.55	0.00	2.09	---	---

[a]All cluster-model computations were done using IGLO-II/9s7p4d basis sets. Orbital shielding, HFC and g-tensor were computed with the PBE40 hybrid functional, ZFS contributions with the PBE functional (see Computational Details in main text). Eq. 1 (main text) with a temperature of 325 K and a Weiss constant Θ = -102 K (Figure S7) taken from experiment were used. ^{1}H shifts were referenced to tetramethylsilane (TMS) at the same level ($\sigma_{ref}^H = 31.68$ ppm).

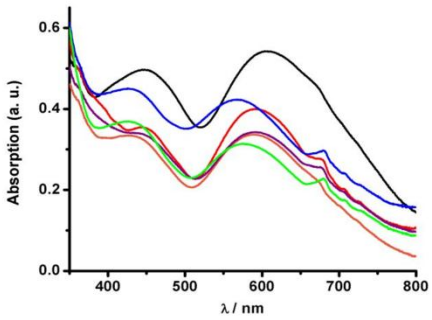

Figure S19: Diffuse reflectance UV-vis spectra of H_2O@Cr-MIL-101 (black lines), 2-AP@Cr-MIL-101 (red lines), 3-AP@Cr-MIL-101 (blue lines), DEA@Cr-MIL-101 (orange lines), 2-AP+DEA@Cr-MIL-101 (violet lines), 3-AP+DEA@Cr-MIL-101 (green lines).

The UV-vis spectra of the Cr-MIL-101 derivatives (Figure S19) show absorption bands at around 450 nm and around 600 nm for the d-d transitions of Cr^{3+}.[41] Since the transition at around 400 nm might be affected by the much stronger ligand to metal charge transfer, we rely only on the transition band at around 600 nm for the following discussion. DEA, 2-AP and 3-AP cause blueshifts from 608 nm for H_2O@Cr-MIL-101 to 592 nm, 593 nm and 568 nm, respectively. This indicates the strongest interaction of Cr^{3+} with 3-AP while DEA and 2-AP exhibit similar and smaller shifts. However, in case of loading two N-donor compounds simultaneously, the UV-vis spectra of, particularly, 2-AP+DEA@Cr-MIL-101 (590 nm) are not decisive for determining the coordinated compound (Figure S19). The spectrum of 3-AP+DEA@Cr-MIL-101 with an absorption maximum at 577 nm, which is in the middle between the respective maxima for the single components, indicates that both species might be coordinated to the CUS (Figure 2).

References

(1) Vaara, J.; Rouf, S. A.; Mares, J. *J. Chem. Theory Comput.* **2015**, *11*, 4840.
(2) Kurland, R. J.; McGarvey, B. R. *J. Magn. Reson.* **1970**, *2*, 286.
(3) Blundell, S. *Magnetism in Condensed Matter (Oxford Master Series in Physics)*, 1st ed.; Oxford University Press: Oxford, 2001.
(4) Chernova, N. A.; Nolis, G. M.; Omenya, F. O.; Zhou, H.; Li, Z.; Whittingham, M. S. *J. Mater. Chem.* **2011**, *21*, 9865.
(5) Cahill, L. S.; Chapman, R. P.; Kirby, C. W.; Goward, G. R. *Appl. Magn. Reson.* **2007**, *32*, 565.
(6) Kim, J.; Middlemiss, D. S.; Chernova, N. A.; Zhu, B. Y. X.; Masquelier, C.; Grey, C. P. *J. Am. Chem. Soc.* **2010**, *132*, 16825.
(7) Clement, R. J.; Pell, A. J.; Middlemiss, D. S.; Strobridge, F. C.; Miller, J. K.; Whittingham, M. S.; Emsley, L.; Grey, C. P.; Pintacuda, G. *J. Am. Chem. Soc* **2012**, *134*, 17178.
(8) Middlemiss, D. S.; Ilott, A. J.; Clément, R. J.; Strobridge, F. C.; Grey, C. P. *Chem. Mater.* **2013**, *25*, 1723.
(9) Arbuznikov, A. V; Vaara, J.; Kaupp, M. *J. Chem. Phys.* **2014**, *120*, 2127.

(10) Rouf, S. A.; Mares, J.; Vaara, J. *J. Chem. Theory Comput.* **2015**, *11*, 1683.
(11) Bertini, I.; Turano, P.; Vila, A. J. *Chem. Rev.* **1993**, *93*, 2833.
(12) Bertini, I.; Luchinat, C.; Parigi, G. *Prog. Nucl. Magn. Reson. Spectrosc.* **2002**, *40*, 249.
(13) Bertini, Ivano; Luchinat, Claudio; Parigi, Giacomo; Ravera, E. *NMR of Paramagnetic Molecules. Applications to Metalloproteins and Models.*, 2nd ed.; Elsevier: Amsterdam, 2016.
(14) Nayeem, A.; Yesinowski, J. P. *J. Chem. Phys.* **1988**, *89*, 4600.
(15) Bertmer, M. *Solid State Nucl. Magn. Reson.* **2016**, *81*, 1.
(16) Aime, S., Bertini, I., Luchinat, C. *Coord. Chem. Rev.* **1996**, *150*, 77.
(17) Bertini, I.; Galas, O.; Luchinat, C.; Parigi, G.; Spina, G. *J. Magn. Reson.* **1998**, *130*, 33.
(18) Machonkin, T. E. *Inorg.Chem.* **2005**, *44*, 779.
(19) Sharp, R. *Prog. Nucl. Magn. Reson. Spectrosc.* **2001**, *38*, 115.
(20) Berliner, L. J.; Reuben, J. *NMR of Paramagnetic Molecules*; Springer Science+Business Media: New York, 1993; Vol. 12.
(21) Honda, Makoto; Morita, Makoto; Date, M. *J. Phys. Soc. Japan* **1992**, *61*, 3773.
(22) Bencini, A.; Gatteschi, D. *EPR of Exchange Coupled Systems*; Springer: Berlin, 1990.
(23) Graaf, C. De; Broer, R. *Magnetic Interactions in Molecules and Solids*; Springer: Cham/Switzerland, 2016.
(24) Kahn, O. *Molecular magnetism*; VCH Publishers, Inc.: New York (USA), 1993.
(25) Ferrer, S.; Lloret, F.; Pardo, E.; Clemente-Juan, J. M.; Liu-Gonzalez, M.; Garcia-Granda, S. *Inorg.Chem.* **2012**, *51*, 985.
(26) Aime, S., Bertini, I., Luchinat, C. *Coord. Chem. Rev.* **1996**, *150*, 131.
(27) Clementini, V.; Luchinat, C. *Acc. Chem. Res.* **1998**, *31*, 351.
(28) Lebedev, O. I.; Millange, F.; Serre, C.; Van Tendeloo, G.; Férey, G. *Chem. Mater.* **2005**, *17*, 6525.
(29) Stoll, S.; Schweiger, A. *J. Magn. Reson.* **2006**, *178*, 42.
(30) Bak, M.; Rasmussen, J. T.; Nielsen, N. C. *J. Magn. Reson.* **2000**, *147*, 296.
(31) Fuess, H.; Hohlwein, D.; Mason, S. A. *Acta Crystallogr. Sect. B Struct. Crystallogr. Cryst. Chem.* **1977**, *B33*, 654.
(32) Clark, S. J.; Segall, M. D.; Pickard, C. J.; Hasnip, P. J.; Probert, M. I. J.; Refson, K.; Payne, M. C. *Zeitschrift für Krist. - Cryst. Mater.* **2005**, *220*, 567.
(33) Perdew, J. P.; Burke, K.; Ernzerhof, M. *Phys. Rev. Lett.* **1996**, *77*, 3865.
(34) Tkatchenko, A.; Scheffler, M. *Phys. Rev. Lett.* **2009**, *102*, 73005.
(35) Pickard, C. J.; Mauri, F. *Phys. Rev. B* **2001**, *63*, 2451011.
(36) Bak, M.; Nielsen, N. C. *J. Magn. Reson.* **1997**, *125*, 132.
(37) Gullion, T. *Concepts Magn. Reson. Part A* **1998**, *10*, 277.
(38) Bärwinkel, K.; Herling, M. M.; Rieß, M.; Sato, H.; Li, L.; Avadhut, Y. S.; Kemnitzer, T. W.; Kalo, H.; Senker, J.; Matsuda, R.; Kitagawa, S.; Breu, J. *J. Am. Chem. Soc* **2017**, *139*, 904.
(39) Ishii, Y.; Wickramasinghe, N. P.; Chimon, S. *J. Am. Chem. Soc* **2003**, *125*, 3438.
(40) Wickramasinghe, N. P.; Shaibat, M. A.; Jones, C. R.; Casabianca, L. B.; De Dios, A. C.; Harwood, J. S.; Ishii, Y. *J. Chem. Phys.* **2008**, *128*, 1.
(41) Tadros, A. M.; Royko, M. M.; Kelley, S. P.; Belmore, K.; Rogers, R. D.; Vincent, J. B. *Polyhedron* **2015**, *100*, 17.

7 Publikationsliste

(1) Wittmann, T.; Siegel, R.; Reimer, N.; Milius, W.; Stock, N.; Senker, J. Enhancing the Water Stability of Al-MIL-101-NH_2 Via Postsynthetic Modification. *Chemistry - A European Journal* **2015**, *21*, 314-323.

(2) Wittmann, T.; Tschense, C. B. L.; Siegel, R.; Senker, J. Introducing Selective Host-Guest Interactions in MIL-101 Frameworks via a Multiple Hydrogen Bond Donor-Acceptor Recognition Site. *to be submitted.*

(3) Wittmann, T.; Mondal, A.; Tschense, C. B. L.; Wittmann, J. J.; Klimm, O.; Siegel, R.; Corzilius, B.; Weber, B.; Kaupp, M.; Senker, J. Probing the Interaction of N-Donor Guests with the Open Metal Sites of Paramagnetic Cr-MIL-101: A Solid-State NMR Spectroscopic and Density Functional Theory Study. *J. Am. Chem. Soc.* **2018**, *140*, 6, 2135-2144.

(4) Tobias W. Kemnitzer, Carsten B. L. Tschense, Thomas Wittmann, Ernst A. Roessler, and Jürgen Senker. Exploring local disorder within CAU-1 frameworks using hyperpolarized 129Xe NMR spectroscopy. *Langmuir*, **2018**, 34 (42), pp 12538–12548.

Die vorliegende Dissertation basiert auf den Publikationen (1), (2) und (3), die in den Kapiteln 6.1, 6.2 bzw. 6.3 dargestellt sind.

8 Danksagung

An erster Stelle möchte ich mich bei meinem Doktorvater Professor Dr. Jürgen Senker bedanken: für die Möglichkeit, dieses sehr interessante Thema bearbeiten zu können, für all die wissenschaftlichen Freiheiten sowie für die zahl- und lehrreichen, wissenschaftlichen Diskussionen und Hilfestellungen.

Herzlicher Dank gebührt auch Dr. Renée Siegel für ihre bedingungslose Unterstützung am NMR Spektrometer, ohne die so manches nicht möglich gewesen wäre. Ebenfalls möchte ich mich herzlich bei Beate Bojer für die EDX-Messungen und ihre unermüdliche Hilfsbereitschaft bei NMR-, vor allem für die Hilfe zum Durchbruch bei den paramagnetischen NMR-Messungen und für die vielen lustigen Unterhaltungen bedanken. Ebenfalls bedanke ich mich bei Lena Geiling für die Physisorptionsmessungen, bei Sonja Lutschinger und Florian Puchtler für AAS-Messungen sowie bei Petra Seidler und Iris Raithel für ihre stete Hilfe zur reibungslosen Bewältigung des bürokratischen Aufwandes.

Vielen Dank auch an Ottokar Klimm und Prof. Dr. Birgit Weber (Lehrstuhl Anorganische Chemie II, Universität Bayreuth), Dr. Wolfgang Milius (Lehrstuhl Anorganische Chemie I, Universität Bayreuth), Arobendo Mondal und Prof. Dr. Martin Kaupp (TU Berlin), Dr. Johannes Wittmann und Dr. Björn Corzilius (Goethe-Universität Frankfurt am Main) sowie an Dr. Nele Reimer und Prof. Dr. Norbert Stock (Christian-Albrechts-Universität zu Kiel) für die erfolgreichen Kooperationen, die maßgeblich zum Gelingen dieser Arbeit beigetragen haben.

Großen Dank spreche ich auch an Carsten Tschense und Dominik Greim für ihre Unterstützung durch Computersimulationen bei so manchen wissenschaftlichen Fragestellungen aus, ohne die ich sonst nur schwer weitergekommen wäre.

Ebenso möchte ich mich bei all meinen Praktikanten und Bachelorstudenten für die tatkräftige Unterstützung bedanken.

Ein aufrichtiger Dank gilt auch meinen Laborkollegen da unten im Keller, Paul Niemietz und Sven Dietler, für die angenehme und kameradschaftliche Atmosphäre und heiteren Diskussionen und Gespräche über und vor allem abseits der Chemie. Auch meinen anderen Kollegen aus der AC III und AC I möchte ich für die angenehme Zusammenarbeit und für die schöne Zeit am Lehrstuhl danken.

Auch meine Stammtischbrüder Benedikt Neugirg, Daniel Forberg, Toni Hille und Mathias Schlenk haben ihren Beitrag geleistet. Vielen Dank für die täglich geführten, sehr interessanten und auflockernden Gespräche während der Mittags- und Kaffeepausen und allen spaßigen Unternehmungen außerhalb der Uni.

Der größte Dank aber gilt Vera, die liebevoll während der gesamten Zeit mit mir durch alle Höhen und Tiefen gegangen ist und meiner Familie für ihren ständigen und bedingungslosen Rückhalt aller Art.

9 (Eidesstattliche) Versicherungen und Erklärungen

(§ 8 Satz 2 Nr. 3 PromO Fakultät)

Hiermit versichere ich eidesstattlich, dass ich die Arbeit selbständig verfasst und keine anderen als die von mir angegebenen Quellen und Hilfsmittel benutzt habe (vgl. Art. 64 Abs. 1 Satz 6 BayHSchG).

(§ 8 Satz 2 Nr. 3 PromO Fakultät)

Hiermit erkläre ich, dass ich die Dissertation nicht bereits zur Erlangung eines akademischen Grades eingereicht habe und dass ich nicht bereits diese oder eine gleichartige Doktorprüfung endgültig nicht bestanden habe.

(§ 8 Satz 2 Nr. 4 PromO Fakultät)

Hiermit erkläre ich, dass ich Hilfe von gewerblichen Promotionsberatern bzw. –vermittlern oder ähnlichen Dienstleistern weder bisher in Anspruch genommen habe noch künftig in Anspruch nehmen werde.

(§ 8 Satz 2 Nr. 7 PromO Fakultät)

Hiermit erkläre ich mein Einverständnis, dass die elektronische Fassung der Dissertation unter Wahrung meiner Urheberrechte und des Datenschutzes einer gesonderten Überprüfung unterzogen werden kann.

(§ 8 Satz 2 Nr. 8 PromO Fakultät)

Hiermit erkläre ich mein Einverständnis, dass bei Verdacht wissenschaftlichen Fehlverhaltens Ermittlungen durch universitätsinterne Organe der wissenschaftlichen Selbstkontrolle stattfinden können.

…….....

Ort, Datum Unterschrift